Université de Liège

UNIVERSITÉ DE GRENOBLE

THÈSE

Pour obtenir le grade de

DOCTEUR DE L'UNIVERSITÉ DE GRENOBLE

Spécialité: **Ingénierie-matériaux mécanique énergétique**

Arrêté ministériel : 7 août 2006

Et de

DOCTEUR EN SCIENCES DE L'UNIVERSITÉ DE LIEGE

Spécialité: **Physique**

Présentée par

Daniel LANGLEY

Thèse dirigée par **Daniel BELLET** et **Ngoc Duy NGUYEN**

préparée au sein du **Laboratoire des Matériaux et du Génie Physique et du Laboratoire de Physique des Solides, Interfaces et Nanostructures,**
dans **l'École Doctorale IMEP-2, l'École Doctorale en Sciences et The International Doctoral School of Functional Materials.**

Silver Nanowire Networks:
Effects of percolation and thermal annealing on physical properties

Thèse soutenue publiquement le **28/10/2014**,
devant le jury composé de :

Joel COURBON
Professeur, MATEIS, INSA Lyon, Président
Catherine HENRIST
Chef de Travaux, LCIS-GREENMAT, Université de Liège, Rapporteur
Vladimir LYSENKO
Chargé de recherche, INL, CNRS-INSA Lyon, Rapporteur
Mona TREGUER-DELAPIERRE
Maître de Conférences, ICMCB-CNRS, Université de Bordeaux, Examinateur
Jean-Yves RATY
Maître de Recherches F.R.S-FNRS, SPIN, Université de Liège, Examinateur
Jean-Pierre SIMONATO
Ingénieur de Recherche, CEA LITEN, Grenoble, Examinateur
Daniel BELLET
Professeur, LMGP, Grenoble INP, Directeur de thèse
Ngoc Duy NGUYEN
Professeur, SPIN, Université de Liège, Directeur de thèse

Acknowledgements:

As with any large work there are many people to thank, first and foremost my thanks go to my wonderful wife Bec, you are my muse and we have made it through this great adventure we set out on. Maybe not in the way we thought we would but the important thing is we made it! Secondly I'd like to thank my parents, as 'The Herd' say I am the sum of it all, and at this stage the majority of my time on earth has been guided by your advice, be it comedic, direct, soft or stern. Both of you have helped to mould me into the man I am. I would like to thank my sister as well for encouraging me to chase my dreams and thanks for all the support from B, Carolyn, Andrew, Dan and Basti the best in laws I could ask for.

Many thanks go to both my supervisors Daniel and Duy, it has been a challenging project to pull together over the past three years. The research meandered through many different avenues and cul-de-sacs but thanks to your guidance we have reached the end. It has truly been my pleasure to work with both of you, best of luck with your on-going collaborations and I hope that fruit would continue to come from this partnership. I also hope that we can continue to work together.

Thanks to Mél, my co-doctorante, for putting up with me for the many hours of experimental work and the many more of lengthy conversations about AgNW. Thanks for being a good friend in the lab and a great colleague but mostly thanks for being patient with my bad French! Hang in there and 'beam on'.

My final thanks go to my other family, in fact I have two additional ones, one from Liege and one from Grenoble. To those from the Kitchen of joy, thank you for making the start of my PhD so enjoyable, thankyou for welcoming me to Europe, and for hosting me all those times I have randomly dropped into whichever cities you live in now. Special thanks go to Gavril and Bilal who both hosted me on my many work visits to Liege. For team Awesome, thanks for the fun outside the lab, for the rock climbing, rafting. Summer skiing, caving and many, many board games. Truly you are all like family to me, come visit in Australia. As a mixed bag of expats and one Française we forged friendships that I hope will last a lifetime, good luck and good science!

Abstract:

The use of transparent conductive materials (TCMs) has rapidly increased in the last two decades as a result of the increasing demand for personal electronic devices and the development of thin film based solar cells. To date, the most commonly used TCM is indium tin oxide (ITO). However indium is a rare earth metal with a complex geopolitical environment surrounding its supply and production. Furthermore, the oxide family suffers from poor mechanical properties such as brittleness and generally requires either high temperature synthesis (>400°C) or vacuum processes for their deposition. For these reasons, research in recent years has focused on the discovery or the design of a TCM to replace ITO.

This thesis applies a dual approach combining simulations and experiments to explore the fabrication and optimisation of silver nanowire networks for use as a TCM and to improve the understanding of their physical properties. The simulation contribution focuses on the application of percolation modelling to 2D nanowire networks while the experimental part explores the electrical and optical properties of silver nanowire networks and their electrical behaviour under thermal annealing. We present in this work the modelling of 2D stick percolation systems initially composed of perfect idealised sticks, and then, investigate the influence of parameters such as length distributions, angular distributions or shape (curved nanowires). We address the divergence of the critical density for the onset of percolation observed for small system sizes and introduce some preliminary work on simulating the collection (or injection) efficiency of charges by a nanowire network.

The experimental component provides a discussion of the impact of wire length, wire diameter, network density and fabrication technique on the optical and electrical properties of silver nanowire networks. An in-depth study of the effect of thermal annealing on the networks properties was undertaken, which revealed several mechanisms responsible for the initial reduction of resistance and the observed final loss of conductivity. An original observation enables the revelation of geometrical quantized percolation for rather sparse networks. Finally we conclude that silver nanowire networks are an excellent prospect as a TCM to replace ITO: these materials have superior mechanical properties and enable comparable and even superior electro-optical properties.

Résumé:

L'utilisation de matériaux conducteurs transparents (TCM) a rapidement augmenté au cours des deux dernières décennies en raison de la demande croissante liée à l'usage d'appareils électroniques personnels ainsi qu'au développement de cellules solaires à base de couches minces. Jusqu'à présent, le TCM le plus couramment utilisé a été l'oxyde d'indium et d'étain (ITO), mais l'indium est une terre rare dont l'environnement géopolitique lié à son approvisionnement et à sa production est complexe. En outre, la famille des oxydes transparents conducteurs possèdent de médiocres propriétés mécaniques (associées à une fragilité mécanique) et exige souvent, pour leur dépôt, soit une synthèse à haute température (> 400 ° C) soit des procédés sous vide. Pour ces raisons, la recherche au cours des dernières années a mis l'accent sur la découverte ou l'élaboration de TCM alternatifs afin de remplacer l'ITO.

Cette thèse est abordée sur une approche double combinant simulations numériques et expériences pour explorer le dépôt et l'optimisation de réseaux de nanofils d'argent pour une utilisation comme électrode transparente d'une part, et d'améliorer la compréhension de leurs propriétés physiques d'autre part. Le volet 'simulation' concerne la modélisation de la percolation de réseaux de nanofils 2D tandis que le volet expérimental explore les propriétés électriques et optiques des réseaux de nanofils d'argent, notamment le comportement de la résistance électrique lors de recuits thermiques. Nous présentons dans ce travail la modélisation 2D de la percolation de systèmes initialement composés de bâtonnets parfaits au sein d'un réseau idéal, puis l'étude de l'influence de paramètres tels que la distribution en longueur des bâtonnets, leur distribution angulaire ou la forme de ces bâtonnets (courbure). Nous nous sommes aussi intéressés à la divergence de la densité critique nécessaire pour observer la percolation au sein de systèmes de petite taille (vis-à-vis de la longueur des bâtonnets). Par ailleurs un travail préliminaire sur la simulation de l'efficacité de collecte (ou d'injection) de charges par un réseau de nanofils est présenté.

Le volet expérimental fournit une analyse de l'influence de la longueur des fils, de leur diamètre, de la densité du réseau et enfin de la méthode de dépôt sur les propriétés optiques et électriques des réseaux de nanofils d'argent. Une étude approfondie de l'effet de recuit thermique sur les propriétés des réseaux a été réalisée, ce qui a révélé plusieurs mécanismes qui sont à l'origine de la diminution initiale de la résistance électrique à relativement basse température puis de la divergence de la résistance électrique observée à haute température. Une observation originale a permis de révéler un phénomène de percolation géométrique quantifiée pour les réseaux peu denses, qui a été associé à la présence de chemins efficaces de percolation indépendants. Ce travail permet de conclure que les réseaux de nanofils d'argent constituent une solution intéressante pour une utilisation en tant qu'électrode transparente en remplacement de l'ITO, notamment en raison de leurs propriétés mécaniques supérieures ainsi que de leurs propriétés électro-optiques comparables voire supérieures.

Table of Contents

Introduction

"We live in a society exquisitely dependent on science and technology, in which hardly anyone knows anything about science and technology."
Carl Sagan[1]

The current era is often referred to as the information age and is increasingly driven by electricity and information technology. The past century has seen the industrial revolution, two world wars, the great depression and the global economic crisis. We live in a changing world and need to take some level of responsibility for the world that we live in. The lancet report on climate change in 2009 made the statement that *"Climate change is the biggest global health threat of the 21st century."*[2] In many ways the academia of the world is responsible for the current crisis as research and development carried out in the past has led to the technologies of the present day, both good and bad. At this point in time we have an opportunity as scientists to work towards a better future, one which allows sustainable energy production and consumption as well as minimizing the inbuilt energy costs associated with advanced technology. Spending time and money on the research and development of renewable energy is an investment for our future and that of our children. The field of 'green' energy is broad and all aspects of it such as photovoltaics, high density energy storage, energy transport and energy-efficient devices are in desperate need of diligent efforts in research and development.

Applied science research has direct benefits to the community but is dependent on the underlying understanding of the world that comes from fundamental research. Fundamental research represents a quest for answers to the question "why?" without necessarily demanding an application for the outcome. As it is often difficult to see the implications and applications of fundamental research until after the questions have been answered we should aim to explore all aspects of the systems we work in, not just those for which an application is immediately obvious. As the reader will see, the present thesis addresses both these aspects: fundamental research (for instance percolation theory, geometrical quantized percolation) and applied research (collection efficiency, optimization of transparent electrodes for solar applications).

For the topic of this thesis we chose to work on Transparent Conductive Materials (TCMs), which play a large role in electronic displays, solar cells and some lighting applications. These types of materials are continuing to attract growing interest due to the high demand for personal electronic devices. Currently, Indium Tin Oxide (ITO), and more generally Transparent Conductive Oxides (TCOs), dominate the market as mature technologies which show excellent transparency (above 80%) combined with very low resistivity (of the order of $10^{-4}\ \Omega$ cm). [3]

However the synthesis of ITO requires the use of indium, a rare earth metal. Due to the scarcity of indium, a replacement for ITO needs to be found and an intense search for new indium-free TCMs is underway.[4,5] In the late 90's this search was focused on alternate TCOs; however, in recent years several new materials[6–9] have emerged to not only replace TCOs in existing applications but fulfil the requirements of future applications which TCOs cannot satisfy, such as flexibility, low temperature deposition and low fabrication cost.[3] Having at our disposal several different types of TCMs with a broad range of physical properties and behaviour will enable the selection of materials and processing methods which are matched to the needs of the application. The demand for transparent electrodes is expected to increase significantly in the next decade as they are increasingly applied to new generations of electronic devices and thin film solar cells.[10]

Among the new emerging materials, such as carbon nanotubes[11], graphene and metallic nanogrids[8,12] one of the most promising emerging TCMs are the metallic nanowire networks,[5] especially those fabricated with silver nanowires.[13,14] Extensive work has been performed to develop the synthesis of nanowires made of silver, as it exhibits the lowest resistivity at room temperature out of all the elements. This effort led to the discovery of a method to fabricate nanowires with very large aspect ratios (length divided by the diameter). Their low resistivity and high aspect ratios allow the fabrication of networks which can simultaneously conduct electricity and be transparent to visible light. These are the two most essential properties required for a transparent electrode.

The goal of this thesis is to explore the fabrication of randomly-oriented silver nanowire networks as an alternative transparent conductive material for use in solar cells or display technologies. In particular we describe the motivation for alternative transparent conductive materials to replace Indium Tin Oxide, and propound the benefits of silver nanowire networks.

Silver nanowire networks have already been shown to produce similar electro-optical properties as commercial ITO,[13,15] however, these materials are still considered an emerging TCM. Therefore, improvements in the electro-optical properties of Silver nanowires networks are expected, especially through post-deposition treatments, which, we anticipate, will lead to silver nanowire networks surpassing the opto-electrical properties of ITO.[3] Several treatments have been studied in the literature such as mechanical pressing,[16] chemical,[17] electrical,[18] and plasmonic sintering.[19]

Important parameters which govern the physical properties of nanowire networks include the network density, nanowire morphology and post-treatments. The network density is a key factor which determines the physical properties of a nanowire network: a trade-off between optical and electrical properties must be balanced to achieve optimal electrode properties as too low a nanowire density results in loss of conductivity (or carrier collection) and too dense networks will absorb too much light.

In this work the impact of wire geometries on the required density for percolation is explored by Monte Carlo simulations: this allows the investigation of the percolative nature of silver nanowire networks. As shown in the thesis,

percolation properties should be studied at the network level but also at much smaller lengths, closer to the diffusion length of carriers (for the collection of photo-generated carriers in a solar cell) when their collection efficiency is concerned. Often, a post-deposition step is required to optimize the electrical properties of the network. In this work, we have focused on the effects of thermal annealing as post-deposition treatment. We show that applying such a process helps to drastically reduce the electrical resistance of silver nanowire networks without degrading the material transparency. Although thermal annealing is widely used for such layers, surprisingly there has been very few or no systematic analysis in the literature focused on the effect of thermal annealing on the electrical resistance of metallic nanowire networks. When performing this study we observed a new phenomenon, the quantized activation of a percolating network: in a sparse network the lowering of the electrical resistance during a thermal ramp was found to occur through sudden dropping steps within a particular temperature range. We interpreted these steps with geometrical quantized percolation. A simple model is proposed and agrees well with experimental data.

This thesis consists of five chapters. The first chapter can be considered a literature review and provides the context of the thesis as well as the discussion of many of the works that have already been undertaken by other groups. It is focused on the possible applications of nanowire networks and the impetus behind the drive to replace indium tin oxide. The second chapter continues the discussion of the literature but is focused on the concept of percolation, discussing the fundamental concepts of percolation and providing the foundations for chapter 3. In chapter 3 we report the development of Monte Carlo simulations and analyse the results on the percolation in 2D systems of sticks. Chapter 4 discusses the electro-optical properties of silver nanowires and Chapter 5 provides an in-depth description of the behaviour of silver nanowire networks under thermal annealing. Finally the thesis concludes with a summary of the work and a discussion of which direction future research should take.

We hope that this work will provide you with an understanding of percolation, silver nanowire networks and their behaviour under thermal annealing. As a global objective of this work, we aimed at contributing to the study of this emerging material which will hopefully be applied in solar energy and display technologies on a large scale within the next few years. Transparent conductive materials made from silver nanowires may also be useful to other applications in different fields such as antennas, lightning, transparent heaters… for which understanding of the physical properties will be of the utmost importance.

References

[1] C. Sagan, *Demon-Haunted World: Science as a Candle in the Dark*, Random House Publishing Group, **2011**.
[2] A. Costello, M. Abbas, A. Allen, S. Ball, S. Bell, R. Bellamy, S. Friel, N. Groce, A. Johnson, M. Kett, others, *The Lancet* **2009**, *373*, 1693.
[3] G. Guisti, D. P. Langley, M. Lagrange, R. Collins, C. Jiménez, Y. Bréchet, D. Bellet, *Int. J. Nanotechnol.* **2014**, *11*, 785.
[4] R. G. Gordon, *Mrs Bull.* **2000**, *25*, 52.
[5] A. Kumar, C. Zhou, *ACS Nano* **2010**, *4*, 11.
[6] S. De, J. N. Coleman, *MRS Bull.* **2011**, *36*, 774.
[7] D. Langley, G. Giusti, C. Mayousse, C. Celle, D. Bellet, J.-P. Simonato, *Nanotechnology* **2013**, *24*, 452001.
[8] D. S. Hecht, L. Hu, G. Irvin, *Adv. Mater.* **2011**, *23*, 1482.
[9] S. Bae, H. Kim, Y. Lee, X. Xu, J.-S. Park, Y. Zheng, J. Balakrishnan, T. Lei, H. Ri Kim, Y. I. Song, Y.-J. Kim, K. S. Kim, B. Özyilmaz, J.-H. Ahn, B. H. Hong, S. Iijima, *Nat. Nanotechnol.* **2010**, *5*, 574.
[10] S. Reuter, R. Das, **2009**.
[11] B. Dan, G. C. Irvin, M. Pasquali, *ACS Nano* **2009**, *3*, 835.
[12] J. van de Groep, P. Spinelli, A. Polman, *Nano Lett* **2012**, *12*, 3138.
[13] S. De, T. M. Higgins, P. E. Lyons, E. M. Doherty, P. N. Nirmalraj, W. J. Blau, J. J. Boland, J. N. Coleman, *ACS Nano* **2009**, *3*, 1767.
[14] V. Scardaci, R. Coull, P. E. Lyons, D. Rickard, J. N. Coleman, *Small* **2011**, *7*, 2621.
[15] J.-Y. Lee, S. T. Connor, Y. Cui, P. Peumans, *Nano Lett* **2008**, *8*, 689.
[16] T. Tokuno, M. Nogi, M. Karakawa, J. Jiu, T. T. Nge, Y. Aso, K. Suganuma, *Nano Res.* **2011**, *4*, 1215.
[17] S. Magdassi, M. Grouchko, O. Berezin, A. Kamyshny, *ACS Nano* **2010**, *4*, 1943.
[18] M. L. Allen, M. Aronniemi, T. Mattila, A. Alastalo, K. Ojanperä, M. Suhonen, H. Seppä, *Nanotechnology* **2008**, *19*, 175201.
[19] E. C. Garnett, W. Cai, J. J. Cha, F. Mahmood, S. T. Connor, M. Greyson Christoforo, Y. Cui, M. D. McGehee, M. L. Brongersma, *Nat. Mater.* **2012**, *11*, 241.

Chapter 1
Motivation

1.1 Transparent Conductive Materials

This chapter provides the general context and motivation for this work. We explore the growing demand for transparent conductive materials, and the design requirements for their use in existing and emerging applications. We highlight the emerging field of indium-free transparent conductive materials, specifically the use of silver nanowires. Much of this initial chapter appeared as a review article in Nanotechnology written with our colleagues from CEA LITEN.[1] Within the framework of this thesis the article has been modified and updated to address the key literature surrounding silver nanowire growth, network fabrication, network properties and several important applications.

Thin films with a combination of high electrical conductivity and optical transparency are crucial for many modern devices such as touch panels, e-papers, organic light-emitting diodes (OLEDs), liquid-crystal displays (LCDs), and solar cells. These films are typically fabricated from transparent conductive oxides (TCOs) such as Indium Tin Oxide (ITO), Fluorine doped Tin Oxide (FTO) or Aluminium doped Zinc Oxide (AZO). Historically the majority of research and current industrial technologies for Transparent Conductive Materials (TCMs) have focused on vacuum deposition processes of TCOs. At present the dominant TCO is ITO, typically a solid solution of approximately 90% indium oxide and 10% tin oxide.[2] Currently geopolitical uncertainty associated with the global distribution of indium, and the growing demand for touch screens in consumer electronics have led to the expectation of an exponential increase in the price of indium in the near future.[3] To understand the current market environment it is quite instructive to look at the global indium production, the price history and the forecasted demand for transparent electronics. Figure 1.1 a) depicts the global indium production of 2012 broken down by country. With over 80% of world indium production being centred in Asia and 51% in China alone, indium prices are dominated by the east, western countries have minimal production apart from Canada.[4] This results in a complex geopolitical situation in which the west is heavily dependent on the east for both device manufacture and raw materials supply. For some indium producing countries such as France, Italy and Belgium[5] (representing 6% of global production) the situation is even more complex as these countries have very limited mine sources of indium. Instead of producing indium ores directly they purchase from other countries indium containing lead/zinc residues, flue dust and drosses which require special extraction techniques to obtain pure indium.[5] As a result their indium production is once again dependent on external sources.

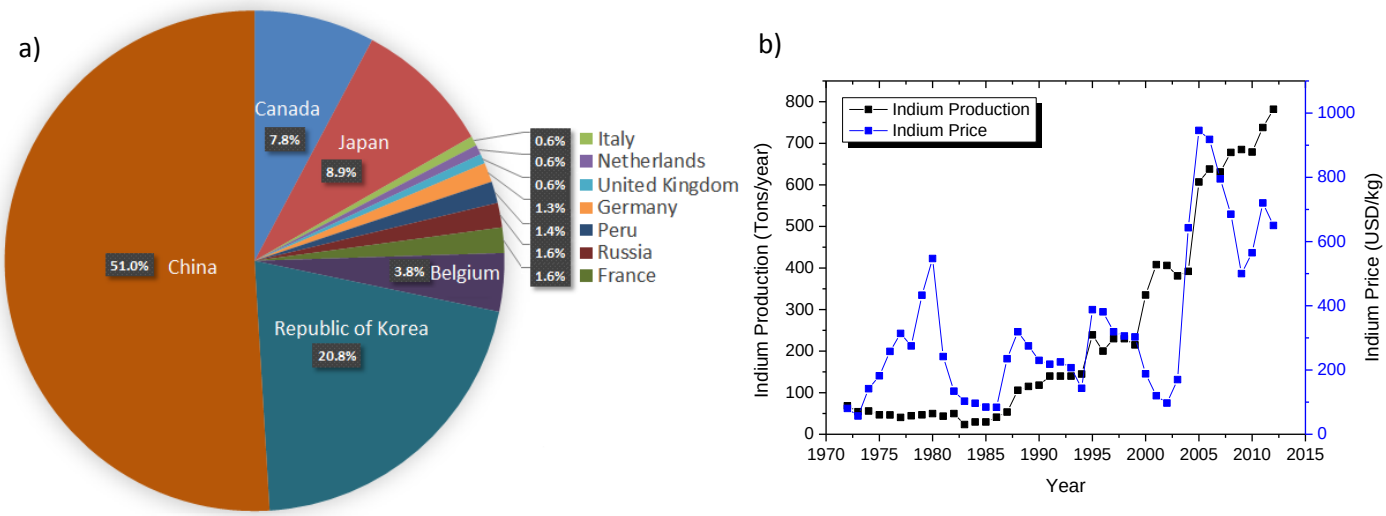

Figure 1.1 a) 2012 Indium production by country as a percentage of the total global production. b) Indium production and price history for the past 4 decades. Information extracted from the U.S. geological survey.[4]

Despite a continued growth in world indium production over the past 40 years as indicated in Figure 1.1 b) the price of indium has grown significantly. This is a result of the rapid expansion in the use of ITO in personal electronic devices. Fears of unpredictable price hikes due to potential political instabilities and expected increase in price due to limited availability of indium are the driving forces behind recent efforts to develop new indium free TCMs. Worldwide a large amount of research, both academic and industrial, is focusing on the development of earth-abundant TCMs, it is unclear yet as to which will be able to replace indium tin oxide.[3] The future of TCMs may come in the form of a TCO or one of the emerging materials such as Graphene, Carbon Nanotubes (CNTs) or metal nanowires.[6] It is likely though that no one material will be able to satisfy all of the requirements for the large variety of applications that rely on TCMs, more likely several TCMs will be used to satisfy the demands of current and emerging applications.

The role and requirements of the TCM layer can vary significantly depending on the type of device in which it will be integrated. In the case of solar cells, the transparent electrode works as the anode for extracting and separating charge carriers from the absorbing layer, as such this can be a large area electrode. Furthermore, for organic light emitting diodes (OLEDs) LCDs and touch screen applications the TCM must be patterned to address the spatial location of the interaction or pixel. The requirements associated with the fabrication of TCMs for these devices continue to grow intensively, expanding with the industrial demand for transparent electrodes in different applications.[7] Therefore numerous scientific investigations have been devoted to explore different possibilities for the fabrication of thin layers exhibiting good compromise between optical transparency and electrical conductivity. These two properties are the most important properties of a TCM though there are many others such as flexibility, toughness and chemical reactivity to name a few. The development of new TCMs is dictated by the requirements of the specific application, however

high conductivity and low optical absorption are always desirable attributes. According to Kumar and Zhou, "*Future generations of opto-electronic devices are anticipated to require conductive electrodes which are flexible, cheap and compatible with large scale manufacturing methods.*"[3]

However, TCM requirements are often application-dependent, thus it is not possible to give an overall set of ideal figures of merits for emerging flexible transparent electrodes. For instance light scattering as measured by the Haze factor (percentage of the transmitted light which is scattered) can be valuable for photovoltaics but is detrimental when electrodes are used for touch panel displays. Many parameters have to be taken into account for each specific application. Cost, optical properties, thermal stability, processability, chemical compatibility with other materials and work function are only few of the key parameters. Three emerging criteria for the next generation of electronic devices are presented in 0: transparency, electrical conductivity and mechanical flexibility, with expected performance requirements for some applications. These properties are expected to be the most important for a successful emerging TCM. Even for these principal properties, different applications require different specifications. The indications provided in table 1.1 are meant as a general guide to the average requirements of a stated application family. With respect to each property there is a broad range of requirements depending on the specific type of application that is being considered.

Table 1.1: Desired properties for the main applications of transparent conductive materials. Number of symbols indicates importance of the property to the application.

Application	Transparency	Conductivity	Flexibility
Photovoltaics	+++	+++	+
OLED/PLED	++	++	+
Film Heaters	+	+++	++
Touch Screens	+++	++	++

Whi

le TCOs are very well adapted for some applications, they suffer from significant limitations such as costly fabrication processes, scarcity (especially concerning Indium based TCOs like ITO) and brittleness. In order to overcome the issue of brittleness a variety of other materials have been intensively investigated recently such as CNTs, graphene thin films, conducting polymers, metallic grids and metal nanowire networks.[3,8–10] Of these emerging TCMs CNTs and graphene are both intrinsically good light absorbing materials, De and Coleman[6] compare CNTs, graphene flakes and Ag nanowires and identify Ag nanowires as the most promising emerging TCM. Sorel et al. also made a similar comparison but included considerations of their heat generation properties comparing the emerging materials to identify the most suitable for transparent conductive heaters.[11] Again the same conclusion that metal nanowires were the most effective materials was reached.

When selecting the appropriate material for an application it is crucial to consider the costs associated with the raw materials and production methods used to fabricate the electrode and whether high temperature or vacuum

processes are required for, or incompatible with, device production and the specific needs of the application.

Table 1.2 provides a brief summary of some fabrication methods of electrodes using transparent conductive materials, it is by no means exhaustive, but allows a simple comparison of the currently available and emerging materials.

Table 1.2: General guide to transparent conductive material electrode fabrication methods. + symbols indicate positive results – symbols represent poor results.

Fabrication Method♦	TCOs	Graphene	CNTs	AgNWs
CVD	+++	+++	+	-
Sputtering	+++	-	-	-
Spin Coating	-	+	++	++
Spray Deposition	++	+	+++	+++
Screen Printing	--	+	++	++
Material Costs	*Medium*	*High*	*High*	*Medium*
Processing Temp (ºC)	*>200▲-1000*	*RT-1000**	*RT-700**	*RT-700**
Uniformity	+++	+	++	++
Typical thickness (nm)	*100-300*	*<5*	*<10*	*25>600#*
Typical R_s (Ω/□)	*5-100*	*300-5000*	*100-300*	*1-50*

♦*Fabrication method refers to the production of electrodes directly not the production of the constituent components which are used to fabricate the electrode itself.*

▲*Deposition temperatures of TCO's usually require several hundred degrees Celsius or the use of vacuum processes such as sputtering.*

**Electrodes can be fabricated at RT but if device fabrication requires high temperature processes, vacuum or encapsulation are required to stabilize the films.*

#*Thickness is diameter and density dependant though with high pressure it can be reduced to the diameter of a single nanowire.*

Reduction of the sheet resistances of both graphene and carbon nanotubes can be achieved by doping the films but typical resistances of undoped films are shown in the table. The processing temperature indicated in Table 1.2 refers to the range of temperatures that the film may be exposed to during device fabrication. The low temperature refers to the lowest temperature that films can be fabricated at and the upper value is related to the stability of the material. Each type of TCM has strengths and weaknesses and in the end the material to use must be determined by the specific needs of the application.

For the properties mentioned in Ag nanowires are able to meet or exceed the toughest demands of existing applications. From this it can be seen that the available deposition methods for Ag nanowires are cheap and compatible with large scale samples. In light of this fact and the properties highlighted by De[6] and Sorel[12] the remainder of this thesis will focus on the use of silver nanowire networks as a TCM. This chapter will discuss the production of Ag nanowires and fabrication of TCMs with very promising properties produced by low-cost, solution-based, methods. Some time is also spent to discuss the application of

this material to devices, although several new applications have been recently demonstrated with silver nanowire networks, like EMI Shielding,[13,14] and RF antenna[15–17] this chapter focuses on applications which will find large improvements thanks to the three properties mentioned in Table 1.1.

1.2 Fabrication of silver nanowires

The synthesis of one-dimensional nanomaterials has grown impressively in the last two decades. In particular, the fabrication of metallic nanowires has been tackled recently for the development of transparent flexible electrodes. One of the very key criteria is the need to obtain materials from low cost solution-based processes. Among possible metallic nanostructures, silver nanowires (AgNWs) have been the most studied for several reasons. Bulk silver has the highest electrical conductivity thus it has been the focus of a lot of research.[18–20] Moreover, synthesis of AgNWs is rather easy whereas protocols for large scale synthesis of nanowires from other metals are still under development. Several other metallic nanowires have been prepared so far and some of them show interesting properties for the fabrication of TCMs. In particular, copper,[21–24] gold[25,26] and cupronickel[27] nanowires have demonstrated promising results. To date, silver nanowires continue to be the most studied metallic nanowires.

Several routes have been followed experimentally to fabricate silver nanostructures with various shapes and form factors. These methods include the hydrothermal method, microwave-assisted process, electrochemical technique, UV irradiation technique, template technique… (see Coskun et al.[28] and Chen et al.[29] and references therein). When compared to these methods, the polyol approach appears as the most promising synthetic procedure regarding ease of mass production, cost and simplicity. This method proposes a simple route for the synthesis of metal nanoparticles through reduction of metallic salts by a polyol, generally ethylene glycol.[30,31] Crystallization of noble metals usually leads to highly symmetric cubic unit cells. Thus, to obtain the growth of nanowires from isotropic solutions, some form of anisotropic confinement must be applied in order to achieve one-dimensional growth.[32] The polyol method of fabrication of AgNWs was first developed by the team of Xia.[18,20] Ethylene glycol reduces the metal precursor (usually silver nitrate) in the presence of a nucleating agent and poly-vinylpyrrolidone (PVP). The PVP plays the role of capping agent capable of controlling the growth rates of different faces of silver nanospecies. Thus the PVP is responsible for the introduction of anisotropic confinement. The near-unanimous choice of ethylene glycol as the reductant is based on its ability to solvate both $AgNO_3$ and PVP, and its boiling point (196 °C) which allows synthesis at high temperature.

The exact mechanism of AgNW growth is complex and as yet has not been entirely clarified. First, ethylene glycol reduces Ag^+ ions in Ag atoms, thereby inducing silver crystal formation and subsequently growth of silver nanostructures. The synthesis of AgNWs has three distinct steps; nucleation, evolution of nuclei into seeds and growth of seeds into nanocrystals. In these

steps the phenomena of atomic addition and aggregate formation are essentially governed by mechanisms of diffusion and surface energy minimization. By modifying the thermodynamics and kinetics of each of these steps, it is possible to have some control on the form of the synthesized nanocrystals.[33] Different approaches have been explored. The addition of particles playing the role of seeds can change the process of nucleation. Various nucleating agents, either in a pure form or as combination of a few salts, have been used to study the effect on AgNW growth.[20,29,34–36] In general, chlorinated derivatives give good results, and in particular NaCl is often preferred. The presence of a nucleating agent directly affects the morphology of metallic seeds during their initial formation. Thus, the addition of NaCl leads to the formation of AgCl nanocrystallites and reduces the concentration of free cationic silver ions in the solution during initial seed formation. These slow reaction conditions enable the formation of the thermodynamically more stable multiply twinned Ag seeds required for wire growth. The seed structures have an important role in the shape evolution of metal nanocrystals and therefore in the resulting materials. It has also been demonstrated that the addition of traces of salts involves selective oxidative etching controlling the structure and population of seeds once formed. Ag nanocubes or AgNWs can be obtained selectively just by modifying salt concentrations.[37–39] These parameters are key for the fabrication of one-dimensional Ag nanostructures. According to Xia et al.,[18,33,40] the nanowires are derived from multiple-twinned particles. Among the various possible seed structures (crystal, simple twin or multiple twins), the multiply twinned decahedra is the most thermodynamically stable seed, as it is bound almost entirely by the lower energy {111} facets. It is therefore the most naturally abundant seed but also the most reactive because of the presence of twin defects.

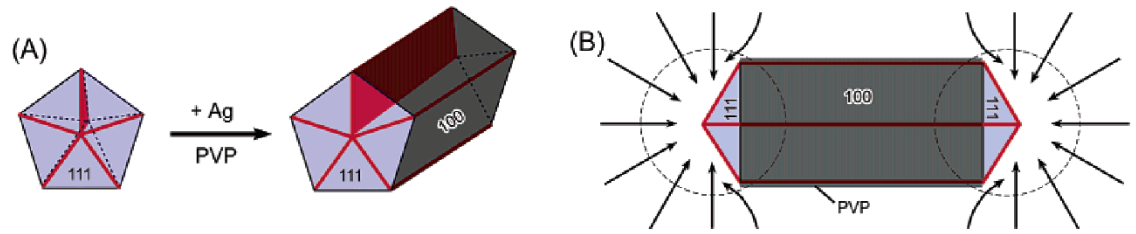

Figure 1.2 Schematic illustration of the mechanism proposed to account for the growth of silver nanowires with pentagonal cross sections: (A) Evolution of a nanorod from a multiply twinned nanoparticle (MTP) of silver under the confinement of five twin planes and with the assistance of PVP. The ends of this nanorod are terminated by {111} facets, and the side surfaces are bounded by {100} facets. The strong interaction between PVP and the {100} facets is indicated with a dark-gray colour, and the weak interaction with the {111} facets is marked by a light-blue colour. The red lines on the end surfaces represent the twin boundaries that can serve as active sites for the addition of silver atoms. The plane marked in red shows one of the five twin planes that can serve as the internal confinement for the evolution of nanorods from MTP. (B) Schematic model illustrating the diffusion of silver atoms toward the two ends of a nanorod, with the side surfaces completely passivated by PVP. This drawing shows a projection perpendicular to one of the five side facets of a nanorod, and the arrows represent the diffusion fluxes of silver atoms.[32]

Sun and co-workers[41] have recently reported that each nanowire is composed of a heavily strained core encapsulated in a less-strained sheath. The crystalline defects where the cores are exposed provide active sites for growth of the nanowires along their longitudinal axes, while the less-strained side surfaces of the nanowires, bound by {100} facets, have lower reactivity towards the deposition of silver atoms (see Figure 1.2).

Once the pentagonal rod is formed, PVP plays a critical role in the growth mechanism. Originally used to prevent the aggregation of nanoparticles, it has also proven to be an agent controlling the structure of the nano-objects. Indeed, it reacts preferentially with the {100} facets of the silver nanoparticles, through interactions between surface silver atoms and the oxygen atoms of the PVP carboxyl groups.[42] Tests performed with other polymers like poly(ethyleneoxide) (PEO) or polyvinylalcohol (PVA) did not lead to good nanowire formation.[20] Concerning the experimental protocol of the synthesis, many parameters have to be tightly controlled, which is a common feature for the synthesis of nanoparticles. A recently published parametric study gives some details related to the effects of temperature, injection rate, molar ratio of PVP to silver, NaCl amount and stirring rate.[28] All of these parameters are important and for some of them tiny changes can lead to dramatic alterations of the nanoparticle's size and shape. It should also be emphasized that the quality of chemical reagents is extremely important, in particular the purity of the ethylene glycol. A few grams of AgNWs can be obtained through a single experiment which allows large area deposition considering that only few tens of mg are deposited per m² to obtain a ~90 % transparency,[43] though this is dependent on deposition technique and wire geometry. The nanowires generally have diameters in the order of a 50-150 nm and lengths of 5-50 µm, resulting in an aspect ratio (length/diameter) typically in the 50-500 range (see Figure 1.3).

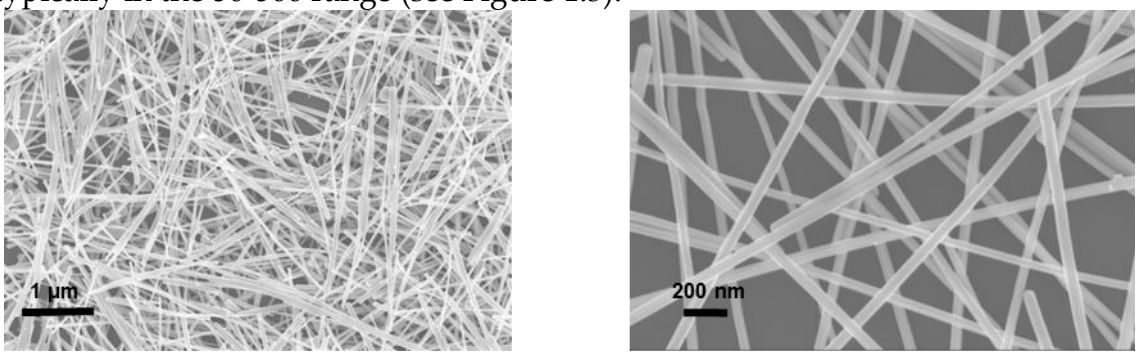

Figure 1.3 SEM images of silver nanowires at two magnifications

Recently, very long AgNWs have been synthetized thanks to a successive multistep growth method. Very high aspect ratio of 1000-3000 with lengths of over 300µm and diameter of less than 150 nm were obtained.[44] According to the percolation behaviour of 2D stick systems as discussed in chapters 2 and 3 these nanowires represent an ideal candidate for transparent electrode fabrication.

After the synthesis, the as-obtained product requires some purification. Indeed, a mixture of nanowires and nanoparticles in organic solvent is generally

obtained. To remove most of the ethylene glycol and excess PVP, several washes with acetone are commonly used. To separate the nanoparticles from the nanowires the product solution is put through a centrifuge. According to different research groups, the parameters of the commonly used centrifugation procedure can be changed from 20 min at 2000 rpm[20,34,45], 6000 rpm[28] or 8000 rpm[46] to 10 min at 16000 rpm.[47] Most of the time the product is then dispersed in another solvent such as water[17,28,46–48], ethanol[28,34] or methanol[49] to be washed a second time. Filtration has also been described to further purify the product, either by filtering through a polycarbonate membrane with 0.8 µm pore size[35,42] or a glass filter with mean pore size of 5-40µm.[50,51] Although less common, cross-flow filtration is also a possibility.[52] Another very straightforward method is to let the crude reaction mixture settling for few days before removing supernatant. This decantation technique allows easy production of a high quantity of nanowires in a single run.[53]

1.3 Fabrication of silver nanowire networks

The development of high performance transparent conductive material is increasingly requiring the use of nanostructures. Therefore, it is necessary to develop simple, reliable and cost-efficient fabrication techniques to achieve both random and ordered nanowire arrays. Assembling such networks is also a critical step to control their resulting electro-optical properties. In respect to their physical properties and ease of synthesis, high aspect ratio metallic nanowires are one of the most attractive materials to fabricate such networks.[54]

Random nanowire networks can be readily and cheaply made by solution-process techniques such as spray coating[50,55–57], drop casting[58–60], spin coating[61,62] or rod-coating.[63] All these techniques are compatible with low temperature deposition processes (<200 °C) and do not require any vacuum equipment. In addition techniques such as spray coating are easily surface-scalable. Such solution-processed electrodes have already demonstrated their ability to be integrated into operational devices such as organic solar cells.[58,62]

Nevertheless, while working with colloidal solutions and depositing them as thin films, it is often difficult to achieve high reproducibility as determined by comparing the opto-electrical properties of different networks. It is well-known that drop cast nanowire networks may show spatial inhomogeneities known as "coffee ring effect" on the substrates during the solvent evaporation step.[63,64] Films obtained from air-spraying coatings are usually more homogeneous and tend to form much more uniform networks.

Methods for ordering and control of nanowire arrangements have attracted increasing interest. Oxide nano templates such as anodic alumina have been used to separate and order metallic nanowires.[65,66] Polydimethylsiloxane stamps have also been successfully used for dry transfer printing.[19,67,68] A wealth of other different and original techniques such as blown-bubble film technique,[69] controlled dip coating,[70,71] microfluidic assembly,[72,73] electronic/magnetic field-assisted assembly,[74,75] convective force driven assembly,[76–79] layer-by-layer

assembly of nanowires,[80–82] direct gravure printing,[83] and electrospinning[23,84] have also been attempted to produce high quality ordered nanowire arrays.

One of the most important points to be addressed for device integration is the surface roughness and the contact resistance between nanowires. The former can be addressed by lamination[85] preventing shunts from occurring,[36] embedding nanowires within a transparent polymer using a wet chemical process as demonstrated by Zeng et al.[86] or by sandwiching a metallic nanowire network in between two ZnO layers.[87] Junction resistances can be lowered by annealing which can be made very spatially selective using plasmonic welding.[88]

Lastly, improving thermal and more generally environmental stability is a critical issue to address for integrating nanostructures in devices. Embedding within oxide materials is proving to be a very promising way to achieve this. Indeed, it has been used to prevent thermal degradation of silver nanowire networks.[65,84,87,89,90] Ramasamy et al.[90] showed that their TiO_2 encapsulated silver nanowires are thermally stable up to a temperature of 750 °C. However in the case of Ramasamy, the thermal annealing was performed under vacuum, in which case as we demonstrate in chapter 5 un-encapsulated wires are also stable to >700 °C.[91] Recently, Chung et al.[61] and Kim et al.[87] also demonstrated that such embedding is also beneficial for lowering junction resistances and smoothing the surface morphology, improving the mechanical adhesion to the substrate while maintaining good mechanical flexibility.

1.4 Electrical properties

The electrical properties of nanowire networks are dependent upon several characteristics of the nanowires themselves and of course the network morphology. In general the resistance of the network increases as the length of the nanowires used decreases, this trend is continued if the wire diameter is decreased.[12,21] This increase of resistance with decreasing wire diameter is due to an increase of the individual nanowire resistance. This phenomena was studied by Bid et al.[92] who attributed the increase in resistance to surface scattering of the electrons, as the diameter of the nanowire reduces close to or below the mean free path of electrons in the bulk material the role of surface scattering becomes dominant. The dominance of surface scattering causes a reduction of the mean free path and causes an increase in the resistivity above that of the bulk.

The role of the nanowire length is less straightforward as the dependence is a direct result of the percolative nature of the conduction mechanism in nanowire networks. In the fabrication of nanowire networks nanowires are deposited onto a substrate layer, when two nanowires touch they form a junction connecting the two wires electrically. The formation of a conductive electrode requires many such junctions to create a conductive pathway across the electrode. Hecht et al.[93] take an elegantly simple view of the conduction mechanism to explain the dependence of network resistance on length, although initially considered for carbon nanotube networks it is also applicable for metallic

networks. Put simply, the concept is that for a given network size the minimum number of nanowires required to cross it is inversely proportional to the square of the nanowires lengths. The orientations of the nanowires determine the number of junctions required to make the network percolate, but the minimum number is determined by the length of the wire. In this model the longer nanowires require fewer wires to make a conduction path across a given space, thus they have less junctions and fewer transfers between wires. This results in the lower resistances observed in networks made of long wires.

Beyond the dimensions of the wires themselves, the wire density plays a large role in the conduction properties of the network. Many studies have shown that increasing the number of wires decreases the resistance, however this also results in a decrease in the optical transmission of the network.[19,21,23,36,86] Striking a balance between the electrical and optical properties has long been the challenge for transparent conductive materials. Among others, there are two specific advantages of nanowire networks as transparent conductive materials. One is the low sheet resistances achievable with nanowire systems which can be on the order of a few ohms per square, and the other is the transparency in the infra-red region of the spectrum. This point will be covered in more detail in section 1.5.

The overall resistance of metallic nanowire networks depends on the material used to make the network, so far mainly copper and silver networks are being studied with the silver networks having the better electrical properties. Resistance of the network is also determined by the nanowire density and the junction resistance. The diameter and length of the nanowires play a crucial role in the required density for percolation and hence the number of conduction pathways through the network. Increasing the density of nanowires above the percolation threshold results in conduction pathways through the network that are in parallel, hence as the number of conduction paths increases the resistance decreases. The junction resistance is determined by the physical properties of the junction, these are dependent on how the nanowires are grown, purified, and deposited. Modification of the junction resistance has been studied in the literature and methods such as thermal annealing[19,43,86,94] high pressure[94], electrical annealing[43], optical sintering[88] and encapsulation[63,86] have all been shown to reduce the resistance of the network. Some examples of post-treatments and their effects on the morphology of the network are provided in Figure 1.4. This provides a contrast in the final electrode geometry, for the thermal annealing (Figure 1.4 2b) case the junctions' electrical properties are improved with some minor changes to the network, in the case of mechanical pressure (Figure 1.4 4b) the network morphology is reduced to the width of a single wire.

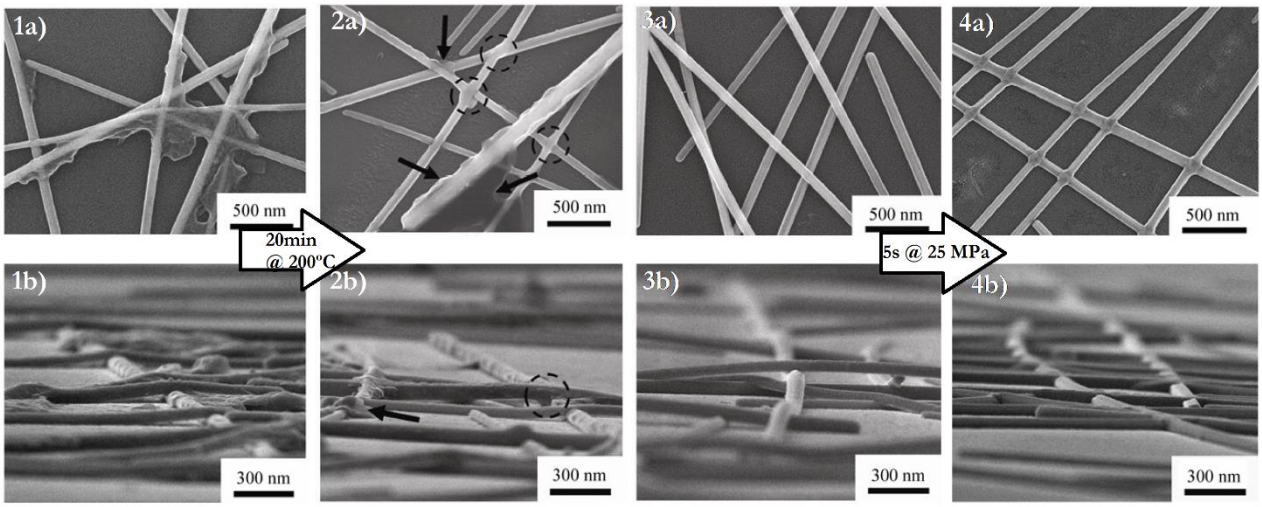

Figure 1.4 SEM images of silver nanowire networks, the a) series are top down views of the sample and the b) series show off angle cross-sectional views. Images 1a-b) are of as-deposited nanowire networks 2a-b) show the effect of thermally annealing at 200°C for 20 min. 3a-b) show an as-deposited network after rinsing in water and ethanol and 4a-b) show the effect of 5s of mechanical pressure applied at 25 MPa. Images adapted from[94]

The I-V characteristics of metallic nanowires at low voltages have been shown to be close to linear[88,95] and at higher voltages the electrical breakdown mechanism of individual single crystal nanowires has been determined to be due to electro-migration of atoms within the wires.[95] The nanowires will be subject to Joule heating as a result of current flow. However, the electrical resistance of the individual wires is low and the thermal conductivity of the wires is high. As a consequence, the thermal energy is quickly distributed throughout the network. In this case it was shown that electro-migration will cause failure of the networks before the critical temperature (the temperature required to cause spheroidization) to cause thermal failure is reached, as shown in Figure 1.5.

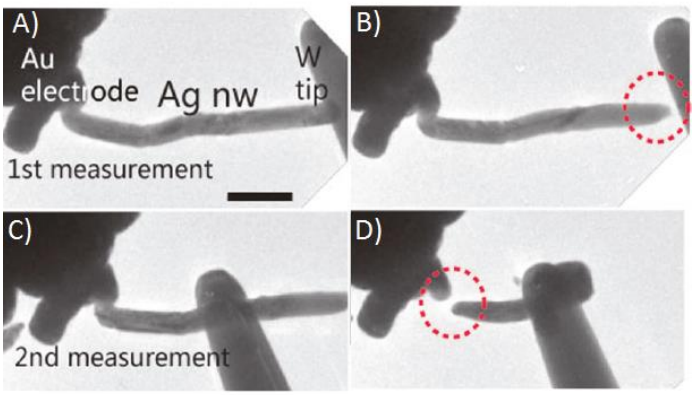

Figure 1.5 Electrical breakdown of a silver nanowire, two measurements were performed (AB and CD). The images show the wire before and after breakdown. Due to the position of the failure in each case it was determined that electro-migration is the most likely candidate as the failure mechanism. Scale bar in A) is 200 nm.[95]

Failure due to electro-migration is expected to occur close to junctions in the nanowire network which carry high current loads. In general electro-migration is expected to dominate the electrode failure under high current loads, the exception to this is the case where the junction resistance is high. In this case the Joule heating is localised at the junctions of nanowires in the network will act to increase the local temperature. Fortunately in this case it typically results in a reduction of the junction resistance through thermal sintering of the junction, which then reduces the heat produced at that point.

1.5 Optical properties

The use of optical properties of nanoscale particles is not really a new development, our ancestors put them in good use when fabricating magnificent colour pigments for stained glass. The vivid colours of metal colloids are a result of elastic light scattering. When an incident electromagnetic field impacts on a metallic nanoparticle, the electric field component will set into collective motion of both the bound and the free electrons with respect to fixed positive ions of the metal. This leads to electronic (which are essentially independent of the particle size) and geometric resonances over some spectral regions, effectively polarizing the material. Such polarization occurs if the particle size (the radius r of a spherical particle for example) is a multiple of the incident wavelength value. In that case, very narrow peaks are added to the extinction and scattering efficiencies. The former can be accurately described using the classical Drude-Lorentz-Sommerfeld equation for the resulting dielectric function:

$$\varepsilon(\omega) = 1 - \frac{\omega_p^2}{\omega^2 + i\omega\omega_{fe}} + \sum_j \frac{S_j \omega_j^2}{\omega_j^2 - \omega^2 - i\omega\omega_j} \qquad (1.1)$$

Where ω_j and ω_{fe} are the resonant frequency and the damping constant of the j^{th} harmonic oscillator, respectively. ω_{fe} is the damping constant of the free electrons and ω_p the bulk plasma frequency.[96]

In metals though, the contribution of free electrons is dominating the dielectric function resulting in a remarkable effect of light coupling to metallic nanoparticles via the excitation of surface-plasmon polaritons (SPPs) (as opposed to "bulk" plasmons) theorised by the pioneering work of Ritchie[97] in the 1950s. Surface plasmons are simply plasmons confined to the surface and are directly responsible for the geometry-dependence of nanoparticle optical responses. They have both longitudinal and transverse components and can actually be observed at high spatial resolution with electron-energy loss spectroscopy experiments[98,99] or scanning near-field optical microscopy.[100,101] SPPs stems from the relative difference of permittivities between the metals and the surrounding non-conducting (dielectric) media. For instance, for metallic cylinders of infinite length and small diameter, the resonance condition for an SPP resonance is given by: $\varepsilon_1 = -\varepsilon_M$ and $\varepsilon_2 \sim 0$ where ε_1 is the real part of the dielectric function of the particle, ε_M the dielectric function of the surrounding medium and ε_2 the

imaginary part of the dielectric function ε.[96] Surface plasmons can be damped by surface roughness, domain boundaries or any other sort of defects.

Having light being concentrated and channelled over the surface of nanoparticles as well as in between them results in a strong electromagnetic field enhancement. Indeed, the amplitude of the electromagnetic field observed in the vicinity of nanoparticles[102,103] can amount to several hundred times that of the incident field in places called "hot spots". Garnett et al. [88] put this effect to a practical use performing plasmonic welding to assist sintering metallic nanowires into large interconnected networks. Spechler and Arnold also used this method but employed a pulsed laser to minimise the excess energy input.[104] This feature is also used for surface-enhanced Raman spectroscopy.[65] These phenomena also illustrate what is called dependent scattering or "optical antenna effects". Indeed, while individual nanoparticles exhibit a single or a few plasmon resonances, much more complex resonance spectra are observed for interacting and coupled structures. Figure 1.6 shows different transmittance spectra of transparent conductors in the visible/near infra-red range.

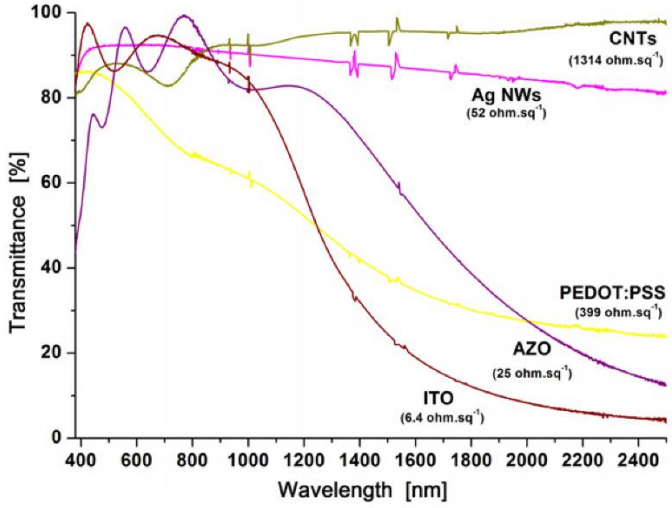

Figure 1.6 Vis-NIR transmittance spectra (substrate subtracted) of indium tin oxide, aluminium-doped zinc oxide, PEDOT:PSS, silver nanowires and single walled carbon nanotubes.

The plasma frequency of indium tin oxide and aluminium-doped zinc oxide falls in the near-infrared so that the transmittance drastically decreases in this region, silver nanowires and carbon nanotubes do not show such a feature and demonstrate similar transmittance in the visible range. For applications requiring conductive films that are transparent in the infra-red region of the spectrum, nanostructured films of metallic nanowires or carbon nanotubes are an excellent choice. In the case of silver nanowire networks, the transmittance loss is mainly accounted for by reflective scattering of light by the nanowires themselves.[61] In addition there is a significant reduction of the reflectance since there is a refraction index gradient (directly resulting from having nanowires suspended in air) which is an inherent factor enabling better coupling of light to the material. [105]

On a final note, the ratio of diffuse transmission to direct transmission of light (the haze factor) of a material can be considered a critical factor for some applications. It is dependent on the experimental conditions and methods used for fabrication of the network. It is possible to fabricate a broad range of metallic nanowire networks with haze factors from <2% to more than 30%.[106] This range allows metallic nanowire electrodes to be fabricated to suit many different applications.

As already briefly discussed in section 1.1 the proportion of scattered transmitted light is an important parameter which should be considered alongside optical transparency and sheet resistance. The Haze factor is associated with the degree to which transmitted light is scattered. A low Haze factor is required for display applications while higher values are desirable for enhancing the path length of light in the absorbing layer of a solar cell, thus improving the photovoltaic efficiency.[107] Haze factor is usually not considered, for instance when calculating the figure of merit (FoM), however recent studies have focused on its importance.[106,108,109] Unfortunately it is still difficult to provide a fair comparison and discussion on AgNWs Haze factor since literature reports very dispersed data relating to the Haze factors of nanowire networks. Actually Haze factor depends upon several parameters including NW density or diameter,[106] deposition method and post processing. Clearly, more work should be dedicated to this topic as it is of crucial importance for the optimal integration of AgNW based transparent electrodes in real devices.

1.6 Optimising the electro-optical properties

Optimising the properties of a TCM is a delicate challenge which depends upon the application considered. Such a task is associated with the inherent trade-off between the two requirements of electrical conductivity and optical transmittance. A material transparency can be improved by decreasing the sample thickness for a thin film (such as TCO) or the density of conducting nanoparticles (such as AgNWs or CNTs or disordered arrays of exfoliated graphene flakes). However a very low thickness or low density results in an increased resistance, in percolating systems this is due to the reduced number of conduction pathways. This feature is well illustrated by Figure 1.7a where transmittance versus sheet resistance has been plotted for graphene, single wall carbon nanotubes (SWNTs), Cu and Ag NWs.[6] Such a set of data points is associated with a series of specimen with varying thickness or density. The data can be fitted by using two different regimes which can be ascribed to bulk-like and percolation behaviour.[6] For each material considered, the bottom left portion of the data (fitted by the solid line and corresponding to thicker films) is associated with bulk-like materials for which dc conductivity is invariant with sample thickness. Another dependency should be considered for the high transparency regime where deviation from bulk-like behaviour and can be explained by percolation effects as revealed by the good fit between the dashed lines and the data in the top right region of Figure 1.7a. A discussion of the

equations used to fit this data can be found in the work of De and Coleman[6] which is also discussed in chapter 2 section 2.5. When the density of nanowires or nanotubes is decreased the sample state approaches the threshold for network percolation. At this point the probability that the network conducts is 50%; as the percolation threshold is crossed the network becomes less and less likely to contain conduction pathways and consequently the sheet resistance soars.

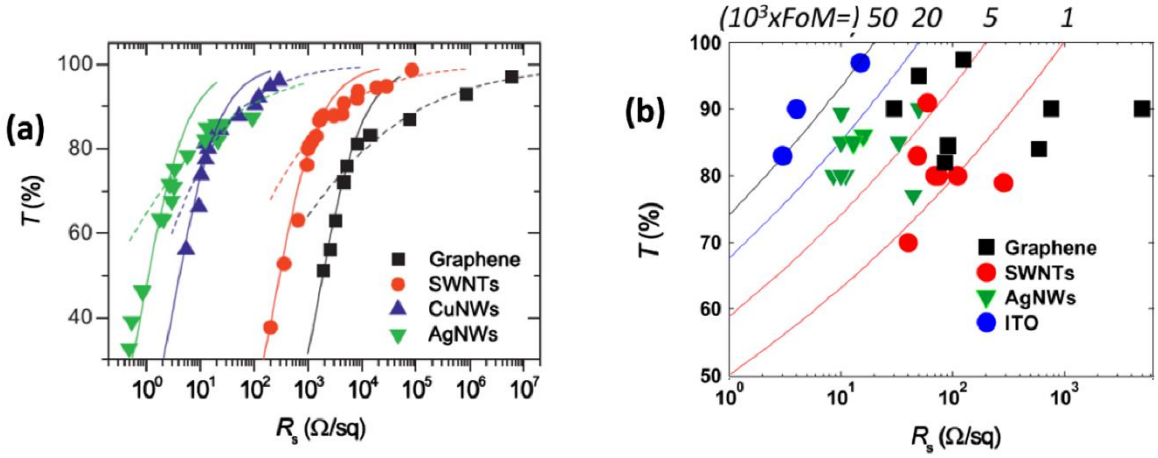

Figure 1.7 (a) Optical transmittance (at 550 nm) versus sheet resistance for transparent conductors composed of nanostructured materials. Each set of points can be divided into two regimes: the bulk regime (solid line) and the percolation regime (dashed line). [6]. (b) Optical transmittance (at 550 nm) versus sheet resistance for graphene,[110–115] carbon nanotubes,[19,56,116–121] Ag NWs[55,57,58,68,88,94,106] and ITO. [10,19,122]

The balance between electrical and optical properties should be quantified to allow comparison of the performance of TCMs. Therefore Figures of merit (FoM) are considered based on the pursued physical properties. A traditional FoM as defined by Haacke[123] is commonly used:[10,113]

$$FoM = \frac{T^{10}}{R_S} \qquad (1.2)$$

Where T is the transmission measured at a wavelength of 550nm, which corresponds to the maximum human visual sensitivity and the peak in photon output of the sun. Note as well that another FoM often considered is the ratio between the electrical conductivity and the optical absorption coefficient.

Figure 1.7b exhibits experimental optical transmission and sheet resistance data associated with graphene,[110–115] carbon nanotubes,[19,56,116–121] Ag NWs[55,57,58,68,88,94,106] and ITO. [10,19,122] The lines show iso-values of the FoM defined by equation 1.2. The larger the FoM values are, the better are the associated electro-optical properties (so the ideal region corresponds to the top left of this graph). While a dispersion of the data points can be observed, general trends can be stated. ITO properties are still the best, while metallic nanowires exhibit rather promising properties. Carbon nanotubes are associated with lower FoM values because of the high junction resistance between carbon nanotubes. Graphene exhibits rather scattered data and except for some studies, such as

Bae,[114] suffer from significantly large values of sheet resistance which, for the moment, still exclude them for applications like solar cells where requirements are the most stringent in terms of FoM.

1.7 Thermal properties

The thermal properties of metallic nanowires concern their thermal conductivity, the temperature dependence of their electrical conductivity as well as their thermal stability.

In recent years, numerous studies of the electrical transport properties of nanostructures have been reported thanks to the possible applications in miniaturized devices.[124] The mainstream research activities in this field are dedicated to oxide or semiconductor nanowires. Few investigations have been reported so far on the thermal conductivity of metallic NWs when compared to electrical conductivity. This stems from the fact that thermal and electrical conductivities of metals are intimately related through the Wiedemann-Franz relation,[125] and electrical conductivity is much directly accessible from an experimental viewpoint. However, recently, thermal conductivity (K) of Pt nanowires (diameter of 100 nm, length of 10 μm) was compared with measurements of electrical conductivity (σ) at room temperature. Compared with bulk data, electrical and thermal conductivity of the nanowire are decreased by a factor of 2.5 and 3.4, respectively.[126] Consequently, the Lorenz number $L=K/(\sigma.T)$ of the nanowire was found to be smaller when compared with the bulk Lorenz number of metals, the difference being of 25%.[126] This decrease is often related to grain boundary scattering of electrons. Indeed, usually small diameter NWs exhibit larger density of extended defects (such as grain boundaries) which affect the electrical resistivity. Other investigations found electrical properties of Au NWs similar to that of bulk without evidence of any polycrystalline grain structure[127] even with a diameter of 55 nm.

When used within an organic material, an AgNW network can substantially increase the thermal conductivity of the organic matrix.[128] AgNW array-polymer composites have also been investigated as thermal interface material for use as a heat sink in electronic cooling applications.[129] Moreover AgNW networks can also be used for the fabrication of flexible transparent thin film heaters. Thanks to the intrinsic conductive properties of random AgNW networks above the percolation threshold, it is possible to combine flexibility, transparency and high heating performance at low voltage (i.e. 12 volts) which is of interest for many applications like defrosting, defogging or fabrication of thermo-chromic displays.[43]

The electrical resistivity ρ of metallic nanowires themselves is a topic of current interest as well, since this is likely to be the dimensions of metallic interconnections in future electronic devices. In the regime where the metallic NWs have a diameter of a few tens of nanometres ρ depends upon the metal itself through its defects (impurities, extended defects such as grain-boundaries or twin boundaries) and their size.[92] Indeed, the electrical resistance for Ag and

Cu of diameters ranging from 15 to 200 nm adhere well to the Bloch-Gruneisen model[92] showing only slight differences with bulk metals. The resistivity of the wires increases when the wire diameter (D_{NW}) decreases, especially when D_{NW} is comparable with the mean free path of the electrons (which is about 30-40nm for bulk Ag at room temperature[130]). This is due to the dominance of surface scattering effects[131] but also because low diameter NWs often exhibit larger defect densities that induce electron scattering.

Few thorough investigations of the electrical contacts between two metallic NWs have been reported yet. However they seem to play a crucial role as one can see from the electrical resistance evolution of AgNW networks during thermal annealing. Indeed thermal annealing is an effective method to form fused contacts between NWs which drastically reduces their electrical resistance. The occurrence of local sintering is the driving force of such an evolution of the electrical properties.

Such thermal annealing exhibits a thermal limit above which the metallic NWs become unstable. This is a case of classical interfacial instability when dealing with liquid or solid cylinders when heated, called the Plateau-Rayleigh instability.[132] The morphological evolution of metallic NWs have been intensively investigated recently for gold,[133] Cu,[134] Pt,[135] Sn,[136] or Ag.[137] In a simple approach, perturbations with wavelengths larger than the original cylinder circumference become unstable. Observations show that upon thermal annealing metallic wires undergo various configuration changes. These lead to the wires breaking into chains of nanospheres at a much lower temperature than the melting point of the metal due to this capillary instability. Obviously, such a thermal instability is very detrimental for the electrical conduction of the NW network. Therefore thermal annealing under controlled conditions should be carefully considered for optimizing electrical properties of the metallic NW network as discussed in chapter 5. The critical temperature at which this instability occurs is dependent on the nature of the nanowires, specifically the diameter and crystallographic structure. The material used also plays a role through its intrinsic properties (surface tension, diffusion coefficients etc.).

A solution for enhancing thermal stability towards higher temperature is to embed the NWs within another material for instance an oxide. A recent investigation shows indeed that AgNWs can be efficiently coated with uniform TiO_2 shells.[90] In-situ TEM thermal annealing observations showed that the AgNWs core remains intact until temperatures of 750°C.[90] Due to this improvement of thermal stability, such coated metallic nanowires can be heated sufficiently to be used as a reusable surface for Surface Enhanced Raman Scattering (SERS).[65]

1.8 Structural and mechanical properties

The morphology of metallic nanowire networks depends greatly on the fabrication method employed for the network production. However the majority of the current processes result in a rough surface morphology that may have a

detrimental impact on the operation of devices. Out-of-plane oriented wires result in an electrode geometry that is not strictly planar. This leads to leakage currents, short circuits and recombination sites in photovoltaic systems. Several methods have been shown to reduce the problems associated with stray nanowires. High mechanical pressure has been shown to increase uniformity in the network geometry and reduce the 3D morphology to a true 2D network.[94] Encapsulation in transparent conductive polymers has also been shown to significantly reduce surface roughness.[85,138]

Understanding the structural behaviour of such networks has proven to be an interesting field of research and one of the main advantages of nanowire based electrodes arises from the mechanical properties of nanowire networks. Recognising that these electrodes are made of metals, it is no surprise that they show excellent properties when submitted to mechanical stress (either compression, tension or torsion). All have little to no effect on the electrical resistance of electrodes manufactured with metallic nanowires.[19,86,139] Figure 1.8 shows a comparison of three transparent conductive materials under the same mechanical stress conditions, from this it is clear to see that AgNW networks provide a significant advantage for flexible electronic applications. The reduced resistance $(R-R_0)/R_0$ depicted in Figure 1.8 indicates the ratio of the change in resistance divided by the initial resistance.

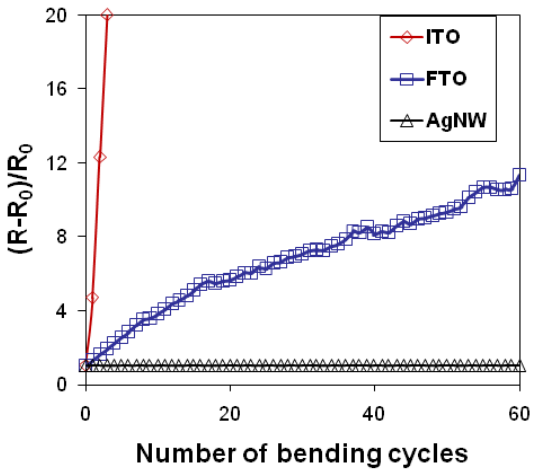

Figure 1.8 Comparison of TCM's under the mechanical bending, one cycle is bending from flat to a radius of curvature of 5 mm and returning to the initial position, the TCM is on the opposite side to the bending radius and is therefore placed under tension.[1]

It has been shown that solar cells, organic light emitting diodes and thermal heaters can be produced on flexible substrates with nanowire electrodes. The ability of these electrodes to withstand external mechanical stresses is far above that of most traditional transparent conductive material. Even crumpling of such transparent electrodes have been demonstrated recently after deposition of nanowires on a very thin (1.3µm) piece of polyethylenenaphtalate.[43]

The major weakness of metallic nanowire networks in the face of mechanical stress is adhesion of the layer to the substrate material. If friction or adhesive tape are applied to the network directly low adhesion of the network to the substrate generally causes the network to fail. If however, the network is

placed under mechanical stress that is applied to the substrate the network has an excellent ability to follow the substrate material if it is flexible. If however the force is applied directly to the network in the form of rubbing or scraping the adhesion of the nanowires generally fails. This can be reduced by encapsulating the conductive network but the feasibility of such an encapsulation depends on the desired application.

Recently a further exhibition of the remarkable mechanical properties of metallic nanowire materials has emerged with several papers on stretchable electronic devices using nanowire networks as the conducting pathways.[140–142] These materials utilise metallic nanowire networks that when placed under strain 'unfold' to expand and fill the space on the stretched surface of the substrate. The work by Xu et al. [141] used short AgNWs to produce the networks, in order to enable the electrodes to maintain conductivity at high strain, networks with high nanowire densities were created. These networks were not transparent but provided a rare opportunity for stretchable electronics. Lee et al.[140] carried this work further to enable transparent stretchable electrodes and managed to achieve networks with an optical transmission of approximately 90% and sheet resistance of between 9-70 Ω/□ that was able to withstand over 460% strain without significant increase in electrical resistance. This result was achieved by using comparatively low densities of very long (200-500 μm) AgNWs.[140]

1.9 General Remarks on Applications of Nanowire Networks

Due to their low sheet resistance and high transparency, silver nanowires are good candidates for device integration in existing applications. Their mechanical properties also provide opportunities for integration in emerging flexible applications. As it has been shown previously, this nanowire-based alternative for flexible transparent electrodes is compatible with low cost and large scale processes. However, some issues must be properly addressed for the successful industrial integration of silver nanowires in devices.

First of all, let us clarify that although the cost of the bulk silver used to fabricate nanowire films is sometimes considered as an issue for this emerging TCM, the extremely small amount of raw metal needed renders this alternative economically relevant. Therefore, the use of a noble metal is not itself an economic issue. For instance, a cost analysis of PV modules suggest that it is three times less expensive with AgNW compared to ITO on PET.[143]

In terms of real applications, control of metallic network roughness is also a major challenge[58] that has to be taken into account. Indeed, a major issue comes from the protruding nanowires from the network that can lead to electrical shortcuts or leakages in multi-layer devices. Roughness of bare AgNW electrode has been evaluated to be in the order of hundreds of nm[36,86] (RMS 30-1000 nm and 200-300 nm top to bottom height). In the literature, different strategies have been developed so far to circumvent electrode roughness. Surface roughness reduction has been achieved by mechanical pressing,[36,85] thermal annealing,[58] polymer coating [85,86] surface peeling and transfer processes.[85,86,138] It has been

shown that the reduction of surface roughness by flattening the network not only reduces the risk of short circuit but also increases sheet conductance.[36,85]

As described earlier another shortcoming of AgNW electrodes is the poor adhesion of the nanowire network to the substrate. This issue can be easily circumvented in device applications by encapsulation with a thin layer of organic materials (Teflon, PEDOT:PSS…).[19,36] Typically devices can be designed in such a way that the adhesion of the nanowire network to the substrate becomes less important as it is incorporated into a multi layered device.

Finally, extended study of silver nanowire based device ageing has not yet been reported. Nevertheless, it is certainly closely related to oxidation and sulfuration of nanowires as well as electro-migration.[86] Device ageing is not directly correlated to silver nanowire electrode ageing and will be dependent largely on the overall architecture of the device and not solely on the AgNW network. Indeed, due to multilayer stacking, it is really a complex mechanism that occurs and further studies are needed to explain possible alteration of electrodes in the long term. However, flexible Ag nanowire electrodes appear rather stable; they keep their optical and electrical performances for more than a year in air, without special care.

In addition to the potential technological integration issues that have been previously listed, device optimization should also require tuning the work function of the electrodes[144] to ease charge carrier injection or collection in optoelectronic devices with any active layers. For this purpose, transparent flexible electrodes can for instance be modified by coating with another transparent layer (organic compounds, metallic oxides…).[58,145,146]

1.10 Solar cells

Many groups are beginning to incorporate silver nanowires as front electrodes for solar applications.[89,139,145,147–150] Depending on the experimental conditions used for their fabrication, metallic nanowire networks can have Haze factors varying between 1-30%.[106] If low Haze factor is desired this can be achieved by using spray deposition and spin coating which can have a haze factors of <2%. This is acceptable for display and window applications. Fabrication and transfer of nanowire networks by vacuum filtration has demonstrated nanowire networks with haze factor of approximately 30% over the 400nm-900nm spectral range .[106] For application in photovoltaic systems a high haze factor implies light scattering into the device and results in a larger effective absorption cross section. As demonstrated by Chih-Hung et al. increasing haze results in an increase in efficiency,[107] Gaynor et al.[145] demonstrated approximately 10% increase in the conversion efficiency by using a Ag nanowire composite electrode over an ITO standard (η=3.4% using ITO on plastic and η=3.8% for Ag nanowire composite). Using low haze networks and taking advantage of the metal nanowire network transparency in the infra-red region of the spectrum, it is possible to create solar cells semi-transparent in the visible region.[148] These cells absorb some of the light in the visible region and

much of the infra-red, resulting in an average transmission of about 61% in the 450-650 nm wavelength range.[148] This type of solar cell could be used to provide tinted windows that produce energy whilst reducing glare.

An advantage of metallic nanowire networks is demonstrated in the production of flexible solar cells,[147] which is unlikely to be achievable on any transparent conductive oxides. The flexible solar cells show a remarkable ability to produce electricity even when bent to angles of 120° as demonstrated in Figure 1.9. These flexible solar cells are organic polymer cells that incorporate AgNW networks embedded in PEDOT:PSS, a conductive polymer.

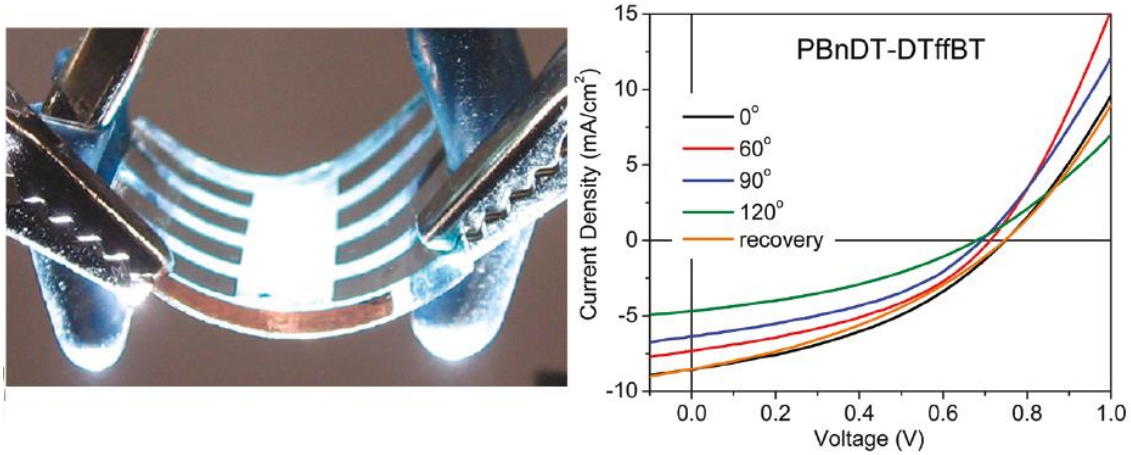

Figure 1.9 Flexible organic solar cell in operation (left) and the I-V curves at different angles (right) from [147].

1.11 Transparent heaters

Transparent heaters have a wide variety of uses. Defrosting windows in airplanes was one of the first applications, allowing flight at high altitude.[151] Most of defrosting or defogging transparent devices are fabricated using layers of ITO. But as explained before, such a material does not have significant resistance to mechanical constraints. Thus random networks of silver nanowires appear to be well adapted if one wants to make transparent film heaters on conformable or flexible surfaces. The operating principle is based on Joule's law. This rule, also named Joule heating, describes the production of heat as the result of a current flowing through a conductor. When an electric current flows through a transparent conductor, electric energy is converted to heat through resistive losses in the material. It can be written according to the equation $P = V^2/R$, where V is the applied voltage, R the total resistance and P the dissipated power.

As it has already been explained, limitations of current in existing commercial technologies can be circumvented by the adequate use of nanomaterials. For this application, devices with excellent properties were reported recently with silver nanowires, in particular on plastic substrates (see Figure 1.10).[11,43,152,153] Interestingly, the excellent optoelectronic properties of AgNW random networks delivers significant power at low voltage (typically below 12 V) which is more suitable for many applications.

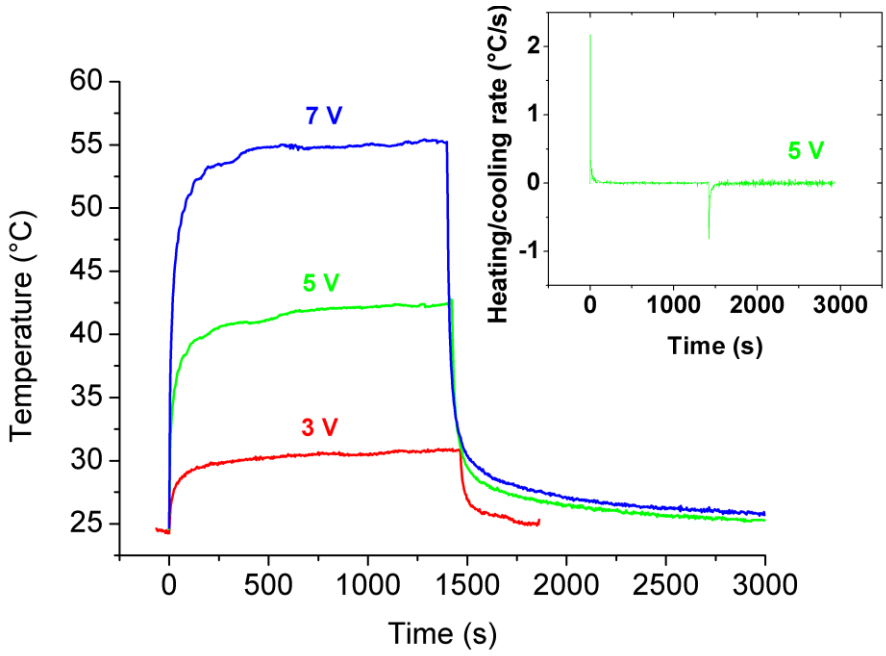

Figure 1.10 Heating experiments showing temperature as a function of time for a 35 Ω/□ film heater on a 125 µm PEN substrate at different applied voltages. Inset: derivative of the temperature vs. time at 5 V applied bias. [43]

Recent works by Sorel et al. also demonstrated that the thermal behaviour of silver nanowire networks was dependent on the percolating nature of the network.[11] This dependence is best observed by plotting the change in temperature as a function of the applied current $(\Delta T/I^2)$ against a modified transmission $(T_R^{1/2}-1)$. In this form two distinct linear functions can be observed, one for the bulk behaviour and one for the different behaviour observed for percolating networks as shown in Figure 1.11.

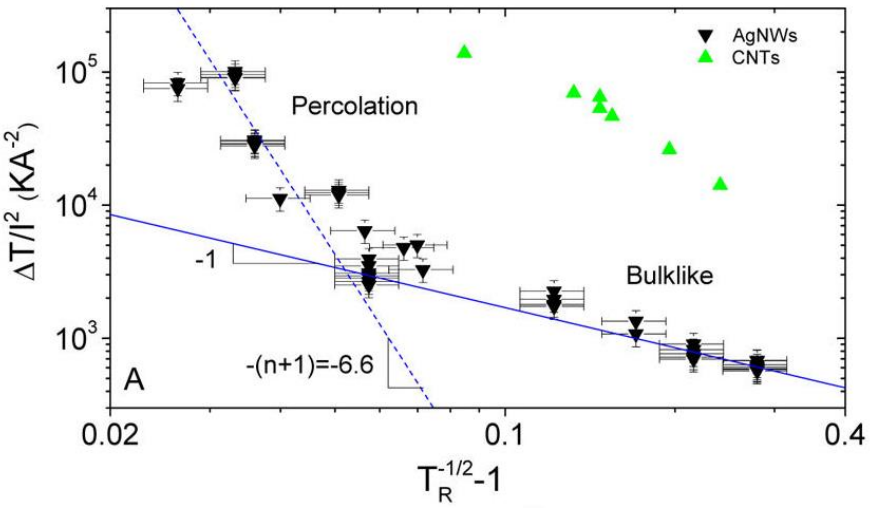

Figure 1.11 Thermal behaviour of silver nanowire networks in the bulk and percolation regimes also included is data for carbon nanotubes (green).[11]

1.12 Displays (OLED)

A key advantage of OLEDs (Organic Light Emitting Diodes) or PLEDs (Polymer Light-Emitting Diodes) is that they can potentially be made entirely by solution process and thus are more suitable for low cost, large area flexible displays and white lighting panels. OLED materials need current flowing through the active layer to light up. This means that charge carrier transport properties play an important role in those devices. Not only the properties of the active layer itself, but also the interfaces with their neighbouring layers and the electrodes are of overwhelming importance.[154] Few studies have pointed out metallic nanowire based OLEDs: good electroluminescent properties have been reported.[86,138,144,155] In particular, Yu et al. have integrated AgNW polymer composite electrodes in large angle bending PLEDs (see Figure 1.12).

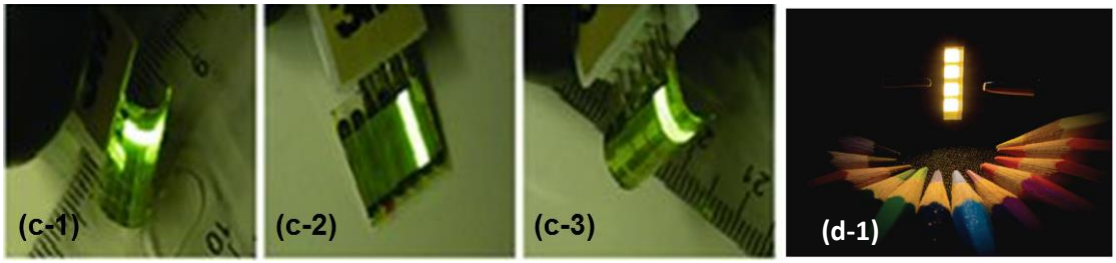

Figure 1.12 Photographs of shape memory PLEDs emitting at around 300 cd m^{-2}, bent to a 2.5 mm radius convex (c-1), recovered to flat shape after heating at 120°C for 1 min (c-2), and bent in the opposite direction as in (c-1) to a 2.5 mm radius concave (c-3). Photographic image of four operating white tandem OLEDs at 1000cd m^{-2} (d-1).), from [138] and[156].

As in OPV devices, a slight increase of device performances through higher power efficiency of Ag NW based OLED devices compared to conventional ITO has been observed.[58,86,144,156–158]

It is partly ascribed to an enhanced scattering of emitted light by Ag NWs. Very recently, Gaynor et al. have demonstrated very high-efficiency ITO-free white OLEDs.[156] The highest luminous efficacy for an ITO-free white OLED with stabilized viewing angle and almost perfect Lambertian emission were reported.(See Figure 1.12d-1) [b] These first studies open the way towards large-scale integration of AgNW based electrodes in emerging flexible display devices.

1.13 Touch panels

Touch screen technology has become very popular in many electronic products. It is widely used for smartphones, tablet PCs, game consoles, electronic information and ticketing kiosks and other technologies. Few approaches are available, but the main industrial products being currently used are based on resistive or capacitive touch panels. Since emitted light from the device comes through the front electrode, it is necessary for it to be very transparent and with low diffusivity (low Haze factor). It is very likely that in the forthcoming years

many displays (in particular for smartphones) will become flexible, and consequently new bendable transparent conductors will be mandatory for these applications. The AgNW-based electrodes appear as promising candidates, as recently reported using resistive type panels.[67,159] Some of the co-authors of the review upon which this chapter is based also fabricated capacitive touch sensors,[53] demonstrating that AgNW-based technology allows good performances for different possible technologies and has the potential to replace in the short term ITO for future flexible touch screen panels (see Figure 1.13). The strength of nanowire networks over ITO or other oxides in the field of flexible electronics lies in the fact that the oxide family is typically brittle resulting in short life spans of structures deposited on flexible materials.

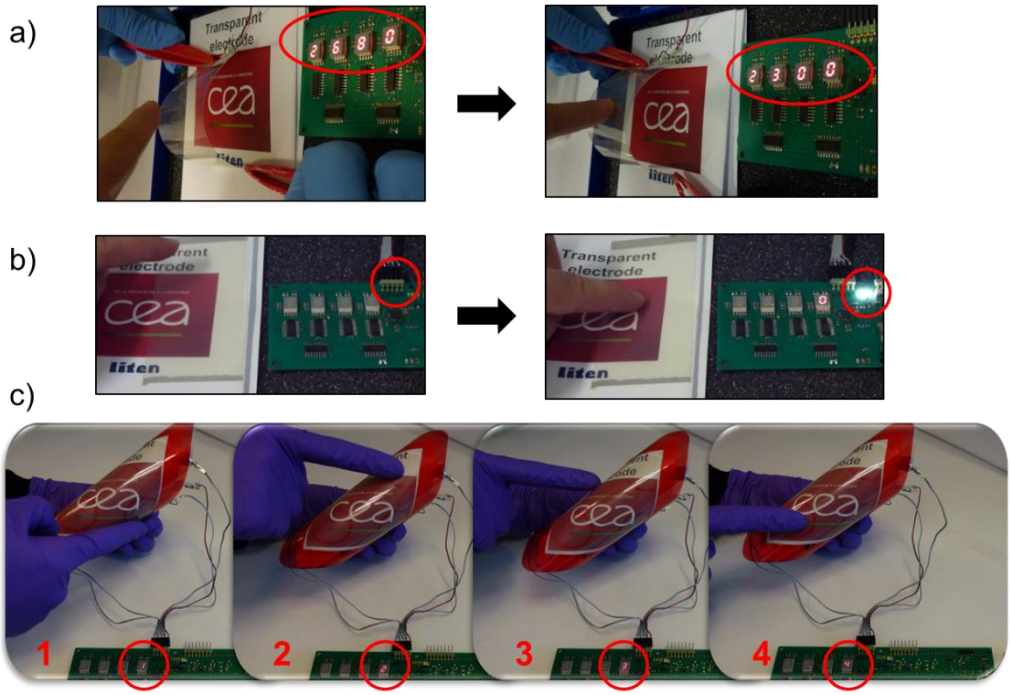

Figure 1.13 a) Left, the finger does not touch the sensor surface and oscillation value is 268 and right, the finger touches the surface and oscillation value is 230. b) Left, finger is far from the surface thus the LED is off, right the finger is touching the sensor which switches on the LED c) Recognition of each electrode (1,2,3,4).[53]

It was also recently demonstrated that flexible transparent capacitive sensors can be used for the detection of deformation and pressure. Capacitive sensor sheets fabricated by employing silver nanowire networks embedded in the surface layer of polyurethane matrix exhibit good stretchability and transparency.[160]

1.14 Closing Remarks

This chapter has provided the contextual framework for our research answering the questions of why TCMs are important and why silver nanowire networks are such a promising material to replace ITO. We have shown that Ag NW networks offer interesting opportunities for fundamental and applied research. Thanks to the simple methods available to fabricate the individual wires and networks and as well to the excellent electrical and thermal properties of silver, Ag NW networks exhibit great potential for being used as flexible transparent conductor in several applications including flat screens, solar cells and transparent heaters. We have discussed the fabrication of AgNWs and their properties. The structural arrangement of the network as well its physical properties (optical, electrical or mechanical). The large range of haze factors achievable with AgNW networks (1-30%) provides a material that can lead to significant advantages in solar cell applications while still being suitable for displays and windows. This remarkable characteristic, combined with their mechanical flexibility, enables a broad application range. Several investigations have shown that the use of AgNW networks can facilitate and improve new technologies such as flexible solar cells, flexible heaters, flexible touch screens and stretchable electronics. In light of the successful application of this emerging TCM to these fields already and the improvement of some properties in standard systems as well, metallic NW networks appear to be a key contender in emerging nanomaterials. In terms of replacing ITO and moving to indium-free TCMs it is unlikely that any one material will succeed alone. On the contrary, due to the broad variety of different requirements, it is likely that a combination of emerging indium-free materials will each take specialised roles within the TCM market. In light of this we suggest that AgNWs are a key material to watch for application in flexible electronics.

1.15 References

[1] D. Langley, G. Giusti, C. Mayousse, C. Celle, D. Bellet, J.-P. Simonato, *Nanotechnology* **2013**, *24*, 452001.

[2] Indium Tin Oxide (ITO) for Evaporation, *Umicore Tech. Data Sheet* **2014**.

[3] A. Kumar, C. Zhou, *ACS Nano* **2010**, *4*, 11.

[4] T. D. Kelly, G. R. Matos, *Historical Statistics for Mineral and Material Commodities in the United States*, U.S. Geological Survey, **2013**.

[5] A. M. Alfantazi, R. R. Moskalyk, *Miner. Eng.* **2003**, *16*, 687.

[6] S. De, J. N. Coleman, *MRS Bull.* **2011**, *36*, 774.

[7] S. Reuter, R. Das, *Transparent Conductive Films for Flexible Electronics 2010-2020 Needs, Players & Opportunities*, IDTechEx, **2009**.

[8] D. S. Hecht, L. Hu, G. Irvin, *Adv. Mater.* **2011**, *23*, 1482.

[9] L. Hu, H. Wu, Y. Cui, *MRS Bull.* **2011**, *36*, 760.

[10] K. Ellmer, *Nat. Photonics* **2012**, *6*, 809.

[11] S. Sorel, D. Bellet, J. N. Coleman, *ACS Nano* **2014**, *8*, 4805.

[12] S. Sorel, P. E. Lyons, S. De, J. C. Dickerson, J. N. Coleman, *Nanotechnology* **2012**, *23*, 185201.

[13] M. Hu, J. Gao, Y. Dong, K. Li, G. Shan, S. Yang, R. K.-Y. Li, *Langmuir* **2012**, *28*, 7101.
[14] Y.-H. Yu, C.-C. M. Ma, C.-C. Teng, Y.-L. Huang, S.-H. Lee, I. Wang, M.-H. Wei, *Mater. Chem. Phys.* **2012**, *136*, 334.
[15] T. Rai, P. Dantes, B. Bahreyni, W. S. Kim, *IEEE Electron Device Lett.* **2013**, *34*, 544.
[16] N. Komoda, M. Nogi, K. Suganuma, K. Kohno, Y. Akiyama, K. Otsuka, *Nanoscale* **2012**, *4*, 3148.
[17] C. Yang, H. Gu, W. Lin, M. M. Yuen, C. P. Wong, M. Xiong, B. Gao, *Adv. Mater.* **2011**, *23*, 3052.
[18] Y. Sun, B. Gates, B. Mayers, Y. Xia, *Nano Lett.* **2002**, *2*, 165.
[19] S. De, T. M. Higgins, P. E. Lyons, E. M. Doherty, P. N. Nirmalraj, W. J. Blau, J. J. Boland, J. N. Coleman, *ACS Nano* **2009**, *3*, 1767.
[20] Y. Sun, Y. Xia, *Adv. Mater.* **2002**, *14*, 833.
[21] A. R. Rathmell, S. M. Bergin, Y.-L. Hua, Z.-Y. Li, B. J. Wiley, *Adv. Mater.* **2010**, *22*, 3558.
[22] A. R. Rathmell, B. J. Wiley, *Adv. Mater.* **2011**, *23*, 4798.
[23] H. Wu, L. Hu, M. W. Rowell, D. Kong, J. J. Cha, J. R. McDonough, J. Zhu, Y. Yang, M. D. McGehee, Y. Cui, *Nano Lett.* **2010**, *10*, 4242.
[24] D. Zhang, R. Wang, M. Wen, D. Weng, X. Cui, J. Sun, H. Li, Y. Lu, *J. Am. Chem. Soc.* **2012**, *134*, 14283.
[25] P. E. Lyons, S. De, J. Elias, M. Schamel, L. Philippe, A. T. Bellew, J. J. Boland, J. N. Coleman, *J. Phys. Chem. Lett.* **2011**, *2*, 3058.
[26] A. Sánchez-Iglesias, B. Rivas-Murias, M. Grzelczak, J. Pérez-Juste, L. M. Liz-Marzán, F. Rivadulla, M. A. Correa-Duarte, *Nano Lett.* **2012**, *12*, 6066.
[27] A. R. Rathmell, M. Nguyen, M. Chi, B. J. Wiley, *Nano Lett* **2012**, *12*, 3193.
[28] S. Coskun, B. Aksoy, H. E. Unalan, *Cryst. Growth Des.* **2011**, *11*, 4963.
[29] D. Chen, X. Qiao, J. Chen, *J. Mater. Sci. Mater. Electron.* **2011**, *22*, 1335.
[30] F. . Fiévet, J. P. Lagier, M. Figlarz, *MRS Bull.* **1989**, *14*, 29.
[31] M. Hu, J. Gao, Y. Dong, S. Yang, R. K. Y. Li, *RSC Adv.* **2012**, *2*, 2055.
[32] Y. Sun, B. Mayers, T. Herricks, Y. Xia, *Nano Lett.* **2003**, *3*, 955.
[33] Y. Xia, Y. Xiong, B. Lim, S. E. Skrabalak, *Angew. Chem. Int. Ed.* **2009**, *48*, 60.
[34] C. Chen, L. Wang, G. Jiang, Q. Yang, J. Wang, H. Yu, T. Chen, C. Wang, X. Chen, *Nanotechnology* **2006**, *17*, 466.
[35] Y. Gao, P. Jiang, L. Song, L. Liu, X. Yan, Z. Zhou, D. Liu, J. Wang, H. Yuan, Z. Zhang, X. Zhao, X. Dou, W. Zhou, G. Wang, S. Xie, *J. Phys. Appl. Phys.* **2005**, *38*, 1061.
[36] L. Hu, H. S. Kim, J.-Y. Lee, P. Peumans, Y. Cui, *ACS Nano* **2010**, *4*, 2955.
[37] S. Chang, K. Chen, Q. Hua, Y. Ma, W. Huang, *J. Phys. Chem. C* **2011**, *115*, 7979.
[38] B. Wiley, Y. Sun, Y. Xia, *Langmuir* **2005**, *21*, 8077.
[39] K. E. Korte, S. E. Skrabalak, Y. Xia, *J. Mater. Chem.* **2008**, *18*, 437.
[40] B. Wiley, Y. Sun, B. Mayers, Y. Xia, *Chem. – Eur. J.* **2005**, *11*, 454.
[41] Y. Sun, Y. Ren, Y. Liu, J. Wen, J. S. Okasinski, D. J. Miller, *Nat. Commun.* **2012**, *3*, 971.
[42] Y. Gao, P. Jiang, D. F. Liu, H. J. Yuan, X. Q. Yan, Z. P. Zhou, J. X. Wang, L. Song, L. F. Liu, W. Y. Zhou, G. Wang, C. Y. Wang, S. S. Xie, J. M. Zhang, D. Y. Shen, *J. Phys. Chem. B* **2004**, *108*, 12877.
[43] C. Celle, C. Mayousse, E. Moreau, H. Basti, A. Carella, J.-P. Simonato, *Nano Res.* **2012**, *5*, 427.
[44] J. H. Lee, P. Lee, D. Lee, S. S. Lee, S. H. Ko, *Cryst. Growth Des.* **2012**, *12*, 5598.
[45] Y. Sun, Y. Yin, B. T. Mayers, T. Herricks, Y. Xia, *Chem. Mater.* **2002**, *14*, 4736.
[46] W. C. Zhang, X. L. Wu, H. T. Chen, Y. J. Gao, J. Zhu, G. S. Huang, P. K. Chu, *Acta Mater.* **2008**, *56*, 2508.
[47] B. Wiley, T. Herricks, Y. Sun, Y. Xia, *Nano Lett.* **2004**, *4*, 1733.
[48] L. Gou, M. Chipara, J. M. Zaleski, *Chem. Mater.* **2007**, *19*, 1755.
[49] Q. N. Luu, J. M. Doorn, M. T. Berry, C. Jiang, C. Lin, P. S. May, *J. Colloid Interface Sci.* **2011**, *356*, 151.

[50] T. Kim, A. Canlier, G. H. Kim, J. Choi, M. Park, S. M. Han, *ACS Appl. Mater. Interfaces* **2013**, *5*, 788.
[51] J. Lee, I. Lee, T.-S. Kim, J.-Y. Lee, *Small* **2013**, *9*, 2887.
[52] K. C. Pradel, K. Sohn, J. Huang, *Angew. Chem. Int. Ed.* **2011**, *50*, 3412.
[53] C. Mayousse, C. Celle, E. Moreau, J.-F. Mainguet, A. Carella, J.-P. Simonato, *Nanotechnology* **2013**, *24*, 215501.
[54] P. B. Catrysse, S. Fan, *Nano Lett.* **2010**, *10*, 2944.
[55] Y. C. Lu, K. S. Chou, *Nanotechnology* **2010**, *21*, 215707.
[56] R. C. Tenent, T. M. Barnes, J. D. Bergeson, A. J. Ferguson, B. To, L. M. Gedvilas, M. J. Heben, J. L. Blackburn, *Adv. Mater.* **2009**, *21*, 3210.
[57] V. Scardaci, R. Coull, P. E. Lyons, D. Rickard, J. N. Coleman, *Small* **2011**, *7*, 2621.
[58] J.-Y. Lee, S. T. Connor, Y. Cui, P. Peumans, *Nano Lett* **2008**, *8*, 689.
[59] J.-Y. Lee, S. T. Connor, Y. Cui, P. Peumans, *Nano Lett.* **2010**, *10*, 1276.
[60] B. E. Hardin, W. Gaynor, I.-K. Ding, S.-B. Rim, P. Peumans, M. D. McGehee, *Org. Electron.* **2011**, *12*, 875.
[61] C.-H. Chung, T.-B. Song, B. Bob, R. Zhu, Y. Yang, *Nano Res.* **2012**, *5*, 805.
[62] D.-S. Leem, A. Edwards, M. Faist, J. Nelson, D. D. C. Bradley, J. C. de Mello, *Adv. Mater.* **2011**, *23*, 4371.
[63] C.-H. Liu, X. Yu, *Nanoscale Res. Lett.* **2011**, *6*, 75.
[64] R. D. Deegan, O. Bakajin, T. F. Dupont, G. Huber, S. R. Nagel, T. A. Witten, *Nature* **1997**, *389*, 827.
[65] Y. Zhou, J. Chen, L. Zhang, L. Yang, *Eur. J. Inorg. Chem.* **2012**, *2012*, 3176.
[66] D. Al-Mawlawi, C. Z. Liu, M. Moskovits, *J. Mater. Res.* **1994**, *9*, 1014.
[67] A. R. Madaria, A. Kumar, C. Zhou, *Nanotechnology* **2011**, *22*, 245201.
[68] A. Madaria, A. Kumar, F. Ishikawa, C. Zhou, *Nano Res.* **2010**, *3*, 564.
[69] G. Yu, A. Cao, C. M. Lieber, *Nat. Nanotechnol.* **2007**, *2*, 372.
[70] J. Huang, R. Fan, S. Connor, P. Yang, *Angew. Chem. Int. Ed.* **2007**, *46*, 2414.
[71] D. Whang, S. Jin, Y. Wu, C. M. Lieber, *Nano Lett.* **2003**, *3*, 1255.
[72] W. Salalha, E. Zussman, *Phys. Fluids* **2005**, *17*, 063301.
[73] Y. Huang, X. Duan, Q. Wei, C. M. Lieber, *Science* **2001**, *291*, 630.
[74] P. A. Smith, C. D. Nordquist, T. N. Jackson, T. S. Mayer, B. R. Martin, J. Mbindyo, T. E. Mallouk, *Appl. Phys. Lett.* **2000**, *77*, 1399.
[75] O. Harnack, C. Pacholski, H. Weller, A. Yasuda, J. M. Wessels, *Nano Lett.* **2003**, *3*, 1097.
[76] B. Sun, H. Sirringhaus, *J. Am. Chem. Soc.* **2006**, *128*, 16231.
[77] Y. Cui, M. T. Björk, J. A. Liddle, C. Sönnichsen, B. Boussert, A. P. Alivisatos, *Nano Lett.* **2004**, *4*, 1093.
[78] Y. Yin, Y. Lu, B. Gates, Y. Xia, *J. Am. Chem. Soc.* **2001**, *123*, 8718.
[79] M. Engel, J. P. Small, M. Steiner, M. Freitag, A. A. Green, M. C. Hersam, P. Avouris, *ACS Nano* **2008**, *2*, 2445.
[80] K. Heo, E. Cho, J.-E. Yang, M.-H. Kim, M. Lee, B. Y. Lee, S. G. Kwon, M.-S. Lee, M.-H. Jo, H.-J. Choi, T. Hyeon, S. Hong, *Nano Lett.* **2008**, *8*, 4523.
[81] S. G. Rao, L. Huang, W. Setyawan, S. Hong, *Nature* **2003**, *425*, 36.
[82] A. Javey, S. W. Nam, R. S. Friedman, H. Yan, C. M. Lieber, *Nano Lett.* **2007**, *7*, 773.
[83] J. Seo, H. Lee, S. Lee, T. I. Lee, J.-M. Myoung, T. Lee, *Small* **2012**, *8*, 1614.
[84] P.-C. Hsu, H. Wu, T. J. Carney, M. T. McDowell, Y. Yang, E. C. Garnett, M. Li, L. Hu, Y. Cui, *ACS Nano* **2012**, *6*, 5150.
[85] W. Gaynor, G. F. Burkhard, M. D. McGehee, P. Peumans, *Adv. Mater.* **2011**, *23*, 2905.
[86] X.-Y. Zeng, Q.-K. Zhang, R.-M. Yu, C.-Z. Lu, *Adv. Mater.* **2010**, *22*, 4484.
[87] A. Kim, Y. Won, K. Woo, C.-H. Kim, J. Moon, *ACS Nano* **2013**, *7*, 1081.
[88] E. C. Garnett, W. Cai, J. J. Cha, F. Mahmood, S. T. Connor, M. Greyson Christoforo, Y. Cui, M. D. McGehee, M. L. Brongersma, *Nat. Mater.* **2012**, *11*, 241.

[89] F. S. F. Morgenstern, D. Kabra, S. Massip, T. J. K. Brenner, P. E. Lyons, J. N. Coleman, R. H. Friend, *Appl. Phys. Lett.* **2011**, *4*, 183307.
[90] P. Ramasamy, D.-M. Seo, S.-H. Kim, J. Kim, *J. Mater. Chem.* **2012**, *22*, 11651.
[91] G. Guisti, D. P. Langley, M. Lagrange, R. Collins, C. Jiménez, Y. Bréchet, D. Bellet, *Int. J. Nanotechnol.* **2014**, *11*, 785.
[92] A. Bid, A. Bora, A. K. Raychaudhuri, *Phys. Rev. B* **2006**, *74*, 035426.
[93] D. Hecht, L. Hu, G. Grüner, *Appl. Phys. Lett.* **2006**, *89*, 133112.
[94] T. Tokuno, M. Nogi, M. Karakawa, J. Jiu, T. Nge, Y. Aso, K. Suganuma, *Nano Res.* **2011**, *4*, 1215.
[95] J. Zhao, H. Sun, S. Dai, Y. Wang, J. Zhu, *Nano Lett.* **2011**, *11*, 4647.
[96] M. Quinten, in *Opt. Prop. Nanoparticle Syst.*, Wiley-VCH Verlag GmbH & Co. KGaA, **2011**, pp. I–XIV.
[97] R. H. Ritchie, *Phys. Rev.* **1957**, *106*, 874.
[98] B. Schaffer, U. Hohenester, A. Trügler, F. Hofer, *Phys. Rev. B* **2009**, *79*, 041401.
[99] C. J. Powell, J. B. Swan, *Phys. Rev.* **1959**, *115*, 869.
[100] H. Ditlbacher, A. Hohenau, D. Wagner, U. Kreibig, M. Rogers, F. Hofer, F. R. Aussenegg, J. R. Krenn, *Phys. Rev. Lett.* **2005**, *95*, 257403.
[101] B. Kenens, M. Rybachuk, J. Hofkens, H. Uji-i, *J. Phys. Chem. C* **2013**, *117*, 2547.
[102] J. Kottmann, O. Martin, D. Smith, S. Schultz, *Opt. Express* **2000**, *6*, 213.
[103] J. P. Kottmann, O. J. F. Martin, D. R. Smith, S. Schultz, *Phys. Rev. B* **2001**, *64*, 235402.
[104] J. A. Spechler, C. B. Arnold, *Appl. Phys. A* **2012**, *108*, 25.
[105] L. Hu, G. Chen, *Nano Lett.* **2007**, *7*, 3249.
[106] C. Preston, Y. Xu, X. Han, J. N. Munday, L. Hu, *Nano Res.* **2013**, *6*, 461.
[107] T. Chih-Hung, H. Sui-Ying, H. Tsung-Wei, T. Yu-Tang, C. Yan-Fang, Y. H. Jhang, L. Hsieh, W. Chung-Chih, C. Yen-Shan, C. Chieh-Wei, L. Chung-Chun, *Org. Electron.* **2011**, *12*, 2003.
[108] C. Guillén, J. Montero, J. Herrero, *Appl. Surf. Sci.* **2013**, *264*, 448.
[109] H. Kuramochi, R. Akiike, H. Iigusa, K. Tamano, K. Utsumi, T. Shibutami, P. Sichanugrist, M. Konagai, *Jpn. J. Appl. Phys.* **2012**, *51*, 10NB13.
[110] P. Blake, P. D. Brimicombe, R. R. Nair, T. J. Booth, D. Jiang, F. Schedin, L. A. Ponomarenko, S. V. Morozov, H. F. Gleeson, E. W. Hill, A. K. Geim, K. S. Novoselov, *Nano Lett.* **2008**, *8*, 1704.
[111] G. Eda, G. Fanchini, M. Chhowalla, *Nat. Nanotechnol.* **2008**, *3*, 270.
[112] U. Kim, J. Kang, C. Lee, H. Y. Kwon, S. Hwang, H. Moon, J. C. Koo, J.-D. Nam, B. H. Hong, J.-B. Choi, H. R. Choi, *Nanotechnology* **2013**, *24*, 145501.
[113] T. M. Barnes, M. O. Reese, J. D. Bergeson, B. A. Larsen, J. L. Blackburn, M. C. Beard, J. Bult, J. van de Lagemaat, *Adv. Energy Mater.* **2012**, *2*, 353.
[114] S. Bae, H. Kim, Y. Lee, X. Xu, J.-S. Park, Y. Zheng, J. Balakrishnan, T. Lei, H. Ri Kim, Y. I. Song, Y.-J. Kim, K. S. Kim, B. Özyilmaz, J.-H. Ahn, B. H. Hong, S. Iijima, *Nat. Nanotechnol.* **2010**, *5*, 574.
[115] A. Reina, X. Jia, J. Ho, D. Nezich, H. Son, V. Bulovic, M. S. Dresselhaus, J. Kong, *Nano Lett.* **2009**, *9*, 30.
[116] P. N. Nirmalraj, P. E. Lyons, S. De, J. N. Coleman, J. J. Boland, *Nano Lett.* **2009**, *9*, 3890.
[117] E. M. Doherty, S. De, P. E. Lyons, A. Shmeliov, P. N. Nirmalraj, V. Scardaci, J. Joimel, W. J. Blau, J. J. Boland, J. N. Coleman, *Carbon* **2009**, *47*, 2466.
[118] H.-Z. Geng, K. K. Kim, K. P. So, Y. S. Lee, Y. Chang, Y. H. Lee, *J. Am. Chem. Soc.* **2007**, *129*, 7758.
[119] D. S. Hecht, A. M. Heintz, R. Lee, L. Hu, B. Moore, C. Cucksey, S. Risser, *Nanotechnology* **2011**, *22*, 075201.
[120] D.-W. Shin, J. H. Lee, Y.-H. Kim, S. M. Yu, S.-Y. Park, J.-B. Yoo, *Nanotechnology* **2009**, *20*, 475703.
[121] B. S. Shim, J. Zhu, E. Jan, K. Critchley, N. A. Kotov, *ACS Nano* **2010**, *4*, 3725.

[122] K. A. Sierros, D. R. Cairns, J. S. Abell, S. N. Kukureka, *Thin Solid Films* **2010**, *518*, 2623.
[123] G. Haacke, *J. Appl. Phys.* **1976**, *47*, 4086.
[124] Y.-Y. Chen, C.-L. Chen, P.-C. Lee, M.-N. Ou, in *Nanowires - Fundam. Res.* (Ed: A. Hashim), InTech, **2011**.
[125] G. Wiedemann, R. Franz, *Ann. Phys. Chem.* **n.d.**
[126] F. Völklein, H. Reith, T. W. Cornelius, M. Rauber, R. Neumann, *Nanotechnology* **2009**, *20*, 325706.
[127] Y. Peng, T. Cullis, B. Inkson, *Appl. Phys. Lett.* **2008**, *93*, 183112.
[128] J. L. Zeng, Z. Cao, D. W. Yang, L. X. Sun, L. Zhang, *J. Therm. Anal. Calorim.* **2009**, *101*, 385.
[129] J. Xu, A. Munari, E. Dalton, A. Mathewson, K. M. Razeeb, *J. Appl. Phys.* **2009**, *106*, 124310.
[130] F. W. Reynolds, G. R. Stilwell, *Phys. Rev.* **1952**, *88*, 418.
[131] R. B. Dingle, *Proc. R. Soc. Lond. Ser. Math. Phys. Sci.* **1950**, *201*, 545.
[132] L. Rayleigh, *Proc. Lond. Math. Soc.* **1878**, *s1-10*, 4.
[133] S. Karim, M. E. Toimil-Molares, A. G. Balogh, W. Ensinger, T. W. Cornelius, E. U. Khan, R. Neumann, *Nanotechnology* **2006**, *17*, 5954.
[134] H. Li, J. M. Biser, J. T. Perkins, S. Dutta, R. P. Vinci, H. M. Chan, *J. Appl. Phys.* **2008**, *103*, 024315.
[135] R. Huang, Y.-H. Wen, Z.-Z. Zhu, S.-G. Sun, *J. Mater. Chem.* **2011**, *21*, 18998.
[136] H. S. Shin, J. Yu, J. Y. Song, *Appl. Phys. Lett.* **2007**, *91*, 173106.
[137] C.-P. Hsiung, H.-W. Liao, J.-Y. Gan, T.-B. Wu, J.-C. Hwang, F. Chen, M.-J. Tsai, *ACS Nano* **2010**, *4*, 5414.
[138] Z. Yu, Q. Zhang, L. Li, Q. Chen, X. Niu, J. Liu, Q. Pei, *Adv. Mater.* **2011**, *23*, 664.
[139] J.-W. Lim, D.-Y. Cho, K. Eun, S.-H. Choa, S.-I. Na, J. Kim, H.-K. Kim, *Sol. Energy Mater. Sol. Cells* **2012**, *105*, 69.
[140] P. Lee, J. Lee, H. Lee, J. Yeo, S. Hong, K. H. Nam, D. Lee, S. S. Lee, S. H. Ko, *Adv. Mater.* **2012**, *24*, 3326.
[141] F. Xu, Y. Zhu, *Adv. Mater.* **2012**, *24*, 5117.
[142] X. Ho, J. Nie Tey, W. Liu, C. Kweng Cheng, J. Wei, *J. Appl. Phys.* **2013**, *113*, 044311.
[143] C. J. M. Emmott, A. Urbina, J. Nelson, *Sol. Energy Mater. Sol. Cells* **2012**, *97*, 14.
[144] L. Li, Z. Yu, W. Hu, C. Chang, Q. Chen, Q. Pei, *Adv. Mater.* **2011**, *23*, 5563.
[145] W. Gaynor, J.-Y. Lee, P. Peumans, *ACS Nano* **2010**, *4*, 30.
[146] T. Sun, Z. L. Wang, Z. J. Shi, G. Z. Ran, W. J. Xu, Z. Y. Wang, Y. Z. Li, L. Dai, G. G. Qin, *Appl. Phys. Lett.* **2010**, *96*, 133301.
[147] L. Yang, T. Zhang, H. Zhou, S. C. Price, B. J. Wiley, W. You, *ACS Appl Mater Interfaces* **2011**, *3*, 4075.
[148] C.-C. Chen, L. Dou, R. Zhu, C.-H. Chung, T.-B. Song, Y. B. Zheng, S. Hawks, G. Li, P. S. Weiss, Y. Yang, *ACS Nano* **2012**, *6*, 7185.
[149] J. Ajuria, I. Ugarte, W. Cambarau, I. Etxebarria, R. Tena-Zaera, R. Pacios, *Sol. Energy Mater. Sol. Cells* **2012**, *102*, 148.
[150] T. Stubhan, J. Krantz, N. Li, F. Guo, I. Litzov, M. Steidl, M. Richter, G. J. Matt, C. J. Brabec, *Sol. Energy Mater. Sol. Cells* **2012**, *107*, 248.
[151] R. G. Gordon, *Mrs Bull.* **2000**, *25*, 52.
[152] T. Kim, Y. W. Kim, H. S. Lee, H. Kim, W. S. Yang, K. S. Suh, *Adv. Funct. Mater.* **2013**, *23*, 1250.
[153] J.-P. Simonato, C. Celle, C. Mayousse, A. Carella, H. Basti, A. Carpentier, *MRS Online Proc. Libr.* **2012**, *1449*, 107.
[154] K. Müllen, U. Scherf, Eds. , *Organic Light Emitting Devices: Synthesis, Properties and Applications*, Wiley-VCH Verlag GmbH & Co. KGaA, **2006**.
[155] L. Li, Z. Yu, C. Chang, W. Hu, X. Niu, Q. Chen, Q. Pei, *Phys. Chem. Chem. Phys.* **2012**, *14*, 14249.

[156] W. Gaynor, S. Hofmann, M. G. Christoforo, C. Sachse, S. Mehra, A. Salleo, M. D. McGehee, M. C. Gather, B. Lüssem, L. Müller-Meskamp, P. Peumans, K. Leo, *Adv. Mater.* **2013**, *25*, 4006.
[157] K.-K. Kim, S. Lee, H. Kim, J.-C. Park, S.-N. Lee, Y. Park, S.-J. Park, S.-W. Kim, *Appl. Phys. Lett.* **2009**, *94*, 071118.
[158] S. Coskun, E. Selen Ates, H. Emrah Unalan, *Nanotechnology* **2013**, *24*, 125202.
[159] J. Lee, P. Lee, H. Lee, D. Lee, S. S. Lee, S. H. Ko, *Nanoscale* **2012**, *4*, 6408.
[160] W. Hu, X. Niu, R. Zhao, Q. Pei, *Appl. Phys. Lett.* **2013**, *102*, 083303.

Chapter 2
A gentle introduction to Percolation Theory:

In the past six decades, percolation has been the topic of numerous investigations. For many of us, the concept of percolation is most closely associated closely with our daily dose of caffeine. This section of the thesis aims to answer the questions: what is percolation? Why is it interesting? How can we model it? And most importantly how can it be used to understand Silver nanowire networks?

Here we cover the literature relevant for the application of percolation theory to silver nanowire networks. The following sections provide a gentle introduction to percolation theory covering the fundamental ideological framework and discussing the key literature and problems that are associated with this field.

2.1 What is percolation?

> **Percolate**
> ˈpəːkəleɪt
> (Of a liquid or gas) filter gradually through a porous surface or substance: '*the water percolating through the soil may leach out minerals*'
> *"Oxford Dictionary of English"*[1]

For the purpose of this thesis we shall define percolation as *the formation and/or use of pathways through a porous material*. Expanded broadly, it concerns anything that can be considered to move through a system exhibiting a collection of open or closed pathways.

Percolation is the process of something finding pathways through a porous medium. Simple examples of percolation are found in everyday life, the most common of which is the percolation of water through ground coffee beans to provide that sweet caffeine hit that seems to drive our modern world. Other instances of percolation vary broadly from large time scales and sedate processes (percolation of water through bedrock) to rapid and destructive (passage of fire through a forest). Percolation has found application in a broad range of topics including mathematics, physics, petroleum,[2] ecology,[3] chemistry,[4] and materials science amongst others. Percolation theory looks at the connectivity of the objects in a given system, these objects can be connected together in a variety of ways and connections can either be considered as open or closed paths.

In general the main goal of studying a percolating system is to determine the density of open pathways at which there is a phase transition in one or more properties of the system. For the example of water seeping through stone, the closed pathways are simply the stone and the open pathways are gaps in it. Consider a stone container: if the stone is complete and perfect one can imagine that it contains no gaps at all, at this point it is not possible for a fluid medium such as water or gas to pass through the stone. Consider then the introduction of

defects into the container, as the density of these defects increases the gaps in the stone grow, at some point a continuous gap is formed from inside of the container to the outside allowing the fluid to pass. This results in a phase transition from a sound container to a leaking one.

Typically all phase transitions in percolating media are associated with the formation of a spanning cluster, *i.e.* a pathway from one side of the system to another). In the study of percolating systems we search to determine the critical density n_c at which this occurs. The most common definition of n_c for a given system is the density at which the probability of finding at least one spanning cluster is 50%. Exact solutions satisfying this definition are currently unobtainable analytically for most systems with dimensionality $d \geq 2$ and is heavily-dependent on the system geometry, lattice type and object type.[5]

In order to consider this problem in relation to the subject of this thesis let us first discuss some of the different flavours of percolation:

Site percolation: Systems in which the open or closed paths are restricted to a regular lattice of sites. A site is considered connected to another site if they share one side of the defined lattice. In this model a site is either open and unoccupied or closed and occupied.

Bond percolation: Systems in which the lattice sides are considered as bonds, in this model the sides of the unit cell are either open or closed. The lattice vertices become sites and are considered connected if they share a closed bond.

Continuum Percolation: Systems in which no discretisation of the sites is performed, in these systems sites are distributed randomly and are considered to be connected if the basis touches or overlaps.

Let us first discuss bond and site percolation together as these are both based on regular lattices and have many similarities. Graphical representations of site and bond percolation on a square lattice are given in Figure 3.1a) and b) respectively.

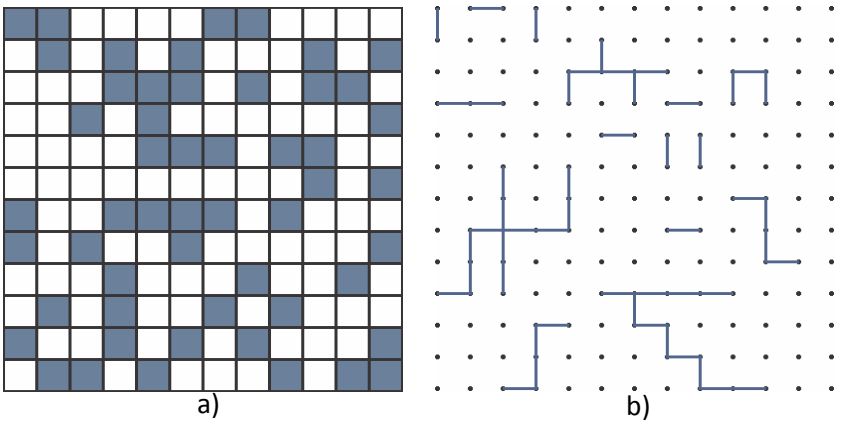

Figure 2.1 Schematic examples of square lattice percolation a) Site percolation and b) bond percolation.

In Figure 2.1 a) we can see open and closed paths as indicated by white and blue squares respectively. At this point it is useful to define the definition of the spanning cluster that will be used throughout this thesis. In a percolation model we are interested in the connectivity between objects within a system, if two objects are connected together they are said to be in the same cluster. In

percolation theory it is actually irrelevant as to whether you consider the open or closed paths, statistically they are two sides of the same problem and mirror one another. Conceptually however, it is nice to have in mind what the open and closed sites are meant to represent, if the system depicted in Figure 2.1 a) were to be the bottom of your coffee mug, and open sites correspond to gaps in the ceramic this would lead to a leaking cup. Conversely we could consider the same system as a polymer matrix with occupied sites representing conductive filler particles, in this case electrons would be capable of percolating through the system. In general within this thesis we will discuss the latter type of concept, in which the occupation of a site or bond represents the presence of a conduction pathway. Thus percolation occurs when enough sites are occupied to create a conduction path across the system.

In order for a system to be percolating, there must be at least one cluster that satisfies the percolation criteria of the system. There are several methods of defining these criteria but we shall use a modified form of the R_1 rule employed by Ziff[6] and originally defined by Reynolds, Stanley and Klein.[7,8]

R_1 simply defines percolation as occurring when at least one cluster spans the given system in the vertical direction. In this definition spanning is considered to occur when one site at the bottom edge of the system belongs to the same cluster as a site in the top edge. In this definition the left and right edges of the system are in open boundary conditions and clusters connecting them together are not considered as spanning clusters. For simplicity on a regular lattice we can define the top and bottom rows of the system as fully occupied rows, and then explore the occupancy density required to satisfy the given percolation criteria. R_1 also specifies that the system must be a square. A schematic representation of a spanning cluster satisfying R_1 is shown in Figure 2.2. For a discussion of alternate percolation criteria, cluster wrapping and the challenges associated with them, the reader is directed to the work of Newman and Ziff.[9] In the case of asymmetric systems the position of the percolation threshold has been shown to shift.[10]

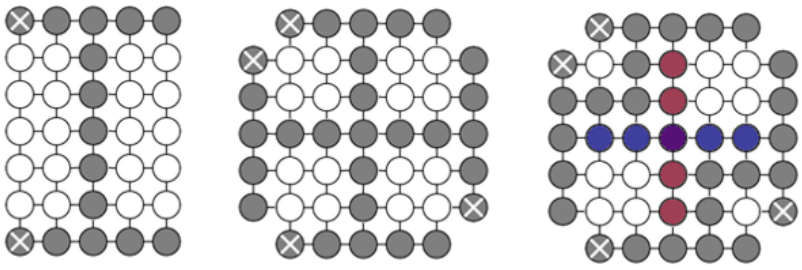

Figure 2.2 Different ways of assigning the percolation criteria, full circles in the schematics represent occupied sites. R_1 is represented on the left. The central image represents spanning allowed in either direction and the system on the right provides an example of when spanning can occur between any combinations of two electrodes. The colours in the image on the right indicate three different possible percolating clusters. Image modified from Newman and Ziff.[9]

When considering a regular lattice it is possible to interchange the density n and the occupancy probability p. On a regular lattice the number of sites or bonds is limited hence, the occupancy probability is directly proportional to the density. Figure 2.3 provides an example of the application of R_1 to a square lattice with the top and bottom edges of the system defined as closed. The spanning cluster in this particular network occurred when 50% of the sites were occupied.

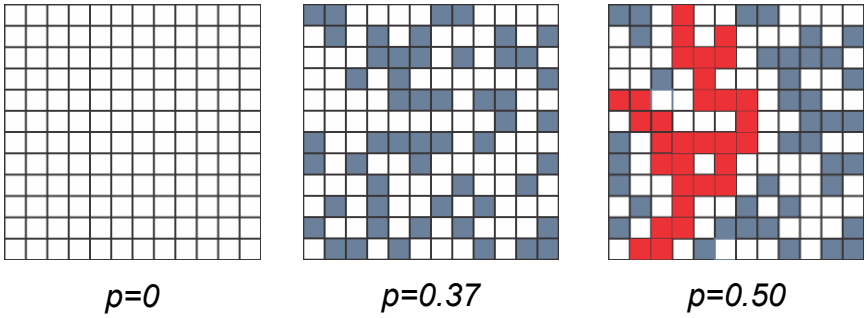

Figure 2.3 An example of the formation of a spanning cluster (indicated in red) according to the rule R_1. Initially all sites are unoccupied; as the occupation probability p is increased, sites are filled and finally a spanning cluster is formed (indicated in red).

In the examples provided in Figure 2.1 the difference in connectivity can be seen between site and bond percolation. In the case of site percolation on the square lattice nearest neighbours in the same row or column are connected to each other if both sites are occupied. The same is not true for bond percolation. Nearest neighbours in the same row or column can both be connected to separate clusters, or in fact to the same cluster, but this does not necessitate that they be connected to each other directly. Applications have been found for both bond and site percolation and the most appropriate type to be used will depend on the system being modelled.

The differences between bond and site percolation are dependent on the lattice basis and the coordination number of the basis set. However, it is typical that on the same lattice type the critical density n_c of a site percolation system will be higher than that of the similar bond percolation system. This arises from the intrinsic definition of these two systems: in site percolation each site can be either occupied or unoccupied, in bond percolation the vertices of the lattice can be considered as sites and a single bond connects to 2 of them. This could incorrectly lead one to think that the n_c of the bond system should be ½ that of its equivalent site system but this is not the case as shown in Table 2.1.

In reality many of the values provided in Table 2.1 are not exact solutions for the percolation threshold of the system. Currently of this list only square bond, honeycomb bond and both triangular lattices have been solved exactly. Some other lattices in 2D have also been solved exactly, for an excellent discussion of the process of determination and the literature surrounding exact solutions see *"Introduction to percolation theory"* by Stauffer and Aharony.[5]

Table 2.1: A small selection of percolation threshold values for specific lattices, values for both site and bond percolation are provided.[5]

Lattice	Site	Bond
Honeycomb	0.692	0.65271
Square	0.592746	0.50000
Triangular	0.500000	0.34729
Diamond	0.43	0.388
Simple Cubic	0.3116	0.2488
BCC	0.246	0.1803
FCC	0.198	0.119

2.2 Dimensionality

The simplest form of percolation is to consider a 1D lattice of sites as depicted in Figure 2.4a). This system has a coordination number of 2, meaning that each site can be connected to a maximum of 2 other sites and there are 3 possible combinations of connections. Connected on both sides, connected to the site on the left or connected to the right. This system is the simplest representation of percolation and is one of the few systems to have an exact solution. In order for there to be a path from one end of the lattice to the other, all of the sites need to be occupied. This results in the phase change occurring at $p_c=1$. Unlike the majority of percolation systems this simple 1D lattice is identical to its bond percolation analogue. Another peculiarity of this system is the abrupt phase transition, as shown in Figure 2.4 b) when the occupation probability $p<1$ there is no possibility for the formation of a cluster spanning from one end of the system to the other. This results in a discrete step function in the cumulative probability of percolation below n_c the probability of a spanning cluster existing in the network is always 0, at n_c there is always a spanning cluster thus the probability is 1. In two or three dimensions the transition from non-percolating to percolating becomes sharper as the system size increases, thus this distinct phase transition in one dimension is comparable to those anticipated for an infinite system at higher dimensions.[5]

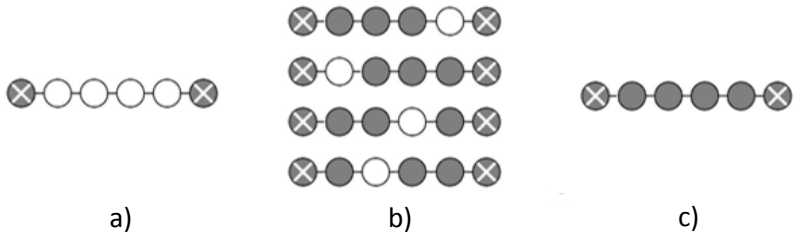

Figure 2.4 1D percolation system a) Chain of 4 empty sites between the two ends of the system b) The four distinct combinations possible at $p=0.75$ c) Percolating cluster is formed.

This example of a 1D system seems quite trivial and indeed it is, but it holds interesting analogues for systems of higher dimensions. If we move now to the 2D square lattice as discussed earlier we can see why it is difficult to find exact solutions for percolating systems in 2D and as yet not possible in 3D. The first complication that arises is that now the system has a coordination number of 4 which means that each individual site can possibly be connected to its' four neighbours in *15* different ways. Also as we have added another degree of freedom to the lattice (the 2nd dimension) we now have to consider bends, kinks and knobs in the percolating cluster. On a regular lattice the clusters are often referred to as lattice animals. Figure 2.5 depicts the 28 possible lattice animals for clusters of size 1-4. If we were to extend this to a cluster with 5 occupied sites we would have to add an additional 63 combinations.

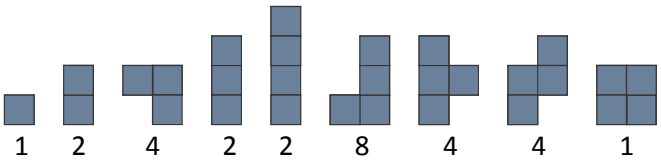

Figure 2.5 Lattice animals up to a cluster size of 4 occupied sites, possible mirrored and rotated clusters are not shown but their number is indicated below each lattice animal. Modified from Stauffer and Aharony[5]

One can see immediately that the problem is significantly more complicated than for the 1D case and it is easy to understand why it becomes a challenge to mathematically define all possible combinations of bonds or sites in such a system. However, this pales in comparison to the complexity of continuum percolation systems, as discussed below.

2.3 Continuum Percolation

Thus far we have discussed only the simplest forms of percolation: those based on a regular lattice. In reality, the world is not so simple. Although many systems exist in which a regular lattice model can be applied there are many in which it cannot. For such systems we must consider a continuum percolation model. In this type of system, defined geometric objects such as ellipses,[11,12] circles,[11] polygons[11] or sticks[11,13,14] are added at random locations within the system. Objects may appear at any location within the system; this causes two immediately obvious issues. Firstly as there can be an object at any location in the system the number of possible objects is effectively infinite. In this case it is then impossible to discuss the occupation probability of a given site any longer. Instead, the behaviour of the system is discussed in terms of the object density. Secondly as objects can be located anywhere the number of objects within range of a given object is not fixed. This results in an effectively infinite coordination number for each of the geometric objects. This makes a mathematically exact solution to continuum percolation impossible. In reality these infinities do not cause much of a disturbance in the behaviour of the system as the percolation

threshold is orders of magnitude lower than that required to obtain a density at which the coordination of an individual site or the number of objects in the system approaches infinity.

In order to explore the formation of clusters in continuum systems, computer simulation methods are used. Most commonly used is the Monte Carlo method.[15] Named for the games of chance for which the city state of Monte Carlo is famous, Monte Carlo simulations rely on the statistics of random processes to approximate the outcome of a given problem. Simply put the idea of Monte Carlo is to define an experiment that produces a binary output, either success or failure. By repeating this process many times and tracking the number of successes, a statistical picture of the system can be produced. An alternate method for calculating the density of geometric shapes required to reach the percolation threshold is the excluded volume method[16] which mathematically defines a volume around each geometric object in which it is possible for an intersection with a second object to occur. The percolation threshold is related then to the density at which the combined excluded volume of all of the objects in the system approaches the total volume of the system.

2.4 Application of percolation theory to 2D stick systems.

In order to understand the formation of conductive nanowire networks by the combination of metallic nanowires, a 2D percolation model can be used. In this particular case the percolating system is the nanowire network and the open paths are the connections through which electrons can travel. There are many ways to consider this problem and a considerable amount of work has been undertaken since the seminal contributions of Pike and Seager in 1974.[11,17]

The electrical properties of 2D nanowire networks do fundamentally originate from a percolation phenomenon. Indeed, the conductivity of the network is determined by the number and length of the electronic pathways through the network. These pathways are formed through the interconnection of sticks across the network and often take on a complex geometry of series and parallel resistances. The exploration of such a percolating behaviour as exhibited by these networks was initiated by the seminal papers of Pike and Seager in 1974[11,17] in which a variety of percolation systems and models were discussed and covered in excellent detail and a high level of accuracy (especially with the technology available at the time) the problem of 2D stick percolation. As yet, no exact solution for the critical density of a system with a given stick geometry and system size currently exists.

The majority of published works focuses on either a constant system size and increasing stick length[11,13] or sticks of unit length and a varying system size.[18–20] In the initial work of Pike and Seager, three networks of 1000 sticks were made with randomly-distributed positions (within a defined system) and orientation. The length of these sticks was increased in a stepwise manner and the interconnections between sticks in the network were observed. Percolation was said to occur when there was a set of connected sticks spanning the initially

defined system. In order to clarify the method by which we determine whether percolation is occurring we need to provide a clear definition of what we mean by percolation. For the purpose of this thesis and for the majority of the articles that we refer to herein we use the rule R_1 as defined by Reynolds, Stanley and Klein and which has already been mentioned in section 2.1.[8] Percolation occurs when both electrodes belong to the same cluster. This cluster is known as the spanning cluster. Thus Pike and Seager were able to determine a critical length l_c of the wires at which percolation would occur.[11]

$$l_c \frac{\sqrt{N\pi}}{2} = 2.118 \qquad (2.1)$$

Where N is the number of sticks in the system. As the system defined by Pike and Seager was of unit length this is also interchangeable with the density of sticks. Balberg *et al.* [13,16] expanded the work of Pike and Seager and introduced the first calculations of system resistance based on resistance networks applied to the 2D stick system.[13] More importantly they showed that it was possible to consider the percolation behaviour based on the excluded volume or area fraction of a given set of geometric shapes. This idea corresponds to the probability of an individual object interacting with another object. When considering 2D objects, if all the objects are identical one can define an area surrounding the object in which an intersection can occur. This becomes the excluded area, as the total excluded area of all objects in the system surpasses the area of the system the probability of intersections between new additions and existing objects becomes 1. [16] The correlation between the shape and size of the object, its excluded volume and the system size allowed Balberg *et al.* to demonstrate that for 2D stick systems:[16]

$$N{l_c}^2 = N_c l^2 \quad (2.2)$$

Where N_c is the critical number of nanowires required to attain a percolation probability of ½. This information is more directly applicable than the work of Pike and Seager as it allows one to discuss the critical density instead of critical length. For the remainder of this thesis we shall consider the percolation threshold to be the critical density n_c at which the probability of percolation as defined by R_1 is ½. As in the work of Pike and Seager, Balberg *et al.* used a system of unit size, hence, $n_c=N_c$. However this is not always the case and it should be remembered that more generally, the equality $n_c=N_c/L_s^2$holds, where is L_s is the size of the system.

Balberg *et al.* also demonstrated that sticks exhibit a high excluded volume and form percolating networks at significantly lower densities than spheres of the same mass.[16] This leads to the conclusion that in order to minimize the material used to obtain a percolating network it is more efficient to use nanowires than nanoparticles. Also due to the anisotropy of these objects the open surface area will be higher resulting in better optical transmission. Another critical observation that Balberg *et al.* provided is that for continuum systems the percolation threshold is critically dependent on the degree of randomness in the system. Initially they started with identical objects distributed randomly in space

but with the same orientation, they then increased the degree of randomness by allowing random orientations and observed a decrease in the required N_c. They further modified the system by allowing objects of different sizes and again observed a decrease in the percolation threshold. This allows the conclusion that for each increase in the degree of randomness the percolation threshold can be expected to decrease.

Unfortunately the excluded volume method tends to overestimate the percolation threshold as *"longer sticks…* [hence] *larger excluded volumes contribute to the onset of percolation to a larger extent than can be gathered from the value of their volume."*[16] This results in a disagreement between Monte Carlo methods and excluded volume predictions of the percolation threshold. Therefore, in order to avoid this issue, the excluded volume method is not used for this work.

In the past much work has been undertaken to overcome the limits of finite system modelling. Understanding the behaviour of a percolating system is often couched in terms of an infinite spanning cluster on an infinite lattice. In the case of lattice and site percolation this formalism makes sense, an infinite system can be expressed in these simple cases in terms of symmetry and can sometimes be solved mathematically. However For a continuum model this is considerably more challenging. In general it was considered that the system of interest (i.e. the device) would be orders of magnitude larger than a system size that could be feasibly simulated. For many systems this holds true, however for some emerging technology this may not necessarily be the case. In order to overcome this issue the works of Reynolds, Stanley and Klein[7,8] demonstrated that the effective critical density n_{ceff} determined for a specific finite system can be related to the critical density of the infinite system in the following way:

$$n_{ceff} - n_c \propto (L_s)^{\frac{-1}{v}} \qquad (2.3)$$

Where L_s is the system size and v is the correlation length exponent. The value of v is dimensionally dependent and is expected to be $v=4/3$ in two dimensions.[5–8] This provides us with a tool to explore the finite scaling of percolation into the infinite system or to a system of specific size.

In 1992, Ziff demonstrated that in some specific cases such as the renormalization group applied to 2D square lattice scaling occurs faster and can be described as:[6]

$$n_{ceff} - n_c \propto (L_s)^{-1-\frac{1}{v}} \quad (2.4)$$

Li and Zhang[20] reproduced the work of Pike and Seager with significantly higher accuracy and showed that in general the critical density at the percolation threshold for a 2D system of sticks is given by:[20]

$$n_c = \frac{5.63726}{l^2} \quad (2.5)$$

However as demonstrated in their article, these values hold only when the system size L_s is several times larger than the nanowire length L_w (L_s>32L_w). Li

and Zhang also demonstrated that the scaling of these systems behaves in the same manner as the 2D square lattice, scaling proportionally with $L^{-1-1/v}$, and they determined a universal finite size scaling function to enable the prediction of n_c for any wire length and system size as long as the ratio L_s/L_w>32.

In this thesis we explore the implication of percolation in small-scale systems bounded on two sides. These systems are analogous to many emerging devices such as carbon nanotube transistors[21], metal nanowire OLEDs, touch screens or solar cells. So far, the discussion of percolation has been carried out in terms of the critical density associated with it and the impact of finite size simulations. In order to predict the properties of a percolating network of silver nanowires for use as a transparent electrode, we should also consider the optical properties and the electrical conductivity.

2.5 Stick Percolation: Semi-Empirical Models for Real Systems

In discussing the physical properties of 2D stick systems it is important to consider the works of Coleman's group from Trinity College. Initially exploring the percolation behaviour of Carbon nanotubes[22,23], Coleman *et al.* have proceeded to explore a variety of emerging materials for application as transparent conducting materials, including graphene[24] and several varieties of metal nanowires.[24–28] The main significance of these works is the development of a set of semi-empirical equations relating an effective film thickness with the actual resistance and the optical transmission of percolating networks. Coleman *et al.* demonstrated that for several percolation systems there is a clear departure from the optical behaviour of bulk films of varying thickness for percolating 2D stick networks. Interestingly, the semi-empirical model also works quite well for percolating networks of graphene flakes. This implies that the lower than expected optical transmission at a given resistance described by the assigned effective thickness is intrinsic to the phase transition observed in percolating materials and not specific to the behaviour of 2D stick systems.

The reason for this universality is the basis of their semi-empirical models on the second order phase transition family of equations to which percolation belongs. This provides the expected power dependence of the conductivity of a percolating system on the density as given by equation 2.6:[5,29]

$$\sigma \propto (n - n_c)^v \qquad (2.6)$$

Where v is once again dimension-dependent and for 2D systems, we have a value of v=4/3. Equation 2.6 also provides a theoretical tool to determine the dimensionality of our experimental percolating systems. By plotting the experimental conductivity as a function of n-n_c and fitting with equation 2.6 we can determine the most appropriate value of v for the real samples. As v is dimensionally dependent this provides information on whether the system is truly a 2D percolating system.

Coleman *et al.* relate this with the typical expression for the optical transmission of a thin film[30], building on the work of Hu, Hecht and Grüner.[29]

Coleman *et al.* assume that for systems of industrial significance $n >> n_c$, this is in general acceptable because for device applications, it is unlikely that densities close to the percolation threshold would be desirable, as this would imply that approximately half of the devices would not be percolating. Using this assumption they replace the density of the system with an effective thickness t and a modified conductivity exponent γ.[24,26]

$$\sigma = \sigma_B (t/t_{min})^{\gamma} \quad (2.7)$$

This allows the thickness dependent conductivity of the percolating material to be correlated with the bulk conductivity of the same material. From this equation they proceed to define expressions for both the sheet resistance R_s and the optical transmission T of the percolating material:[26]

$$R_s = \frac{t_{min}^{\gamma+1}}{t_{min}\sigma_B t^{\gamma+1}} \quad (2.8)$$

$$T = \left[1 + \frac{1}{\Pi}\left(\frac{Z_0}{R_s}\right)^{1/(\gamma+1)}\right]^{-2} \quad (2.9)$$

Where Π represents a percolative figure of merit correlating the optical and electrical conductivity with the critical thickness and the modified conductivity exponent, given by:

$$\Pi = 2\left[\frac{\sigma_B/\sigma_{op}}{\left(Z_0\sigma_{op}t_{min}\right)^{\gamma}}\right]^{1/(\gamma+1)} \quad (2.10)$$

Where Z_0 is the permittivity of free space and σ_{op} is the optical conductivity of the material.

This collection of equations 2.8 through 2.10 allowed Coleman *et al.* to compare the percolative behaviour of graphene, carbon nanotubes and metallic nanowires. At this point in time, of all the transparent conductive materials based on percolating systems, Ag nanowires continue to provide the highest figure of merit.[24,26,27] As an interesting note to further applications which will not be considered in this work, Coleman *et al.* also developed an equation for the thermal behaviour of transparent thin film heaters based on percolating systems.[31] The recent work of Mutiso et al.[32] combined these equations with 2D stick Monte Carlo simulations employing Kirchhoff's laws to calculate the resistance of the simulated networks and assuming a rather simple shadowing model for calculation of the transmission. Mutiso's work shows the impact of wire aspect ratio on the resistance and transmission of percolating systems, and most importantly provides some evidence of an unexpectedly large reduction of the critical density of the system with the introduction of a small percentage of large wires.

2.6 Closing Remarks on Percolation

Within this chapter we have provided an introduction to some of the key concepts related to percolation, and in particular highlighted the key works in the past four decades relating to 2D stick percolation systems. In general percolation is a statistical problem relating to the density or occupation probability of objects within a system. In particular, in relation to 2D stick systems, we highlight that it is a continuum percolation system, and hence the onset of percolation can only be discussed in terms of critical density n_c or critical number N_c.

Several works have been done exploring the finite size scaling of 2D stick systems and it has been suggested that these systems should follow the same trend as the 2D square lattice with the scaling of the system asymptotically approaching a linear dependence with $L^{-1-1/\nu}$ with an intercept at n_c of the infinite system. Finally a brief discussion was dedicated to the semi-empirical equations formulated by Coleman *et al.* which allow correlation of the optical and electrical conductivities in such a way that one can define an appropriate percolative figure of merit with which to compare different systems and materials.

2.7 References

[1] A. Stevenson, *Oxford Dictionary of English*, Oxford University Press, **2014.**

[2] P. R. King, S. V. Buldyrev, N. V. Dokholyan, S. Havlin, Y. Lee, G. Paul, H. E. Stanley, *Phys. Stat. Mech. Its Appl.* **1999**, *274*, 60–66.

[3] C. L. Henley, *Phys. Rev. Lett.* **1993**, *71*, 2741.

[4] A. Belashi, Percolation Modeling in Polymer Nanocomposites, THE UNIVERSITY OF TOLEDO, **2011**.

[5] D. Stauffer, A. Aharony, *Introduction to Percolation Theory, 2nd Revised Ed.*, Taylor And Francis, London, **1994**.

[6] R. M. Ziff, *Phys. Rev. Lett.* **1992**, *69*, 2670–2673.

[7] P. J. Reynolds, H. E. Stanley, W. Klein, *J. Phys. Math. Gen.* **1978**, *11*, L199.

[8] P. J. Reynolds, H. E. Stanley, W. Klein, *Phys. Rev. B* **1980**, *21*, 1223–1245.

[9] M. E. J. Newman, R. M. Ziff, *Phys. Rev. E* **2001**, *64*, 016706–016706–16.

[10] M. Žeželj, I. Stanković, A. Belić, *Phys. Rev. E* **2012**, *85*, 021101–021106.

[11] G. E. Pike, C. H. Seager, *Phys. Rev. B* **1974**, *10*, 1421–1434.

[12] Y.-B. Yi, A. Sastry, *Phys. Rev. E* **2002**, *66*, DOI 10.1103/PhysRevE.66.066130.

[13] I. Balberg, N. Binenbaum, C. H. Anderson, *Phys. Rev. Lett.* **1983**, *51*, 1605–1608.

[14] I. Balberg, N. Binenbaum, *Phys. Rev. B* **1983**, *28*, 3799–3812.

[15] W. L. Dunn, J. K. Shultis, *Exploring Monte Carlo Methods*, Elsevier, **2011**.

[16] I. Balberg, C. H. Anderson, S. Alexander, N. Wagner, *Phys. Rev. B* **1984**, *30*, 3933–3943.

[17] C. H. Seager, G. E. Pike, *Phys. Rev. B* **1974**, *10*, 1435–1446.

[18] I. Balberg, N. Binenbaum, N. Wagner, *Phys. Rev. Lett.* **1984**, *52*, 1465–1468.

[19] M. E. J. Newman, R. M. Ziff, *Phys. Rev. Lett.* **2000**, *85*, 4104–4107.

[20] J. Li, S.-L. Zhang, *Phys. Rev. E* **2009**, *80*, 040104–040104–4.

[21] M. Engel, J. P. Small, M. Steiner, M. Freitag, A. A. Green, M. C. Hersam, P. Avouris, *ACS Nano* **2008**, *2*, 2445–2452.

[22] J. N. Coleman, S. Curran, A. B. Dalton, A. P. Davey, B. McCarthy, W. Blau, R. C. Barklie, *Phys. Rev. B* **1998**, *58*, R7492.

[23] P. N. Nirmalraj, P. E. Lyons, S. De, J. N. Coleman, J. J. Boland, *Nano Lett.* **2009**, *9*, 3890–3895.
[24] S. De, J. N. Coleman, *MRS Bull.* **2011**, *36*, 774–781.
[25] S. De, T. M. Higgins, P. E. Lyons, E. M. Doherty, P. N. Nirmalraj, W. J. Blau, J. J. Boland, J. N. Coleman, *ACS Nano* **2009**, *3*, 1767–1774.
[26] S. De, P. J. King, P. E. Lyons, U. Khan, J. N. Coleman, *ACS Nano* **2010**, *4*, 7064–7072.
[27] P. E. Lyons, S. De, J. Elias, M. Schamel, L. Philippe, A. T. Bellew, J. J. Boland, J. N. Coleman, *J. Phys. Chem. Lett.* **2011**, *2*, 3058–3062.
[28] P. N. Nirmalraj, A. T. Bellew, A. P. Bell, J. A. Fairfield, E. K. McCarthy, C. O'Kelly, L. F. C. Pereira, S. Sorel, D. Morosan, J. N. Coleman, M. S. Ferreira, J. J. Boland, *Nano Lett.* **2012**, 121016084703001.
[29] L. Hu, D. S. Hecht, G. Grüner, *Nano Lett.* **2004**, *4*, 2513–2517.
[30] M. Dressel, G. Grüner, *Electrodynamics of Solids: Optical Properties of Electrons in Matter*, Cambridge University Press, Cambridge ; New York, **2002**.
[31] S. Sorel, D. Bellet, J. N. Coleman, *ACS Nano* **2014**, *In press*, DOI 10.1021/nn500692d.
[32] R. M. Mutiso, M. C. Sherrott, A. R. Rathmell, B. J. Wiley, K. I. Winey, *ACS Nano* **2013**, *7*, 7654–7663.

Chapter 3
2D Stick Percolation Simulations:

As described in Chapter 2 much work has been done previously on 2D stick percolation systems. Within the scope of this thesis we aim to explore the impact of length distributions, angular distributions and curved nanowires on the formation of a percolation pathway. This results in an exploration of the impact on the critical density for a variety of different stick shapes and sizes. In the first section of this chapter, we describe the fundamental framework which is used to determine percolation. In section 2.2 the ideal width less stick system is explored using an alternate way of viewing the data in which a clear pattern emerges for the system. This method is based on looking at the number of objects in the system at the percolation threshold rather than the density. Observing the critical number of objects for a variety of different nanowire lengths and system size elucidates the relationship between the wire length and system size. From this view of the data we are able to extend the model to accommodate small-scale systems in which the system size approaches the same order of magnitude as the nanowire length. Following this we explore the impact of distributions in the length of the wires and the angular orientation of the wire on the critical density of the system.

With the aim of combining these simulations with experimental observations we implemented a modification of the wire geometry to produce curved nanowires. The methodology of application and the impact of curvature of the wires on the formation of percolating pathways is described in section 2.5.

Finally we have attempted to address one of the fundamental issues of random nanowire networks by simulating the collection efficiency of a nanowire network based on the diffusion of electrons through the adjacent layer. It is inherent to the topology of 2D nanowire networks that there are regions of the film in which no nanowire pass, in these regions the collection or injection of electrons will be lower than in the regions in contact with nanowires. Initial assumptions based on this idea lead to the conclusion that this will result in a lower collection efficiency in real devices when compared to a continuous film such as a TCO. This is observed experimentally in solar cells with short diffusion lengths in the active layer[1] but can be overcome by using a buffer layer which aids in charge separation, helps to minimizes recombination and shunting and can also provide some local conductivity in the gaps between nanowires.[1,2] Section 2.6 tries to address this idea and determine its impact on the nanowire networks' average collection efficiency by exploring the impact of the diffusion length of the adjacent material on the collection efficiency of a silver nanowire network.

3.1 Percolation Simulation Framework

All simulations reported in this work were undertaken on personal computers utilizing a MATLAB algorithms developed specifically for this thesis. The basis of each set of simulations is the formation and detection of a percolating network. The core algorithm involved was developed to use the percolation criterion R_1 as described in section 2.1. Several of the key ideas for this algorithm are based on the principles presented by Newman and Ziff[3,4] in terms of cluster formation and path identification. In all cases the system was defined as a square of side length L_s with nanowires of length L_w. Two electrodes were defined at the top and bottom edges of the system with a length L_s and spacing L_s. This configuration of contacts allows us to study the formation of *in-plane* percolation pathways. This exact formation is analogous to an individual pixel in real devices such as LCD or OLED displays. In terms of application to solar cells this architecture defines a characteristic length over which the occurrence of percolation is explored.

Nanowires were added into this space with randomly generated x,y centre coordinate and a randomly-generated angle θ. All simulations used the pseudorandom number generators built into MATLAB, the commands `rand` and `randn`. Both of these commands draw from the same global stream of pseudorandom numbers. The seed site of the pseudorandom number generator is initialised on start-up of MATLAB and uses the Mersenne Twister[5] algorithm mt19937ar; this pseudorandom number stream has a period of 2^{19937}-1 which is sufficient for our needs. The command `rand` selects a set of random numbers from the global stream with a uniform distribution whereas `randn` uses the Ziggurat method[6] to restrict the selection process of the random numbers to those of a normal distribution.

As each nanowire was generated it was assigned an initial cluster number and then checked for intersections with existing nanowires in the network. If the new nanowire had an intersection then it was assigned to the cluster of the existing nanowire. If the new nanowire had more than one intersection then nanowires in the smaller of the two clusters were reassigned to the larger cluster as well as the new wire. The system was considered to be percolating when both the electrodes become part of the same cluster. The cluster formed by connecting the top electrode to the bottom electrode is called the spanning cluster and is indicated in Figure 3.1 b) and c) by the blue nanowires.

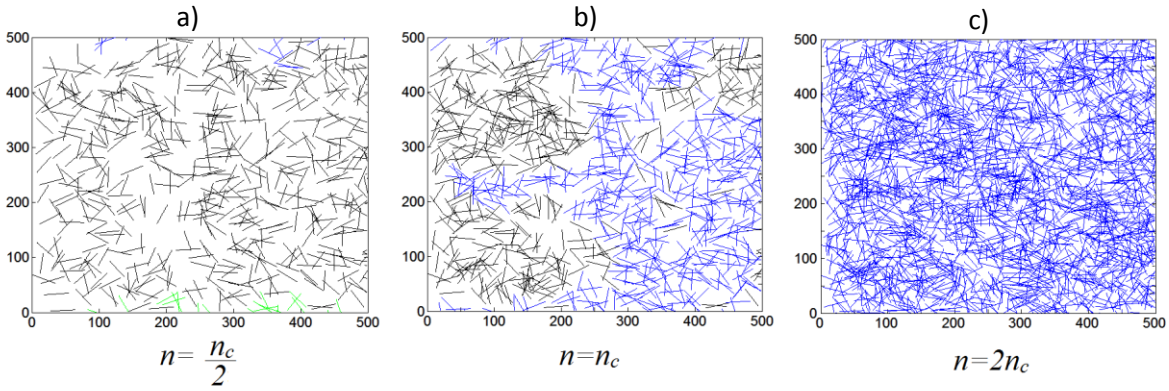

Figure 3.1 Monte Carlo simulations of the same network at three different densities, in this example is L_s=500 μm and L_w=37.5 μm. a) At approximately half n_c, nanowires connected to either the top or bottom electrode are indicated in colour. b) The network when the first spanning cluster is formed. c) The network at double the critical density.

One of the key observations we can see from Figure 3.1 is that at n_c many of the wires are not connected to the percolating cluster. As n increases a larger percentage of the nanowires (and thus the network) can play an active role in electron transport. For the determination of the percolation threshold (defined by the density at which the probability that a percolation pathway exists is ½), we generate a network by adding wires and checking connectivity after each addition until a percolating network is formed. The number of wires in the system is then stored as the outcome of one simulation. This is repeated many times, at the end of the series of simulations the highest and lowest number of nanowires in a percolating system is determined from the list of outcomes. All these values are then used to define the range of the probability distribution function. The list of outcomes is then sorted to determine the occurrence of each value on that range. These occurrences divided by the total number of simulations gives the probability that a network with that number of sticks will percolate for the first time $p(N)$. As once a network is percolating it will remain percolating when the density increases, we can assume that if a network percolates at N_1 it will continue to percolate at all $N>N_1$ thus the probability that any network will be percolating at a given density N_a can be determined from the accumulation of $p(N)$ for all densities up to and including N_a. Thus by adding these probabilities in sequence we can define the cumulative probability distribution function $cp(N)$:

$$cp(N) = \sum_{0}^{N} p(N) \quad (3.1)$$

where N is the number of wires in the network. From $cp(N)$ we can directly determine N_c. As this is a transition state the $cp(N)$ is expected to take the form of a step function. In the case of a system of infinite size or the 1D system the $p(N)$ is a delta function and $cp(N)$ is a perfect step function 0 below N_c and 1 above N_c. In the case of finite systems $p(N)$ typically takes the form of a Gaussian and results in a smoothed step function for $cp(N)$. In the particular case of 2D

sticks the value of N is a discrete variable, as it is not possible to add fractions of a nanowire, and $cp(N)$ becomes asymmetric at low values (small system size) therefore it is more appropriate to relate the $p(N)$ function to a Poisson distribution.[7] These functions are displayed for a particular simulation in Figure 3.2.

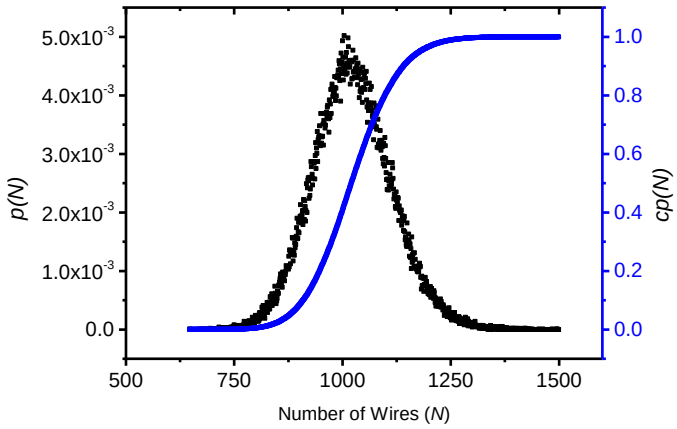

Figure 3.2 Output of a simulation in terms of $p(N)$ and $cp(N)$: each data point on these curves is the result of 10^5 simulations. For this particular case L_s=500μm and L_w=37.5μm

By performing these calculations, it is possible to view how the average value of N_c varies with the number of simulations. As the number of simulations increases the variation of the average value decreases. The convergence of this value is a measure of the accuracy of the simulation, a graph of this convergence is shown in Figure 3.3. For the purpose of this thesis we maintained the number of simulations at 10^5, which we determined to be sufficiently high for the convergence of N_c for all calculations which were achievable with the computational power available. As the system size increases the number of objects within the system also increases thus the convergence rate decreases. The type of simulation being run and the values of L_s and L_w in each case determined the largest system size possible to investigate. The restriction here was as usual computational time. The largest system simulated was 5000 µm however this could only be explored for a small number of repetitions and it was not possible to determine the percolation threshold for this system size. As the number of nanowires is closely related to the system size, for different nanowire lengths different ranges of system sizes were accessible.

Experimentally, we have used several different types of nanowires with different characteristics, the majority of the experimental work in this thesis was performed with Ag115 nanowires purchased from Seashell Technology[8] the physical characteristics of these nanowires were an average wire diameter of ≈105nm and average length of ≈37.3µm. Therefore, many of our simulations employed sticks with lengths of 37.5µm.

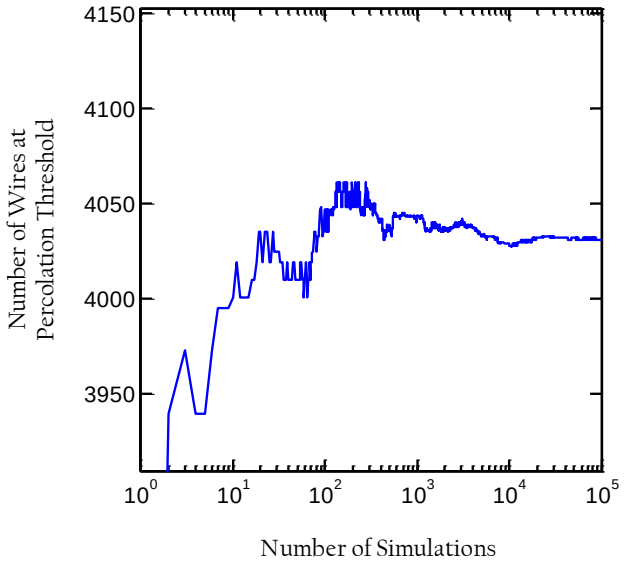

Figure 3.3 Convergence of N_c with increasing number of simulations. For this particular case L_s=*1000μm* and L_w=*37.5μm*

3.2 Ideal System

The initial motivation for this work stemmed from the fact that in the literature the majority of percolation simulations performed on systems of 2D sticks or cylinders were based on ideal systems.[7,9–13] For these simulations all of the sticks in the system have exactly the same length and were also width less with the exception of White et al.[12] and Bergin[13]. In practice it is rare to have an experimental situation in which all sticks have the same length. Inevitably there is a distribution of lengths around some average length resulting from the nanowire synthesis process. For percolating systems with basis objects that have high aspect ratios (>100), such as those achievable with metallic nanowires, the diameter of the wire plays a minor role in the formation of the percolating cluster. However, we anticipated that the distribution of lengths observed experimentally might play a significant role in the formation of percolating clusters. Initially we set out to explore the perfect system in order to validate the Monte Carlo code which we would then utilise for the simulation of systems with distributed lengths.

In doing so we observed a divergence of the critical density at the percolation threshold from the general value $n_c=5.63726/l^2$[7] in Monte Carlo simulations of small-scale systems. The origin of this deviation arises from edge effects and the lack of circular symmetry of the 2D rods: if circles or disks are used instead of sticks a uniform density as a function of system size can be obtained. However due to the dual symmetry planes of the 2D sticks, only when the orientations of the wires are restricted to 90° or 0° does the reduction of size result in a continuous nanowire density. Thus in systems with randomly-oriented wires the density required to attain percolation increases as the system

size approaches the length of the nanowire. This departure is illustrated in Figure 3.4, and led to the investigation of small-scale 2D stick systems to identify if an improvement to the existing model could be made to enable accurate predictions of the percolation density for small-scale systems.

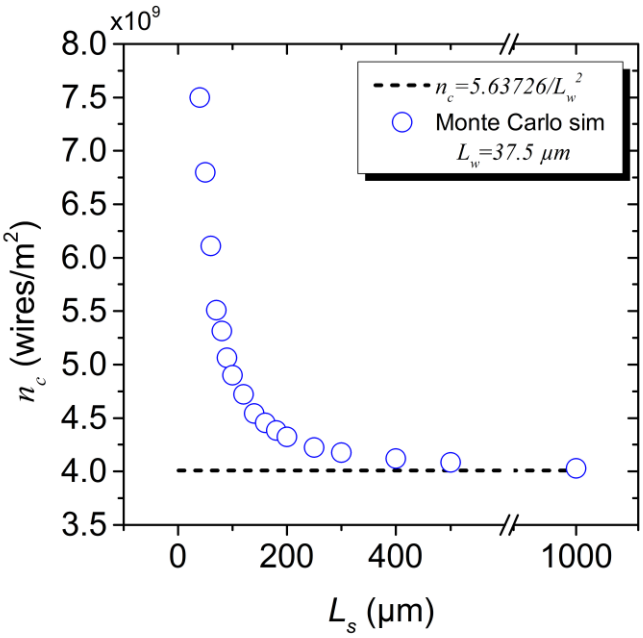

Figure 3.4 Monte Carlo simulations for the determination of n_c (open circles) compared to the accepted model in the literature (dashed line).[7] This reveals an increase in the density required to reach percolation when the system size is reduced which is not supported by the current model.

The nanowire length used for the Monte Carlo simulation shown in Figure 3.4 was 37.5μm. This figure demonstrates that for systems approaching the length of the nanowire n_c diverges from the anticipated value of infinite systems. Even for comparatively large system such as the system where L_s=*400 μm* (>10L_w) the critical density is already beginning to diverge. Traditionally when considering a percolating system the simulations and data are presented as a relationship of occupancy probability for bond or site percolation or system size and basis density in continuum percolation. In the case of 2D stick systems the sticks are the basic geometrical objects, hence we typically explore the relationship of the percolation critical density n_c as a function of the number of sticks N_c divided by the system size L^2 (for symmetric systems). Such a view of the data results in graphs such as that shown in Figure 3.4 and Figure 3.5a). One of the issues with such a depiction is that a mathematical relationship between the nanowire length, the system size and the resultant critical density is not immediately obvious.

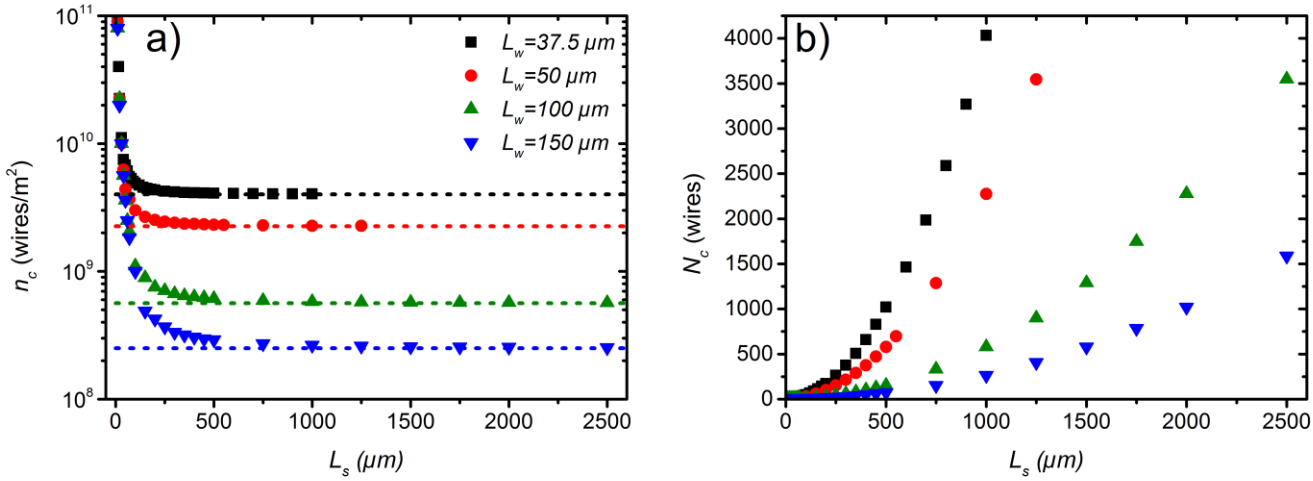

Figure 3.5 a) Typical depiction of critical density for four different nanowire lengths, symbols represent Monte Carlo simulation results. Dashed lines indicate the expected percolation threshold from Li and Zhang.[7] Initial divergence from the expected value is observed when the system is less than five times the nanowire length. b) Number of wires at the percolation threshold as a function of system size for the same simulations shown in a). Error bars are smaller than the symbols for data points. Legend in a) is consistent for both graphs and L_w are given in microns.

The expected percolation threshold for the systems depicted in Figure 3.5a) are added as dashed lines in the graph, as the system size increases the observed percolation threshold converges to the expected value. Again it can be seen that when the system side length is less than five times the nanowire length there is a significant divergence of the observed percolation density from the expected values. If instead the data is plotted as the relationship between the number of wires at the critical density and the system side length as shown in Figure 3.5 b) it becomes obvious that the relationship can be described by a quadratic equation as a function of length. With this simple shift in perspective the impact system size becomes more evident. However the impact of wire length is still not directly apparent. In the case of the 2D stick percolation, the relationship between the system size and the nanowire length is the critical parameter which determines the number of wires required to form a percolating network. This idea may seem self-evident but has thus far often been overlooked in the literature. A final transformation of the data can be made to reveal a general relationship between the system size and the nanowire length and the number of nanowires in the system. Plotting the number of nanowires in the system at the percolation threshold as a function of a normalized system size (the ratio of system size divided by nanowire length L_s/L_w) results in a coalescence of the four data sets shown in Figure 3.5b to a single curve which can be fitted by a quadratic function of L_s/L_w.

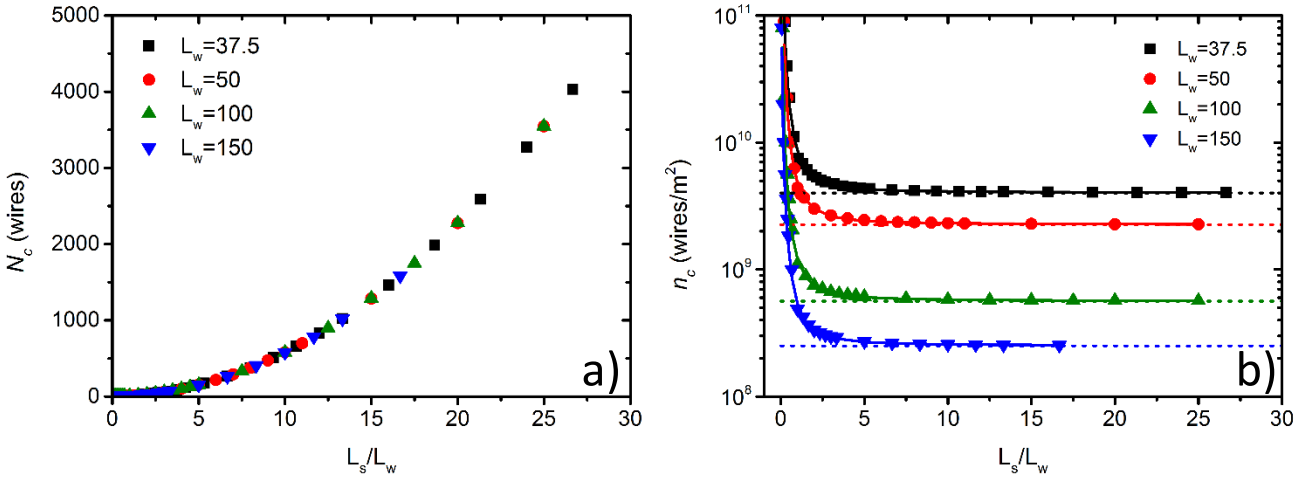

Figure 3.6 a) Coalescence of the four curves in Figure 3.5b by plotting the density against the ratio of system size to nanowire length. b) Partially-normalised critical density plots, only the horizontal axis has been normalised to demonstrate the divergence is ratio dependent and occurs at the same rate for all wires. Solid lines are a quadratic fit of the data in Figure 3.6a divided by the appropriate system size for each ratio. Error bars are smaller than the data points. Values of L_w given in the legends are in μm.

The coalescence of the different data sets reveals a universal curve which can be used to relate any given nanowire length and system size to the critical density of the system. This generalized equation was used to fit the data in Figure 3.6 and is given by:

$$N_c = \frac{5.63726{L_s}^2}{{L_w}^2} + \frac{L_s}{L_w} + 5.5 \qquad (3.2)$$

Where N_c is the critical number of wires to have a percolation probability of ½. The first term of equation 3.2 can be considered as relating the possible interaction area of surrounding a nanowire to the area of the system and corresponding to the exact relation of the infinite system. The second term can be seen as the minimum number of nanowires required to span the system assuming that they are connected end to end. The final constant is a result of the way in which the percolation condition R_1 is defined in the 2D stick system. As discussed in Section 2.1, it is defined that a system percolates if two opposing electrodes on a specific axis of the system are connected. If an alternate percolation condition which allows for spanning between either electrode pairs is used this constant would be reduced. If the condition considers connections between any two electrodes this term should converge to unity. The physical basis for this last term arises from the fact that regardless of the system size or wire length there is always the need for at least one wire to make the system percolate. When the ratio L_s/L_w is less than 1 (i.e. the wire is larger than the system size) the first two terms are less than one and this final term is responsible for providing the necessary wire.

Using this equation 3.2 it is possible to accurately predict the number of wires necessary to achieve a percolation probability of ½ and hence the critical density for systems with ratios >1.33 . Below this value there is still a divergence, though much less than for the currently accepted formula as indicated in Figure 3.7.

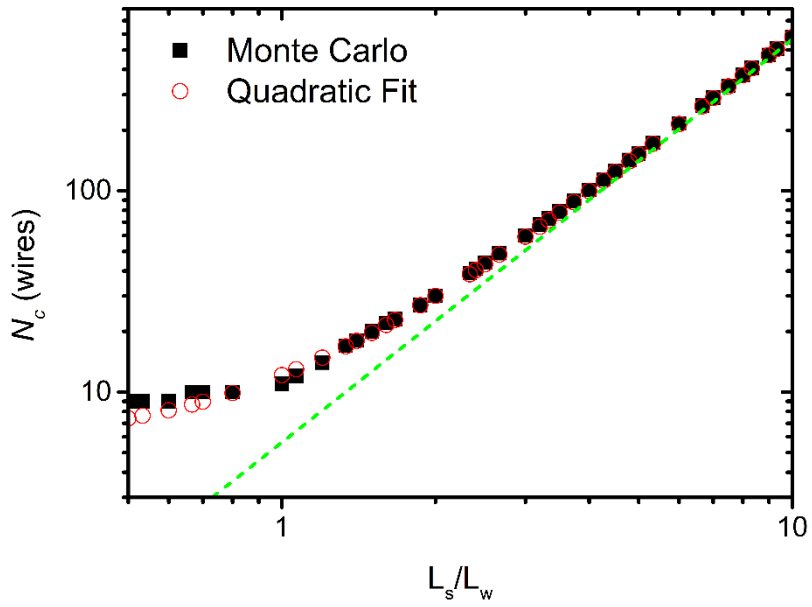

Figure 3.7 A plot of the same data in Figure 3.6a with axis in log scale compared to a parabolic fit to the data of $N_c = 5.63726L^2/l^2+L^2/l^2+5.5$. Error bars for the black points are smaller than the data points. The dashed line corresponds to the first term of equation 3.2 which is essentially the equation defined by Li and Zhang.[7]

One may question the significance of such a result when the majority of devices will be several orders of magnitude larger than the nanowire length. A further consideration should be made when thinking about the application of these formulae, the application of interest may place a further demand on the critical threshold of the system. Although it is true that the ratio of the system size to the nanowire length dominates the onset of percolation, in some cases we will require a higher density than that required to make the network percolate in order to obtain the desired properties for a given application. In this case the critical density of the system is no longer related solely to the formation of a percolating network but is also related to the achievement of the desired network properties. While in the majority of applications the device or system size will be more than 10x the nanowire length, in emerging technologies the actual length scale at which the conductivity is required can differ from the physical system size. Depending on the application the scale of the percolating cluster required will vary. At one extreme we have antistatic applications where the percolating cluster is of the order of tens of cm, and it is not particularly important if small regions (<0.25 cm^2) of the network are not connected to the percolating cluster. At the other extreme we can consider pixels in liquid crystal display, in this case the system is on the order of 250 µm thus is much less than 10x the nanowire length. In the middle of these two extremes there is a certain grey area where the desired

percolation scale may not be immediately obvious, for example in the application of metal nanowire networks as transparent electrodes for solar cells.

For use as electrodes in solar cells the device size is typically on the order of tens of centimetres. However, in order to collect charges efficiently the network must be conducting on a much smaller length scale than that of the external system size. This leads to a desired length scale of percolation which is very different from the size of the physical system. In reality the desired length of percolation is on the same order of magnitude as the diffusion length of the carriers in the active region of the cell. For standard crystalline silicon solar cells the diffusion length is roughly 100-300 μm,[14] in TiO_2-based dye-sensitised solar cells it ranges between 2-40 μm[15] and it is typically less than a micron in organic solar cells.[16]

As the density required to reach percolation is dependent on the ratio of L_s/L_w and, for constant L_w, decreases as the system size increases, conductivity on a shorter length scale is not always guaranteed for a large system at the percolation threshold. This means that, for large systems some regions of the network may not be connected to the percolating cluster, the larger the system the higher the percentage of unconnected nanowires. As these wires are not connected to the percolating cluster, they cannot carry charge to or from the edges of the system and thus result in regions which cannot contribute to the collection or injection of electrons. This point will be discussed in greater detail in the last section of this chapter. A simulation of a large-scale system is shown in Figure 3.8, the regions shown in black are not connected to the percolating cluster.

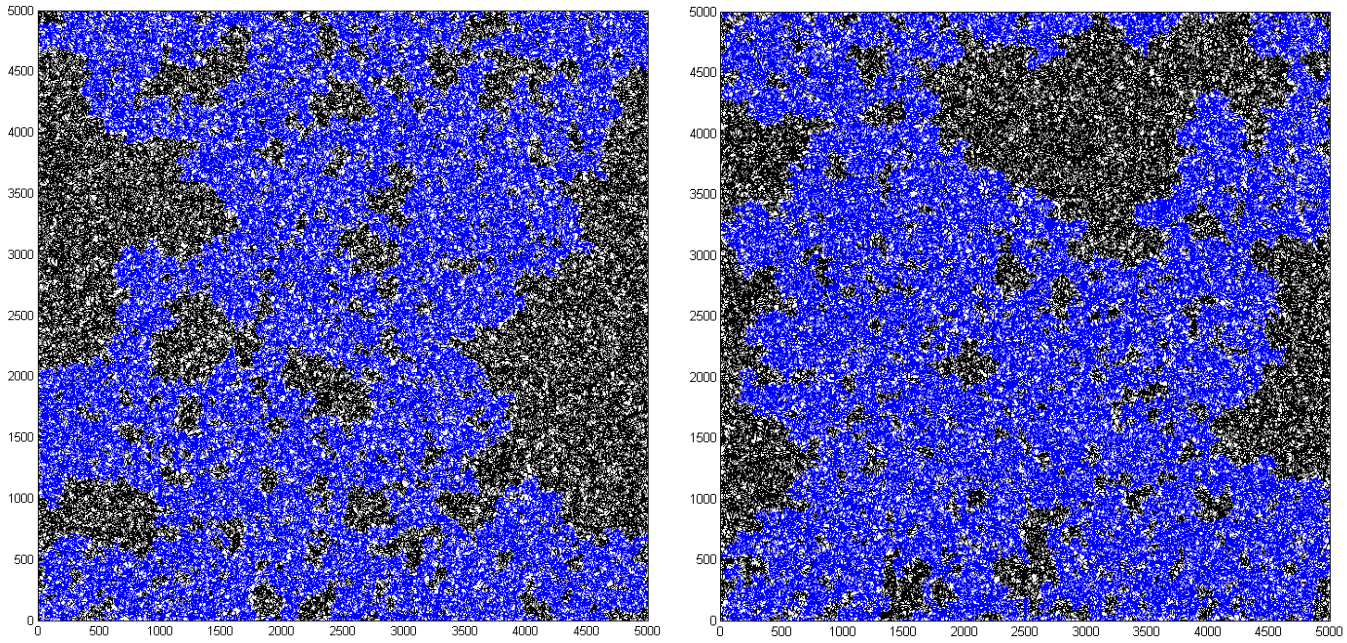

Figure 3.8 Two examples of large systems at the percolation threshold, where percolating clusters are indicated in blue. In these examples L_s=5000 μm and L_w=37.5 μm.

Of note in Figure 3.8 is the fact that there are some regions as large as 1 mm² which are not connected to the percolating cluster. The nanowires not connected to the percolating cluster constitute ≈40% of these two particular

networks. The regions indicated in black will not contribute to the collection or injection of charge carriers and will then result in a decrease of the device efficiency.

The percentage of nanowires in a network which are not connected to the percolating cluster when the density is at n_c increases with system size. Indeed, by running the percolation simulation 1000 times at the percolation threshold and by recording how many nanowires are connected to the percolating cluster and how many are not, we can determine the average number of nanowires which are not contributing to the systems percolating cluster (N_{ncp}). The percentage of wires in the system not connected to the percolating cluster as a function of L_s/L_w is displayed in Figure 3.9, and clearly demonstrates that as the system size increases less of the actual electrode area is in fact connected to the boundary electrodes.

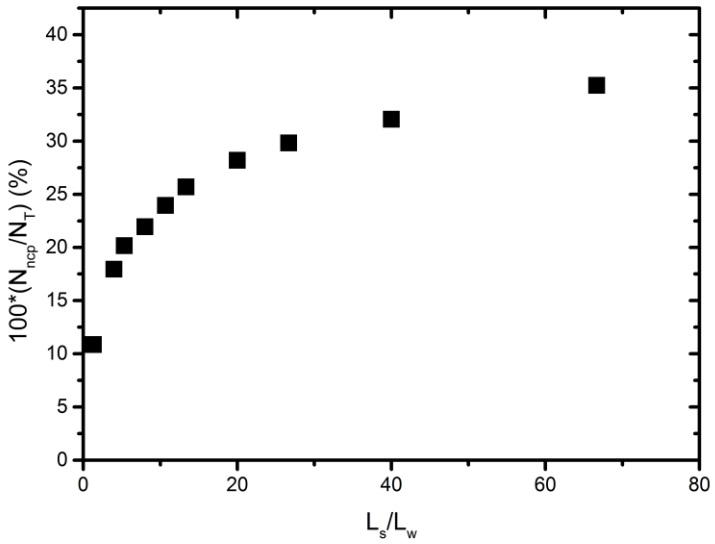

Figure 3.9 Percentage of network which is not connected to the percolating cluster as a function of the system size. Error bars are smaller than the data points.

The fact that wires are not connected to the percolating cluster means that these wires do not contribute to the conduction of electrons in the plane of the electrode, this results in non-conducting regions of the electrode. One way to avoid this issue is to check whether the system is percolating at smaller length scales. This can be achieved by defining an effective system size L_{seff} as the size of the desired percolating cluster instead of the actual physical system size. By defining l_{seff} as smaller than the physical device size we impose a higher critical density which ensures percolation at the desired length scale. As the critical density for small systems is higher than that of large systems (as shown in Figure 3.6b) percolation is guaranteed at the larger length scale of the physical system. As a result of defining our system size in this manner we are naturally moving to the left in the curve depicted in Figure 3.9 due to the increased density required at smaller system size more nanowires in total are connected to the percolating cluster. This means that depending on the desired application and the

requirements of the device it may be necessary to define L_{seff} much smaller than the device size in order to estimate what the required density of wires for the desired behaviour will be. Through these considerations, we would like to highlight that the critical density is not simply dependent on the ratio of the physical system to the wire length but actually on the ratio of the desired length scale of electrical conductivity given by L_{seff} to the wire length. Thus in some cases the application will define the critical density instead of the density implied in the standard system by the onset of percolation, in these instances the critical density determined from L_{seff} will be higher than the typical one.

To clarify this idea let us consider the example of a Si solar cell, the electron diffusion length is typically 100-300 μm[14] but the system size might be 5 cm x 5 cm. In order to have the optimal collection of photo-generated charges, we should define the length scale of the percolating cluster to be no less than the diffusion length of electrons in Si. This will result in a network density which will achieve percolation across all distances larger than 100-300 μm and ensure that the nanowire density is sufficient to allow all electrons regardless, of their point of generation, to reach parts of the spanning cluster.

For the design of optimal devices the required length scale of conductivity should define L_{seff}; thus it will be, in general, the determining factor of the optimal nanowire length. For transparent conductive applications we can assume the highest optical transparency will be achieved at the lowest nanowire density hence using nanowires which are of the same order of magnitude as the required L_{seff} would be ideal, however this is not always achievable.

This method could be a useful way of ensuring electrical conductivity at length scales different from the physical system size however it is unlikely that in real device manufacture, we would use densities at the percolation threshold, as this implies that only ½ of the devices will actually work. In reality it is not particularly realistic to discuss creating devices at the percolation threshold, it is important then to consider probabilities of percolation other than ½ such that we can extract N_p the number of nanowires required to have P percent of the networks percolate. To this end we extracted the values of N_p for P=1,25,50,75 and 99. These results are displayed in Figure 3.10. In these simulations the system size was held constant at 500 μm and the wire length was varied such that the ratio L_s/L_w ranged between 1 and 50. The results of the quadratic fit determined in this work for P=50 (N_c in the standard definition) and the accepted fit from the literature (Li and Zhang[7]) are shown as solid and dashed lines, respectively. At shorter nanowire length (L_s/L_w>10) the quadratic fit and that of Li and Zhang converge as do the N_p for all values of P. At longer wire lengths (L_s/L_w<10) we can clearly see the divergence of the N_p and the literature fit from the values of N_c (N_{50}). This is also highlighted as a percentage error (absolute difference between fit and Monte Carlo value divided by the Monte Carlo value times 100) in the inset curves in Figure 3.10a and b.

Figure 3.10 highlights several important results, the number of nanowires required to ensure that 99% of the networks with that density will percolate is obviously always higher than N_c but this data reveals that it is also dependent on the ratio L_s/L_w and increases significantly at small values of L_s/L_w. At a value of

L_s/L_w=50 N_{99} is still 8.4% larger than N_c. In light of this it is useful to consider using equation 3.2 with modified constants to fit the N_{99} curve resulting in a new formula to estimate the density which enables 99% of the networks to be percolating ($n_{99} = N_{99}/L_s^2$).

$$N_{99} = \frac{5.86{L_s}^2}{{L_w}^2} + \frac{15.23L_s}{L_w} + 9.9 \quad (3.3)$$

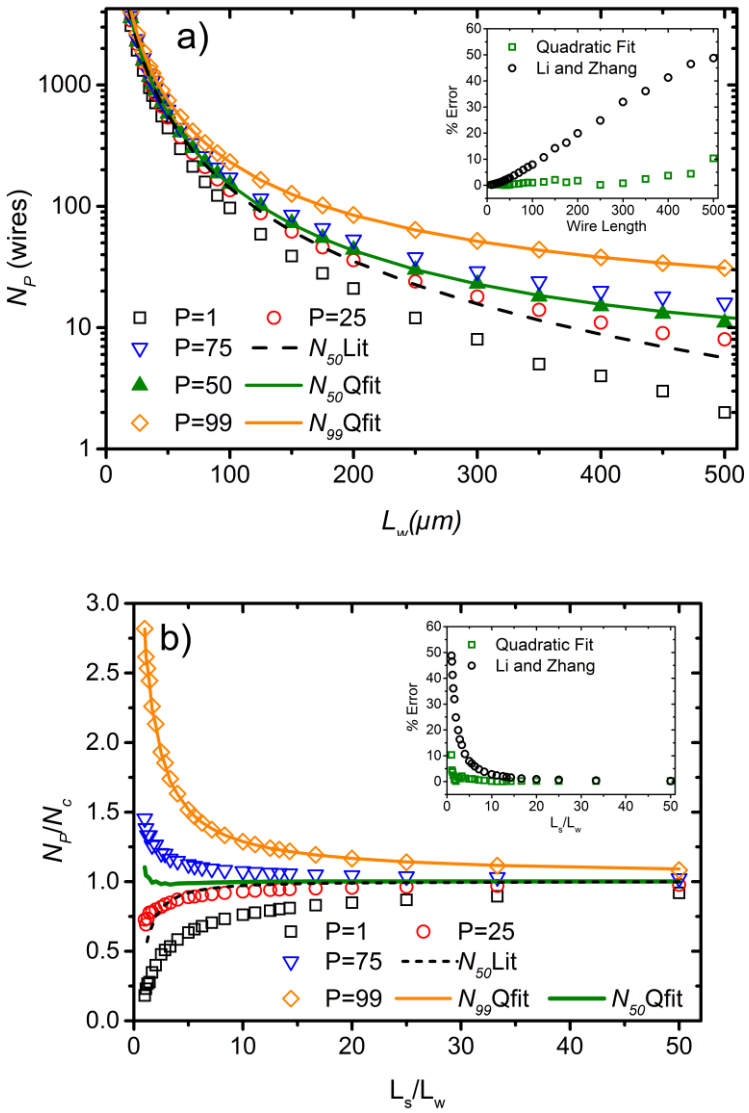

Figure 3.10 Monte Carlo simulations of different nanowire lengths in a 500 µm x 500 µm square system. a) Depicts the different numbers of nanowires required to achieve different percentages of percolation. Data sets are Monte Carlo simulation values and the solid lines are quadratic fits (Qfit) using equations 3.2 and 3.3 for N_{50} and N_{99}, respectively. b) Displays the same data as a) normalized by the typical percolation threshold (N_c=N_{50}). On both graphs the quadratic fit from equation 3.2 is indicated by the solid green line, the quadratic fit for N_{99} from equation 3.3 is indicated by a solid yellow line and the expected value of Li and Zhang is indicated by dashed black line. Both insets are the percentage error between the first two fits and the Monte Carlo results for N_c

Using the results of equation 3.3 and running Monte Carlo simulations at the higher density of n_{99} allows us to again look at the percentage of wires connected to the percolating cluster. In Figure 3.11 a particular network is shown at four different densities.

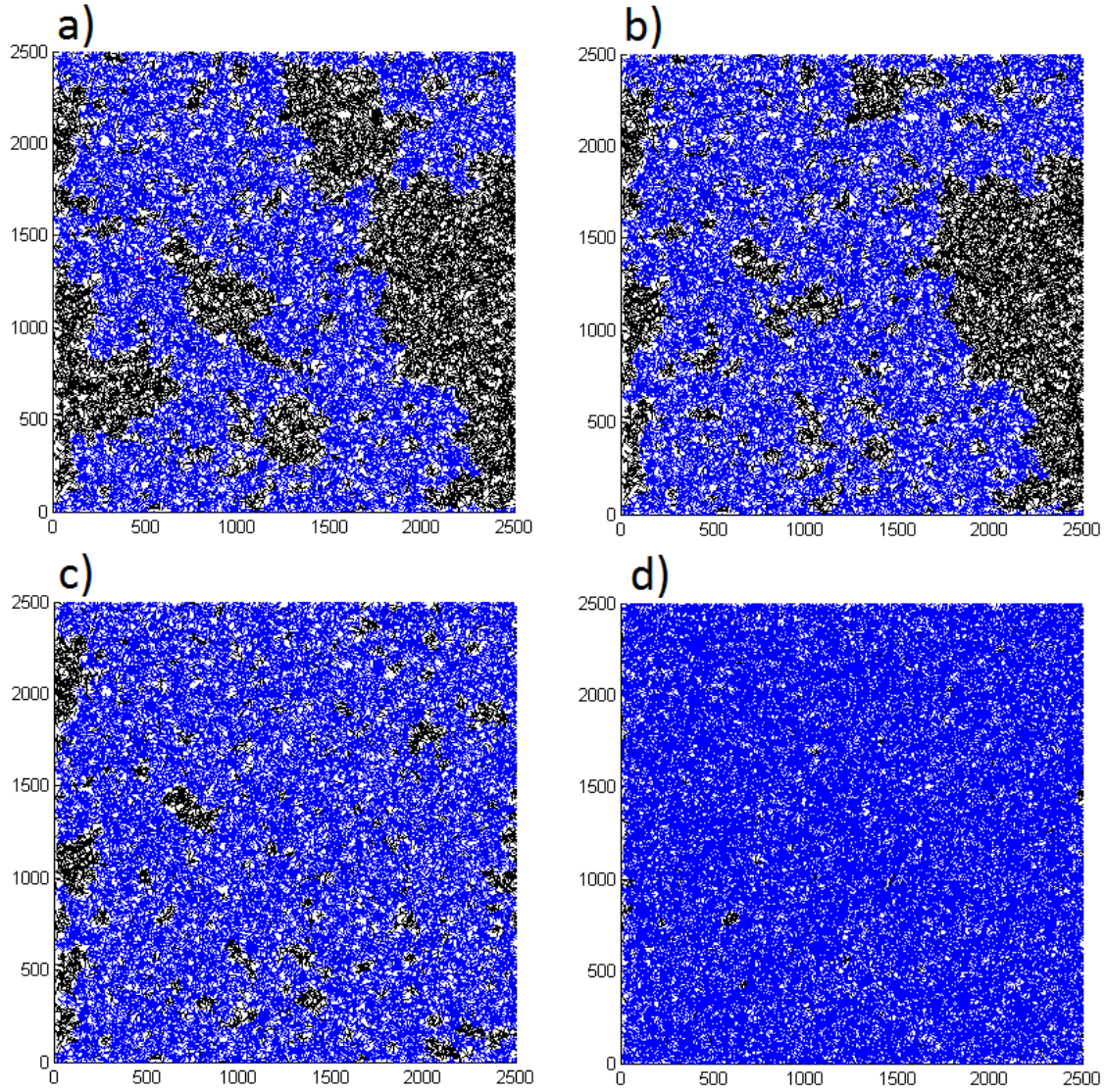

Figure 3.11 The same 2.5 mm x 2.5 mm network at four different densities, nanowire length is 37.5 µm. Nanowires connected to the spanning cluster are indicated in blue. a) The first occurrence of a spanning cluster in this particular network. b) The network at n_c (n_{50}) c) The network at n_{99} d) The network at $1.5n_{99}$.

It is immediately obvious that as the density increases, a larger percentage of the network is connected to the percolating cluster. Operating at n_{99} allows a significant improvement over that of the n_c. Combining this with the idea mentioned previously of defining an effective system size as the minimum desired length of electrical conductivity allows an inflated critical density to be defined which will guarantee electrical conductivity at the desired length scales and in the majority of networks. As Figure 3.11d demonstrates operating at $1.5n_{99}$ results in almost 100% of the nanowires being connected to the percolating cluster. By plotting again the percentage of nanowires not connected to the

percolating cluster we can readily observe the reduction associated with the shift in density to n_{99} or $1.5n_{99}$. This result is shown in Figure 3.12.

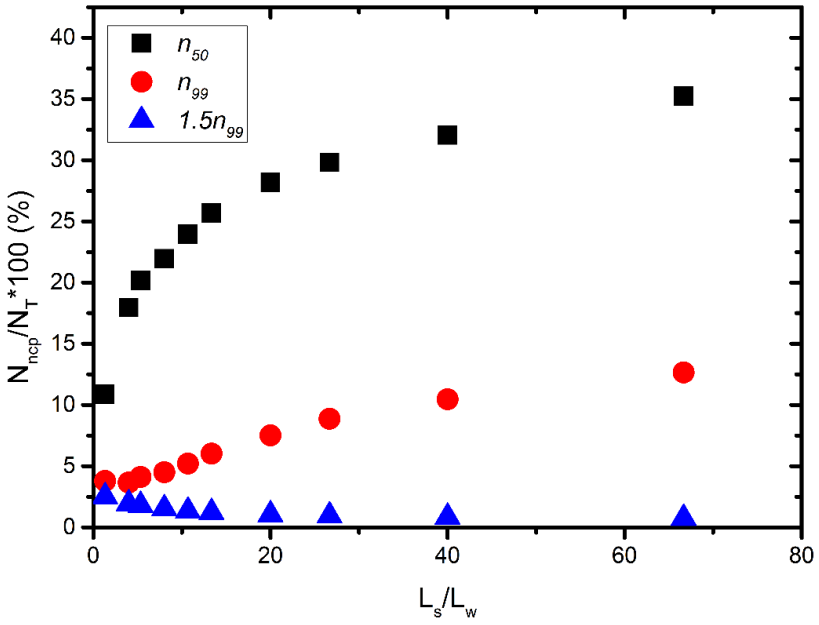

Figure 3.12 Percentage of wires not connected to the percolating cluster at three different densities as a function of the ratio L_s/L_w.

As seen in Figure 3.12 working at a density of $1.5n_c$ results in the number of nanowires that are non-percolating being less than 4% of the total nanowires at all length scales. This result suggests that working at a density of $1.5n_{99}$ is sufficient to satisfy the requirement that the majority of the nanowires be connected to the percolating cluster. This means that any significant loss in collection or injection efficiency will be a result of the carrier recombination during their diffusion in the surrounding material in the regions between nanowires and not due to the collection of electrons by wires not connected to the percolating cluster. An in-depth investigation into the collection or injection efficiency as a function of network density is provided later in this chapter in section 2.6.

As a final validation of our simulation approach and results, we plot the nanowire density normalised to a nanowire length of unity as a function of $L_s^{-1-1/v}$ where v is 4/3 for 2D percolation systems. According to the literature[7,17,18] the normalised percolation threshold density for 2D stick systems should scale linearly as a function of $L_s^{-1-1/v}$ for large system sizes. The results are displayed in Figure 3.13 and indicate that the Monte Carlo simulations are behaving in the expected manner.

Also plotted in Figure 3.13 are the normalized data for the density at different probabilities of percolation. n_p with $P=1,25,50,75$ and 99. It is interesting to note that although the P=50 (n_c) scales linearly the other values do not.

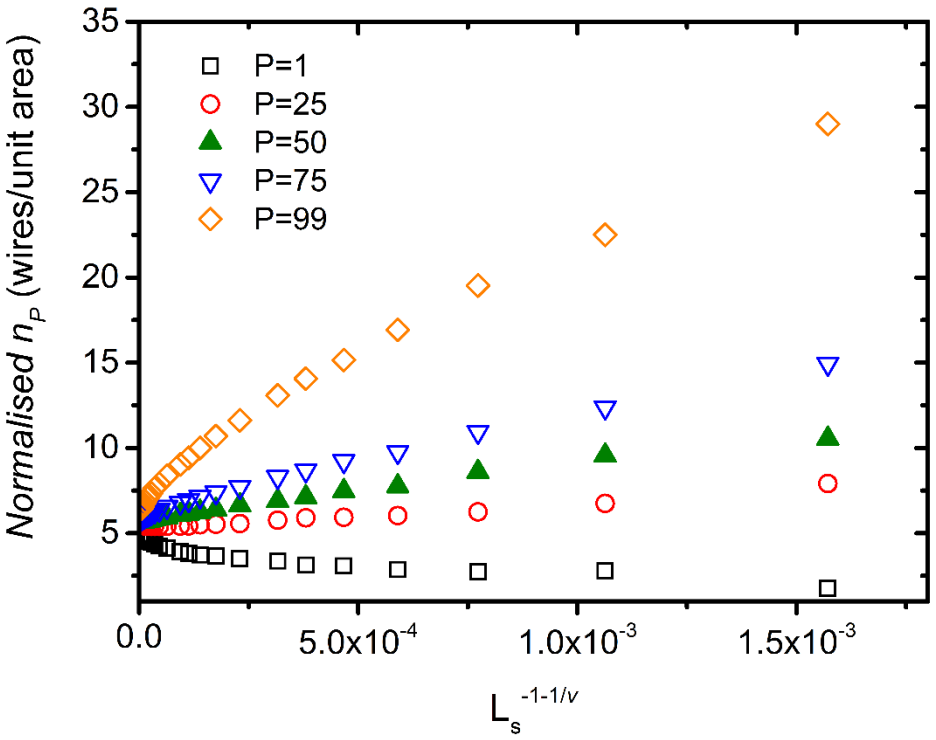

Figure 3.13 Finite scaling in the 2D stick system, as suggested by Li and Zhang[7], Ziff[18] and Stauffer and Aharony[17] the n_c scales linearly as a function of $L_s^{-1/-1/\nu}$

This section has detailed the development and validation of Monte Carlo simulations for the ideal system of percolating 2D sticks (i.e. straight, widthless and constant length). We have compared these simulations with those in the literature and determined that there was a departure from the predicted behaviour at small system size. We explored this effect and proposed a modified formula to allow more accurate predictions of the percolation threshold across a broad range of system sizes and nanowire lengths. We also introduced the concept of an effective system size L_{seff} and discussed the impact of wire density on the percentage of wires connected to the percolating cluster. This then leads to a discussion of the realistic nanowire densities which would be required to produce a probability of percolation of 99%. When defining the probability of percolation as 99% as the critical density the percentage of wires which are not connected to the percolating cluster was shown to significantly decrease. We then showed that by increasing the density to $1.5n_{99}$ we were able to reduce the unconnected wires to less than 4% of the network at small system size and that this continued to decrease as the system size was increased. This value of $1.5n_{99}$ is also much more realistic in terms of determining the desired nanowire density of an actual device as it will ensure the operation of percolation-dependent conductivity in the majority of devices. A new formula was determined which can estimate the required density to achieve $P=99$. Finally the scaling behaviour of the model was plotted and observed to match that of 2D stick systems in the literature thus validating the model that we have developed. The following

sections will look at introducing realistic imperfections in this ideal system, similar to those which can be observed in the real world.

3.3 Length Distributions

The length of real, experimentally-produced, nanowires is very rarely exactly the same for all nanowires produced. Typically there is an average nanowire length with some distribution of lengths surrounding it. This section explores what the influence of such a distribution of lengths will be on the required critical density.

In the simplest view, one could look at the number of wires required at the critical density as a function of the nanowire length (shown in Figure 3.10), take a weighted average of the values according to the distribution of nanowire lengths and estimate what the required density would be. Doing so suggests that the introduction of a length distribution would result in an increase in the critical density of the system. This is a due to the fact that the number of nanowires required increases more rapidly as the length of the wire is decreased. This is a very simplistic view of the behaviour and is not necessarily valid. In order to determine what the real effect would be and to improve the estimation of the percolation threshold of real systems we have added length distributions to the Monte Carlo simulations for the determination of the percolation threshold.

The distributions used are based on a normal distribution, initially suggested by Gauss[19,20] and further developed by Laplace this distribution is a common statistical distribution which can be described by the mean value μ and the standard deviation σ. Using the normal distribution the probability of finding a wire with length x is given by the function:[21]

$$P(x) = \frac{1}{\sigma\sqrt{2\pi}} e^{\frac{-(x-\mu)^2}{2\sigma^2}} \quad (3.4)$$

In our particular case we set the value of $\mu = L_w$ and define σ_L the standard deviation of the lengths as follows:

$$\sigma_L = \frac{D_L L_w}{4} \quad (3.5)$$

where L_w is the average wire length and D_L is the length distribution parameter. This implies that the nanowires generated will be distributed around the average nanowire length with four standard deviations of the distribution being within $\pm D_L L_w$ Thus when D_L is zero all nanowires are the same length, increasing D_L to 0.1 results in a normal distribution around L_w such that the maximum and minimum values of L_w are $\approx L_w \pm 0.1 L_w$.

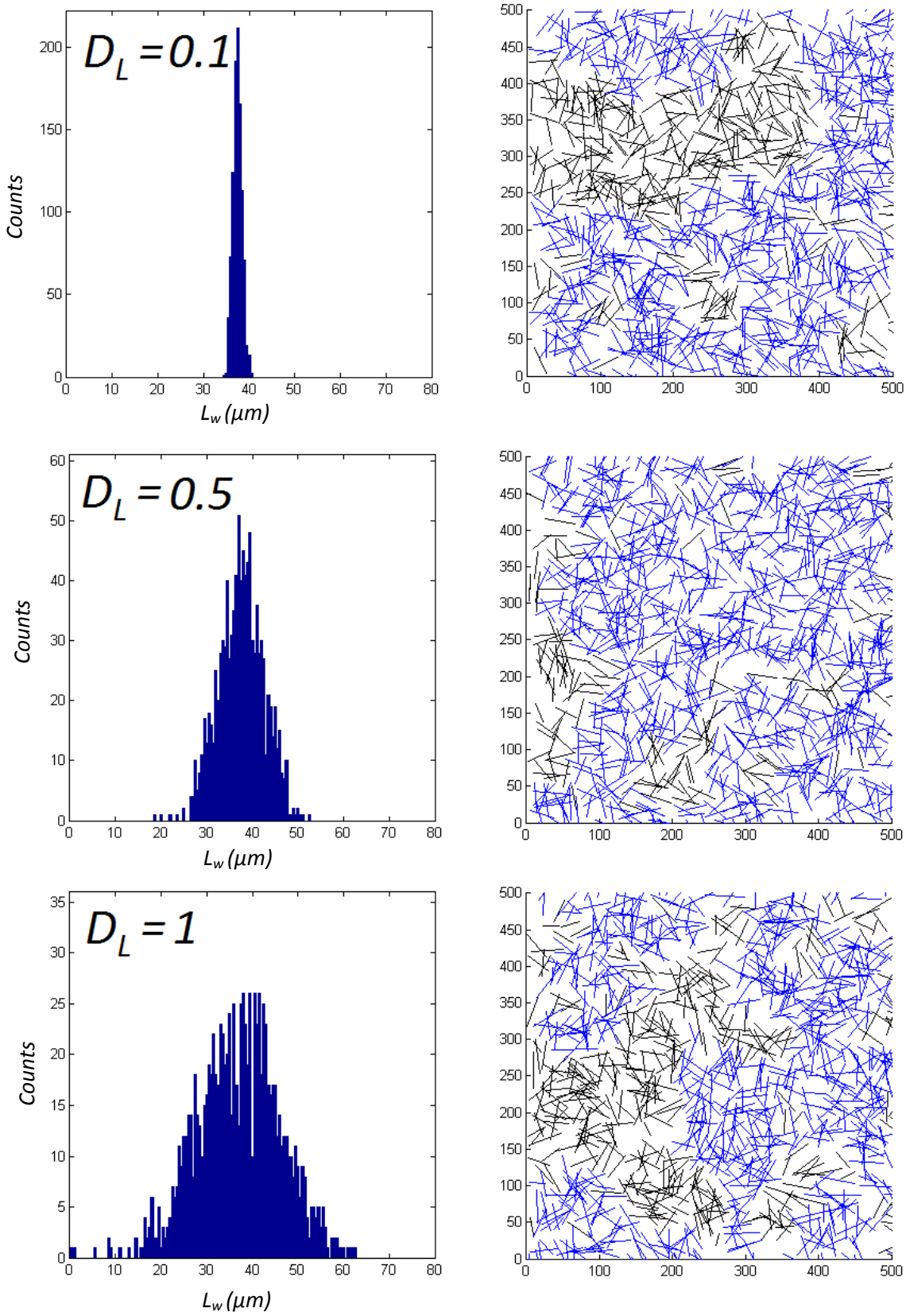

Figure 3.14 A series of histograms of nanowire lengths with different length distribution parameter D_L and their resultant networks. Wire length is 37.5 μm and the system size is 500 μm. Percolating cluster is indicated in blue.

Figure 3.14 demonstrates 3 different wire length distributions and the resultant network morphologies. Though the histograms in Figure 3.14 are roughly representative of the length distributions applied broadly to each simulation one must remember that the values are drawn from a random stream of values, hence the actual distribution of the nanowire lengths will approach the normal distribution defined by the program as the number of wires drawn from the random stream increases.

For the simulations exploring the impact of the length distribution each network was again simulated 10^5 times and hence the actual distribution of all wires in all networks will be quite close to that of the expected normal distribution. The histograms and networks shown in Figure 3.14 are the particular results generated in one instance of the simulation and are meant only as a visual aid to allow one to see what the lengths of the wires in a system with the given distribution would look like. This is not representative of the whole of the cluster formation behaviour of each of these systems but is representative of the wire lengths. For these examples a reasonably-sized system was chosen to keep the number of nanowires small and allow the observation of the different nanowire lengths.

Having defined the method to apply different length distributions to the 2D stick simulations we proceeded to carry out 10^5 simulations with different values of D_L. The results reveal a surprising trend and are displayed in Figure 3.15.

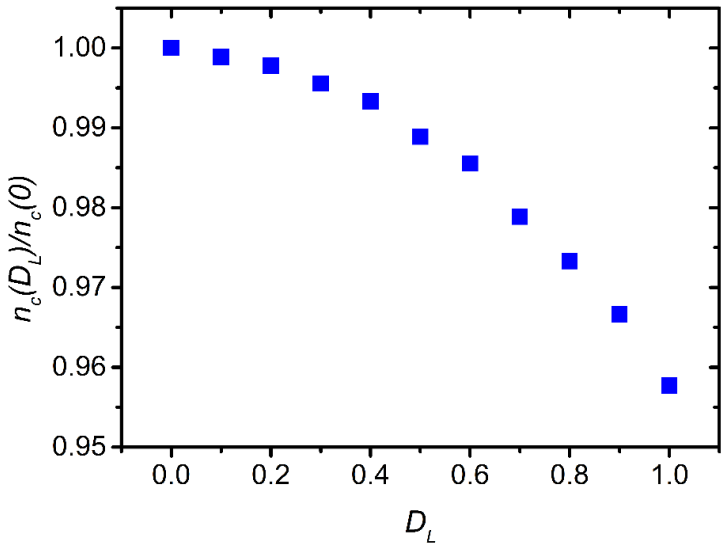

Figure 3.15 Density of a system with a given of value of D_L divided by the density of the ideal nanowire system. The largest length distribution results in a downward shift of n_c by 4.3%±0.1%. Error bars are smaller than the data points.

Contrary to the simple argument discussed earlier the introduction of a length distribution causes a reduction in the density required to achieve percolation. Though slight, <5% for the largest distribution $D_L=1$, this result is significant as it indicates that it is actually beneficial to the onset of percolation to have a distribution of lengths. As it can be quite difficult to isolate a single length

of nanowire from chemical growth processes this result allows some reprieve from the demand for a mono disperse nanowire supply. This reduces costs of production both through reduced material losses and reduced processing. The reduction in the onset of percolation can be ascribed to the ability of an individual nanowire to connect clusters increasing faster as the length increases, thus with the length distribution the longer nanowires contribute more significantly to the formation of a spanning cluster than the shorter nanowires detract from it. In reality the short wires are still less efficient at forming clusters and will contribute to the absorption or scattering of light and so ideally one would remove the majority of wires shorter than the average length if possible.

For the nanowires used in the experimental components of this thesis we observed a length dispersion similar to that of $D_L=0.5$. Which would suggest that we should observe the onset of percolation at roughly 1% lower than that predicted by the ideal stick system. Experimentally however this is not the case and percolation is only observed at densities higher than the predicted n_c of the distributed length system. The reason for this is likely due to further imperfections such as angular anisotropy and wire curvature. These issues have not as yet been thoroughly investigated in the literature and we begin to address them in the following sections.

3.4 Angular Distributions

Having now explored the impact of wire length we decided to explore the impact of the angular distribution of wires on the physical properties of AgNW network. Some experimental techniques (most notably spin coating) result in an anisotropic angular distribution. The impact of the angle between intersecting wires on the formation of percolating clusters has been studied briefly in the past[22] but this work addressed the problem from the point of view of nanowire length and length distribution rather than the network density. It also used a small number of simulations, hence we attempt here to produce a more accurate result that addresses directly the value of nanowire density. This is an important redressing of the problem, as although it is possible to control the wire length during growth as demonstrated by Bergin et al.[13] and after growth by using sonication as shown by Sorel et al.[23] it is significantly more difficult experimentally to modify the length distribution or wire length than it is to control the density. Also the sonication approach only allows one to shorten the length of the wires which is detrimental to the opto-electrical properties of the network. Therefore as it is simpler to control the nanowire density for a given nanowire geometry, it is useful to explore the impact that an angular distribution has on the critical density n_c.

In order to look at the impact of this we implemented an angular distribution within the Monte Carlo simulations of the percolation threshold. Similar to the length distributions discussed above the implementation of the angular distributions was achieved by defining an average angle and imposing a

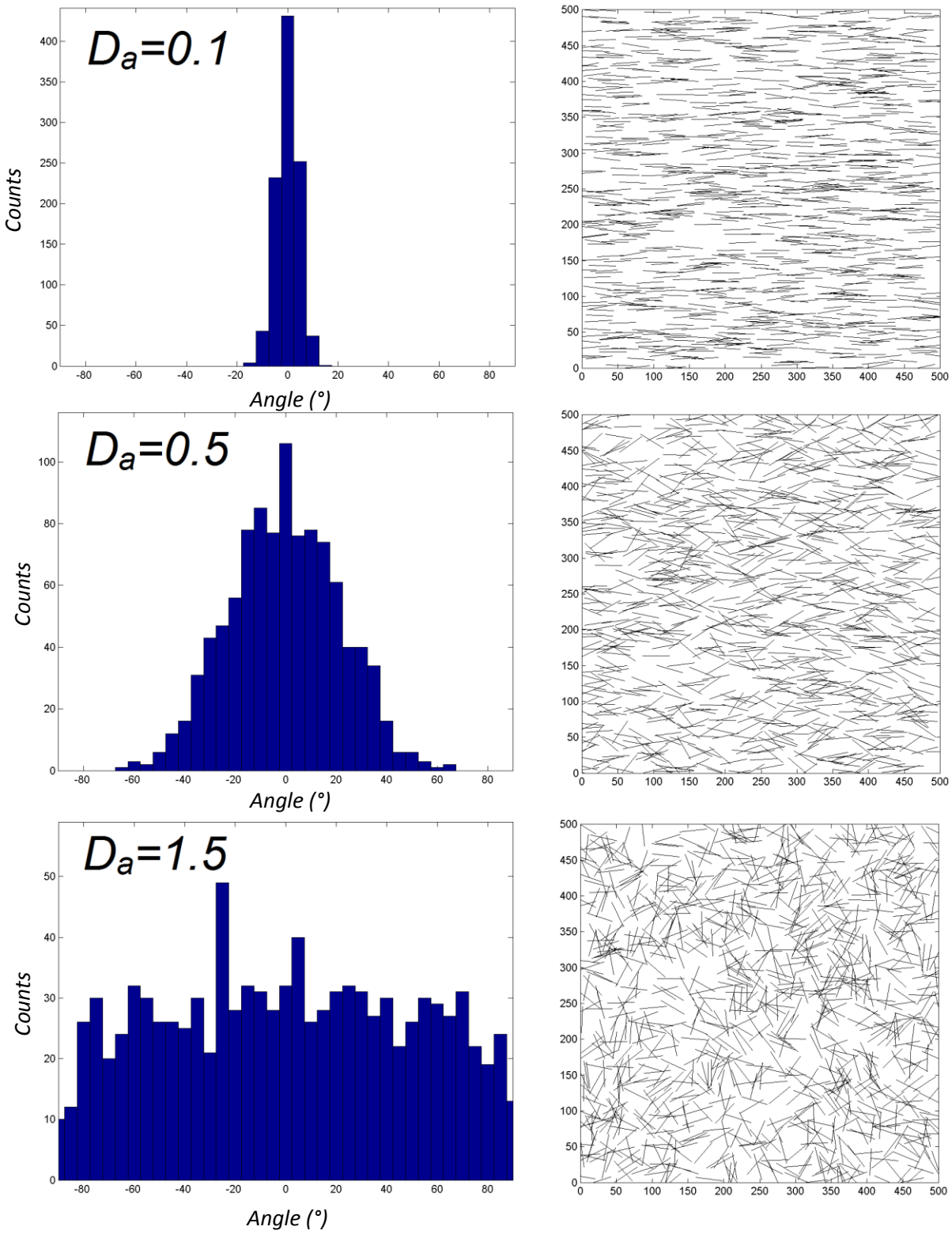

Figure 3.16 A series of histograms of nanowire angles with different values of the angular distribution parameter D_a and their resultant networks. As D_a is increased the angular distribution approaches uniformity. L_w= 37.5 μm and L_s= 500 μm wire density is n_c of the ideal stick system for L_s/L_w.

normal distribution of angles around that average. The angles generated were restricted such that all angles fell between $\frac{\pi}{2}$ and $-\frac{\pi}{2}$ due to the symmetry of the wires this does not impact on the isotropy of the system. The width of the distribution was modified to allow a smooth transition between a sharp normal distribution and a uniform distribution of angles over the allowed range. This was achieved using an angular distribution parameter which we call D_a to modify the standard deviation of the distribution of angles σ_a:

$$\sigma_a = \frac{D_a \pi}{4} \quad (3.6)$$

The relationship between D_a and the standard deviation is such that four standard deviations of the generated angular distribution will fall within $\pm D_a \pi$ of the mean angle. This implies that 99.99% of all angles generated are within this range. As D_a is increased the width of the distribution increases however, as we have restricted the allowed range of angles generated, angles that are outside the allowed range are translated back to an equivalent angle within reduced domain. This results in a uniform distribution of angles for large values of D_a.D_a was allowed to vary between 0.1 and 4, with completely isotropic angular distribution occurring at D_a=4. As the angular distribution decreases the connectivity of the wires in the network decreases as seen in Figure 3.16, this results in a loss of percolation even though the wire density is at n_c of the ideal system for this particular combination of L_s and L_w.

Of note is the fact that the network formation is no longer symmetric in the case of low width angular distributions, thus unlike in the isotropic case it becomes important which axis are defined as the electrodes in the system. Balberg and Binenbaum[22] also observed this and defined longitudinal and transverse percolation as two cases where the axis of percolation is either parallel or perpendicular to the average angle, respectively. In our case we use the same definition but maintain the top and bottom of the system as the electrodes of interest and set the average angle for each dispersion as either 0 or $\pi/2$. To check the behaviour of the onset of percolation in these two cases we explore the impact of varying D_a on the critical number density of percolation in the longitudinal ($N_{c\parallel}$) and transverse ($N_{c\perp}$) directions.

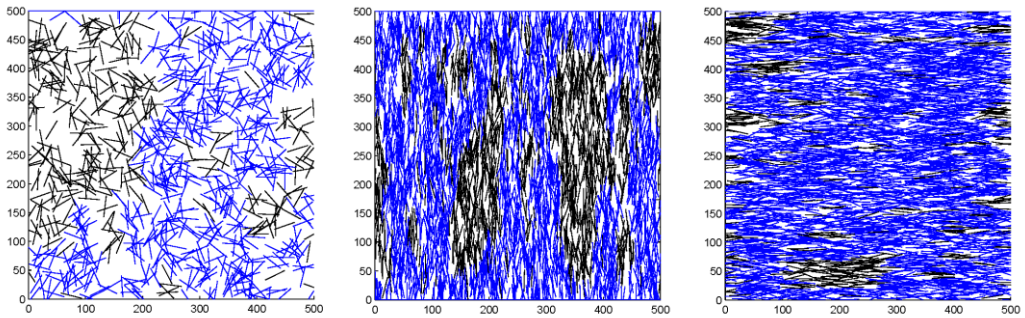

Isotropic D_a=4 | Longitudinal D_a=0.2, $<\theta>=\pi/2$ | Transverse D_a=0.2, $<\theta>=0$

Figure 3.17 Three different angular conditions explored. The longitudinal and transverse cases refer to the relationship between the average angle and the direction of percolation. In all three cases percolation occurs when cluster connects to the top and bottom of the system. Percolating clusters are indicated in blue. L_s=500μm L_w=37.5μm

These two cases are depicted in Figure 3.17 along with the isotropic case. The networks depicted are at the density at which the first percolating cluster appears. It is quite evident that both the longitudinal and transverse cases require a significantly higher density than the isotropic case in order to form a percolating cluster. Of note is the fact that the longitudinal case has a lower density than the transverse case, this is to be expected as the average effective length (the distance that each nanowire covers in the direction of percolation $L_{we}=L_w.sin\ \theta$ in the longitudinal case is close to L_w, however in the transverse case it approaches 0. As demonstrated in 2.2 decreasing the wire length results in an increase in N_c. In the case of the angular distributions we cannot directly associate L_{we} with L_w, as the full wire is still capable of forming clusters, however it does provide a guide to the origin of the anticipated behaviour of the system.

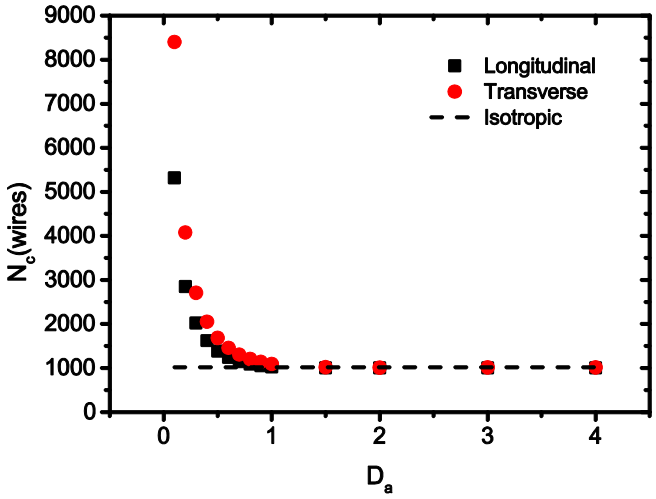

Figure 3.18 Critical density of percolation in the longitudinal ($N_{c\parallel}$) and transverse ($N_{c\perp}$) directions as compared to the value of the isotropic system (dashed line).

As yet we have been unable to determine a satisfactory equation to relate the behaviour of N_c to the angular anisotropy of the system, however the simulations here provide an interesting insight into the onset of percolation in anisotropic systems. The first observation is that the isotropic system has the lowest critical number and hence is the most desirable. Secondly the direction of the anisotropy in relation to the electrode geometry has an influence on formation of the percolating cluster. All of the experimental results provided within this thesis use spin coating as the deposition method which results in a radial anisotropy in the network. As such it would appear that the discrepancy in the onset of percolation discussed at the end of the length distributions chapter could largely be addressed by the required increase in density due to the angular anisotropy.

3.5 Curved Nanowires: Circles

To date no research has been devoted to the impact of wire curvature on the onset of percolation in a 2D stick network. Straight sticks may be an acceptable approximation for CNTs and short metallic nanowires but in reality many of the metallic nanowires used for transparent conductive materials have sufficiently high aspect ratios that curved wires are more likely. A cursory SEM observation of silver nanowire networks with an average nanowire length of 37.3 μm reveals that this assumption is realistic as shown in Figure 3.19.

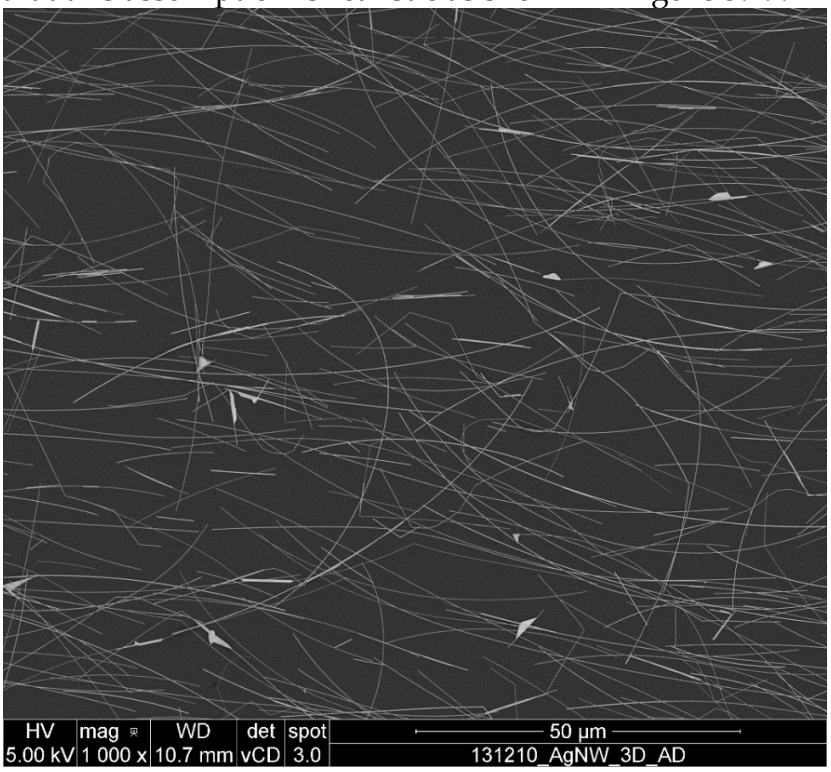

Figure 3.19 SEM image of Ag115 nanowires deposited via spin coating.

The silver nanowires shown in Figure 3.19 have a broad distribution of curvatures and can in general be approximated, for a sake of simplicity, by a circular arc. This is not always entirely accurate as for some cases the curves are more parabolic in nature and in others the wires bend twice in opposing directions but as a first approximation we chose to employ circular arcs to define curved nanowires to study the impact of wire curvature on 2D stick percolation.

In this approximation we make several assumptions:

1. Nanowires take the form of a circular arc
2. Wire arc is restricted such that the smallest radius of curvature results in a half circle
3. A nanowire with a radius of curvature of 10,000 is a straight line. (Curvature is determined from the inverse of the radius of curvature and for small arc lengths this assumption is reasonable)

The distribution of curvatures for the nanowires are selected such that the radii are uniformly spaced between the smallest allowed by assumption 2 and a

radius of 10,000. In order to generate nanowires with an appropriate length, their arcs were defined by the following coordinate equations:

$$x = rcos\theta + x_{cen} \quad (3.7) \quad and \quad y = rsin\theta + y_{cen} \quad (3.8)$$

where x_{cen} and y_{cen} are the coordinates of the centre of the circle. Each nanowire is assigned a randomly-generated centre position and radius. The minimum allowed radius of curvature was defined as:

$$r = \frac{L_w}{\pi} \quad (3.9)$$

This definition restricts the wires to at most a half circle. For wires with radii of curvature larger than this we need to restrict the arc length such that the nanowire defined within the system will be the appropriate size. Defining the circular arcs in this form allows the use of the angular range to restrict the length of the arc. In line with our second assumption the angular range of magnitude θ_r was restricted such that the length of each wire was L_w this was achieved by defining:

$$\theta_r = \frac{L_w}{r} \quad (3.10)$$

Thus the equations for each of the nanowires could be defined such that the wires produced had the desired length and some radius of curvature r such that:

$$\frac{L_w}{\pi} \leq r \leq 10{,}000 \quad (3.11)$$

A set of nanowires satisfying this criteria with their angular ranges centred on $-\frac{\pi}{2}$ and the same centre positions are displayed in Figure 3.20.

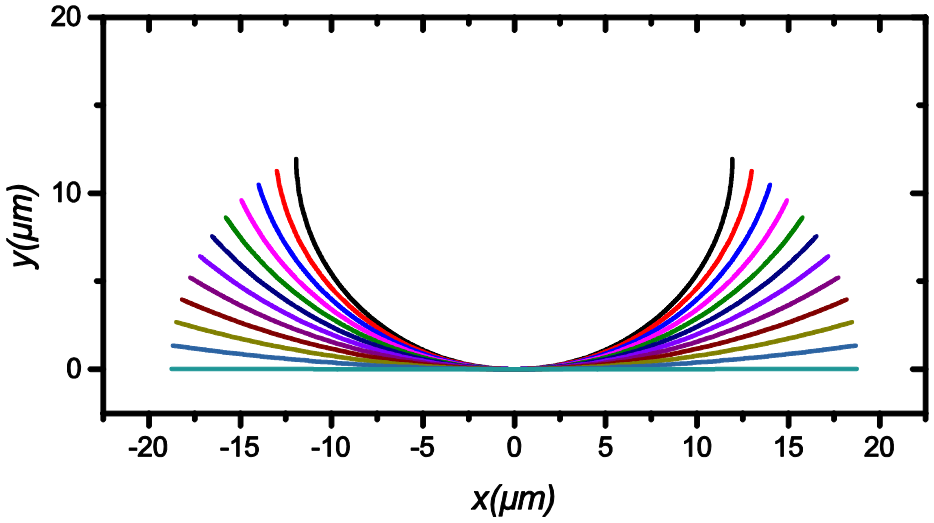

Figure 3.20 Depiction of several wires with a constant wire length $L_w = 37.5\ \mu m$ and linearly spaced curvatures between r_{min} and $r=10000$.

For the addition of the generated nanowire to the system some modifications of their arc equations had to be made so that the centre was in such a position that the wire location was within the defined system. It is also necessary to add a secondary angle φ which allows rotation of the nanowires as they are added to the network to achieve an isotropic orientation of the network.

This means that for nanowires with large radii of curvature their centres were actually located outside the defined system. The modification was made by setting the middle of the wire arc as the reference for the addition to the nanowire network, this was achieved by subtracting the position of the arc mid-point from the centre points of the defined arc as given by equations 3.7 and 3.8. The rotation of the nanowires is achieved by the addition of φ such that:

$$x = rcos(\theta + \varphi) + x_0 \ (3.12) \quad and \quad y = rsin(\theta + \varphi) + y_0 \ (3.13)$$

The terms x_o and y_o are also dependent on the rotation φ however for simplicity the presentation of this dependence is omitted here. Having defined the equations for individual wires and modifying them in the requisite manner the wires could be added to the simulation space. As each wire was added it was necessary to determine whether it intersected with other wires. This is essentially the intersection of two circles with a secondary condition that the point of intersection must exist within both the allowed ranges of each arc. The method employed for the identification of the points of intersection p_2 and p_3 used similar triangles to calculate their x and y coordinates. A graphical representation of the problem is shown in Figure 3.21. The known components of this system are the coordinates of c_1 and c_2 and the two circle radii r and R.

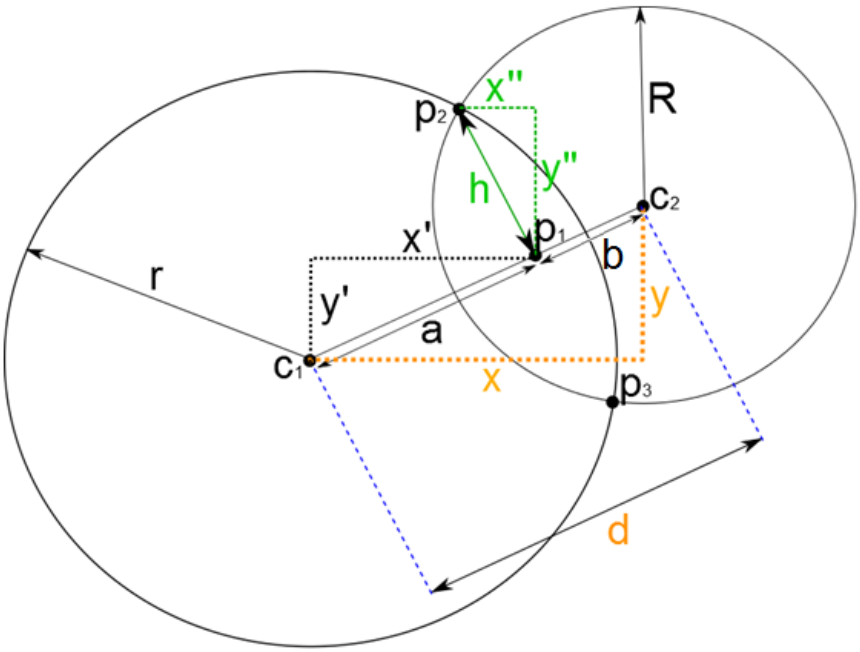

Figure 3.21 Geometric depiction of the intersections of two circles, the MATLAB algorithm developed used the similar triangles indicated here in yellow, black and green to calculate the position of the intersections.

Using Pythagoras theorem and similar triangles it is quite straightforward to define the sets of equations which provide the coordinates of the intersections.

$$d = \sqrt{x^2 + y^2} \quad (3.14) \qquad r^2 = a^2 + h^2 \quad (3.15)$$

$$d = a + b \rightarrow \quad b^2 = d^2 - 2ad + a^2 \quad (3.16)$$

$$R^2 = b^2 + h^2 \rightarrow \quad h^2 = -d^2 + 2ad - a^2 + R^2 \quad (3.17)$$

Substituting equation 3.17 into equation 3.15 and rearranging for *a* produces:

$$a = (d^2 + r^2 - R^2)/2d \quad (3.18)$$

Then now that we have descriptions of *a* and *h* which rely only on the known values of the coordinates of c_1 and c_2 and the two circle radii *r* and *R* (as *d* is defined by equation 3.14) we can use similar triangles to equate the ratios of the different side lengths indicated in Figure 3.21.

$$x' = \frac{a}{d}x \quad (3.19), \qquad y' = \frac{a}{d}y \quad (3.20)$$

$$x'' = \frac{h}{d}x \quad (3.21), \qquad y'' = \frac{h}{d}y \quad (3.22)$$

From here we can calculate the absolute positions of the required points from the position of the centre of the first circle and combinations of *x′*, *y′* and *x′′*, *y′′*.

$c_1=(x_1,y_1)$, $p_1=(x_3,y_3)$

$$x_3 = x_1 + x' \quad (3.23) \qquad y_3 = y_1 + y' \quad (3.24)$$

$p_2=(x_4,y_4)$

$$x_4 = x_2 + x'' \quad (3.25) \qquad y_4 = y_2 - y'' \quad (3.26)$$

$p_3=(x_5,y_5)$

$$x_5 = x_2 - x'' \quad (3.27) \qquad y_5 = y_2 + y'' \quad (3.28)$$

Once the intersections are identified they are then checked against the points defined by the arc equations of each wire to determine whether they exist for both wires. If at least one of these points exists for both wires then the wires are placed in the same cluster. The MATLAB program continues in the same manner as for the straight wires adding wires, checking for intersections and relabeling them as appropriate until a percolating cluster is formed. Once again 10^5 simulations were performed for each ratio of lengths to system size.

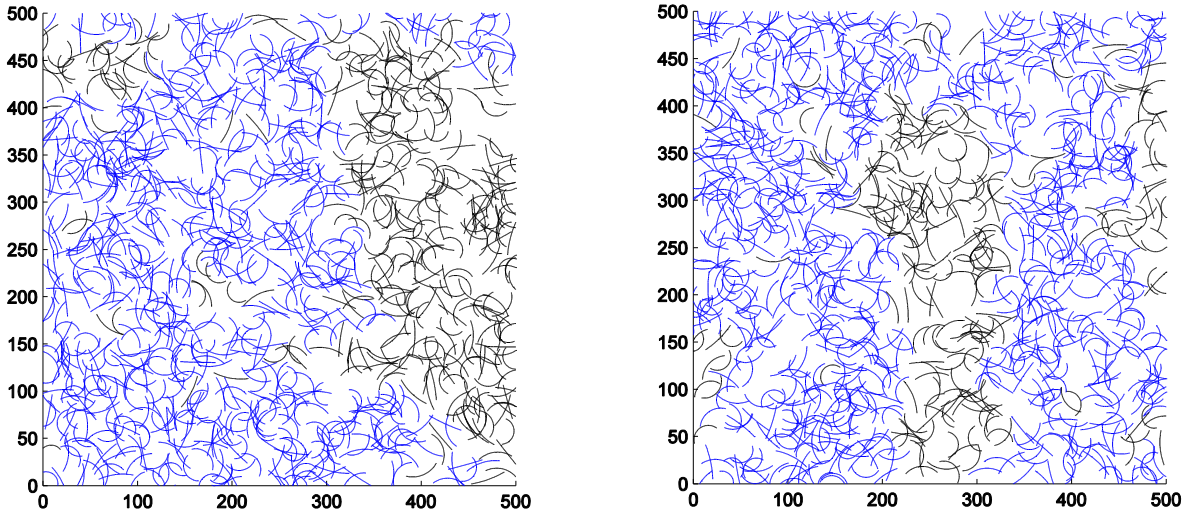

Figure 3.22 Two examples of the outcome of a single Monte Carlo simulation of curved nanowires. Systems shown are just percolating, i.e. the density is close to n_c with the percolating clusters indicated in blue. In these examples L_s=$500\mu m$ and L_w=$37.5\mu m$ nanowire radii are randomly distributed between L_z/π and 10000.

The outcome of two simulations based on the method outlined above is shown in Figure 3.22. The nanowires in the network are quite evidently curved and it can be seen that the cluster identification is able to identify the percolating cluster. In these examples the nanowires all have the same arc length meaning that the results from this simulation are comparable with the ideal system discussed in section 2.2. For the initial investigation of the impact of wire curvature we chose to explore the case that the nanowires had a uniform distribution of curvatures between completely straight and a half circle as defined by the assumptions above. This choice was based on the consideration of the physical networks as observed by SEM and appears to be a reasonable approximation of the physical networks.

Results from the Monte Carlo simulations of curved nanowires are plotted in Figure 3.23a with the values of the ideal stick system for comparison. Again in this plot we see the quadratic behaviour as observed for the ideal stick system and can fit the function according to the equation:

$$N_c = \frac{6.06{L_s}^2}{{L_w}^2} + \frac{0.17L_s}{L_w} + 1.2 \qquad (3.29)$$

From this fit and comparing it to equation 3.29 we can see that at low ratios of system size to wire length the curved wire system has a smaller N_c than the ideal system. At a ratio L_s/L_w=5 the critical number of the two systems is effectively equal, as the ratio is increased the value of N_c for the curved system grows larger than that of the ideal system. In Figure 3.23b we can see the relationship between the ideal N_c and the curved N_c more clearly. The curved system starts off with an N_c which is 66.6% of the value of the ideal system for a ratio of L_s/L_w=1. From here it increases rapidly with the ratio of L_s/L_w before asymptotically approaching a value of 107% of the ideal system.

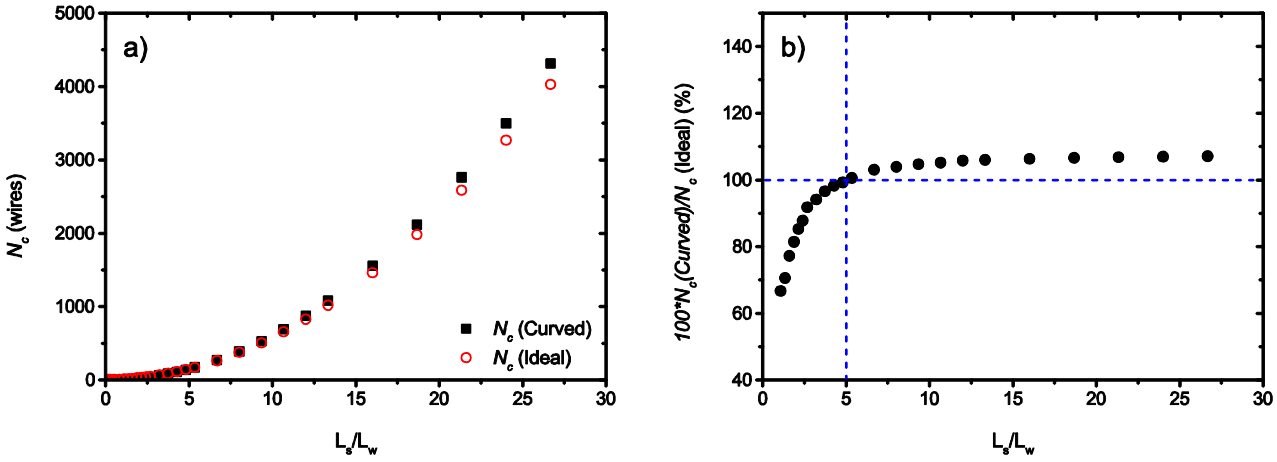

Figure 3.23 Comparison of Monte Carlo simulations of curved sticks with those of the ideal straight stick system. a) N_c as a function of L_s/L_w : initially the circles have a lower critical number but as the system size is increased there is a cross over resulting in a higher N_c for values of L_s/L_w > 5 b) Normalization of the data by dividing by N_c of the ideal system to reveal the impact of simulating curved wires. Dashed blue lines indicate the cross over point.

This behaviour suggests that the critical number of the infinite curved nanowire system with a uniform distribution of curves will be 7% larger than that of its' straight stick counterpart. The exact origins of the transition in percolation as compared to the ideal system is difficult to discern from the information available and ongoing work is needed to explore it further.

As a final qualitative comparison we can look at comparing experimentally obtained SEM images like that shown in Figure 3.19 with similar simulated nanowire networks.

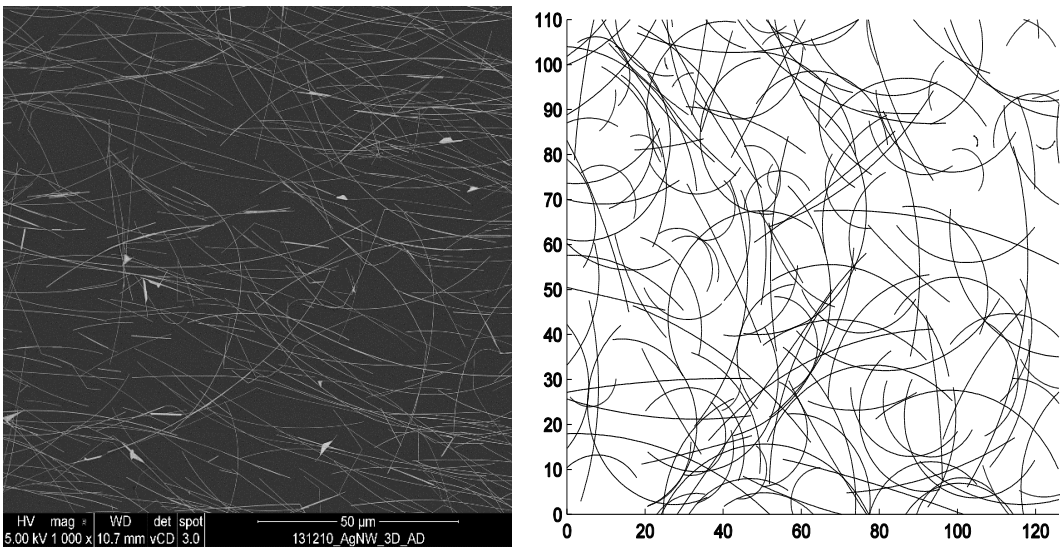

Figure 3.24 Comparison of physical network with a curved nanowire network generated by the MATLAB algorithm. Simulated network is at the same scale as the physical network and a length distribution and density were selected to approximate that of the physical network.

Such a comparison at this stage is only qualitative giving a general sense of the system and allowing one to see that the assumptions given on page 79 are reasonable. With further work to develop this tool it may be possible to use image analysis to quantitatively generate an exact replica of a given physical network, allowing the calculation of the network density with much higher accuracy.

3.6 Collection or Injection Efficiency

The use of Ag nanowires in devices such as solar cells or LEDs has already been demonstrated.[24–26] In such devices the transport of electrons from or to all regions of the active material is of critical importance. From a quick thought experiment one may consider that due to the fact that nanowire networks are not continuous films, charges will not be able to be collected at all locations in the film. From this idea some may assume that it implies that the collection efficiency of a silver nanowire network will play a restrictive role on the overall efficiency of a solar cell using silver nanowire electrodes. This section of the thesis explores this idea and attempts to demonstrate that due to the small size of the gaps in the nanowire network and the nature of charge generation in solar cells there is not a significant loss of charges. This section presents the work that we have undertaken to estimate the collection efficiency. Although the model we have developed so far has not yet reached a state where conclusive results can be determined the basic idea appears worth investigating in the future.. Therefore this section describes the thought process behind the development, the current state of the simulations and provides evidence as to why the model does not yet work and suggestions for possible future development.

In general charges will have a finite lifetime in the active region of the cell before undergoing recombination.[27,28] The average distance that an electron can travel before recombining depends on the carrier mobility and lifetime in the material, this distance is called the diffusion length (L_d). As a silver nanowire network is discontinuous in 2D, having some regions of the plane which are non-conductive, the collection efficiency of such an electrode is dependent on two main characteristics of the system:

1. The nanowire density: This determines the average size of the non-conductive regions,
2. The L_d of electrons in the material in contact with the nanowire network.

The neighbouring material could be the active region of the cell, where charges are generated or it may be a hole/electron blocking layer depending on the design of the solar cell. If the nanowire network is in direct contact with the active region then the exciton lifetime and mobility determines the diffusion length. If the adjacent material is a blocking layer then the lifetime of the majority carrier in the blocking layer will determine the relevant L_d. As diffusion lengths are inherently material dependant-dependent there is a large variation associated with different types of solar cells.

In organic solar cells the exciton L_d can be as short as 6nm[29,30] which represents a significant challenge for the use of nanowire networks directly in contact with the active region as the spaces between wires may be several times larger than L_d. A result that supports this argument was reported by Stubhan et al.[1]. I who compared organic solar cells with transparent electrodes based on silver nanowires, ITO and combinations of nanowires and ZnO. The efficiency of the cells with bare nanowire electrodes was found to be significantly lower than nanowires coated with ZnO with photon conversion efficiencies of 1.65% and 2.46%, respectively.

One could argue that the difference in efficiency was due to the flattening of the surface morphology associated with embedding the nanowire network in a TCO resulting in less short circuits and less loss of current through shunting of the cell. However, in this case both cells had similar shunt resistances; hence losses were not due to differences in surface roughness. In this arrangement the ZnO layer acts as a charge separation layer providing an electron-selective buffer layer between the nanowire network and the active region of the cell. As charges are injected directly into the conduction band of the ZnO they are free to move through the layer to the silver nanowires. Thus the ZnO with $L_d \approx 100\mu m$[31] provides local conductivity in the regions lacking silver nanowires. Due to the low thickness of the intrinsic ZnO layer its' in plane conductivity is not sufficient to act as a macro scale TCO so the electrical properties of the electrode are dominated by the nanowire network.

In other solar cell architectures such as silicon or Dye Sensitised Solar Cells (DSSCs) this is not such a problem as the diffusion length is significantly larger, on the order of 1-5µm in TiO_2 DSSCs and as large as 1 cm in silicon.[32] Though this is of course dependent on the dopant concentration. In silicon solar cells, L_d is more typically on the order of 100-300µm.[14] However, for crystalline silicon cells the L_d of holes (12µm) is much lower than that of electrons (1100µm).[14] This means that the nanowire electrode should be connected to the n-type side of the cell to maximise collection efficiency.

In considering the idea of collection efficiency in 2D nanowire networks there is a strong dependence on the diffusion length of the material from which the electrons need to be extracted. As yet this problem has yet not been studied in depth: the development of a model which would allow the estimation of the collection efficiency of a network at a given nanowire density with a given diffusion length will thus prove to be a vital tool for the application of nanowire networks to solar cells.

A secondary issue also needs to be discussed: as mentioned in section 2.2, some regions of the nanowire network will not be connected to the percolating cluster. The number of wires not connected to the percolating cluster is dependent on the system size and the network density, but the treatment of these wires in a calculation of the collection efficiency is not straightforward.

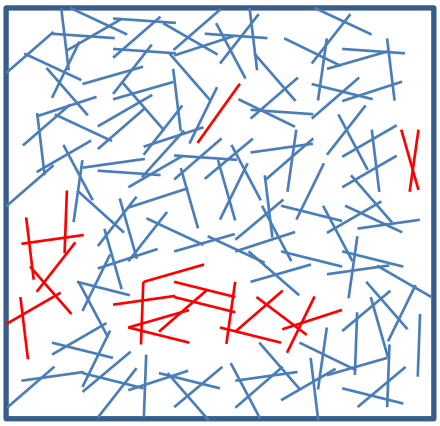

Figure 3.25 Simple nanowire network schematic, percolating nanowires are indicated in blue.

If one considers a simple nanowire network as depicted in Figure 3.25 Electrons collected by the red nanowires cannot be extracted from the system as they are not connected to the percolating path and will undergo recombination. In working devices the actual network density should be sufficiently high so that the number of non-percolating wires will be low and losses due to them will not play a large role in the collection efficiency. However it is still important to consider these wires as part of the simulation, to identify how significant the contribution of these wires will be.

Initially we used the work of Gonzalez-Vazquez and Bisquert[28] and that of Nelson[27] to develop a mathematical description of the collection efficiency of the nanowire network, this method proved to be incorrect as described below but may provide some usefulness as a basis for a future work. We therefore describe it here.

To minimise computation time, the estimation of the collection efficiency was made using the probability of finding an electron at a given distance from its point of generation as calculated by Gonzalez-Vazquez and Bisquert as shown in Figure 3.26.

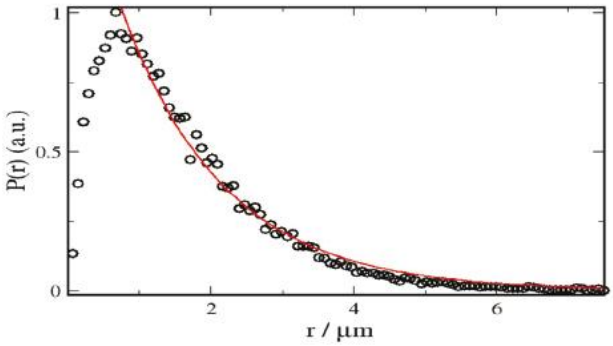

Figure 3.26 Probability of finding an electron at a given distance from its point of generation as determined from random walk numerical simulations of the diffusion of electrons (data points). Red line is a fit to the data with an exponential decay where the decay constant is the diffusion length of 1.33 µm.[28]

The results of 2.26 were fitted with an decaying exponential function which yields the diffusion length. We used this probability distribution to calculate the probability of collection at a distance x from the nanowire. Performing this computation on a 2D mesh allowed us to make a spatial map of the probability distribution around a single nanowire based on the minimum distance from the point in space to the nanowire. This leads to the result of the simulated collection efficiency of a single wire, as depicted in Figure 3.27. This mathematical treatment is extremely rapid, allowing the calculation of ten thousand points in less than 1s and allows for high resolution estimation of the collection probability at each point.

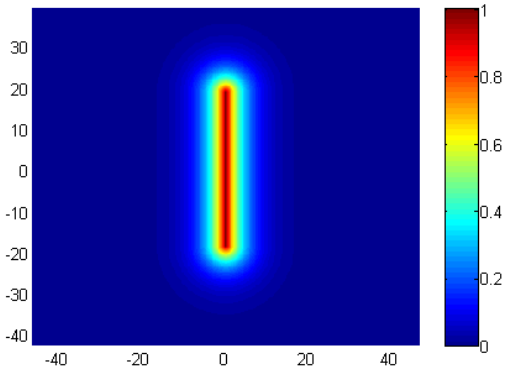

Figure 3.27 Probability of collection map of a single wire based on the probability of collecting an electron at a given distance from its point of generation. Parameters of the simulations include the following values: L_w=37.5µm L_d=1.33µm. The units of spatial x and y axes are in microns.

Considering that the collection of an electron by a nanowire in the network is a mutually exclusive event, meaning that if one nanowire collects an electron it cannot be collected by another, we made the initial assumption that the probability distribution of each of the nanowires in the network could be directly added with the condition that the probability of collection at a given point was never greater than unity. This allowed the generation of collection efficiency maps of entire networks by simple matrix summations of the collection efficiency of the individual wires as depicted in Figure 3.28.

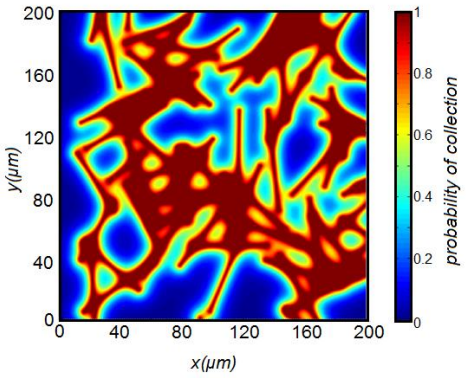

Figure 3.28 Combined probability maps of individual nanowires to allow calculation of the network collection efficiency. Collection efficiency estimated here is 58.3% L_w=37.5μm L_s=200μm and L_d=1.33μm

After building this initial model and running several simulations we found out that the simulation was over-estimating the collection efficiency. This can be seen in Figure 3.28 as the network represents the first percolating cluster and as such would be expected to have a low collection efficiency. We can see from this figure that in the regions where nanowires intersect the collection probability becomes unity for a large area surrounding the junction. This was found to be due to two issues with the assumptions that we had made. Both issues are related to the probability distribution derived from the work of Gonzalez-Vazquez and Bisquert. Indeed, their work used random-walk numerical simulations to determine the probability of finding an electron at a given distance from its point of generation. In our initial simulation we had assumed that this was a one dimensional probability. However, the value given in Ref. [28] is actually a 2D probability of finding the electron at a given displacement from its origin in any direction. Thus, by using the values determined by Bisquert as a function of the minimum distance from the nanowire, the simulation was effectively integrating the 2D probability and assigning it to a single point. The second issue comes from calculating the probability based on only a single vector from the point of generation to the nanowire. The definition of the distance as the minimum distance to the nanowire creates a perfectly symmetric probability distribution which can be observed in 2.27 by the fact that the probability distribution is uniform around the entire nanowire. In reality one would expect that the probability for a given distance from the end of the nanowire would be significantly lower than the probability the same distance from the centre of the nanowire, as at the centre of the nanowire the wire extends in both directions away from the origin of the electron, allowing a much larger interaction cross section.

In order to address these over estimations we have developed a random-walk Monte Carlo simulation based on the diffusion of carriers within the layer adjacent to the nanowire network. Charges generated at some distance from a nanowire undergo a diffusion process with some chance of recombining before arriving at the nanowire. If the generated electron crosses a nanowire during its lifetime then we assume that the electron is collected. This model is computationally expensive as it requires very small steps in the electrons' random walk and a large number of electrons at each point to determine the probability of an electron generated at this point being collected. For the development of this simulation the following assumptions were made:

1. As all of the charges must be collected in the plane of the silver nanowire network, the material can be modelled as a 2D system with losses due to recombination in the regions between nanowires.
2. All electrons which cross a nanowire during their random walk are collected.
3. Nanowires not connected to the percolating cluster will have a negative impact on the collection efficiency.

From these assumptions a MATLAB algorithm was made which simulated the random walks of electrons and their collection by a single nanowire. In order

to set the diffusion length of the electrons within the simulation we rely on the fundamentals of the random walk process. A typical random walk has a Gaussian probability distribution of being found at a given distance from the origin of the walk with the root mean square expected distance travelled being equated to the number of steps taken N and the size of the steps s by:[33]

$$\sqrt{< x^2 >} = s\sqrt{N}$$

Hence as L_d is the average distance the electron will diffuse during its lifetime we can define L_d in terms of N and s. Rearranging the equation to yield N as target function, we define the number of steps each electron should take on average before recombining.

$$N = \left(\frac{L_d}{s}\right)^2$$

Using this method we can set the average number of steps that an electron will take during its random walk such that the average displacement of electrons at the end of their lifetimes matches the desired L_d.

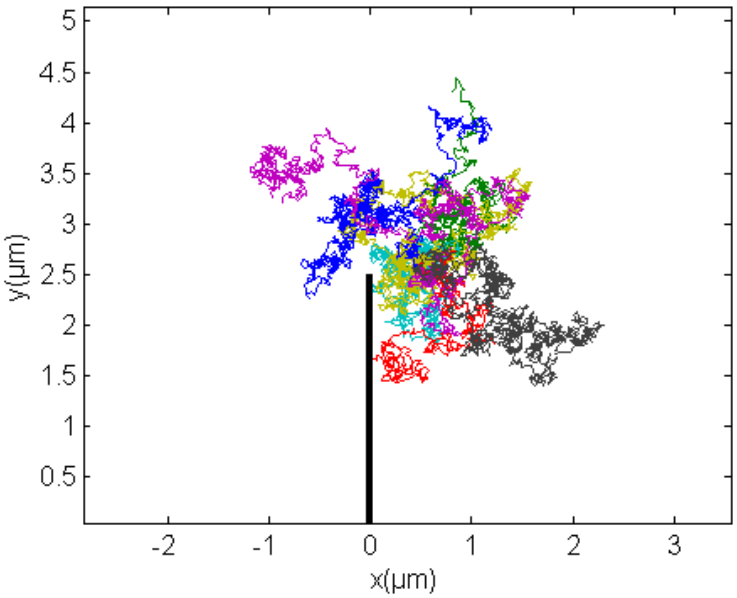

Figure 3.29 Six Monte Carlo simulations of electron diffusion as random walks around a single nanowire (thick black line). The electrons take a finite number of steps before recombining. If a step crosses the nanowire the electron is collected.

Figure 3.29 shows several random walks of electrons from a single origin, note that some end at the nanowire (red, cyan and lime) and are considered as being collected whilst others (black, purple, royal blue and dark green) end in open space and are considered to have recombined.

The step size used in the simulations should be associated with the diffusion mechanisms of the electron motion. Depending on the system of interest the scale of this may change significantly. In poly crystalline TiO_2 as used in DSSCs, the conduction mechanism involves hopping from deep trap states, so the step size is associated with the trap density and is on the order of a few nanometres.[28] However, using step sizes as small as this is inhibitive to the

simulation process, as each electron path will have an enormous number of steps associated to it thus leading to an unacceptable amount of computational time. As the step size is in most cases much smaller than the diffusion length (except for organic solar cells without a buffer layer)), we have approximated the electron paths by using a set of larger steps which terminates at the electron position after a number of smaller steps. This approach is essentially a time averaging of the position, it causes a loss of time resolution and the average width of the electrons path is reduced but the spatial average is maintained. As N is proportional to $1/s^2$ even small increases of s provide a significant reduction in the number of steps needed. Through this approach we minimize the number of steps required to make the random walk and enable the random-walk model to be computationally feasible.

Having determined the method to achieve the desired L_d we looked at the convergence of the probability of collection of electrons by a nanowire, $P(C)$, as a function of the number of simulations at several different values of L_d and at several different distances from the wire x, the results are shown in Figure 3.30.

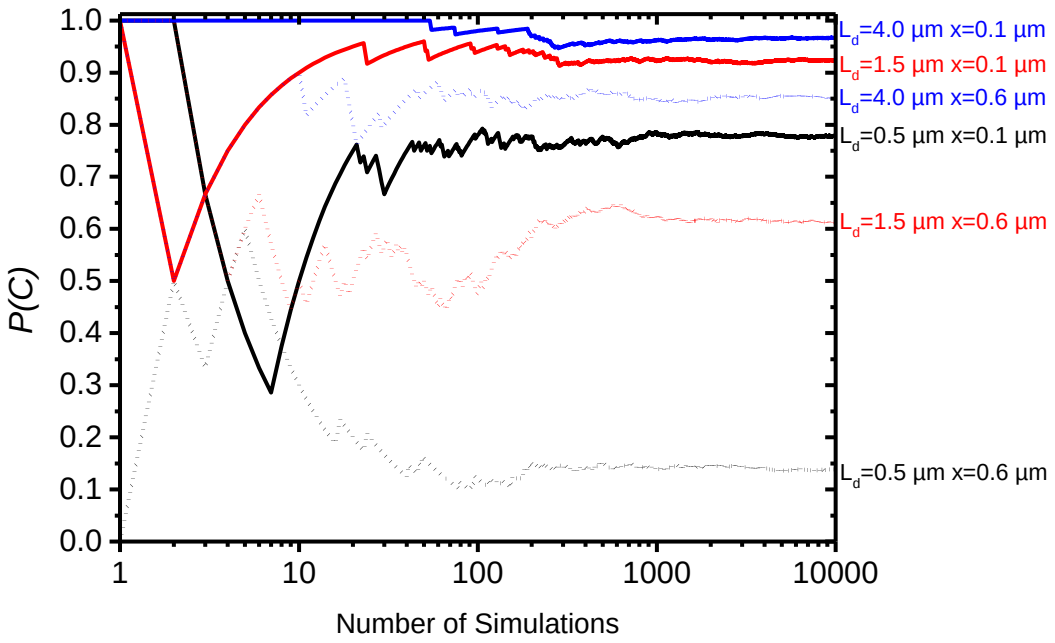

Figure 3.30 Convergence of $P(C)$ for several different conditions. These results indicate that 1000 simulations are sufficient to determine $P(C) \pm 0.025$ for each of the values of L_d and x.

Having now determined the minimum number of simulations required to achieve a reasonable accuracy P(C) it was possible to run a set of simulations for a single nanowire. To ensure reliable results we used 10^4 simulations.

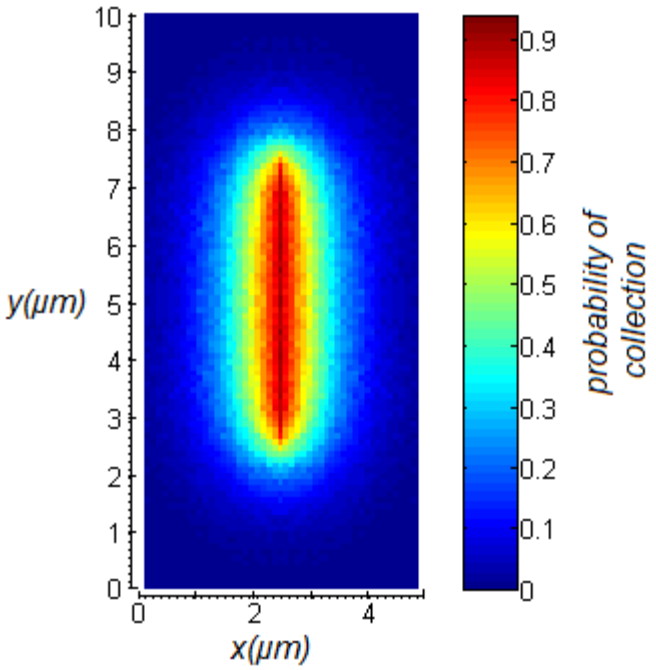

Figure 3.31 Spatial map of P(C) determined from Monte Carlo Random Walk simulations. Number of simulations= = 1000, L_d=1.33μm

Figure 3.31 shows the anticipated anisotropy in the collection efficiency at the ends of the nanowires and also an effective decrease in collection efficiency at each site due to the correct estimation achieved by using the random walk model directly. The resolution of Figure 3.27 and Figure 3.31 are actually the same, but Figure 3.27 includes a much larger area so the pixels appear smaller. Comparatively the random walk method takes on the order of 10^8 times longer than the mathematical approximation but it determines the collection efficiency correctly. Ongoing work should focus on a mathematical fit of the data of Figure 3.31 allowing the correct result to be defined mathematically instead of by a random walk process. Figure 3.31 is actually an image made from the simulation of ¼ of the nanowire. Indeed, thanks to the symmetry of the system it is possible to simulate just one part of the system and then apply symmetry operations to obtain the whole image. This also helps to reduce the calculation time. Figure 3.31 shows signs of noise, which we attribute to an insufficient number of simulations. Even though the number of simulations used was 10^4, which is one order of magnitude above what the convergence study suggested would be sufficient. This is likely due to a spatial dependence of the convergence relating to the geometry of the nanowire, in the convergence tests the y position relative to the wire was held constant.

In order to validate the assumption that nanowire collection was a mutually exclusive event we ran a simulation of a single wire and made the convolution of it with itself, but offset and rotated by 90°, and compared it to a simulation of two wires with the same geometry. Upon doing this it was revealed that at the junction, the convolution of the two nanowires from the individual simulation over-estimates the collection efficiency. For this single junction at 90° the over estimation is approximately 35% of the total collection efficiency of the

two wires. This demonstrated that we cannot use the combination of several single-wire probability distributions to tentatively estimate the collection efficiency of a network.

From this study, we learnt that the random work model needs to be applied to the network as a whole, which unfortunately could not be achieved within this work. The origin of the problem is that although the collection of electrons by nanowires are mutually exclusive events, the electron has a lifetime. In the case of the single nanowire system, all electrons that can cross the wire in their entire lifetime do so and are collected. Hence, when the convolution is performed to create a two-wire system, it assumes that both wires collected all the possible electrons. In the case of the two wire simulation of the two-wire system, once an electron is collected by one of the two wires, its lifetime is cut short and it cannot, obviously, be collected by the other one. In order to perform the convolution correctly it would require tracking the temporal and spatial position of the electron and adding a condition based on the position of the nanowires. This method would actually be longer than performing the random walk model for the two individual wires.

3.7 Closing Remarks

This chapter has provided insight into the computer simulations which were undertaken in order to explore the percolating nature of perfect wire network as well as the impact of imperfect wires on the percolation threshold. The main contributions of this work include the extension of percolation threshold approximations into small-scale systems approaching the length of the nanowire, the redefinition of the percolation threshold to n_{99} allowing for the prediction of densities required for use in real devices and the introduction of L_{seff} as a defining system characteristic. Foundational work has been undertaken, including the implementation of curved nanowires into a percolation determination algorithm and the exploration of a method to simulate the collection efficiency of a network. Further work is needed to develop a clear understanding of the interrelation of angular anisotropy and the critical density of the system. Each of the percolation algorithms developed within this thesis have the potential to be employed in conjunction with Kirchhoff's laws to enable the estimation of different networks electrical conductivity in a similar manner to that used by Žeželj and Stanković[34] however. However superior computational resources than those we have used for this work would be needed to perform those simulations within an acceptable time frame. We would like to highlight here that all of the simulations undertaken within this thesis were performed using MATLAB on a portable personal computer without the parallel computing toolbox.

Further development of the collection efficiency calculations are needed in order to achieve a relevant network collection efficiency however. However, from the initial results, we have shown that direct convolution of the probability

distribution function of a single wire cannot be used to model the behaviour of the whole network.

3.8 References

[1] T. Stubhan, J. Krantz, N. Li, F. Guo, I. Litzov, M. Steidl, M. Richter, G. J. Matt, C. J. Brabec, *Sol. Energy Mater. Sol. Cells* **2012**, *107*, 248.

[2] D.-S. Leem, A. Edwards, M. Faist, J. Nelson, D. D. C. Bradley, J. C. de Mello, *Adv. Mater.* **2011**, *23*, 4371.

[3] M. E. J. Newman, R. M. Ziff, *Phys. Rev. Lett.* **2000**, *85*, 4104.

[4] M. E. J. Newman, R. M. Ziff, *Phys. Rev. E* **2001**, *64*, 016706.

[5] M. Matsumoto, T. Nishimura, *ACM Trans Model Comput Simul* **1998**, *8*, 3.

[6] G. Marsaglia, W. W. Tsang, *J. Stat. Softw.* **2000**, *5*, 1.

[7] J. Li, S.-L. Zhang, *Phys. Rev. E* **2009**, *80*, 040104.

[8] *Accessed 06 July 2013* **n.d.**, *http://www.seashelltech.com/index.shtml*.

[9] I. Balberg, N. Binenbaum, C. H. Anderson, *Phys. Rev. Lett.* **1983**, *51*, 1605.

[10] G. E. Pike, C. H. Seager, *Phys. Rev. B* **1974**, *10*, 1421.

[11] M. Žeželj, I. Stanković, A. Belić, *Phys. Rev. E* **2012**, *85*, 021101.

[12] S. I. White, B. A. DiDonna, M. Mu, T. C. Lubensky, K. I. Winey, *Phys. Rev. B* **2009**, *79*, 024301.

[13] S. M. Bergin, Y.-H. Chen, A. R. Rathmell, P. Charbonneau, Z.-Y. Li, B. J. Wiley, *Nanoscale* **2012**, *4*, 1996.

[14] A. Luque, S. Hegedus, *Handbook of Photovoltaic Science and Engineering*, Wiley, **2003**.

[15] P. R. F. Barnes, A. Y. Anderson, S. E. Koops, J. R. Durrant, B. C. O'Regan, *J. Phys. Chem. C* **2009**, *113*, 1126.

[16] J. Nelson, *Curr. Opin. Solid State Mater. Sci.* **2002**, *6*, 87.

[17] D. Stauffer, A. Aharony, *Introduction to Percolation Theory, 2nd Revised Ed.*, Taylor And Francis, London, **1994**.

[18] R. M. Ziff, *Phys. Rev. Lett.* **1992**, *69*, 2670.

[19] C. F. Gauss, *Theoria Motvs Corporvm Coelestivm in Sectionibvs Conicis Solem Ambientivm*, Hambvrgi, Svmtibvs F. Perthes Et I. H. Besser, **1809**.

[20] C. F. Gauss, *Theory of the Motion of the Heavenly Bodies Moving about the Sun in Conic Sections: A Translation of Gauss's "Theoria Motus." With an Appendix*, Little, Brown And Company, **1857**.

[21] W. L. Dunn, J. K. Shultis, *Exploring Monte Carlo Methods*, Elsevier, **2011**.

[22] I. Balberg, N. Binenbaum, *Phys. Rev. B* **1983**, *28*, 3799.

[23] S. Sorel, P. E. Lyons, S. De, J. C. Dickerson, J. N. Coleman, *Nanotechnology* **2012**, *23*, 185201.

[24] J.-Y. Lee, S. T. Connor, Y. Cui, P. Peumans, *Nano Lett.* **2010**, *10*, 1276.

[25] Z. M. Beiley, M. G. Christoforo, P. Gratia, A. R. Bowring, P. Eberspacher, G. Y. Margulis, C. Cabanetos, P. M. Beaujuge, A. Salleo, M. D. McGehee, *Adv. Mater.* **2013**, *25*, 7020.

[26] W. Gaynor, S. Hofmann, M. G. Christoforo, C. Sachse, S. Mehra, A. Salleo, M. D. McGehee, M. C. Gather, B. Lüssem, L. Müller-Meskamp, P. Peumans, K. Leo, *Adv. Mater.* **2013**, In Press.

[27] J. Nelson, *Phys. Rev. B* **1999**, *59*, 15374.

[28] J. P. Gonzalez-Vazquez, J. A. Anta, J. Bisquert, *J. Phys. Chem. C* **2010**, *114*, 8552.

[29] A. Haugeneder, M. Neges, C. Kallinger, W. Spirkl, U. Lemmer, J. Feldmann, U. Scherf, E. Harth, A. Gügel, K. Müllen, *Phys. Rev. B* **1999**, *59*, 15346.

[30] D. R. Kozub, K. Vakhshouri, S. V. Kesava, C. Wang, A. Hexemer, E. D. Gomez, *Chem. Commun.* **2012**, *48*, 5859.

[31] E. Guillén, L. M. Peter, J. A. Anta, *J. Phys. Chem. C* **2011**, *115*, 22622.

[32] S. M. Sze, Ng, *Physics of Semiconductor Devices*, Wiley-Interscience, Hoboken, N.J., **2007**.

[33] D. Koks, *Explorations in Mathematical Physics: The Concepts Behind an Elegant Language*, Springer Science & Business Media, **2006**.
[34] M. Žeželj, I. Stanković, *Phys. Rev. B* **2012**, *86*, 134202.

Chapter 4
Physical Properties of Ag Nanowire Networks

4.1 Opening Remarks

This chapter focuses on the physical properties of silver nanowire networks. One of its objectives is to assess whether this material will provide the necessary balance to meet the needs of emerging and existing TCM applications. In particular this chapter will provide a brief discussion of the potential application of silver nanowire electrodes as front electrodes for solar cells. This chapter represents a significantly modified and expanded version of an article published in "*Solar Energy Materials & Solar Cells*".[1]

There are many different routes through which silver nanowire network electrodes may be fabricated. Several of them are compared to explore how large a role the fabrication process plays in the final resulting optical and electrical properties of the network. In order to obtain a transparent silver nanowire electrode with optimal properties one can play with several parameters such as the morphology of the metallic nanowires (NW), the density of the NW network and the use of post-processing such as mechanical pressing[2,3], chemical treatments[4] and thermal annealing[2,5]. Within the scope of this work the influence of wire morphology, density and annealing on the physical properties of silver nanowire networks are explored.

4.2 Experimental section

For the previous three chapters the discussion has been focused on the simulation of AgNW networks using virtual wires. At this point in the thesis it is important to highlight some of the distinctions between the theoretical work and the experimental work. In the computer simulations performed in chapter 3 the AgNWs are assumed to be widthless sticks, in the experimental chapters 4 and 5 of this work there were several different types of silver nanowires used. The AgNWs (Ag115, Ag60 and Ag25 in isopropanol) were purchased from SeaShell Technology.[46] These wires have an average length varying between 6-37.5µm and average widths ranging between 25 nm and 105 nm.

These nanowires were obtained from the polyol process[18,47,48] for which NWs are grown in solution and are stabilized by polyvinylpyrrolidone (PVP). The stock solution was then diluted with isopropyl alcohol (IPA) to various concentrations allowing control of the network density of the deposited wires.

Deposition was performed at room temperature by spin-coating at 1500 rpm as follows: 1 mL of solution was introduced onto the rotating substrate (25 mm x 25 mm Corning 1737 glass slide) in a drop-wise manner of two stages (0.5 mL each) with a 30sec pause between each deposition. The sample was

maintained at a constant rotation throughout the deposition. This produces random networks of AgNWs on glass substrates.

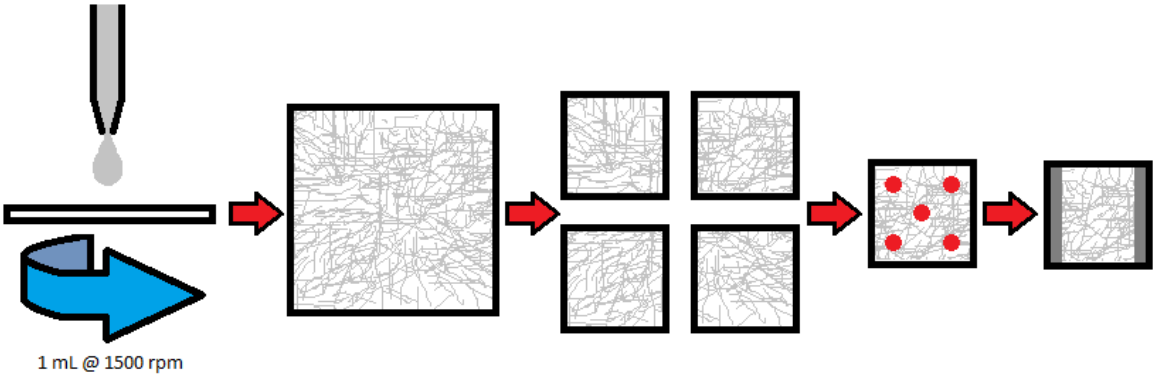

Figure 4.1 Sample preparation for the spin coated samples discussed in this thesis.

Square specimens of 12 mm x 12 mm were cut from the larger substrates and observations of the AgNWs were performed using a field-emission scanning electron microscopy (FESEM) ZEISS Ultra Plus microscope using an accelerating voltage of 10 kV. The density was determined by taking 2 SEM images at 4000x magnification close to each of the sites marked in red in Figure 4.1. Resulting in a total of 10 SEM images for a 12 mm x 12 mm sample, these images were then analysed using the software ImageJ to determine the total area covered by the AgNWs in each of the images. From the total covered area and the average nanowire dimensions an estimation of the total mass of silver per unit area of the sample was made. Measurement of the sheet resistance of these networks was performed using a 4 point probe and for the thermal studies discussed in chapter 5 Ag paint electrodes were deposited on two opposing edges of the sample for *in-situ* measurement of the electrical resistance of the AgNW network during thermal annealing.

This was performed with a two-point probe system where the electrical resistance was recorded using a Keithley sourcemeter (model 2400). Temperature was PID-controlled and recorded via two thermocouples mounted inside the heating stage and on the surface on which the sample rests, respectively. Any annealing or pre-annealing was performed in air unless otherwise stated.

4.3 Electrical and Optical Properties

Of the properties that are desirable for Transparent Conductive Materials (TCMs), the obvious selection criteria are the transmission of light and the electrical resistance. Considering this, it is appropriate to make an initial comparison of silver nanowire networks electro-optical properties with those of TCOs. Figure 4.2 shows a comparison of the transmission spectra for bare glass, a silver nanowire network on glass and Fluorine doped Tin Oxide (FTO) on glass.

The substrate used for all optical measurements was 1.1mm thick corning C1737-S111 Boroalumino-silicate glass microscope slides. Figure 4.2 illustrates the significant differences in the transmission spectrum of silver nanowire when compared to standard TCOs. They both have very similar transmission values from 250-1250 nm at which point a significantly higher rate of transmission is observed for the silver nanowire network in the region 1250–2500 nm. This stems from the plasmon absorption of TCOs: above a certain wavelength λ_P (which depends upon the carrier density) the electromagnetic wave is damped thanks to the collective excitation of the carrier gas.[6] Increasing the carrier density (by doping) in most TCOs results in a decrease of λ_P leading to a trade off in transparency to gain conductivity. This again illustrates the need to determine an optimal carrier concentration which balances conductivity and transmission. This provides an immediate advantage for silver nanowire networks integration for solar cells employing low band gap active regions or tandem cell architecture.[7] As the infra-red component of the solar spectrum can be transmitted into the cell it can be used for energy production. The origin of the absorbance of the TCO is a result of the material being a continuous thin film. Unlike TCOs which absorb light for $\lambda > \lambda_P$ the nanowire networks provide a large amount of empty space between wires that allow light to pass between the wires without being absorbed.

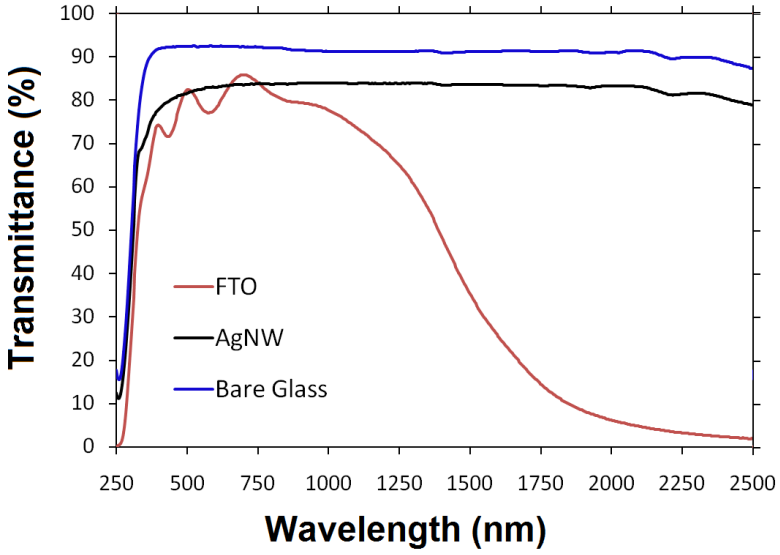

Figure 4.2 Total transmission spectra of a glass substrate (blue), a silver nanowire network (black) and fluorine-doped tin oxide (FTO) (red). The associated sheet electrical resistance for silver nanowire network and FTO are 9.5 Ω/sq, and 7.4 Ω/sq, respectively.

The slightly higher average transmittance of the silver nanowire film in the 250-1250 nm range indicates that silver nanowires provide a promising alternative to some TCOs in terms of electro-optical properties. Furthermore, recent studies have shown that increasing the Haze factor(as defined in chapter 1 as the ratio of diffuse light to total transmitted light) of a given transparent electrode can help to improve the efficiency of a solar cell.[8] Light scattering increases the path length of light through the absorber layer of a solar cell and consequently increases the current generated in the solar cell.[9] The Haze factor

of a silver nanowire network is dependent upon several key factors: length and diameter of the wires used, network density and fabrication method. It is possible to achieve a significant increase in the haze factor with only a small trade-off in optical transmission. As shown in Figure 4.3 it is possible to achieve a 3-fold increase (from ~10% to ~30%) in the average Haze factor and only takes 2-3% from the optical transmission. This trade-off is also balanced to a certain extent in that the electrical resistance of electrode B is 9.5 Ω/sq as compared to 17.3 Ω/sq for electrode A.

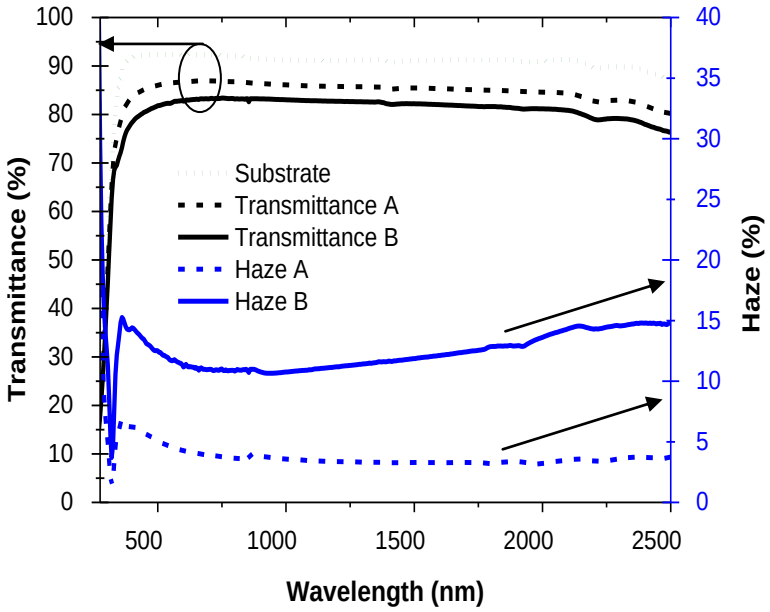

Figure 4.3 Transmittance spectra (upper curves, dotted line is the bare glass substrate, dashed and solid lines are silver nanowire networks of different density: A) 57mg/m² and B) 117mg/m²) and the related haze spectra of the same samples (lower curves). Nanowire average length was 37.5 μm and average diameter was 105 nm

As stated, the haze factor of a silver nanowire network is determined by NW density amongst other properties of the network. Intuitively, it would seem that decreasing the NW density per unit area, n, should lead to higher optical transparency. It is by no means a direct relationship, as complex scattering and graduated refractive indices convolute the relationship of density to transmission.[10] In a simple model though, it is possible to calculate the approximate transmission and this follows to some extent the intuitive idea, decreasing density results in higher optical transparency.

However, the electrical resistance of the NW networks is also density-dependent. Again the trade-off emerges with a three way balance that needs to be struck to produce the optimal network. The relationship of the network resistance to NW density can be defined as a percolation problem. Several works in the past have devoted effort to understanding the problem of 2D conductive

stick percolation. As discussed in Chapter 2 Pike and Seager[11] and Li and Zhang[12] produced some excellent theoretical results that defined the problem in its infancy and have led to further understanding. The theoretical aspects of this current work have also aimed to build a more accurate estimation of the required critical densities for realistic systems. Application of percolation theory so far has mainly been restricted to theoretical works and it is a good opportunity here to observe whether the theory supports the experimental data for silver nanowire networks. Coleman's group has already applied percolation theory to Transmission data.[13] We incorporate these results and focus below more on the electrical properties.

4.4 Impact of network density on the electrical properties

The electrical properties of silver nanowire networks are dominated by the wire geometry, density and post-processing. For the sake of reproducibility all electro-optical properties that are discussed in this chapter were measured on silver nanowire networks after a thermal annealing step which was found to significantly decrease the resistance without having an impact on their transmittance. This post-processing step was identified by an in-depth study into the impact of thermal annealing on silver nanowire networks which is discussed in chapter 5. The changes of resistance are due to several factors that will not be discussed in depth here but in majority are caused by local sintering at the junctions between the nanowires (as shown by Figure 4.4). The local sintering occurs as a result of atomic migration to reduce the surface energy at points of high curvature. Figure 4.4 exhibits Scanning Electron Microscopy observation of two different junctions between two nanowires before and after annealing for two hours at 200°C in air. Although this is not the same junction before and after annealing these images represent typical morphologies. Local sintering at the junction is present after annealing, which leads to a decrease of sheet electrical resistance from 1000 Ω/sq to 8 Ω/sq.

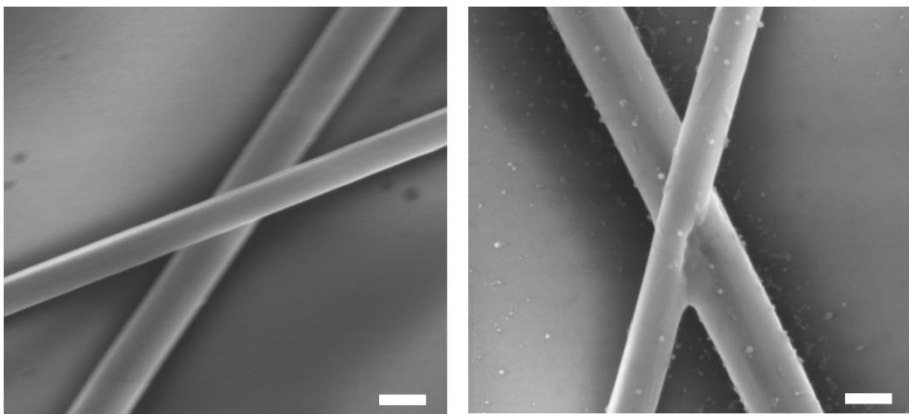

Figure 4.4 SEM images of silver nanowire junctions before (left) and after (right) annealing, the sheet resistance of this network reduced from 1000 Ω/sq to 8 Ω/sq. Scale bars indicate 100 nm.

The reduction of resistance via thermal annealing allows the production of highly conductive layers. Modifying the annealing profile enables networks with R_s<20 Ω/sq to be created with 2 minutes at 250°C or if there is a temperature restriction the same can be achieved with a longer annealing at lower temperatures. At 200°C the network resistance continues to drop for 2 hours though the majority of the change occurs in the first 5 minutes.

The resistance and transmittance of silver nanowire networks are dependent on the wire length and diameter as well as the density of the network.[14] The nanowire diameter plays a key role in the optical scattering properties of the network as highlighted by Preston et al.[10]

It is common to plot the Transmittance as a function of sheet resistance[15]. Figure 4.5 shows that the general behaviour of transmittance is not drastically dependent upon the deposition method.

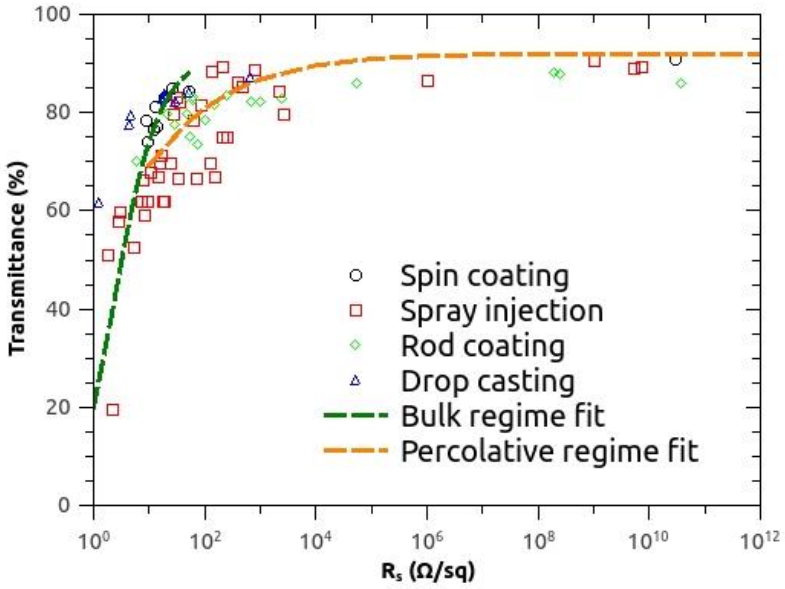

Figure 4.5 a) Optical transmittance at 550 nm (including the substrate contribution) versus the sheet resistance after annealing, for different deposition techniques: spin coating, rod coating, drop casting and spray injection. The green line represent fits to the bulk regime while the red line represent fits to the percolative regime (see chapter 2 and De et al. [15] for more details on the equations used).

A comparison of silver nanowire networks, silver flakes, carbon nanotubes and graphene was also made by De et al.[15] Their results concern NW networks created by vacuum filtration of a colloidal solution of silver nanowire onto a membrane to form the network, which is then transferred to a PET substrate. The experimental results of the current contribution are presented in Figure 4.5 for silver nanowire networks generated by the various techniques mentioned in the legend of the figure. The comparison of these results with those of De et al.[15] suggests that there is a dependence of electro-optical properties of silver nanowire networks on the deposition method used. The majority of the behaviour is dominated by the geometry of the wires. In strong agreement with

the work of De et al.[15], the data fits well in both regimes: the percolation regime for sparse networks and bulk regime for dense networks. As discussed below an optimal density has to be considered to reach a trade-off in order to get high optical transmittance T and low sheet resistance R_S. Generally speaking a good quality transparent electrode for solar applications corresponds roughly to: T ≈ 90% and R_S ≈10 Ω/sq. When considering the substrate contribution, as in Figure 4.5, such requirements would lead to T ≈ 80%. As depicted by Figure 4.5, silver nanowires already meet the requirements for being an efficient transparent electrode for solar cells applications.

Upon further research into the different network fabrication methods we determined that the spray injection method which used an ultra-sonication bath to separate the nanowires in solution before spraying them was causing the nanowires to break apart. This caused reduction of the optical properties for the spray injection data. This process is called sonic scission and is a process that leads to the cutting of long particles into smaller ones by the strain induced from cavitation bubbles. The mechanism for this process was described thoroughly for scission of carbon nanotubes by Hennrich et al.[16] and sonic scission has since been employed by Sorel et al.[14] to study the impact of wire length on percolation. After some optimization of the spin coating process we were able to obtain reproducible and uniform films with good electro-optical properties. A comparison of the same nanowire solution deposited by spin coating and spray injection after sonication is shown in Figure 4.6.

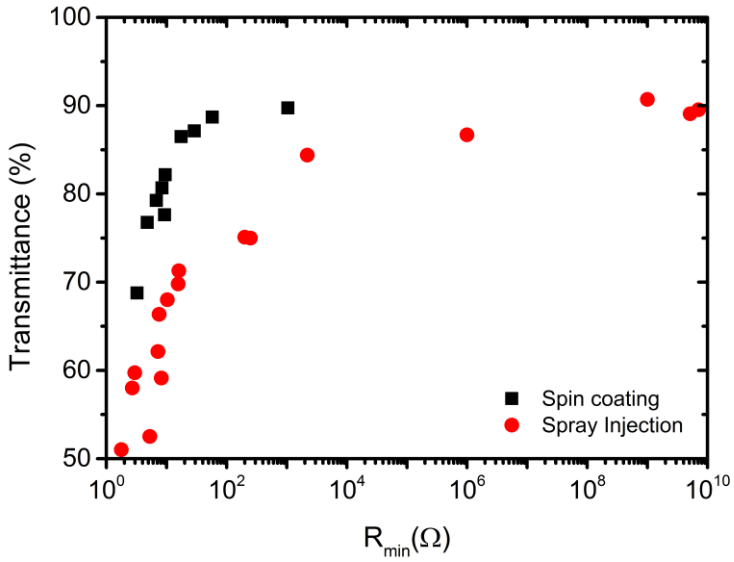

Figure 4.6 Comparison of two different network fabrication techniques. There is a dependence of network properties on fabrication method, in this case due to modification of the wire length by ultrasonic treatment during the deposition process.

This demonstrates the importance of handling procedures for silver nanowires in solution as sonication leads to detrimental impact on the electro-optical properties of the networks when fabricated. In practice we have observed some radial alignment of nanowires as a result of the spin coating which, as described in chapter 3, should also result in sub-optimal optical and electrical

properties, however this method is clearly superior to the ultrasonic spray injection process. Isotropic nanowire networks generated by spray deposition without using ultrasonic treatment are however expected to produce even better results.

From both Figure 4.5 and Figure 4.6 it is clear that the optical and electrical properties are interrelated, this relationship is tied together by the density of the nanowires in the network. For a given nanowire type (i.e. length and diameter) reducing the number of NWs per unit area creates a sparser network that may fail to form enough conducting paths across the network. At low density in the percolation regime, the properties of the network differ from the bulk material values. In this percolating regime the electrical resistivity ρ_{dc} depends on the nanowire density n and the critical density n_c following the power scaling law:

$$\rho_{dc} \propto (n - n_C)^{-t} \qquad (3.1)$$

Where n_c is the percolation threshold and t is the universal conductivity exponent (equal to 1.33) [17,18] equation 3.1 is valid when n is larger, but close, to n_c. The percolation threshold of a system can be defined by the density of the sticks at which there is a 50% chance that a network with that density will have a percolating cluster that spans the network. For large systems with nanowires of length l, it has been found that the critical number density n_c can be defined as:[12]

$$n_c = \frac{5.63726 \pm 0.00002}{l^2} \qquad (3.2)$$

Equation 2 clearly states that longer nanowires are associated with a lower percolation threshold density. Hence it is anticipated that at a given nanowire density longer wires will have better electrical (lower resistance due to the decrease of n_c) and optical properties (higher transmission). This is in agreement with the electrical behaviour observed in Figure 4.6, the nanowires used for both deposition methods had identical diameter distributions however the spray injection process reduced the average nanowire length. Thus we can see the dependence of the electro-optical properties on the nanowire length. This was further confirmed experimentally by spin coating solutions of nanowires grown with different lengths as shown in Figure 4.7. However the diameters of these as grown wires also differ.

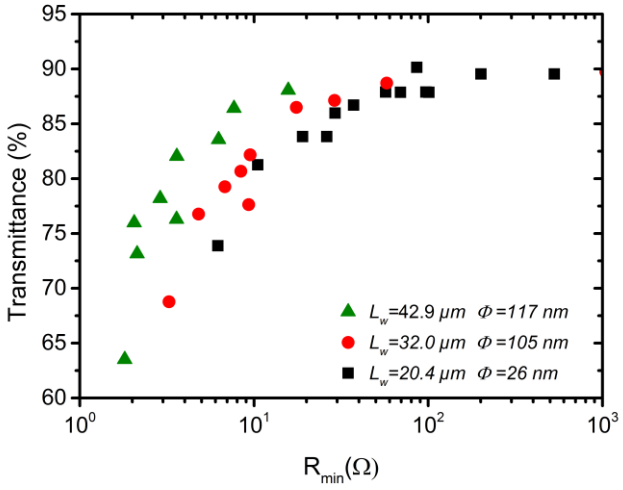

Figure 4.7 Electrical and optical properties of three different wire types. As the wire length increases so does the optical transmission at a given resistance.

However equation3.2 is only valid in the consideration of large scale systems, while for the purpose of photovoltaics and many other applications this requirement is not always met. This description of n_c is only accurate for large systems where the ratio of the system size to nanowires length is greater than 30.[12] In the network shown in Figure 4.8a) and b) it is clear that there are some regions of the network which will not contribute to the conduction pathway or in a solar cell to the collection of photo generated electrons. As discussed in chapter 3, this will result in reduced collection efficiency for nanowire-based electrodes.

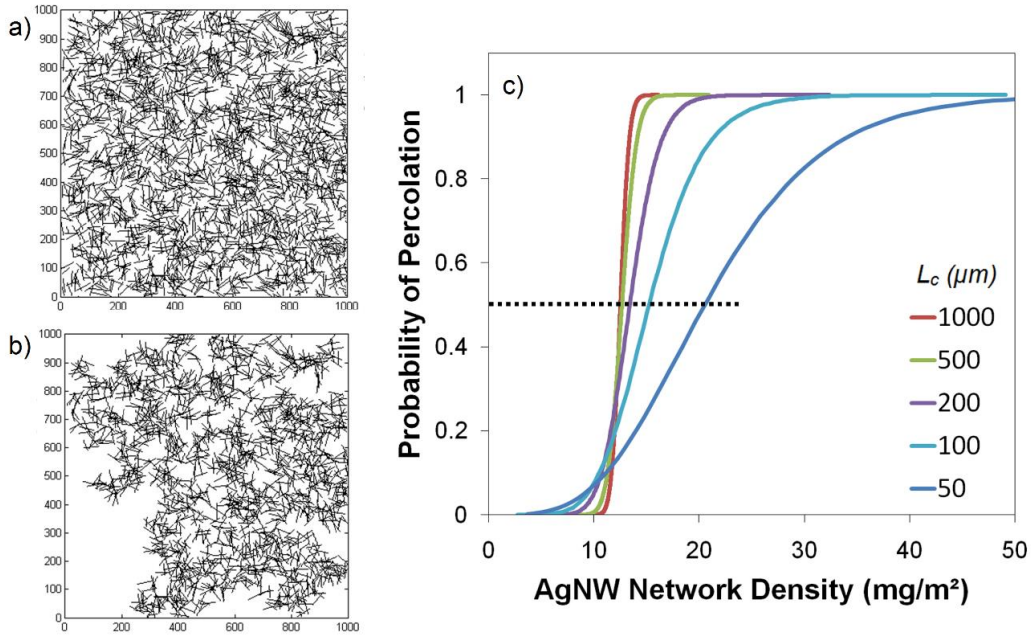

Figure 4.8 a) Simulated image of the 1000x1000 μm² network, b) same network with wires that are not part of the percolating cluster removed, c) Graph showing the probability of percolation versus the silver nanowire network density for various characteristic lengths of percolation (L_C). Decreasing the length of percolation results in an increase in the density required to reach the percolation threshold.

In order to determine the density required to produce a network which has a higher percentage of the network contributing to the percolating cluster a characteristic length can be defined. This definition allows one to define an experimental critical density required to achieve percolation at the desired critical length. Defining this length L_c as the minimum distance over which the probability of percolation at the given density n_c is equal to 50% we can then simulate the required densities for various values of L_c. Figure 4.8c) is a result of Monte Carlo simulations performed using the fast Monte Carlo method of Newman and Ziff [19] and displays the effect of decreasing L_c which corresponds to an increase in n_c. This result is rather intuitive since a high collection efficiency should be associated to percolation clusters occurring on a shorter scale which is associated with a higher silver nanowire network density.

For exploring the influence of the network density one should investigate the dependence of both the electrical resistance and optical transparency (usually considered at a wavelength of 550 nm). The electrical resistance of silver nanowire networks versus density is reported in Figure 4.9.

The vertical dotted line indicates the value of n_c as defined in equation 3.2. The electrical resistance corresponds to the minimum electrical resistance measured in-situ during a thermal annealing with a ramp of 15 K/min. As discussed above, thermal annealing causes a decrease of the resistance, by reducing the junction resistance between adjacent nanowires. However longer annealing or annealing at higher temperature can cause a morphological change of the silver nanowires (eventually leading to spheroidization) which prevents the network from percolating. Therefore a minimum of sheet resistance is observed during a thermal annealing ramp.

The dark blue line in Figure 4.9 corresponds to a fit using both equations 3.1 and 3.2 which consider percolation over an infinite size system. A good agreement is observed, showing that the percolation regime is valid for the whole network density range investigated. As already mentioned, any experimental values are certainly not necessarily associated with infinite size system but with finite system size over which the percolation is observed. Experimentally we observe the percolation and electrical behaviour in effectively infinite systems ($L_s >> L_w$ so much so that the electrical behaviour is close to that of the infinite system), it is expected therefore that the electrical behaviour will match that of the theoretical infinite system. In fact as shown in Figure 4.9 a finite value of L_c=50µm constitutes a better agreement with experimental data. This does not suggest that the critical density is in some way restricted in these experiments, but indicates that the network density is in fact sufficiently dense as to provide percolation to a large proportion of the network.

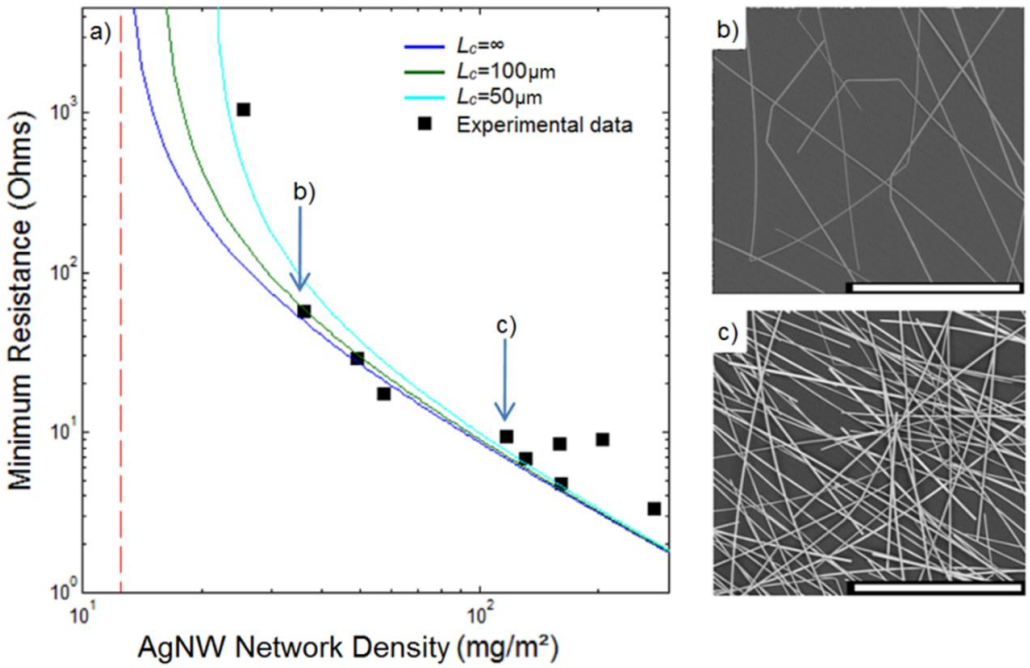

Figure 4.9 a) Experimental resistance values as a function of network density. The blue line on the graph represents a curve fitted to the data using equations3.1 and 3.2, associated to an infinite system. The other curves are associated with two different L_c values (L_c=100 µm and 50 µm). SEM images exhibit a sparse network (b) and a denser one (c) (the areal mass density being ~15.7mg/m² and ~108.7mg/m², respectively. The scale bars represent 10 µm.

The optical transmittance can also be investigated versus the nanowire density and the Lambert-Beer law is usually employed as a first approximation [15]. The data of the present study is in good agreement with this approach and is used to simulate the properties of the silver nanowire networks when calculating the figure of merit of the obtained transparent electrode.

A commonly used figure-of-merit for transparent electrodes is ϕ_H defined by Haacke [20]:

$$\Phi_H = \frac{T^{10}}{R_{sh}} \qquad (3.3)$$

where T is the optical transmittance and R_{sh} is the electrical sheet resistance. The experimental values of ϕ_H are reported in Figure 4.10. An optimal density is observed close to a NW mass density of 120 mg/m² which is associated to a sheet resistance of 9.5 Ω/sq and a total transmittance of 82.9% without removing the losses due to the substrate. Subtraction of the substrate leads to a total transmittance of about 90%. The dotted line of Figure 4.10 corresponds to the calculated figure-of-merit values using equations 3.1, 3.2 and 3.3 as well as the Lambert-Beer law. A reasonable agreement is obtained between the calculated and experimental values, especially considering the simplicity of the model used. This clearly indicates that the optimal silver nanowire density which is considered as the trade-off between high optical transparency and low electrical resistance is close to about 100 mg/m². This would correspond to the same amount of silver (for a given area) as a thin silver film of 10 nm thick as

compared to 200-300 nm for usual TCOs. The observed optimal silver nanowire network density observed in Figure 4.10 is in rather good agreement with the results obtained by De et al.[13] who found optimal performances for a density of 47 mg/m² for a different silver nanowire morphology and using vacuum filtration to fabricate the network. Finally the value ϕ_H obtained ($16x10^{-3}$) is comparable to most TCOs except for the best ITO thin films.[6]

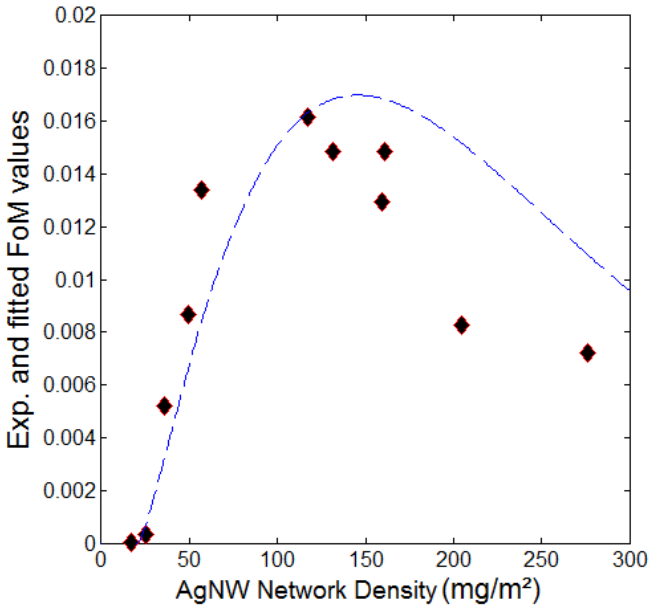

Figure 4.10 Experimental (symbols) and calculated (dotted line) values of the Haacke figure of merit defined by equation 3.3 versus the silver nanowire network density.

4.5 Impact of wire diameter

Thus far the discussion of the electrical properties of silver nanowire networks has only considered the impact of wire length. In general for large aspect ratio wires this assumption that the nanowires diameter does not play a major role in the formation of the percolating cluster is valid. In the case of nanowire network conductivity the role of the diameter is slightly more subtle than the impact of the wire length, for large diameters (>100nm) the influence of the diameter on the electrical properties of the network is negligible, for small diameters, however, the impact is quite significant. This is illustrated in Figure 4.11, in which the electrical properties of several different wire geometries have been normalized to remove the impact of the wire length by plotting the minimum resistance against the wire density minus the critical density for the given wire geometry. If the electrical properties of the network are independent of wire diameter then this plot should result in all 6 data sets overlapping the same line.

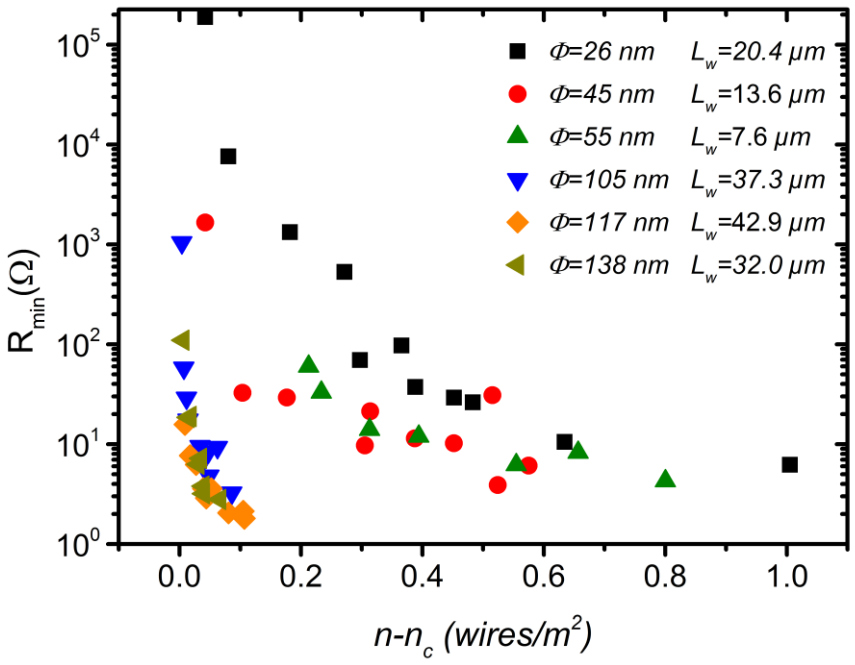

Figure 4.11 Resistance of nanowire networks fabricated from several different types of nanowires plotted against n-n_c. Traditionally electrical properties are associated solely with the relative density as determined by equation 1 and 2. This implies that if the network density of a given nanowire network is the same amount larger than the critical density as another network then both networks should have similar electrical properties. This is observed for all curves with wire diameters >100 nm, however this is not the case for nanowires with small diameters.

As seen in Figure 4.11 this is not the case and at low wire diameters the resistance of the nanowire networks increases significantly above that of the larger diameter networks. This is indicative of a strong dependence of the electrical properties on the wire diameter. Interestingly this phenomenon is not observed for the larger wire diameters. This provides a clue as to the origin of this effect. As the wire diameter approaches the mean fre path of electrons in the nanowire the wire diameter becomes increasingly important for the electrical properties of the system. This is an example of the properties of a material changing at the nanoscale, in this case the resistivity of the individual wires is increasing significantly as the wire diameter decreases. This phenomena was first described theoretically and compared to experimental results from mercury wires by Dingle[21] and further developed by Chambers[22] in 1950, since then it has also been reported for individual silver nanowires by Bid et al.[23] The origin of this effect is due to an increased influence of surface scattering of the electrons as the wire diameter decreases. As the diameter approaches the mean free path of electrons in the material the probability of electrons scattering at the surface increases dramatically. The equation that describes the relationship of the wire resistivity to the wire diameter as given by Bid is:

$$\rho_w = \rho_0 + \frac{\rho_0 \lambda_0 (1 - s)}{d} \qquad (3.4)$$

Where ρ_0 is the bulk resistivity ($1.59 \times 10^{-8}\ \Omega m^{-1}$ for silver), λ_0 is the bulk mean free path (30-40 nm at room temperature), s is the specularity which indicates the fraction of electrons which experience specular reflection at the surface of the wire and d is the wire diameter. Typical values for s in the literature range between 0.3 and 0.5, the value observed for silver nanowires by Bid et al. was 0.5. Assuming a similar specular reflection for the silver nanowires employed here equation 3 becomes:

$$\rho_w = \rho_0 \left(1 + \frac{\lambda_0}{2d}\right) \quad (3.5)$$

This phenomenon provides some explanation for the behaviour observed in Figure 4.11 however the observed deviation is much higher than surface scattering alone predicts. As for the nanowires used in these experiments ρ_w has the range $1.1\rho_0 < \rho_w < 1.7\rho_0$ one would assume that the value of R_{min} would not vary by more than a factor of 2 from the normalised curves of large diameter wires. In Figure 4.11 however the value of R_{min} is seen to vary by several orders of magnitude. The source of this discrepancy is likely the increased significance of grain boundaries and point defects in small nanowires, as the conduction pathway is constricted the likelihood of scattering from these sites is increased.

4.6 Potential for incorporation into solar cells

Many groups have already started to incorporate silver nanowires as front electrodes for solar applications.[24–27] As mentioned, high haze factors result in light scattering into the device and increases the effective absorption cross section. The ability of silver nanowire networks to produce high haze networks while maintaining sufficient electro-optical properties shows the real potential to integrate them into solar cells. Gaynor et al.[26] demonstrated an increase of approximately 10% in conversion efficiency of bulk organic hetero-junction solar cells, by using a silver nanowire composite electrode as compared to an ITO standard (η=3.4% using ITO on plastic and η=3.8% for Ag nanowire composite). Taking advantage of the metallic nanowire network transparency in the infra-red region of the spectrum Chen et al. [25] created polymer solar cells that were semi-transparent in the visible region and had an $\eta \approx 4\%$. These cells have an average transmission of about 61% in the 450-650 nm wavelength range.[25] This type of solar cell could for instance be used as an energy producing window tinting. Another advantage of silver nanowire networks as front electrodes for photovoltaic applications is that they allow production of flexible solar cells,[24] which is difficult to achieve with TCOs due to their brittleness. Within the field of photovoltaics there are many different device architectures which have restrictions associated with them, for some such as Dye Sensitized Solar Cells and CdTe, the transparent electrode must be deposited first with high temperature processes to follow for example TiO_2 dye sensitized solar cells require annealing at 450°C,[28,29] CdTe layers are deposited at 360°C and annealed at 420°C.[30,31] CIGS solar cells on the other hand generally require that the TCM is added last and has to be deposited at low temperature to prevent diffusion of the active

layers into one another. Depending in which application the silver nanowire electrodes are to be employed the processing steps required will differ. Kim et al. [32] demonstrated the incorporation of ZnO/silver nanowire/ZnO multilayer electrode into CIGS solar cells and also demonstrated that ZnO encapsulation improves the thermal stability of silver nanowires. Improved thermal stability by encapsulation has also been shown by several other groups,[33,34] and there are several low temperature routes to highly conductive silver nanowire networks,[2–4,35]hence there are many options to support the application of silver nanowires to a broad variety of solar cell architectures.

In considering the incorporation of silver nanowire networks into solar cells we must also consider the fact that the network presents a discontinuous film. This means that as a function of position relative to the network the probability of a photo-generated electron being collected will vary. This is especially important when considering the mobility of electrons in the active region of the cell. For cells where electrons and excitons can support a long diffusion length to the collecting electrode, silver nanowire networks provide an interesting and viable solution as a front electrode. When the diffusion length is below 1μm such as in organic solar cells, silver nanowire networks alone are insufficient. However, as shown by Kim *et al.* the incorporation of silver nanowire network embedded in a conductive matrix can aid in the collection efficiency.[32] In this case the silver nanowire network is used to provide the majority of the electrical performance of the electrode and the matrix material allows continuous conductivity. In this manner, materials which have a low mobility such as PEDOT:PSS may be enhanced.

Let us also note that roughness can be an issue: if some nanowires are not well aligned along the substrate some short-circuits may occur. The use of high mechanical pressure has been shown to overcome such problems.[3] As a final remark it is worth mentioning that embedding silver nanowires within a transparent oxide such as ZnO or TiO_2 could be interesting, for instance the silver nanowires stability (either chemical or thermal) could be improved and properties such as work function could be tuned. This might help as well with the integration of silver nanowires into a solar cell, since band alignment plays a crucial role for the solar cell efficiency. Some preliminary work in this regard was undertaken within this thesis, several different deposition methods such as hydrothermal growth (ZnO), Sol gel (TiO_2) and Chemical Solution Deposition (CSD) (Al:ZnO and Nb:TiO_2) were attempted with mixed results. The hydrothermal growth method for intrinsic ZnO appeared quite promising initially with apparent thermal stabilization to 540°C however it was difficult to reproduce the results. For the use of CSD method several different precursor solutions were tried with the most promising results coming for a butoxyethanol solution with zinc acetate dehydrate, aluminium nitrate nonahydrate and ethanolamine[36], these films provided excellent conductivity and optical properties but did not significantly improve the thermal stability of the nanowires. Further research is required to determine if these types of coatings can enhance chemical stability and the lifetimes of electrodes. One of the major advantages of an oxide-coated silver nanowire network over the standard

electrode is substrate adhesion. The bare nanowire network is completely destroyed by a scotch tape test, however with a 50 nm layer of Al:ZnO deposited on the network by CSD the electrical resistance of the composite electrode does not change after several attempts with the scotch tape test. The Nb:TiO_2 CSD coatings were considerably more problematic as the organic precursors used for the CSD were completely removed only after annealing at 720°C in air. This generally resulted in degradation of the silver nanowire network and loss of conductivity. If the electrodes were annealed in forming gas at 720°C it was possible to maintain the wire network morphology due to the surface stabilization of the polyvinylpyrrolidone as discussed in the following chapter, however the other organics also remained and resulted in a black semi-transparent film. Sol gel growth of TiO_2 appears to successfully produce a transparent TiO_2 film on the nanowires but the resistivity of the intrinsic oxide is too high to allow conduction through the oxide to the nanowire network.

4.7 Closing Remarks

Random Ag nanowire networks demonstrate electro-optical properties better than many TCOs and close to that of ITO. Their physical properties depend both on the morphology of the metallic nanowires and the density of the network. Post-processing treatments also play an important role in the resulting electro-optical properties. Several of these treatments are currently under investigation in the literature suggesting that the gap with ITO could be bridged in the near future. The influence of wire length predicted by simulation is a valuable tool to gain insight into the electro-optical properties and predict the properties of networks from different wire geometries. This chapter has shown that the optical transmission of nanowire networks is superior to that of TCOs in the infra-red region of the spectrum and comparable or better in the optical region. We have demonstrated that, as suggested by percolation theory, longer nanowires produce lower resistances for the same optical transmission. From this work, it is clear that silver nanowire networks currently provide sufficient electro-optical properties to be incorporated into solar cells. Although not yet matching the best ITO films in terms of optimal sheet resistance and transmittance, silver nanowires provide sufficient properties and are expected to continue to improve. They are amenable to low-deposition temperatures, solution processing, flexibility and variable haze of the resulting electrode. These aspects suggest that this material could become more important in emerging applications, particularly in the field of photovoltaics.

4.8 References

[1] D. P. Langley, G. Giusti, M. Lagrange, R. Collins, C. Jiménez, Y. Bréchet, D. Bellet, *Sol. Energy Mater. Sol. Cells* **2014**, *125*, 318.
[2] L. Hu, H. S. Kim, J.-Y. Lee, P. Peumans, Y. Cui, *ACS Nano* **2010**, *4*, 2955.
[3] T. Tokuno, M. Nogi, J. Jiu, T. Sugahara, K. Suganuma, *Langmuir* **2012**, *28*, 9298.
[4] C.-H. Liu, X. Yu, *Nanoscale Res. Lett.* **2011**, *6*, 75.
[5] J.-Y. Lee, S. T. Connor, Y. Cui, P. Peumans, *Nano Lett* **2008**, *8*, 689.
[6] K. Ellmer, *Nat. Photonics* **2012**, *6*, 809.
[7] Z. M. Beiley, M. G. Christoforo, P. Gratia, A. R. Bowring, P. Eberspacher, G. Y. Margulis, C. Cabanetos, P. M. Beaujuge, A. Salleo, M. D. McGehee, *Adv. Mater.* **2013**, *25*, 7020.
[8] T. Chih-Hung, H. Sui-Ying, H. Tsung-Wei, T. Yu-Tang, C. Yan-Fang, Y. H. Jhang, L. Hsieh, W. Chung-Chih, C. Yen-Shan, C. Chieh-Wei, L. Chung-Chun, *Org. Electron.* **2011**, *12*, 2003.
[9] D. S. Hecht, L. Hu, G. Irvin, *Adv. Mater.* **2011**, *23*, 1482.
[10] C. Preston, Y. Xu, X. Han, J. N. Munday, L. Hu, *Nano Res.* **2013**, *6*, 461.
[11] G. E. Pike, C. H. Seager, *Phys. Rev. B* **1974**, *10*, 1421.
[12] J. Li, S.-L. Zhang, *Phys. Rev. E* **2009**, *80*, 040104.
[13] S. De, T. M. Higgins, P. E. Lyons, E. M. Doherty, P. N. Nirmalraj, W. J. Blau, J. J. Boland, J. N. Coleman, *ACS Nano* **2009**, *3*, 1767.
[14] S. Sorel, P. E. Lyons, S. De, J. C. Dickerson, J. N. Coleman, *Nanotechnology* **2012**, *23*, 185201.
[15] S. De, P. J. King, P. E. Lyons, U. Khan, J. N. Coleman, *ACS Nano* **2010**, *4*, 7064.
[16] F. Hennrich, R. Krupke, K. Arnold, J. A. Rojas Stütz, S. Lebedkin, T. Koch, T. Schimmel, M. M. Kappes, *J. Phys. Chem. B* **2007**, *111*, 1932.
[17] M. Žeželj, I. Stanković, *Phys. Rev. B* **2012**, *86*, 134202.
[18] D. Stauffer, A. Aharony, *Introduction to Percolation Theory, 2nd Revised Ed.*, Taylor And Francis, London, **1994**.
[19] M. E. J. Newman, R. M. Ziff, *Phys. Rev. E* **2001**, *64*, 016706.
[20] G. Haacke, *J. Appl. Phys.* **1976**, *47*, 4086.
[21] R. B. Dingle, *Proc. R. Soc. Lond. Ser. Math. Phys. Sci.* **1950**, *201*, 545.
[22] R. G. Chambers, *Proc. R. Soc. Lond. Ser. Math. Phys. Sci.* **1950**, *202*, 378.
[23] A. Bid, A. Bora, A. Raychaudhuri, *Phys. Rev. B* **2005**, *72*, DOI 10.1103/PhysRevB.72.113415.
[24] L. Yang, T. Zhang, H. Zhou, S. C. Price, B. J. Wiley, W. You, *ACS Appl Mater Interfaces* **2011**, *3*, 4075.
[25] C.-C. Chen, L. Dou, R. Zhu, C.-H. Chung, T.-B. Song, Y. B. Zheng, S. Hawks, G. Li, P. S. Weiss, Y. Yang, *ACS Nano* **2012**, *6*, 7185.
[26] W. Gaynor, J.-Y. Lee, P. Peumans, *ACS Nano* **2010**, *4*, 30.
[27] F. S. F. Morgenstern, D. Kabra, S. Massip, T. J. K. Brenner, P. E. Lyons, J. N. Coleman, R. H. Friend, *Appl. Phys. Lett.* **2011**, *4*, 183307.
[28] U. Bach, D. Lupo, P. Comte, J. E. Moser, F. Weissörtel, J. Salbeck, H. Spreitzer, M. Grätzel, *Nature* **1998**, *395*, 583.
[29] J. E. Boercker, E. Enache-Pommer, E. S. Aydil, *Nanotechnology* **2008**, *19*, 095604.
[30] G. Kartopu, A. J. Clayton, W. S. M. Brooks, S. D. Hodgson, V. Barrioz, A. Maertens, D. A. Lamb, S. J. C. Irvine, *Prog. Photovolt. Res. Appl.* **2014**, *22*, 18.
[31] V. Barrioz, S. J. C. Irvine, E. W. Jones, R. L. Rowlands, D. A. Lamb, *Thin Solid Films* **2007**, *515*, 5808.
[32] A. Kim, Y. Won, K. Woo, C.-H. Kim, J. Moon, *ACS Nano* **2013**, *7*, 1081.
[33] A. Mayoral, L. F. Allard, D. Ferrer, R. Esparza, M. Jose-Yacaman, *J Mater Chem* **2010**, *21*, 893.
[34] P. Ramasamy, D.-M. Seo, S.-H. Kim, J. Kim, *J. Mater. Chem.* **2012**, *22*, 11651.
[35] Y.-J. Noh, S.-S. Kim, T.-W. Kim, S.-I. Na, *Sol. Energy Mater. Sol. Cells* **2014**, *120, Part A*, 226.
[36] K. Schellens, B. Capon, C. De Dobbelaere, C. Detavernier, A. Hardy, M. K. Van Bael, *Thin Solid Films* **2012**, *524*, 81.

Chapter 5
Thermal Annealing of Nanowire Networks

5.1 Opening Remarks

In this chapter, we report on the study of the effects of thermal annealing on the electrical properties of AgNW networks. The main goal is to better understand their behaviour and to optimize the electrical properties of the annealed network. Since several physical mechanisms are at play, different types of annealing have been employed (isothermal, thermal ramps and pre-annealing) in order to disentangle the possible causes responsible for the variations of the electrical resistance observed *in-situ*. In addition we report the use of *in-situ* AFM to study the morphological evolution of the nanowires under thermal annealing. This chapter represents a significantly expanded version of an article which has been accepted for publication in Nanoscale.[1]

Optimizing the electrical resistance and transmission of nanowire networks involves tuning several key parameters including the experimental conditions of deposition, wire geometry,[2] network density and post-deposition treatments such as mechanical pressing,[3] light-induced plasmonic nanowelding[4] or thermal annealing.[5–7] All of these post-deposition treatments have been shown to decrease the electrical resistance. However, thermal annealing has not yet been the subject of a detailed investigation. The impact of thermal annealing on the electrical resistance of metallic NW networks is dominated by desorption of organic residues and local sintering at the junction between neighbouring nanowires,[5,7] both of which lead to a significantly lower contact resistance. This is a clear asset of metallic NW network when compared with carbon nanotubes which suffer from high junction resistance between nanotubes.[8]

Although thermal annealing can lower the electrical resistance of metallic nanowire networks, instability of the nanowires upon an excessive heating results in a critical limit of the thermal budget applied on the system, which requires investigation.[9] Cylindrical metallic nanowires are known to be energetically unstable and can fragment at temperatures significantly lower than their melting point.[10–13] This is the result of a morphological instability, called the Rayleigh instability, and is a critical issue for the long-term reliability of micro- and nano-electronic devices. These thermal instabilities place limitations on the thermal budget that an electrode may undergo during device fabrication. For example the use of AgNW electrodes in TiO_2 Dye Sensitized Solar Cells (DSSCs) is restricted due to the need to sinter the TiO_2 nanoparticle layers at 450°C.[14,15] It has been suggested recently that a second instability may also be observed due to Joule heating when metallic nanowire networks are used with current densities similar to those found in a solar cell of $\approx$10% efficiency, leading to electrode failure in a matter of days.[16] Such instabilities and the mechanisms

leading to them need to be understood to enable the efficient integration of metallic NW networks in real devices.

5.2 Electrical and morphological evolution during thermal annealing

The most direct way to probe the effect of thermal annealing on the electrical resistance of AgNWs is to measure their resistance in-situ during a thermal ramp in air. The evolution of the electrical resistance of an AgNW network versus temperature during a thermal ramp at 15°C/min in air is shown in Figure 5.1 a). The electrical resistance varies by several orders of magnitude and clearly exhibits a minimum. Several mechanisms are responsible for the observed variations in resistance as a function of temperature.

This type of annealing, with $T(t) = T_0 + \dot{T} \cdot t$, where *T(t)* is the temperature at time *t*, T_0 is the initial temperature and $\dot{T}$ is the heating rate, is classically used for the quantitative determination of the desorption activation energy.[17] At low temperatures (50-125°C) several sudden drops of resistance *R(t,T)* can be observed in Figure 5.1a and f (both within the dashed frames) and will be discussed in detail below. In Figure 5.1 b) a SEM image of an as-deposited nanowire network is displayed. It can be seen that the nanowires are coated with a carbonaceous shell which is approximately 30 nm thick. This shell is a combination of polyvinylpyrrolidone (PVP) from the nanowire synthesis[18] and organic residues. The thickness of the PVP coating is approximately 2.5 nm as shown in Figure 5.2. With the remainder of the carbonaceous shell coming from the solution based deposition process. The removal of these organic contaminants and/or residual isopropyl alcohol (IPA) decreases the electrical resistance of the contact between NWs. The reduced resistance leads to the formation of efficient conduction pathways through the network.

At higher temperatures (125-170°C) *R(t,T)* continues to decrease with increasing temperature and becomes a continuous process which resembles an exponential decay. This can be assigned to the continued desorption of organic residues and the polymer coating (PVP) from the AgNWs. Figure 5.1c exhibits a SEM image of a specimen annealed at 200 °C for 10 minutes: it is clearly visible that the majority of the carbonaceous film has been removed, however the thin film (~2.5 nm) of PVP remains on the surface. At ≈170 °C the rate of reduction in *R(t,T)* slows down as the desorption of organic components tails off due to the decreased concentration of remaining isopropanol and other organic residues. Above 200 °C local sintering begins at NW junctions, as revealed by the SEM picture shown in Figure 5.1c. The rate of sintering is slow at first due to remaining PVP, thermo gravimetric analysis revealed that there is an exothermic reaction occurring between 250 °C and 270 °C. This result is similar to that found previously by Lee et al.[19] and was assigned to the degradation of PVP. Above 270 °C sintering starts to occur at NW junctions, as revealed by the SEM picture shown in Figure 5.1c.

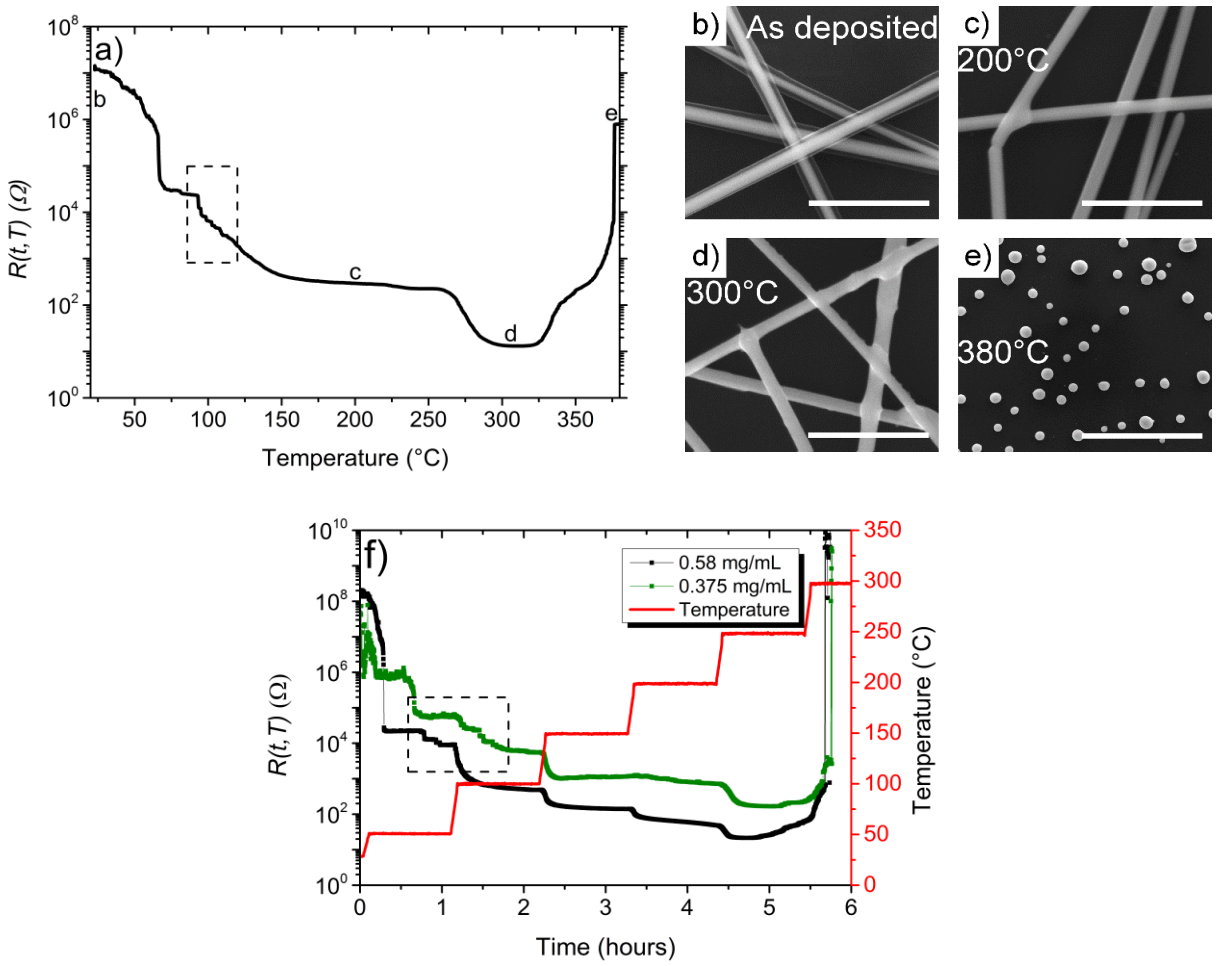

Figure 5.1 a) Evolution of the electrical resistance of a Ag nanowire network during a continuous thermal ramp of 15°C/min from room temperature (associated with deposition solution of 0.75 mg/mL and an areal mass density of ≈105 mg/m²) b-e) Scanning electron microscope (SEM) images of: b) as-deposited sample and of specimen annealed for 10 minutes at different temperatures: c) 200°C, first occurrence of observable sintering; d) 300°C all junctions are sintered; e) 380°C complete spheroidization of the network. Image e) is at a lower magnification than the others to demonstrate that although the nanowires are completely spheroidized the resultant nanoparticles are still aligned at the original position of the wires. The scale bars in images b), c) and d) are 1 µm whereas that of image e) is 4 µm. f) Resistance response of two specimens to a series of increasing isothermal anneals (associated with deposition solutions of 0.58 mg/mL and 0.375 mg/ml resulting in areal mass densities of ≈81 mg/m² and ≈53 mg/m², respectively). All data shown in Figure 5.1 were obtained using AgNW for which average wire diameter was 105 nm and average wire length was 37.3 µm. Dashed boxes in a) and f) indicate regions of the curve which are explored in more detail in section 5.3

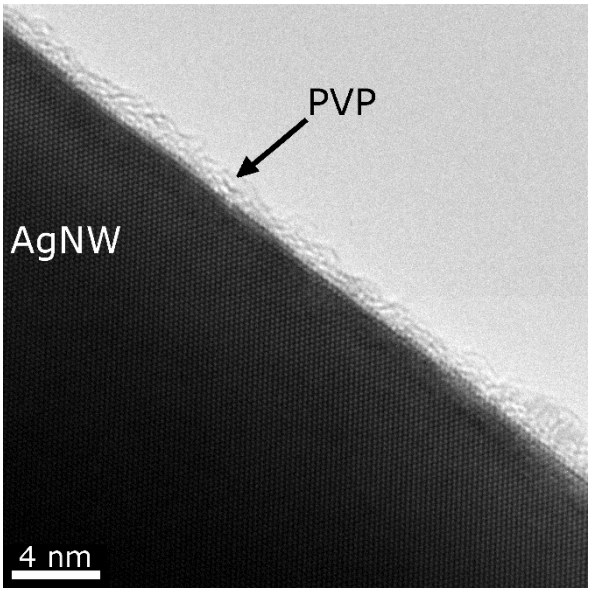

Figure 5.2 High resolution TEM image of PVP coating on silver nanowire. The crystalline nature of the nanowire can be observed.

The rate of sintering is slow at first and does not have a significant impact on the sample resistance, above 270°C sintering occurs more rapidly resulting in a continued drop in resistance. Again, this takes the form of an exponential function. For this temperature range, as the population of unsintered junctions decreases the rate of junction sintering decreases. A minimum in $R(t,T)$ is observed at about 300-320°C for the considered heating ramp (15°C/min). For higher temperatures $R(t,T)$ increases sharply. This is attributed to the onset of a morphological instability which results in spheroidization of the nanowires as observed in SEM image of Figure 5.1e.

Since the mechanisms responsible for the changes in the electrical properties for a given thermal equilibrium state and kinetic effects are intertwined, it is difficult to determine the exact temperature ranges over which the above-mentioned stages occur from the data shown in Figure 5.1a (temperature ramp). However, observation of Figure 5.1a-e leads to a general trend of the effect of temperature on silver nanowire networks electrical resistance, which can be described by three main stages:

1- Reduction: Initially the resistance drops as the residual solvents and PVP are removed from the network. A second reduction phase is observed due to the onset of local sintering at the junctions.

2- Stabilisation: As the number of unsintered junctions decreases the electrical resistance reduction rate slows down and the resistance value stabilizes briefly, this is associated with the minimum resistance.

3- Spheroidization: Morphological instabilities of the nanowires occur and the resistance increases rapidly as the NW network evolves into separated spheres and loses its percolative nature.

Experiments with in-situ monitoring of the resistance variation using a thermal ramp provide a nice overview of the thermal annealing effects. However, during a thermal ramp multiple processes may occur simultaneously as they

have not had enough time to reach completion before a second mechanism starts. One method to shed light on the thermal annealing effects is thus to consider isothermal annealing with plateaus at various temperatures, as reported in Figure 5.1f.

The same 3 stages seen in Figure 5.1a are observed for the isothermal stepped annealing process depicted in Figure 5.1f. Due to the separation of kinetics and activation temperature the mechanisms at play occur at different temperature ranges compared to the ramped annealing shown in Figure 5.1a.

Figure 5.1f also exhibits sharp drops in the specimen resistance at low temperature ($\leqslant$ 100°C) again a detailed discussion of this behaviour is provided in section 5.3. At 100°C and above, *R(t,T)* exhibits an initial rapid decrease for each temperature plateau lower than 250°C. At 250°C the resistance plateaus and for a period of several minutes remains constant before *R* increases due to the onset of the morphological instability of the AgNWs. This then gives indication of both the optimized temperature where the electrical resistance of the network can be minimized through balancing the sintering effects and thermal stability of the AgNWs. The denser network exhibits a lower electrical resistance as a result of the increased number of conduction pathways and at the expense of a lower optical transparency. The network density results in a trade-off between high optical transparency (obtained for sparse networks) and efficient electrical conductivity (associated with a high NW density).[20]

5.3 Quantized activation of Percolation

The drops of electrical resistance observed in both Figure 5.1a and f can be understood in the following way; they correspond to the creation of the first efficient pathways through the network composed of AgNW and junctions between them. The junction resistances are high before thermal annealing and decrease as a function of time when the temperature is increased, as shown by Figure 5.1a and f. For all specimens studied the resistance drops occur at a resistance of several thousands of ohms, which is of the same order of magnitude as the resistance of a long hypothetical NW crossing the whole network. This estimate is based on Ohm's law applied on an efficient percolating path (EPP) which is a cylinder of length L (in this case the width of the whole network $\approx$7 mm long), cross-sectional area S and electrical resistivity ρ. The associated electrical resistance R_{EPP} can be written as:

$$R_{EPP} = \frac{K\rho L}{S} \quad (5.1)$$

where K is a constant associated with the actual path length of the percolating path (which is longer than the network width due to the tortuous nature of percolating paths as schematically shown by Figure 5.3a, and therefore on the density of the network, as well as the electrical resistance of the junctions which act as series resistances along the conduction pathway. Therefore, K is expected to be larger than one.

The validity of using silver bulk resistivity (1.59 x10^{-8} Ωm) for nanowires of this size is questionable as the wire diameter is approaching the mean free path of electrons in bulk silver. The reduced diameter results in a significant increase in the impact of surface scattering on the resistivity of the wires. It has been demonstrated that the resistivity of nanowires is dependent on the wire diameter and increases above that of the bulk significantly.[21] In the case of AgNWs with a diameter 100nm, Bid *et al.* found the resistivity to be 2.78 x 10^{-8} Ωm.[21] Considering the NW diameter (105 nm on average), R_{EPP} is on the order of a few thousand ohms, in good agreement with the steps in resistance observed at low temperature in Figure 5.1a and f.

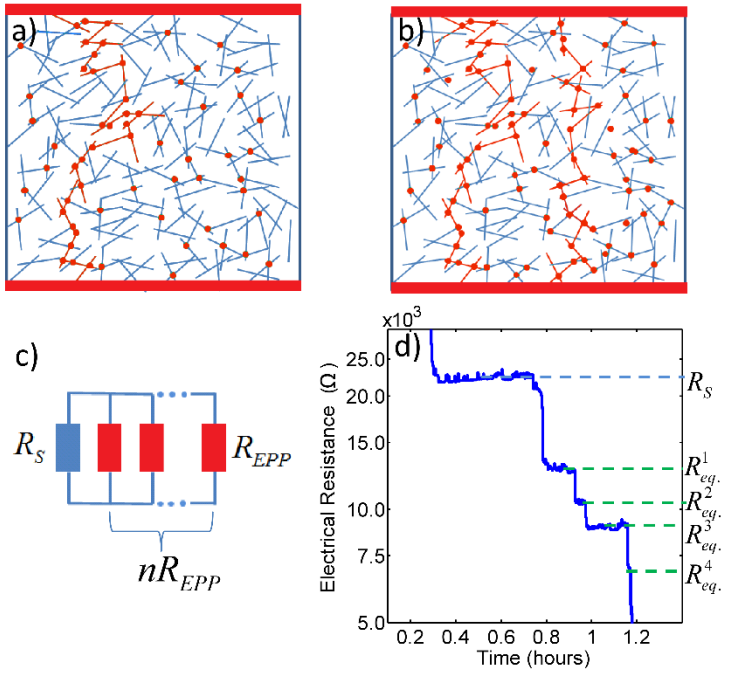

Figure 5.3 a) Schematic representation of a NW network; under thermal annealing, some of the junctions become efficient (indicated by red dots). When a sufficient number of junctions are activated, an efficient percolating pathway forms between the top and bottom electrodes. b) As heating continues, additional efficient pathways form. c) The pathways can be considered as n resistances R_{EPP} in parallel with an initial system resistance R_S. d) Experimental data exhibiting plateaus in resistance which can be assigned as equivalent resistances R^n_{eq} which are the parallel sum of R_s and n resistances R_{EPP}, where n is an integer which increases as thermal annealing proceeds.

This first efficient percolating pathway (EPP) (represented schematically in Figure 5.3a by thicker red NWs) exhibits an electrical resistance, named R_{EPP}, which should contribute in parallel to the resistance of the initial network, noted R_S. A second EPP appears slightly later, as shown in Figure 5.3b and again acts as an additional parallel resistance R_{EPP}, which leads to another drop of R as shown experimental by Figure 5.1a and f. Therefore the simplest model defines the electrical resistance R^n_{eq} of the network after the n^{th} resistance drop as the

equivalent resistance consisting of R_S in parallel with n electrical resistances R_{EPP} (as shown in Figure 5.3c, leading to the following expression:

$$\frac{1}{R_{eq}^{n}} = \frac{1}{R_S} + \frac{n}{R_{EPP}} \qquad (5.2)$$

The experimental values of R_{eq}^{n} are schematically shown on Figure 5.3d. R_S can be defined by the experimental resistance before the appearance of the first drop. R_{EPP} can be determined by equation 5.1 where all parameters are known except K which remains the only fitting parameter of the model and is kept constant for all resistance drops observed on a given specimen. The regions which exhibit steps in the resistance from Figure 5.1 a and f are enlarged and compared in Figure 5.4a and b to the R_{eq}^{n} values calculated by fitting K using equations 5.1 and 5.2 (shown as solid lines to the right of the experimental data).

Despite the simplicity of the model, the agreement between the experimental data and the calculated values is excellent. From Figure 5.4c it is clear that the resistance is described well by equation 5.2 and that the fitting parameter K for equation 5.1 can be calculated. R_s and R_{EPP} values were determined from a linear fit of the experimental data (see Figure 5.4c) according to equation 5.2. The R_s values obtained from these fits correspond well to those observed experimentally, while R_{EPP} values are larger than $\frac{\rho L}{S}$, in agreement with equation 5.1. The latter enables calculation of the K values which are 1.15, 1.31 and 1.91 for specimens associated with solution concentration of 0.75, 0.58 and 0.375 mg/mL, respectively.

In Figure 5.4d a comparison is given between experimental data and values calculated with equations 5.1 and 5.2, showing excellent agreement with a K value varying between 1.15 and 1.91 as the network density decreases. It is not surprising that the value of K increases as the density of the network decreases, as K is a proportionality factor relating to the actual length of the individual conduction pathways. In a dense network there are many more junctions per unit area and the probability of finding a direct path is much higher. As the network density decreases the path becomes more tortuous thus increasing the effective distance between electrodes, and hence the value of K.

As with all models there are simplifications that must be made, the proposed model assumes that all pathways are independent and electrically connected in parallel. In reality the system can be more complicated and partial pathways and series connections between pathways may also appear (a schematic way to imagine such a pathway is to consider a Y shape for the partial pathways and a H shape for the series connections between paths). Examples can be seen in Figure 5.4b where the plateaus indicated by blue arrows do not match a calculated data point, these plateaus might be considered as partial pathways connecting to one of the existing efficient conductive paths.

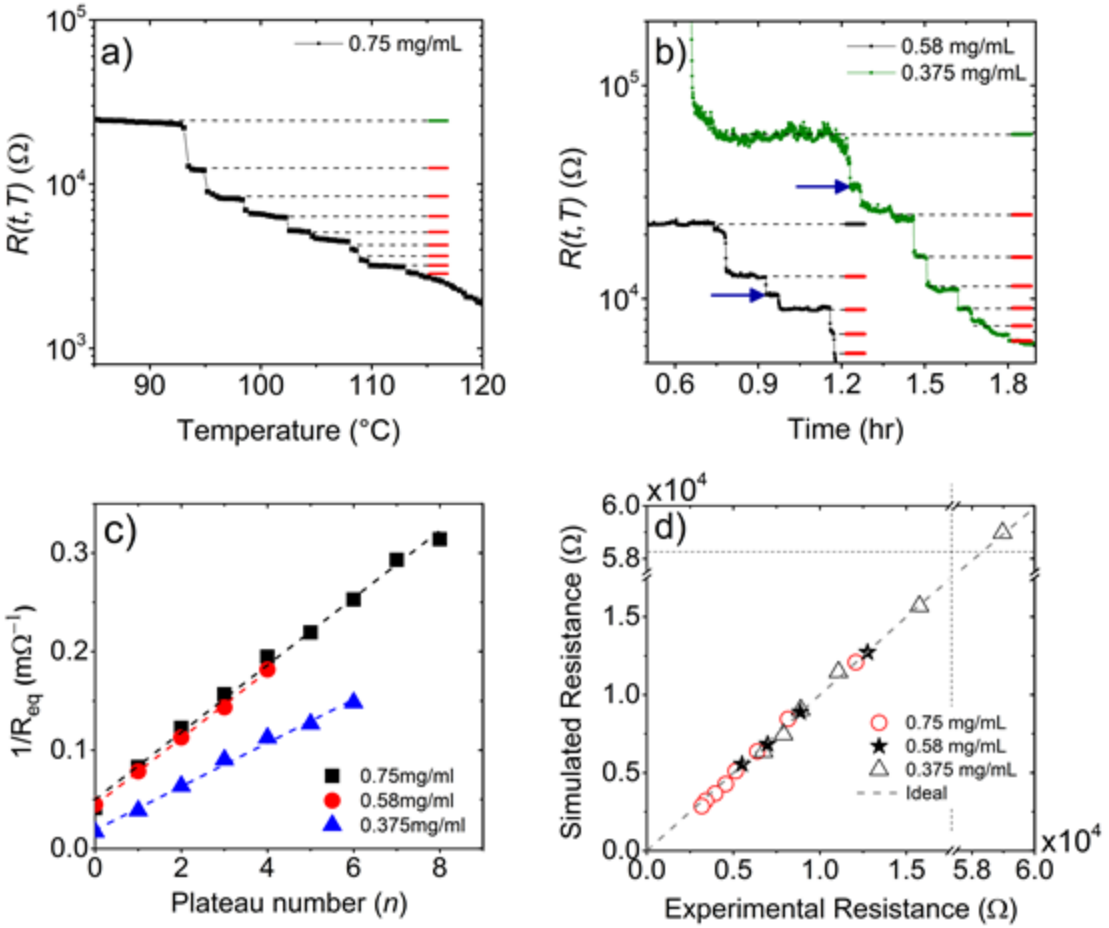

Figure 5.4 Experimental electrical resistance drops observed during thermal annealing (continuous line) for samples of different densities and comparison with the proposed model (dashed lines). Data shown in a) corresponds to the highlighted section of Figure 5.1a (i.e. during a thermal ramp) while data in b) corresponds to the highlighted section of Figure 5.1f (along a temperature plateau). Arrows in the plot indicate plateaus which were identified as partial percolating pathways. c) Plot of $\frac{1}{R_{eq}^{n}}$ as a function of plateau number n extracted from the experimental plateaus of the curves in Figure 5.4 a and b. d) Comparison of the predicted values to experimental electrical resistances, the dashed line represents a slope of one indicating a perfect correlation. The used K values were 1.15, 1.31 and 1.91 associated with deposited solution concentration of 0.75, 0.58 and 0.375 mg/mL, respectively. All of the data shown in this figure comes from nanowires with an average diameter of 105 nm and an average length of 37.5 µm

Initially when the number of efficient junctions is low the probability of observing the formation of a new EPP is low. As annealing continues more junctions are sintered and the chance to form an EPP increases. After the formation of the first efficient percolating path it is expected that the efficient junction density is sufficiently high that other pathways also begin to form in a more and more rapid succession. When plotted in the time domain (Figure 5.4b) this should be seen as the length of plateaus decreasing on average as the number of plateaus increases. However this is a statistical process, so the length of the

plateaus are somewhat random, hence the experimental variability of the plateau length. As the number of EPP increases it becomes increasingly likely that new efficient paths overlap with existing paths, thus as n increases so too does the probability of partial path formation, this results in the loss of quantized steps in the $R(t,T)$ decrease as the number of plateaus increases and a continuous drop in resistance is eventually observed (typically for values lower than 1000 Ω) for long annealing or at higher temperature.

Let us finally consider that while stick percolation is generally a density problem, in the present case the model works at a constant stick density upon which a network of junction resistances is applied which play the role of the percolation sites. Each site has a given resistance which is reduced by thermal annealing; conduction through the system will occur predominantly through low resistance junctions. These junctions represent a very large population (measured experimentally as $\approx 10^7$ cm^{-2} for a specimen with similar density to that shown in Figure 5.1a) with a large distribution of junction resistances. In the as-deposited state the majority of the junctions have a high electrical resistance. By heating, some of these junctions become more conductive. As the annealing proceeds, clusters of nanowires are connected by efficiently conducting junctions. When a large enough number of junction resistances are reduced, an efficient percolating pathway is formed spanning the network resulting in the sudden drops of the resistance reported in Figure 5.4. The sudden electrical resistance drops observed in Figure 5.4 can therefore be considered as quantized activation of percolation.

5.4 Pre-annealing

Another way of studying the effects of thermal annealing is to perform a pre-annealing at low temperature (in the present paper, a pre-annealing is considered as an isothermal anneal performed after the AgNW network fabrication and before a continuous ramp annealing). The effects of such pre-annealing on an experiment similar to the one reported in Figure 5.1 (i.e. thermal ramp) are shown on Figure 5.5. Pre-annealing was performed at 100°C, 150°C and 200°C for 8, 6 and 2 hours, respectively. The appropriate duration of each pre-anneal was determined by monitoring in situ the resistance of the network: when the resistance became stable the pre-anneal was considered to have reached completion. This allows the exploration of temperature ranges over which different mechanisms are active.

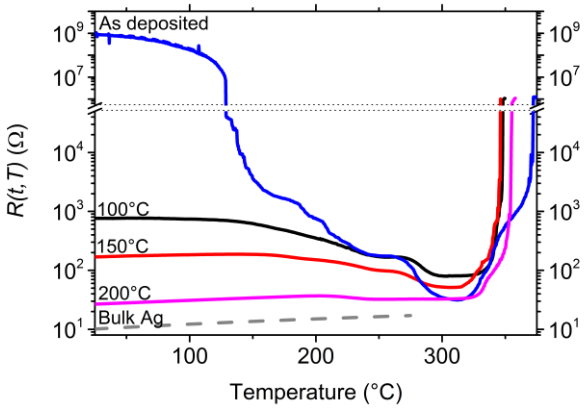

Figure 5.5 Temperature dependence of the electrical resistance *R(t,T)* of silver nanowire networks (concentration of 0.75 mg/mL) during a ramp thermal annealing of 15°C per minute for 4 different samples: as-deposited and pre-annealed at 100°C, 150°C and 200°C. The dashed curve is associated with the temperature-dependence of bulk silver resistivity, showing a good agreement between the slopes deduced from experimental data and from phonon-induced increase of bulk silver resistivity for the 200°C pre-annealed specimen up to 200°C.

The effects of the pre-annealing is drastic for the *R(t,T)* dependence in the low temperature range (i.e. below 270°C). There is a continuous effect of pre-annealing for which a higher associated temperature corresponds to a lower initial resistance for the subsequent thermal ramp. Then for the higher temperature range the *R(t,T)* behaviour remains similar for all specimens: the pre-annealing does not appear to influence the onset of the NW instability.

Note that for the pre-annealing at 200°C, the increase of the *R(t,T)* versus temperature (below 200°C) corresponds rather well to the increase of the electrical resistivity of bulk Ag associated with the scattering of electrons by the phonon population. This corresponds to the resistivity temperature dependence:

$$\rho(T_0 + \Delta T) = \rho_0(T_0).(1 + \beta.\Delta T) \qquad (5.3)$$

where β is equal to 2.8 x 10^{-3} K^{-1} for bulk silver.[22] Such dependency is shown as the dashed line in Figure 5.5: the experimental slope of the 200°C preannealed AgNW network is close to the one calculated with the bulk silver β value (although such a simple calculation does not consider the junction resistances between adjacent NWs).

The key observation of the pre-annealing study is the demonstration that annealing at 200°C until the resistance is stable produces a network with a resistance comparable to the minimum resistance obtained for samples on a thermal ramp. This demonstrates that it is possible to optimize the resistance with a controlled temperature and extended time.

5.5 Physical mechanisms at play during thermal annealing:

We discuss now the relevant physical mechanisms at play for the evolution of the networks electrical properties during thermal annealing. These mechanisms are: solvent desorption, PVP desorption, sintering at contacts between adjacent nanowires and spheroidization. The first three mechanisms act to decrease the electrical resistance of the network while the last one leads to a drastic increase of *R(t,T)*. We will discuss these four mechanisms and their impact on the experimental results presented above.

The prevailing mechanism at play at low temperature (30-140°C) is desorption. At first, physical desorption of organic residues is responsible. Organic residues in the form of a very thin shell as visible in Figure 5.1b are present between AgNWs due to capillary effects and act as electrical barriers, resulting in a high electrical resistance. The physical desorption of these residues enables a more intimate contact between NWs reducing the electrical resistance. After a pre-annealing at 100°C for 8 hours is performed, the *R(t,T)* curve exhibits a continuous behaviour (no more sudden drops are observed) and *R(t,T)* values are much smaller, indicating that there are already a large number of efficient conduction paths through the network. At 150°C the glass transition temperature of PVP is reached, the thin shell of PVP coating the AgNWs (≈5nm) begins to flow; this allows a more intimate contact between adjacent AgNWs, also decreasing the electrical resistance.

At higher temperatures (150-250°C) the PVP undergoes thermal degradation and is completely removed from the surface of the wires (at least in air while different behaviour can be observed under vacuum[23]). The reduction in *R(t,T)* observed from 200-250°C in Figure 5.1f originates from the onset of local sintering, as indicated by the SEM observations (see Figure 5.1c and d). It is important to note that for ramped annealing as shown in Figure 5.1a and Figure 5.5 this drop in *R(t,T)* due to sintering is observed at higher temperature (275-300°C).

This difference is due to the kinetics of the system. As both the experiments depicted by Figure 5.1a and Figure 5.5 are performed as thermal ramps at 15°C/min there is insufficient time for all of the PVP and organic residues to be removed in the temperature range 200-250°C, which results in a delay of the sintering. The preannealing shown in Figure 5.5 allows some separation of the kinetics and critical temperatures of various mechanisms. Comparing the *R(t,T)* of the as deposited sample to the initial resistance of the preannealed samples reveals that for each of the preanneal treatments the initial resistance corresponds closely to a plateau in the as-deposited *R(t,T)*. These plateaus result from a kinetic pinning of the onset of different mechanisms; as the samples are exposed to a thermal ramp the temperature continues to increase before each mechanism has reached completion.

By performing isothermal anneal until the resistance stabilizes at different temperatures before performing the thermal ramp we reveal what the final resistance of the network obtained is once the mechanisms activated at the given temperature reach completion. This leads to the observation that sintering

processes can reach completion at a temperature as low as 200°C if sufficient time is provided.

Sintering is the term usually used to describe the increase in mechanical strength and decrease in porosity of powder particle network when heated at a temperature approaching, but below, its melting point.[24,25] In the present study, as the sintering mechanism concerns only the contacts between adjacent NWs, this process is called local sintering. This corresponds to the initial stages of the usual sintering phenomenon in powder metallurgy. The associated driving force for sintering is the reduction of surface energy. In general the smaller the particle size the lower the temperature where sintering will be observed. For instance the investigation of the sintering effect on the morphology and conductivity of Ag particles of 40 nm in diameter showed that sintering occurred at 100°C and probably even below,[26] while the melting point of silver is 962°C.[22] In the case of AgNWs, sintering appears to be nearly complete after a pre-annealing at 200°C for 2 hours since no further $R(t,T)$ decrease is observed as shown in Figure 5.5 (as compared to the specimens pre-annealed at 150°C or below).

5.6 Spheroidization

When submitted to a thermal annealing, nanowires can fragment into a chain of nanospheres above a certain temperature.[27,28] This well-known morphological instability is often called Rayleigh or Plateau-Rayleigh instability and has been the subject of many investigations since its first study in the nineteenth century.[29,30] Due to the major role played by metallic and semi-conductor nanowires in nanoelectronics and optoelectronics,[31] the morphological Rayleigh instabilities of these materials have been investigated in the past. Studies of the role of wire diameter, temperature and annealing on the nanowire morphology evolution have already been reported.[27,28,32] The physical origin of the Rayleigh instability is also the reduction of the surface energy. If one considers a liquid cylinder with initial radius r and a sinusoidal perturbation along its axis, *i.e.*

$$r(x) = r_0(\varepsilon) + \varepsilon \cdot \sin\left(\frac{2\pi x}{\lambda}\right) \qquad (5.4)$$

simple calculations show that the perturbations with wavelength $\lambda > 2\pi r_o$ will increase spontaneously in amplitude and thus lead to a fragmentation of the initial cylinder.[33] In reality, the morphological instabilities of a solid wire are slightly more complicated but the overall trend that is experimentally observed still remains the same.[10,11,34] For instance the average distance between Ag nanoparticles in Figure 5.1e is about 750 nm, a value larger but of the same order of magnitude as $2\pi r$ (330 nm) (the difference stemming from the substrate influence, the fivefold twin structure of the wire as well coalescence which occurs after spheroidization). The Rayleigh criterion ($\lambda > 2\pi r_o$) is valid for all wire sizes, but since nanowires exhibit much higher surface to volume ratio the associated kinetics are much faster for nanowires with small diameters. The origin of this diameter-dependent kinetics stems from the dependence of the Rayleigh instability on surface diffusion. Smaller diameter wires have a higher ratio of surface to volume and a lower total volume. This means less atoms are required to move before spheroidization occurs and a higher proportion of the atoms are moving at a given time. This morphological instability leads to a loss of the percolation character of the network and hence a sharp increase of the electrical resistance at high temperature as observed in Figure 5.1 and Figure 5.5. Figure 5.6 demonstrates that the diameter of the wires is an important factor for the onset of the Rayleigh instability, as the wire diameter decreases so does the temperature of spheroidization.

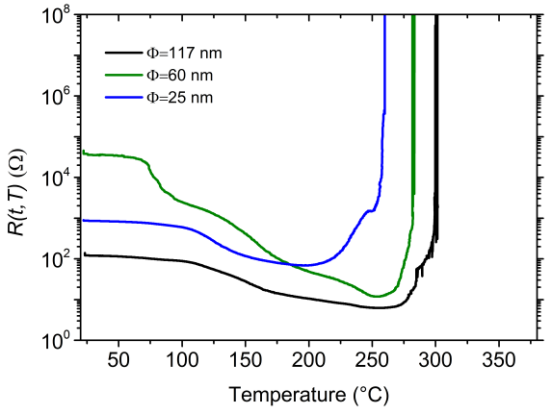

Figure 5.6 The impact of diameter on the response of AgNW networks to temperature when thermal ramps are used from room temperature at a rate of 2°C per minute. The three AgNW networks have similar areal mass density of ≈50 mg/m².

Knowing that in order to improve the electro-optical properties of AgNW networks, NWs with small diameter and large aspect ratio are often preferred,[2] underlines the significance of the Rayleigh instability which becomes more of a limitation when the NW diameter decreases. Another possibility for the increase in electrical resistance observed at high temperatures during thermal annealing is the thermal grooving of grain boundaries which will be discussed in section 5.9.

Finally a rather direct comparison can be outlined between the present work and the investigation of Chou *et al.*[26] who studied the thermal effects on the properties of a film composed of Ag nanoparticles (also surrounded by a PVP layer). In both studies, in spite of the large difference in the morphology of the Ag nanostructures, the electrical resistance of the network exhibits a minimum versus the annealing temperature. In the study of Chou and co-authors, desorption of PVP and sintering lead to a decrease of *R(t,T)* at low temperatures 50-200°C, while above 200-250°C (depending on the nanoparticle size), *R(t,T)* increased and the networks lose their conductive properties above 400°C due to the growth of both Ag particles and pores and the eventual breakdown of conduction pathways. These observations on spherical nanoparticles by Chou *et al.* are partially analogous to the thermal behaviour presented here for Ag nanowires.

5.7 Individual Junctions *In-Situ* SEM Observations

In order to further investigate the impact of thermal annealing on silver nanowires, in particular exploring the evolution of individual junctions during thermal annealing, we employed a FEI Quanta 250 environmental Field Emission Scanning Electron Microscope equipped with a thermal stage. This allowed us to observe a specific site of the nanowire network and watch for changes in the nanowire morphology as we exposed the sample to a thermal ramp. The aim was

to observe the morphological changes and identify on a local scale at which temperatures they occur. This section is an updated excerpt of the work which was reported at the EMRS 2013 fall conference and resulted in a proceeding publication in the International Journal of Nanotechnology.[35]

The networks, deposited on p doped silicon in order to prevent charging whilst imaging, were initially heated from room temperature to 600°C, under vacuum conditions (10^{-4} Pa). No morphological changes were observed in this temperature range, even though the nanowires have previously been seen to undergo Rayleigh instability in air at much lower temperature. Heating to above 700°C, the nanowires start to disappear. Figure 5.7 shows the evolution of a given location of the sample at three different temperatures. The traditional morphological changes highlighted earlier in section 5.2 do not appear to occur under vacuum and there is no evidence of local sintering or spheroidization.

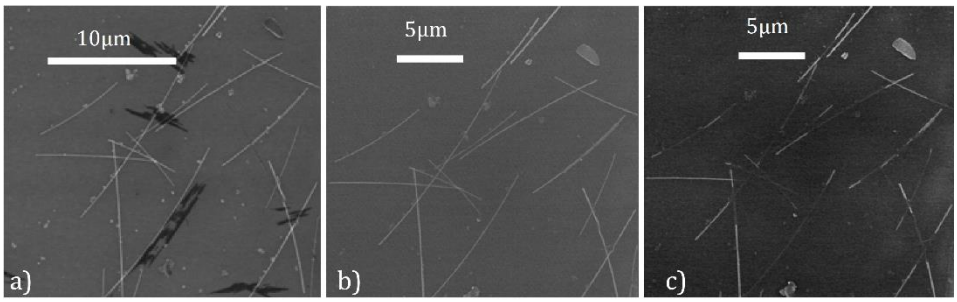

Figure 5.7 In-situ annealing observation of Ag nanowires at different temperatures a) at 30°C, b) at 620°C, and c) at 717°C.

Contrary to what was observed when annealing in air, spheroidization does not occur. Above 700°C, the silver directly evaporates, leaving behind an empty carbonaceous shell. It is suggested that this shell is the remnants of the PVP coating which cannot undergo decomposition under vacuum due to the absence of oxygen. Similar behaviour was also observed by Mayoral et al.[23] under TEM for individual AgNWs. Ramasamy et al.[36] also report similar observations of TiO_2 coated silver nanowires under *in-situ* annealing up to 750°C and ascribe the stability of the wires to the presence of the TiO_2 however, in light of this work and the work of Mayoral it is more likely that the thermal stability observed by Ramasamy is a result of the presence of organic components (in their case 2-mercaptoethanol) and the lack of oxygen during the annealing process. In Chemical Solution Deposition tests performed for the growth of Nb:TiO_2 on silver nanowires we found that the TiO_2 layers were not sufficient to stabilize the wires above 350°C in air but that the wires were stable in vacuum and under forming gas (10% Hydrogen 90% Nitrogen) up to 720°C for at least fifteen minutes.

When considering this behaviour in relation to the network properties when submitted to a thermal treatment, the *in-situ* SEM provides evidence that PVP acts to stabilize the AgNW and prevent morphological changes. In order to assess whether the stability was due to the inherent PVP layer or an interaction with the SEM electron beam, we measured the resistance of a silver nanowire network while annealing under vacuum (0.1 Pa). The nanowires remain stable

under a thermal ramp up to 500°C (temperature limit of the in-situ resistance setup) and a resistance similar to the minimum resistance achieved (at around 320°C) during annealing in air is obtained. The resistance of a sample annealed under vacuum initially remains almost constant until 150°C which corresponds to the glass transition temperature of PVP. This may suggest that some local rearrangement of the PVP can occur without actually removing it from the wires. This rearrangement may allow local relaxation of the wire surfaces between two nanowires at a junction though no sintering is observed.

Due to the presence of the PVP and the absence of oxygen in the SEM chamber it was not possible to observe the morphological changes *in-situ*. This led to the use of atomic force microscopy to attempt to characterise the annealing behaviour of nanowires in air.

5.8 AFM Observations of Individual Junctions Before and After Annealing

Atomic Force Microscopy (AFM) is an excellent technique for exploring the properties of small scale objects and particularly the surface topology of a sample. AFM in itself is an enormous topic which will not be covered here as it is already well known and covered much more thoroughly in published media. If the reader is unfamiliar with this technique (or familiar in practice but not in theory) I would suggest the book *"Atomic Force Microscopy: Understanding Basic Modes and Advanced Applications"* by Greg Haugstad.[37] This text covers the technique in an easy-to-read manner which gently introduces the reader to the physics of AFM before delving into the fundamental mathematical origins of the technique and advanced concepts.

For the purpose of this work we are mainly interested in the height data from silver nanowire networks and its evolution with time and temperature. Due to the physical nature of the AFM tips interaction with the sample there is always a convolution of the tip shape with the sample morphology. Recognizing that this convolution is strongest in the lateral direction we will focus mainly on the height data of the highest points in the regions of interest. As these locations are the least likely to experience variations due to changes in the tip morphology. All height measurements were made relative to average height of the substrate at the closest available location and these locations were kept as constant as possible for each of the consecutive measurements. In this work two different approaches were made for the observation of the impact of thermal annealing. In this section several sites on a sample were measured with AFM before annealing at a given temperature for 30 min, the same sites were then reimaged after the sample had cooled to room temperature. This process was repeated with the same sample at 180°C and 240°C. The second approach is discussed in the following two sections and involved *in-situ* observations of a single site whilst annealing at a range of temperatures in air.

All AFM measurements were performed on an Asylum Research MFP-3D BIO AFM using standard Nanosensors NPP-NHCR Silicon AFM cantilevers with

a guaranteed tip radius <10nm. Heating was achieved with the MFP-3D polymer heating stage which is pictured in Figure 5.8

Figure 5.8 MFP-3D PolyHeater stage, the stage consists of a metal heating element 1.5cm in diameter (centre of the image) surrounded by a Teflon insulating layer (inner black ring) which is then framed by a Polyether ether ketone (PEEK) support (beige outer ring). This heating stage is designed to allow in-situ AFM measurements at elevated temperature in air or a controlled gas environment. Allows heating from room temperature to 300°C.[38]

As described in section 5.2 the silver nanowires are initially coated with residual isopropanol and PVP as a result of the growth process and spin coating. This film of organics varies in thickness depending on the deposition conditions and the length of time since deposition and sample storage conditions. It is expected that thermal annealing will completely remove the organic coating and thus we anticipate that the height profiles of the silver nanowires should decrease relative to the surface of the substrate.

In order to maintain comparability between measurements and to ensure a minimal error in the measurements all heights were referenced to the average substrate level of the image. As much as possible the same locations were measured at room temperature after deposition, after annealing at 180°C and after annealing at 240°C. The images are not perfectly aligned and there is some lateral expansion due to changes in the tip morphology with usage but the height profiles of the highest points are expected to remain accurate. Three images for one of the locations observed are displayed in Figure 5.9. In total six different sites on the sample were observed, allowing for the measurement of 28 different wires and 25 individual junctions. From each set of images each of the individual nanowires was measured to determine the average height of that particular wire, this was achieved using the image processing software Gwyddion. For each nanowire a segment of the nanowire was chosen as the region to measure the average height of the nanowire. The region was selected such that the nanowire was sitting flat on the substrate surface. The same section of the nanowire was measured for each of the three temperatures, within this region the maximum value of each scan line was taken, this provides the highest points along the length of the given nanowire.

The average of these values was then taken to give an average height of that particular wire. For the measurement of junction heights the same process was used but only the highest point in the region of interest was used, i.e. no average was taken. This was done to ensure that the highest point at the junction

site is used as a reference, as the nanowires sag on either side of the junction (unless another junction is close by). . By using the highest point as the reference value of the junction height we ensure that the height changes with temperature observed are associated with the same point.

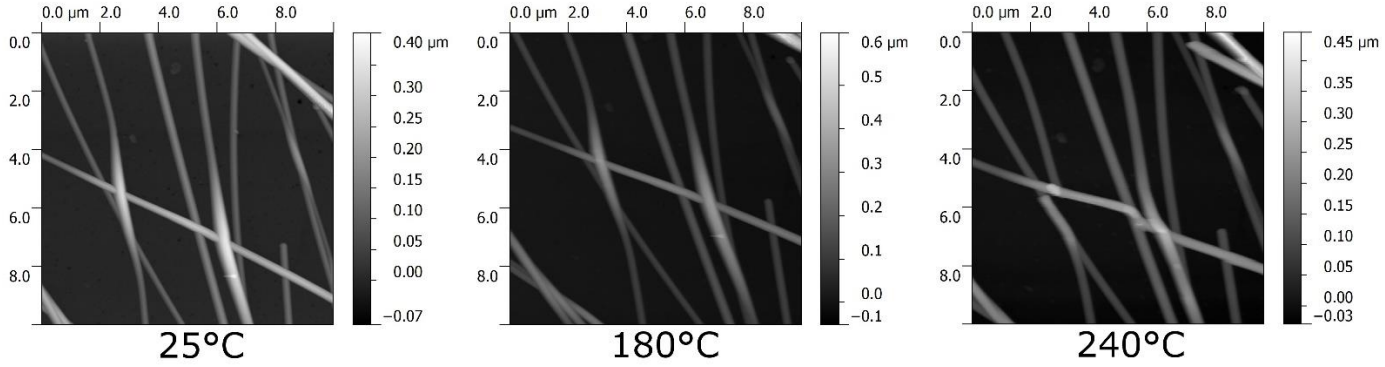

Figure 5.9 AFM images of one of the six sites. From these three images the average heights of the wires and junctions after each temperature were measured. Notice that between the 25°C and 180°C images there are no immediately obvious changes to the network morphology. After annealing at 240°C we can see several changes to the junctions in the centre of the image.

Due to the distribution of wire diameters in the solution there was a range of different wire heights (corresponding to diameters) measured by AFM furthermore as some junctions involved more than one wire the distribution of junction heights was even broader. In order to limit this only junctions involving three or less nanowires were used for the junction height measurements. The wire and junction heights sorted in ascending order of the initial height are displayed in Figure 5.10.

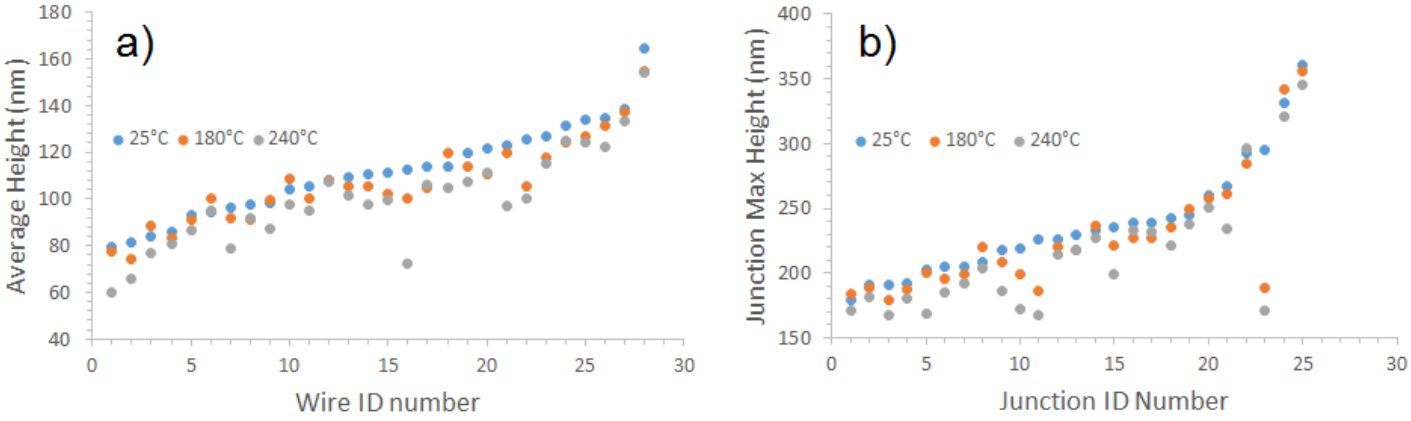

Figure 5.10 a) Average wire height as measured by AFM at 25°C, and after annealing at 180°C and 240°C. b) Maximum junction height in the same conditions as a).

The initial distribution of nanowire heights and the variations in the amount that the nanowires change in thickness after each annealing step is in part due to the random nature of the network formation. As the wires are deposited at room temperature and the boiling point of isopropanol is at 80°C depending on the local environment of the nanowires different thicknesses of isopropanol are left behind. Similarly for the PVP shell the thickness will vary,

initially as the nanowires start growing the concentration of PVP in the growth solution is high as the nanowires grow the PVP adheres to the sides of the wire causing the anisotropic growth as outlined in chapter 1. This depletes PVP from the growth solution and means that new wires forming late in the growth process may have less PVP. These two factors combine to produce a large amount of variability on top of the intrinsic wire diameter distribution. This said, it is still possible to observe the general trend in the data. As shown in Figure 5.10 a) and b) both the wire diameters and junction heights in general decrease as the annealing temperature increases. The initial decrease between 25°C and 180°C is expected to be due to the removal of solvents and low molecular mass organic residues. Between 180°C and 230°C little change is anticipated however thermo gravimetric analysis suggests that a degradation of the PVP begins at around 200°C but significantly increases in rate above 230°C. As shown by a decreased heat flow into the sample and a shift in the mass behaviour as seen in Figure 5.11. The reaction reaches its fastest rate at about 270°C and rapidly tails off by 285°C suggesting that the PVP is completely removed at this stage. As degradation of PVP starts at around 200°C the same result should be achievable by a sustained annealing step at lower temperatures. This is in agreement with the results of the pre-annealing studies.

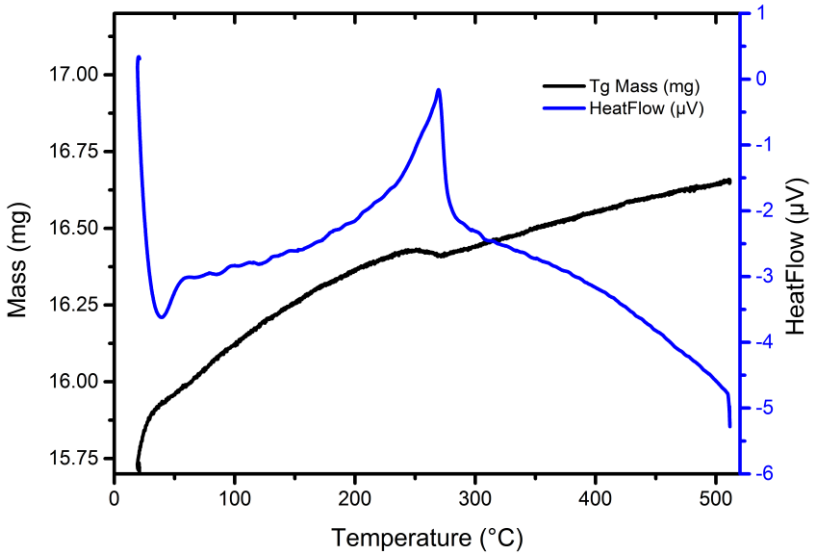

Figure 5.11 Thermo-gravimetric analysis data for PVP coated silver nanowires from room temperature to 500°C.

Taking the average of all wire and junction heights in each of the three conditions (i.e. non annealed and annealed at 180°C and 230°C) allows us to view the trend in a clearer manner these results are shown in Figure 5.12.

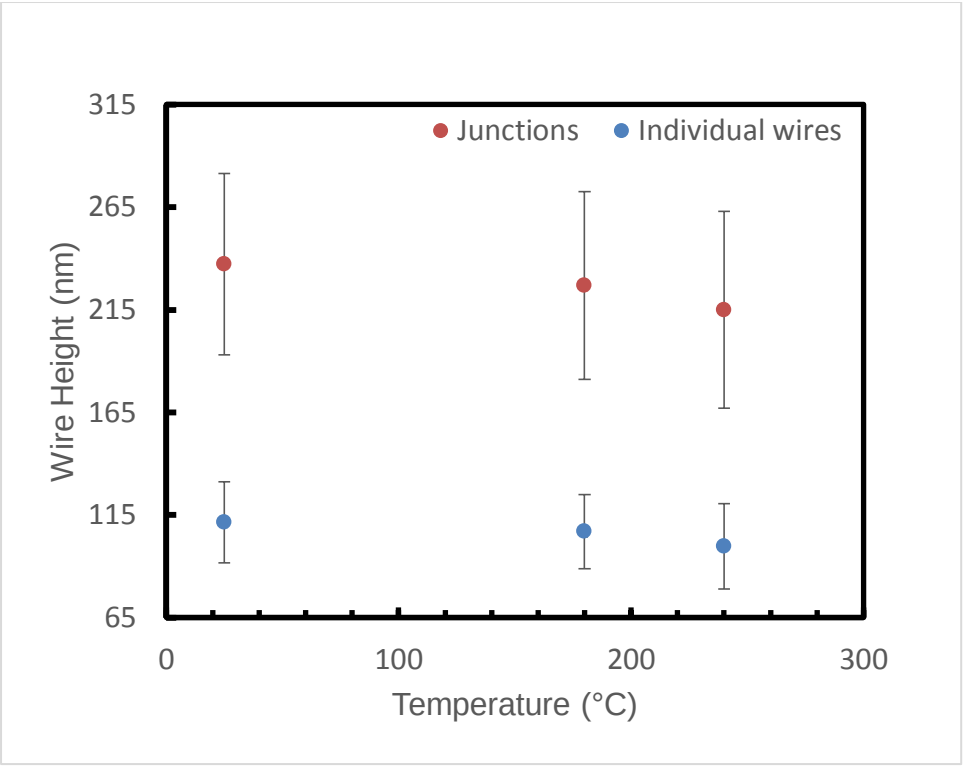

Figure 5.12 Trend observed in *ex-situ* AFM measurements for the as-deposited (25°C) sample, after annealing at 180°C and after annealing at 240°C. Error bars represent one standard deviation of the data at each point.

This confirms the expected behaviour, one may note that the standard deviation is quite large but as mentioned previously this is due to the fact that many different nanowires and junctions have been measured and each wire is unique. As expected the reduction of the junction heights is on average approximately double that of the individual nanowires, however we had also anticipated that it would be possible to observe some local sintering resulting in a junction height that was lower than the combined average width of the two wires involved. On average this was the case with an additional 3.7 nm of height lost over the expected result from a combination of the changes in thickness of the wires involved. However of the 25 junctions investigated only half of them exhibited a reduction in excess of the wire reductions, thus this result is not entirely conclusive. Further studies including a much larger sample of junctions would provide additional information.

5.9 In-situ AFM observation of Thermal Grooving

The second type of AFM performed involved *in-situ* measurements while heating the sample. This measurements are quite challenging as there is a critical balance between the position of the AFM cantilever head relative to the sample whilst heating. One of the advantages of the MFP-3D AFM system is that it does not employ a tube piezo for the *x,y,z* scanning. This allows a complete decoupling of the height scan from the *x* and *y* axes. This is achieved by mounting the sample

on a specific stage with *x* and *y* piezo flexures which allow the substrate to be rastered in the plane of the sample surface. The tip is mounted on a separate cantilever holder which contains the *z* piezo responsible for the control of the cantilever height. The feedback is controlled in the typical way with a four-quadrant light-sensitive diode and a laser reflected off the back of the cantilever tip. The *x* and *y* axes have a 90 μm range of motion and the *z* piezo has a range of 140 μm. The MFP-3D polyheater stage can be used in either an open or closed cell configuration, with the closed cell achieving thermal equilibrium faster and allowing the use of controlled atmospheres. In our case we chose to mimic the open system used in the afore mentioned thermal annealing with *in-situ* resistance studies to view the behaviour of the nanowires, thus the open cell was used.

Whilst heating the sample stage, sample itself and the cantilever head all undergo thermal expansion. If the experiment is not carefully monitored this can result in either a loss of contact with the surface or more likely the crashing of the cantilever into the surface. The MFP-3D is equipped with manual micro-positioning dials to allow a coarse positioning of the sample and movement of the cantilever as the thermal expansion of the apparatus and sample were larger than the *z* range of motion the height had to be constantly monitored to ensure that the *z* axis was in the centre of its range of motion, this was a challenging task as it meant manually manipulating the cantilever head without moving it in the *x* or *y* direction to allow the same location to be measured constantly whilst annealing. Also as a consequence of the heating there was a small amount of thermal drift in the in plane axes as well though typically this was significantly less than the range of motion and could be compensated in part by the AFM software.

The in-situ observations follow two different behaviours. In this section we discuss the thermal grooving of grain boundaries of silver nanowires as observed by AFM in-*situ* during thermal annealing, in the following section we describe the degradation of nanowires and hence the loss of network conductivity. While the thermal annealing studies discussed so far provide insight into the electrical properties of the network as a whole *in-situ* AFM studies allow us to follow the morphological evolution of a few individual wires. While the *ex-situ* SEM images reveal beyond doubt that in the case of a thermal ramp the dominant mechanism for the loss of electrical conductivity is the Rayleigh instability as described in section 5.6 we anticipate that grain boundaries within individual nanowires will fail before spheroidization occurs. It is currently unclear the origin of grain boundaries in silver nanowires, typically the silver nanowires grown by the polyol process wires start from a single seed nanoparticle. The anisotropic growth is maintained by the preferential binding of PVP to the {100} crystal plane, it is expected that this would lead to perfect single crystals without grain boundaries however upon observation by SEM and TEM as shown in Figure 5.13 grain boundaries are observed.

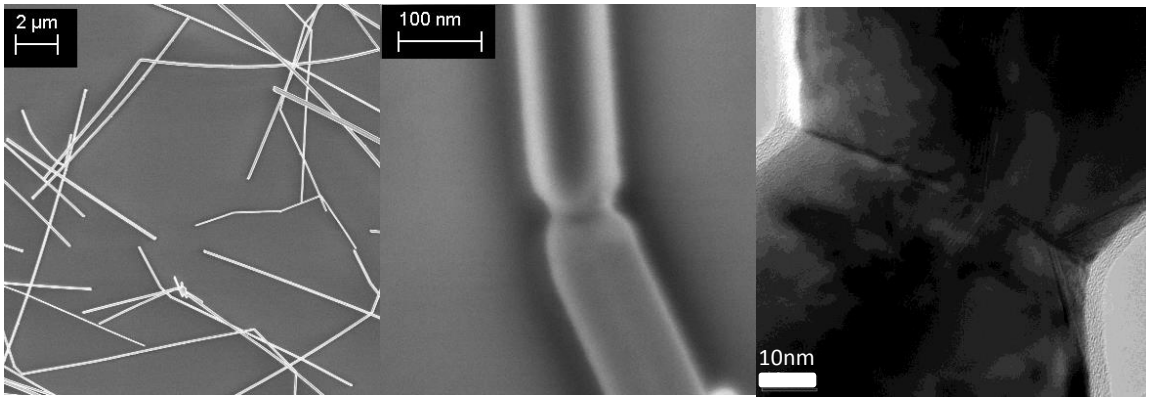

Figure 5.13 Images of silver nanowire grain boundaries. From left to right : low magnification SEM, the grain boundaries can be recognized as distinct kinks in the nanowires, high magnification SEM of an individual grain boundary and TEM image of grain boundary. In the TEM image the PVP can be observed at the edges of the wire. In the centre of the wire it is also possible to observe striations which are related to the five-fold twinned structure of the silver nanowires.

The origin of these grain boundaries is beyond the scope of this thesis but could either arise from the joining of two nanowires during the growth process or surface defects on the exposed {111} growth faces resulting in an offset of the growth direction.

Regardless of their origin grain boundaries are expected to play a role in the electrical behaviour of silver nanowire networks as they will increase the resistance of the wire due to the smaller diameter at the grain boundary and electron scattering associated with the local change in lattice structure. They also present regions which are more likely to degrade under thermal processes. This section aims to observe the process of thermal grooving, as initially reported for crystal grains in polycrystalline metals by Bailey and Watkins[39] and further developed by Mullins[40] by observing a grain boundary during thermal annealing. In traditional thermal grooving atoms migrate away from the grain boundary causing a groove to develop surrounding the grain. In the case of nanowires the thermal grooving is confined to a ring around the central axis of the nanowire resulting in a pinching off of the nanowire as the groove forms. In the opening paragraphs of Mullins paper[40] he introduces the fundamental theory behind the origin of thermal grooving which is the balance of the surface tensions of the two grains with the tension inherent in the grain boundary itself. An equilibrium state is reached when the angle β of the surfaces at the grain boundary relative to the flat surface of the material (in this case the nanowire) is related to the surface free energy γ_s and the boundary free energy γ_b by:[39,40]

$$2\sin\beta = \frac{\gamma_b}{\gamma_s} \quad (5.5)$$

Kudrman and Čadek[41] found values for the ratio γ_b/γ_s of 0.216±0.002, Mullins points out that this equilibrium state is reached by the movement of atoms away from the grain boundary such that the local angles at the interface match β. This flux of atoms results in a ridge next to the junction boundary, this sharp convex ridges produce a high local surface energy and hence tend to preferentially flatten by surface diffusion or evaporation.[40] From AFM

measurements of the angle β we identified ratios of γ_b/γ_s ranging between 0.79 and 1.13. Unfortunately as these measurements were only of a single junction and it is not sufficient to quantitatively compare these results to those of Kudrman and Čadek, however these results are quite large in comparison to the expected ratio for silver. This suggests either a high grain boundary energy or low surface energy. Experimental observations of Cr nanowires supported by a CuAg matrix performed by Raabe and Ge[44] suggests that for grain boundaries in a thin filament such as a nanowire the extent of thermal grooving is exacerbated resulting in deeper thermal grooves and faster groove formation. Recent work by Klinger and Rabkin[42,43] have expanded upon Mullins work to apply it to polycrystalline filaments, however their predictions for stable nanowire radii are still about 1/3 lower than observed experimentally.

Formation and flattening of ridges in close proximity to the grain boundary can be observed in Figure 5.14 as a local maxima which changes size and position as a function of temperature and time. Traditionally this is expected to occur in a symmetric fashion however in this case it is only observed on one side of the grain boundary.

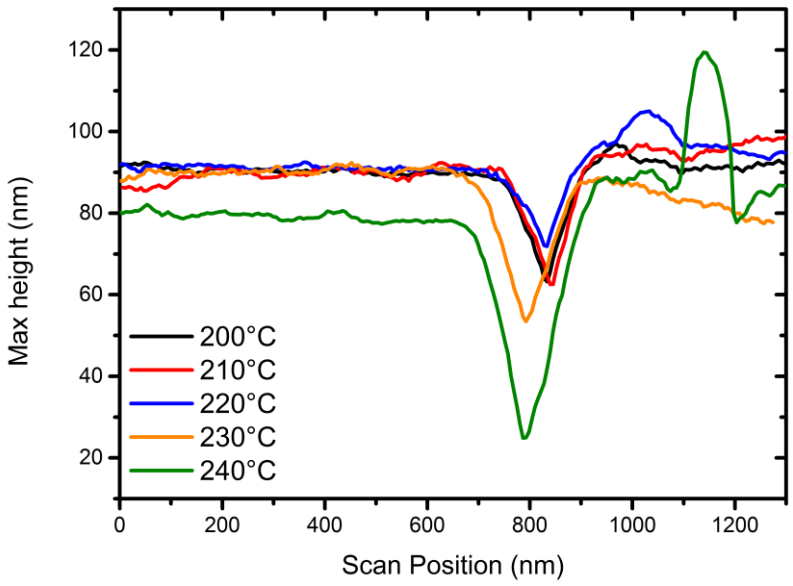

Figure 5.14 AFM profile of the highest points in each scan line across a single nanowire this nanowire came from a batch of nanowires with an average diameter of 105nm and average length of 37.5µm. Nanowire was annealed at each temperature for about 30min.

The flattening and dispersion of this ridge geometry is the as a result of surface energy minimization drives the growth of the thermal groove, as when the material is dispersed it upsets the equilibrium at the grain boundary causing another reconstruction of the surface and leading to the growth of another ridge. This process continues until the ridges are located sufficiently far from the grain boundary that their dissipation no longer impacts the balance of tensions. Due to this mechanism of growth the channel width is proportional to the depth and approximately the same side slopes are observed throughout the thermal groove

growth process. In Figure 5.15 it can be seen that there is little to no change between the 200°C and the 210°C profiles, the 230°C profile presents an increase in the depth and width of the thermal groove and the 240°C presents a decrease in the wire diameter of approximately 10 nm and a significant increase in the groove size. To the right of the groove a significant ridge can be observed this is a result of the increased temperature and the relatively rapid migration of atoms occurring away from the grain boundary. At this temperature the dissipation mechanism for the flattening of the ridges is restricted to surface diffusion as we are too far below the melting point (720°C below the melting point of 960°C) to have a significant vapour pressure. Locally at the grain boundary the meeting of the surface with the grain interface tension creates a high driving force for surface diffusion, hence the atom flux away from the junction is higher than at the surface resulting in the formation of the observed ridge.

All of the heights measured in this section were again taken relative to the glass substrate surface. The sample was heated to a given temperature and held there for 30 minutes while AFM images were obtained, then the temperature was increased by 10°C at a rate of 1°C per minute. Again AFM images were taken during the thermal ramp, however due to thermal expansion as the sample and cantilever were not in equilibrium these images were not reliable so were excluded during the analysis. The grain boundary results in a ring shaped groove around the long axis of the nanowire, in 2D under AFM this is observed as a saddle shaped geometry as seen in Figure 5.15.

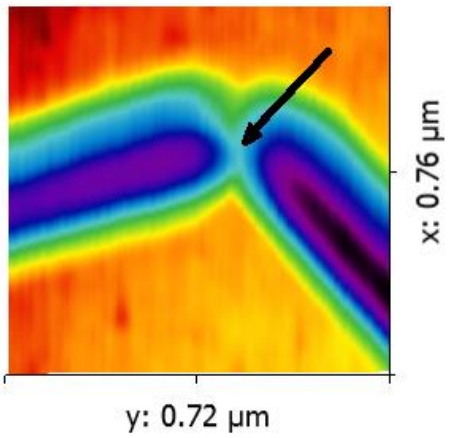

Figure 5.15 AFM image of a grain boundary, colour bands represent regions of similar heights, the approximate position of the saddle point is indicated by the arrow, average wire height would be measured from the average height of the purple section of the wire on the left or the dark brown section of the wire on the right.

For the purpose of observing the evolution of the grain boundary groove under thermal annealing the saddle point of the groove was used as the point of reference. At each temperature several AFM images were taken and the height of the wires and the saddle point were measured for at least 5 separate images at each temperature. The average results at each temperature from these measurements are plotted in Figure 5.16.

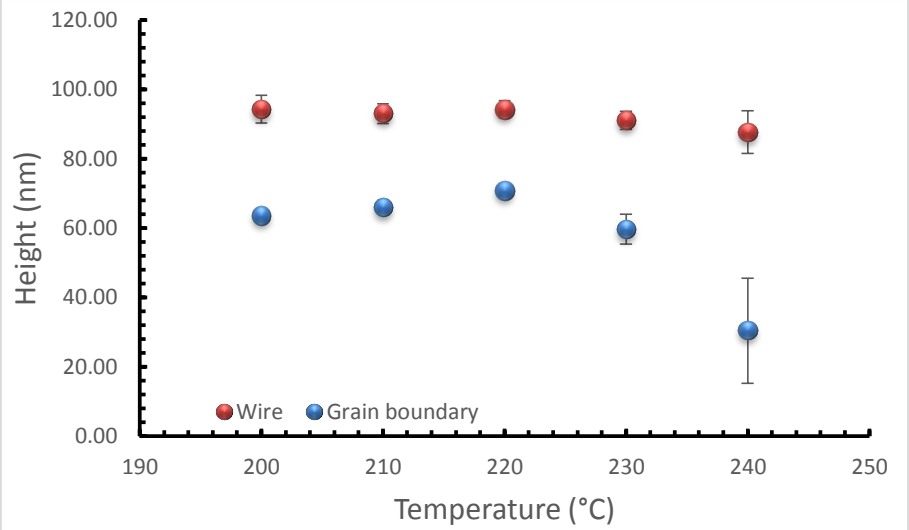

Figure 5.16 Evolution of wire height and thermal groove with temperature. At each temperature the sample was annealed for 30 minutes several AFM images were taken *in-situ*. The data shown here represents the average maximum heights of the nanowires and the average height of the saddle point of the grain boundary. Error bars represent one standard deviation of the averaged data.

The increase in the standard deviation of the results as the temperature increases is likely due to the increased rate of change of the surface morphology. It is clear that the nanowire diameter is stable up until 220°C and then begins to decrease at 230°C and continues decreasing at 240°C. The behaviour is similar for the saddle point of the wire although initially it unexpectedly increases between 200°C and 220°C, the origin of this increase is expected to be an artefact of the imaging technique, this is supported by the loss of detail and lateral smearing observed for the images obtained at 220°C as shown in Figure 5.16. Due to the groove geometry the saddle point height is much more sensitive to changes in the tip than wire height. Initial increase aside the behaviour at 230°C and 240°C is clear: there is a significant decrease in the saddle point height corresponding to an increase in the thermal groove depth and the pinching off of the nanowire at the grain boundary.

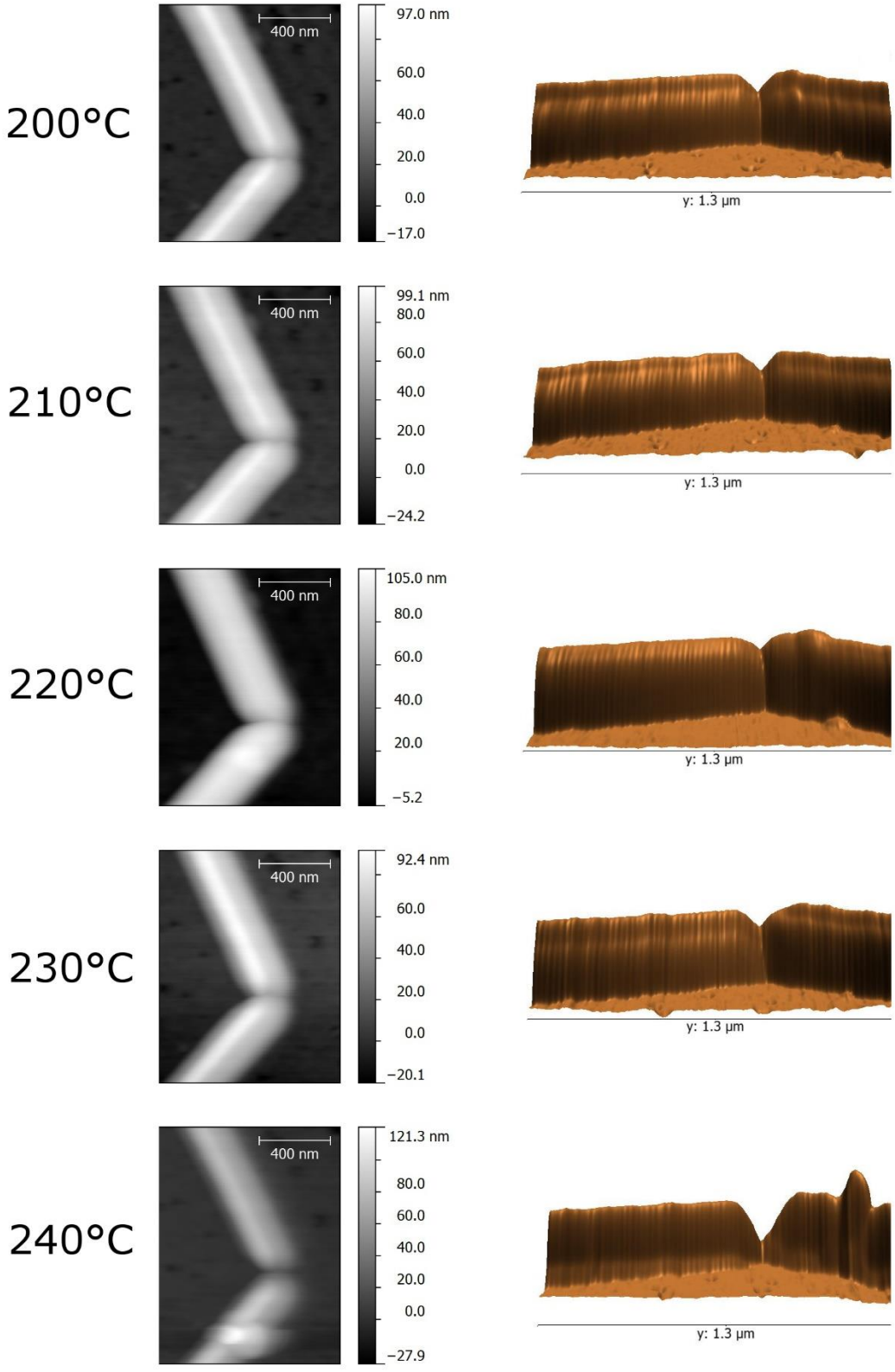

Figure 5.17 AFM images of a single nanowire grain boundary, taken *in-situ* at the temperatures indicated on the left. Images on the right are the 3D profiles viewed at 10° from the plane of the substrate along the line of the grain boundary. The 3D profiles are not all the same scale but act as a guide providing the relative difference from top of the nanowires and the bottom of the trench to the substrate.

These results provide a clear idea of the behaviour of silver nanowires under thermal annealing it is apparent that the thermal grooving has an activation temperature around 230°C above which thermal grooves develop rapidly. Coupling this with the TGA data presented earlier suggests that the PVP provides stabilization against thermal grooving and spheroidization alike.

5.10 Observation of wire break down in-situ

The second *in-situ* AFM experiment focused on the observation of *in-situ* spheroidization. Unfortunately due to constraints of the AFM cantilever head at high temperatures the cantilever holder of the MFP-3D had to be switched to an alternate system in order to go to temperatures above 240°C. This meant that it was no longer possible to observe the same locations as had previously been imaged. The sample was then heated back to 230°C but due to the fact that the PVP had already been removed by the prior thermal annealing process the nanowires were already beginning to undergo spheroidization.

The theory of the Rayleigh instability suggests that a perturbation of the nanowire surface should be observed before the formation of isolated spheres on the surface of the glass substrate as described in section 5.6. In the *ex-situ* experiments the spheroidization is observed after a thermal ramp to 500°C and is quite a beautiful sight with uniform spheres aligned along the previous path of the nanowires.

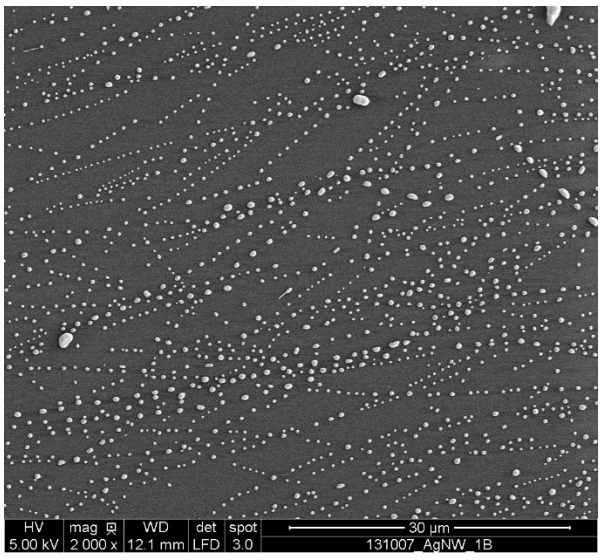

Figure 5.18 Spheroidized nanowire network after being annealed on a thermal ramp of 12°C/min to 500°C. SEM image captured at 2000x magnification using an accelerating voltage of 5.00 kV. Scale bar in the image is 30µm

In the case for the in-situ observation the temperature was significantly lower and a slightly different mechanism was observed. This is most likely due to the extended period of time that the nanowires were annealed in the in-situ experiments. In the ex-situ experiments the temperature was elevated at a rate of 12°C/min constantly and the total annealing time was 40 minutes, in the in-situ

studies the nanowires were annealed at each progressive temperature for 30 minutes giving a total annealing time of over 3 hours. Also as the end temperature was much lower than in the ex-situ case it is possible that we had not provided the system with sufficient energy to complete the morphological change associated with Rayleigh instability. It is possible to see the onset of the Rayleigh instability in the ex-situ AFM discussed in section 5.8 in the form of a periodic perturbation of the nanowire height if an appropriate height scale is selected as shown in Figure 5.18.

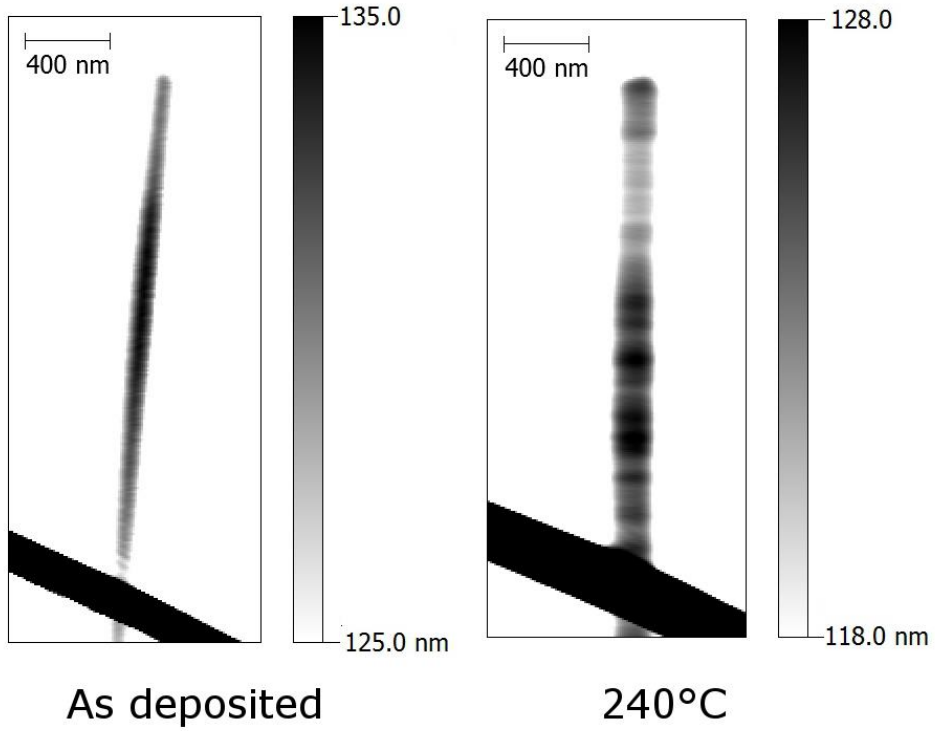

Figure 5.19 A single nanowire as-deposited and after annealing at 180°C and 240°C for half an hour. The height scales in these images as depicted by colour have been restricted to the first 10 nm of the nanowire.

For the as deposited nanowire the height is reasonably uniform along the whole length of the wire, in contrast with the annealed wire we can observe a series of bands of different heights. This is in agreement with the onset of Rayleigh instabilities which should then lead to spheroidization.

However at 230°C once the PVP was removed the degradation observed *in-situ* of the nanowires did not quite reproduce the anticipated uniform spheroidization pattern. As AFM is a rastered imaging technique it takes a certain amount of time to generate each image thus the changes observable in the network during thermal annealing have a rate limit, if they occur faster than the acquisition rate then the steps in the process cannot be observed. Coupling this with the required time for the system to stabilize at thermal equilibrium made *in-situ* observation of the spheroidization a challenging task. To enable imaging a small scan size was selected to minimize the acquisition time, the initial scan location had to be selected blind due to the large initial temperature step (room

temperature to 230°C) the large amount of thermal expansion anticipated meant that the cantilever had to be raised from the surface and manually lowered once the sample reached equilibrium. This type of manual manipulation often results in a shift in scan location due to the design of the MFP-3D. If the mechanical micrometre positioning system was electronically-controlled greater precision may be possible. As the initial position was selected blind some small adjustments were made during the set of scans shown in Figure 5.19. The initial degradation of the wires occurred much faster than anticipated and can be seen already in the first image (A1) time progression is from left to right and then by rows.

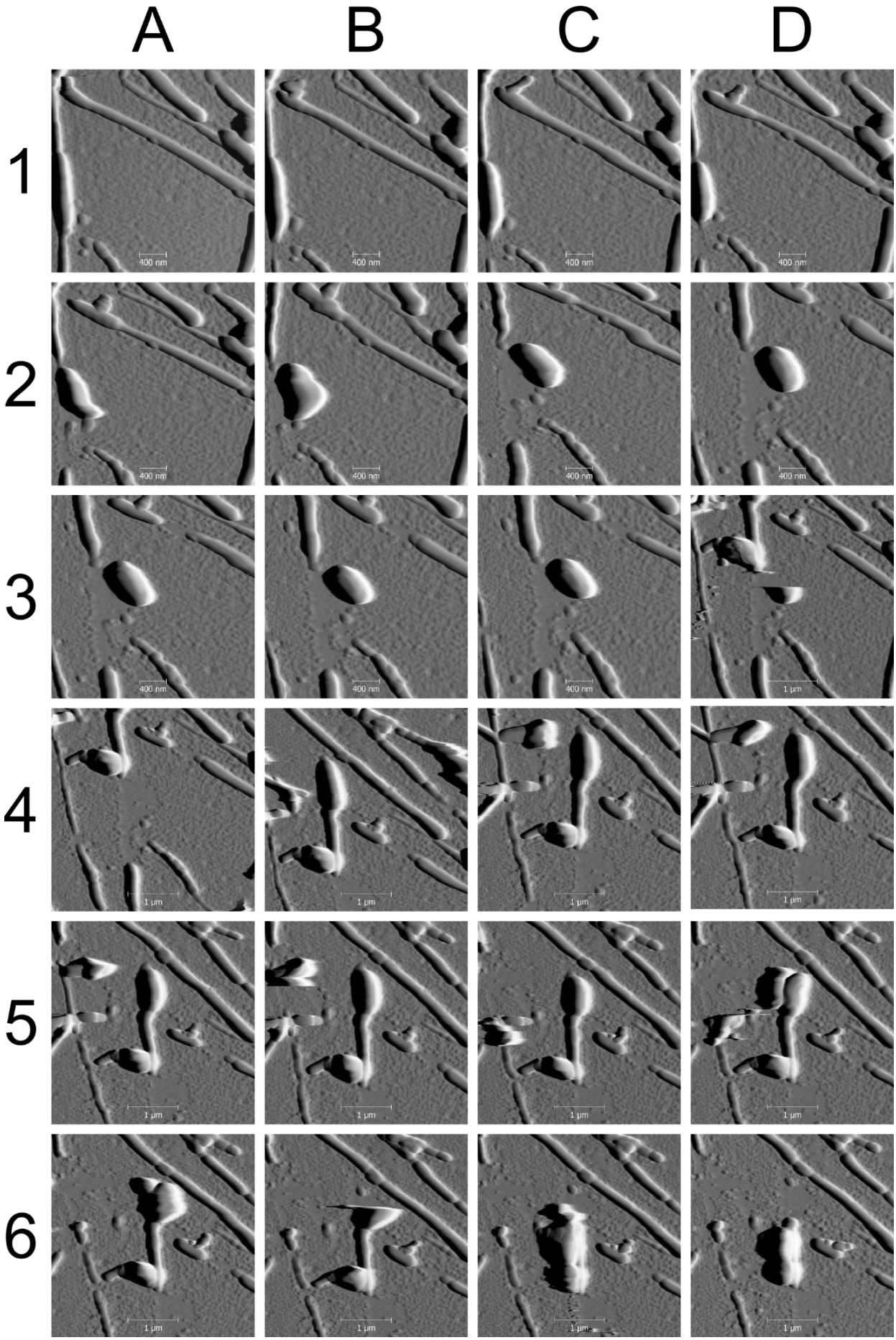

Figure 5.20 In-situ AFM depicting nanowire degradation, amplitude traces are shown.

The series of AFM images in Figure 5.20 shows the degradation of silver nanowires *in-situ*. In row 1 it can be seen that the junction on the left-hand edge of the image breaks and begins to coalesce. In row 2 the droplet coalesces and breaks away from the parent nanowires. It is possible to observe the break down of the diagonally oriented wire in the top right quadrant of images C1 and D1. In row 3 the scanned region on the surface of the sample is shifted slightly to the left over the course of the first 3 images, in the fourth image the scan region is increased and the coalesced droplet changes position during the scan, the scan direction is upward from the bottom of the image. It can be seen that the droplet is initially visible but as the scan crosses its bottom third the droplet is no longer visible. The droplet then reappears attached to the remainder of the top section of its parent nanowire as the scan continues.

In row 4 the scan position is adjusted to bring the parent nanowire that the initial droplet has re-joined into the centre of the scan region, this shift of view reveals that coalescence has also occurred at the junction at the other end of the parent nanowire which was previously out of view. This results in a small section of original nanowire between two large droplets as seen in D4. Partial coalescence can also be observed on the left edge of the images in row 4 with the extension of the diagonal nanowire mentioned previously coalescing into a horizontal 'T' shape in the top left hand quadrant of image C4. This 'T' shape changes slightly in size and is still visible in image A5, just beneath it a segment of wire can be seen that disappears in the following image B5. The droplet formed by the 'T' and this wire moves out of the scan region in image C5 but returns and adheres to the top of the wire segment in the middle of the scan area. The new droplet begins to coalesce with the existing droplet at the top end of the wire segment in image A6, this is quickly followed by the convergence of the top and bottom droplets and the absorption of the remainder of the initial wire, in the remaining images the consolidation of these two droplets can be seen resulting in a decrease in size of the final droplet.

From these observations it is clear that the coalescence occurs faster at the nanowire junctions. Contrary to expectations the nanowires did not spheroidize in the typical manner associated with Rayleigh instability. In the prior AFM images morphological changes in the wires were observed but it appears that at 230°C the thermal energy is still insufficient to provide a perturbation greater than $2\pi r_o$ meaning that the spontaneous degradation of the wires into equally spaced spheres as observed in Figure 5.18 does not occur. Instead, the surface diffusion driven by the reduction of the total surface energy leads to sintering and coalescence at the junctions. This leads to necking of the nanowires near the junction and the reduction of the network conductivity.

These morphological changes only occurred after the complete removal of PVP which was achieved by annealing at 240°C for 30min. Further work is needed to determine the onset temperature for actual spheroidization.

5.11 Closing remarks

The effects of thermal annealing on the electrical properties of AgNW networks were investigated. Several thermal annealing methods including thermal ramp, annealing with successive plateaus and pre-annealing were applied. While the associated kinetics were different in each type of annealing process, the electrical resistance of the network exhibits in all cases a minimum for an annealing temperature spanning from 200 to 320°C. Four physical mechanisms have been identified at the origin of this resistance variation with temperature: desorption of organic residues, desorption/degradation of PVP, local sintering and Rayleigh instability of the NWs. All these mechanisms were discussed and their effects described. Such an investigation enables the determination of the thermal treatment required to produce the minimum electrical resistance for a given NW density. As demonstrated by the pre-annealing study discussed in section 5.5 annealing at 200°C until the resistance is stable produces the minimum resistance for the given nanowire network.

This work clearly demonstrates that thermal annealing can drastically lower the electrical resistance of AgNW network post deposition. For instance annealing an AgNW network fabricated with wires of 105 nm in diameter and 37.3µm in length at 200°C for 2 hours results in a reduction in the sheet resistance from approximately 10^7 Ω/□ to 9.5 Ω/□ associated with an optical transmission of 90% at 550 nm (once the substrate transmission losses are removed) resulting in state-of-the-art transparent electrodes.[20] Moreover sudden drops of the networks' electrical resistance were observed and interpreted as the creation of efficient percolating pathways through the network. A simple model was proposed and describes well the experimental observations. The thermal annealing behaviour was observed *in-situ* in vacuum by SEM and in air by AFM. The behaviour of the wires under these two conditions is very different and is ascribed to the stabilizing nature of the PVP layer which inhibits diffusion of the silver atoms in vacuum. In air this layer undergoes thermal degradation and is removed allowing silver atoms to diffuse and allowing sintering to occur. This is observed in the AFM data as a reduction of the height of the nanowires. Thermal grooving was observed in-situ and found to have a critical temperature below which it does not occur, this was again assigned to the thermal breakdown of PVP and confirmed by TGA. Above 230°C, thermal grooving occurs rapidly resulting in the necking of grain boundaries and the pinching-off of the conduction pathway in this local region, this is expected to be detrimental to the networks conductivity but may not necessarily play a huge role in operational devices as the network density should be sufficiently high enough to allow the current to bypass these regions of high resistance.

In-situ observation of the nanowires at high temperature revealed a different mechanism of degradation than observed from *ex-situ* SEM images of samples subjected to a thermal ramp. Due to the inherent challenges of AFM at high temperature arising from thermal expansion of the sample and the cantilever assembly, it was not possible to perform a similar ramp *in-situ.*

Based on the results of the present research, there is a clear direction that future investigations should focus on improving the thermal stability of nanowires. If one could replace the PVP layer with a thin film which is stable at high temperature in air such as a transparent oxide layer, it could provide an efficient method to prevent morphological instabilities**.** This idea has already been considered with thin transparent oxide films (ZnO or TiO_2) for which higher thermal stability was achieved.[45] Finally the quantitative estimation of the different kinetics involved for each physical mechanism and especially the determination of the surface energy and grain boundary energy would enable better separation of their relative influences and would help identify their importance during thermal annealing. This could yield an efficient way to foresee the evolution of the morphological and electrical properties of metallic nanowire networks as induced by thermal annealing and allow further optimization of the physical properties of metallic nanowire networks.

5.12 References

[1] D. P. Langley, M. Lagrange, G. di
, C. Jiménez, Y. Béchet, N. duy Nguyen, D. Bellet, *Nanoscale* **2014**, In Press.
[2] S. Sorel, P. E. Lyons, S. De, J. C. Dickerson, J. N. Coleman, *Nanotechnology* **2012**, *23*, 185201.
[3] T. Tokuno, M. Nogi, M. Karakawa, J. Jiu, T. T. Nge, Y. Aso, K. Suganuma, *Nano Res.* **2011**, *4*, 1215.
[4] E. C. Garnett, W. Cai, J. J. Cha, F. Mahmood, S. T. Connor, M. Greyson Christoforo, Y. Cui, M. D. McGehee, M. L. Brongersma, *Nat. Mater.* **2012**, *11*, 241.
[5] J.-Y. Lee, S. T. Connor, Y. Cui, P. Peumans, *Nano Lett* **2008**, *8*, 689.
[6] L. Hu, H. S. Kim, J.-Y. Lee, P. Peumans, Y. Cui, *ACS Nano* **2010**, *4*, 2955.
[7] S. B. Sepulveda-Mora, S. G. Cloutier, *J. Nanomater.* **2012**, *2012*, 7.
[8] S. De, T. M. Higgins, P. E. Lyons, E. M. Doherty, P. N. Nirmalraj, W. J. Blau, J. J. Boland, J. N. Coleman, *ACS Nano* **2009**, *3*, 1767.
[9] S. Coskun, E. Selen Ates, H. Emrah Unalan, *Nanotechnology* **2013**, *24*, 125202.
[10] H. S. Shin, J. Yu, J. Y. Song, *Appl. Phys. Lett.* **2007**, *91*, 173106.
[11] H. Li, J. M. Biser, J. T. Perkins, S. Dutta, R. P. Vinci, H. M. Chan, *J. Appl. Phys.* **2008**, *103*, 024315.
[12] H. Wong, *J. Appl. Phys.* **2012**, *111*, 103509.
[13] A. Kim, Y. Won, K. Woo, C.-H. Kim, J. Moon, *ACS Nano* **2013**, *7*, 1081.
[14] L. Kavan, M. Grätzel, J. Rathouský, A. Zukalb, *J. Electrochem. Soc.* **1996**, *143*, 394.
[15] C.-C. Yang, H. Q. Zhang, Y. R. Zheng, *Curr. Appl. Phys.* **2011**, *11*, S147.
[16] H. H. Khaligh, I. A. Goldthorpe, *Nanoscale Res. Lett.* **2013**, *8*, 1.
[17] H. Ibach, *Physics of Surfaces and Interfaces*, Springer, Berlin; New York, **2006**.
[18] Y. Sun, B. Mayers, T. Herricks, Y. Xia, *Nano Lett.* **2003**, *3*, 955.
[19] J. H. Lee, P. Lee, D. Lee, S. S. Lee, S. H. Ko, *Cryst. Growth Des.* **2012**, *12*, 5598.
[20] D. Langley, G. Giusti, C. Mayousse, C. Celle, D. Bellet, J.-P. Simonato, *Nanotechnology* **2013**, *24*, 452001.
[21] A. Bid, A. Bora, A. K. Raychaudhuri, *Phys. Rev. B* **2006**, *74*, 035426.
[22] D. R. Lide, *CRC Handbook of Chemistry and Physics 2004-2005: A Ready-Reference Book of Chemical and Physical Data*, CRC Press, **2004**.
[23] A. Mayoral, L. F. Allard, D. Ferrer, R. Esparza, M. Jose-Yacaman, *J Mater Chem* **2010**, *21*, 893.
[24] R. M. German, *Sintering Theory and Practice*, Wiley, **1996**.

[25] A. Vagnon, O. Lame, D. Bouvard, M. D. Michiel, D. Bellet, G. Kapelski, *Acta Mater.* **2006**, *54*, 513.
[26] K.-S. Chou, K.-C. Huang, H.-H. Lee, *Nanotechnology* **2005**, *16*, 779.
[27] M. E. Toimil Molares, A. G. Balogh, T. W. Cornelius, R. Neumann, C. Trautmann, *Appl. Phys. Lett.* **2004**, *85*, 5337.
[28] S. Karim, M. E. Toimil-Molares, A. G. Balogh, W. Ensinger, T. W. Cornelius, E. U. Khan, R. Neumann, *Nanotechnology* **2006**, *17*, 5954.
[29] J. Plateau, *Transl. Annu. Rep. Smithson. Inst.* **1873**, 1863.
[30] L. Rayleigh, *Proc. Lond. Math. Soc.* **1878**, *s1-10*, 4.
[31] J. Ji, Z. Zhou, X. Yang, W. Zhang, S. Sang, P. Li, *Small* **2013**, *9*, 3014.
[32] C.-P. Hsiung, H.-W. Liao, J.-Y. Gan, T.-B. Wu, J.-C. Hwang, F. Chen, M.-J. Tsai, *ACS Nano* **2010**, *4*, 5414.
[33] P.-G. de Gennes, F. Brochard-Wyart, D. Quéré, *Capillarity and Wetting Phenomena - Drops, Bubbles, Pearls, Waves*, Springer New York, **2004**.
[34] J. P. Naik, K. Das, P. D. Prewett, A. K. Raychaudhuri, Y. Chen, *Appl. Phys. Lett.* **2012**, *101*, 163108.
[35] G. Guisti, D. P. Langley, M. Lagrange, R. Collins, C. Jiménez, Y. Bréchet, D. Bellet, *Int. J. Nanotechnol.* **2014**, *11*, 785.
[36] P. Ramasamy, D.-M. Seo, S.-H. Kim, J. Kim, *J. Mater. Chem.* **2012**, *22*, 11651.
[37] G. Haugstad, *Atomic Force Microscopy: Understanding Basic Modes and Advanced Applications*, John Wiley & Sons, **2012**.
[38] "PolyHeater Dry Sample Thermal Accessory for the MFP-3D AFM Asylum Research Data Sheet 18," can be found under http://www.asylumresearch.com/Products/PolyHeater/PolyHeaterDSHR.pdf, **2014**.
[39] G. L. J. Bailey, H. C. Watkins, *Proc. Phys. Soc. Sect. B* **1950**, *63*, 350.
[40] W. W. Mullins, *J. Appl. Phys.* **1957**, *28*, 333.
[41] J. Kudrman, J. Čadek, *Czechoslov. J. Phys. B* **1969**, *19*, 1337.
[42] L. Klinger, E. Rabkin, *Scr. Mater.* **2005**, *53*, 229.
[43] L. Klinger, E. Rabkin, *Acta Mater.* **2006**, *54*, 305.
[44] D. Raabe, J. Ge, *Scr. Mater.* **2004**, *51*, 915.
[45] F. S. F. Morgenstern, D. Kabra, S. Massip, T. J. K. Brenner, P. E. Lyons, J. N. Coleman, R. H. Friend, *Appl. Phys. Lett.* **2011**, *4*, 183307.
[46] *Accessed 06 July 2013* **n.d.**, *http://www.seashelltech.com/index.shtml*.
[47] Y. Sun, B. Gates, B. Mayers, Y. Xia, *Nano Lett.* **2002**, *2*, 165.
[48] Y. Sun, Y. Xia, *Adv. Mater.* **2002**, *14*, 833.

Conclusions and future work

"The whole purpose of education;
is to turn mirrors into windows"
Sydney J. Harris

Silver nanowire networks are an extremely promising emerging transparent conductive material. However many efforts are still needed to better control and/or optimize their deposition and to better understand the role of the key parameters such as network density, silver nanowire morphology or post-treatments such as thermal annealing on their physical properties. As well efforts should be focused on more fundamental aspects to better understand the physical mechanisms responsible for their properties. The present work provides a general approach and contributes from both experimental and modelling aspects. Despite numerous works devoted to this research topic, much effort is still needed to better understand the percolation mechanisms occurring in these networks particularly in relation to the finite system size and the behaviour of imperfect nanowire systems. Within this work we have developed and demonstrated a range of algorithms which allowed us to reach a better understanding of the onset of percolation in 2D stick networks through simulations. We have introduced several new ideas, which will enable better predictions of the required nanowire density for specific device applications, among which is the introduction of a formula for the calculation of n_{99} and the concept of defining an effective system size L_{seff} to ensure percolation at the required length scale. By combining experimental work with simulations we have developed models for imperfect 2D nanowire networks and demonstrated their pertinence for the interpretation of experimental data. These models notably allowed us to investigate the effects of nanowire length distributions, angular anisotropy and wire curvature on the onset of percolation.

The addition of length distributions to the 2D percolation model results in the reduction of the percolation threshold. This important result is counter-intuitive to what one would expect from looking at the relationship of n_c to L_w which corresponds to the inverse of a parabolic dependence. From that perspective, one would assume that the addition of some small wires and some large ones, such that the average length remains the same, would result in an increase in the critical density. The reason for this behaviour arises from the ability of longer nanowires to connect clusters much more efficiently than the short nanowires. The addition of a length distribution to the simulation results in an increase of the maximum wire length. As the addition of a length distribution results in the reduction of the n_c it appears that the maximum length is more critical than the average wire length.

The results that we present related to the angular anisotropy are in line with expectations: the larger the anisotropy of the system, the higher the critical density becomes. Experimentally we observe that the onset of percolation occurs at a significantly higher density than expected from the 2D ideal stick percolation

simulations; this is likely due to the angular anisotropy induced from the spin-coating deposition method that we used to fabricate our nanowire networks. The impact of the angular distribution on both longitudinal and transverse percolation was explored and it was found that percolation in the longitudinal direction always occurred at a lower density than in the transverse direction. This result is of critical importance to experimentalists as it signifies a potential method to minimise the impact of an angular anisotropy. Ideally one would chose to use a production method which will produce isotropic networks however this is not always feasible. In the case of spin coating and some forms of gravure or Mayer rod coating process, an angular anisotropy in the nanowire network is inherent to the fabrication process, knowing which direction the average angle will be allows the orientation of the electrodes on the surface such that they are perpendicular to the average angle allowing longitudinal percolation.

To our knowledge we present the first instance of the simulation of percolation in a system of curved nanowires. There is still a significant amount of work that needs to be done in this area such as looking at the impact of length distributions on percolation of the curved nanowire system and applying Kirchhoff's laws to estimate the electrical resistance of such systems.

Initial work has been performed on the simulation of the collection efficiency of silver nanowire networks and some key issues related to this field have been identified. A random walk based Monte Carlo method has been developed to estimate the collection efficiency. However at this stage, we were unable to run the simulation on a suitable system size within the time frame of this project. Much work is still needed in order to produce an accurate estimation of the collection efficiency of silver nanowire networks. This could take the form of improvements to the current algorithm, developing a new and faster algorithm or re-writing the current simulation for parallel processing on a supercomputer.

Computer simulations of nanowire networks have shown to be a very useful tool to explore the onset of percolation. Currently, very little work has been done exploring the impact of nanowire density and geometry on the optical properties of such networks. Although our work did not did not focus on the simulation of the optical properties of nanowire networks, it is evident that this is an area to which substantial effort should be dedicated in the future.

Experimentally we have explored several different techniques for the fabrication of silver nanowire networks. We have shown that the use of sonication to disperse nanowires damages them and results in adverse effects on the electro-optical properties of the resulting networks. Through the optimisation of the spin-coating method we were able to obtain nanowire networks with electro-optical properties comparable to that of ITO. In comparison to TCOs, silver nanowires provide a clear advantage due to their flexibility and the possibility to deposit them using low-cost, solution-based, methods. Experimentally, we observe the trend that is predicted by the 2D stick percolation models: as the length of the wires increases the electrical resistance for a given optical transmission decreases. This arises from the decrease in the percolation threshold as the wire length increases. Furthermore we showed that there is a

dependence of the network conductivity on the wire diameter. This result is not expected to be due to changes in the onset of percolation but is much more likely to be due to changes in the resistivity of the silver nanowires as the wire diameter approaches or indeed falls below the mean free path of electrons in the material. We demonstrated this by plotting the resistance of the nanowire networks against a length-normalised effective network density. If the network properties were solely dependent on the nanowire length, all of the curves for different sets of nanowires would overlap in the length normalised density plots, this is true for large diameter wires however when the wire diameter is less than two times the electron mean free path we start observing an increase in the resistance.

Ongoing work is exploring the impact of wire density and wire diameter on the electrical and optical properties of silver nanowires. Currently, we anticipate that the electro-optical properties of silver nanowires will continue to improve as the nanowire synthesis methods are refined to produce longer wires with fixed diameters. As all of the best results presented in this thesis represent networks fabricated via spin coating we anticipate that the fabrication of truly isotropic networks with will lead to a significant reduction in resistance at a given optical transmission. This requires a method which can support the spray deposition of very long nanowires, with minimal use of ultrasonic. Recent works in the literature have shown that this can be achieved with the use of an airbrush type spray head and high pressure. An alternate route that we are currently developing involves an ultrasonic spray head. In this case the nanowires are only exposed to a short pulse of ultrasonic power as they pass through the nozzle of the spray head, this results in the formation of very small droplets and the dispersion of the nanowires within them. We anticipate that this will lead to anisotropic networks without damaging the nanowires. However this project is yet to be completed.

Finally we performed a thorough exploration of the behaviour of silver nanowire networks under thermal annealing. We used two-point-probe measurements to explore the resistance behaviour *in-situ* under thermal annealing and were able to identify several different mechanisms which were responsible for the initial reduction in resistance and final rapid increase. Further work in this field is being undertaken to explore the impact of heating rate and to try to determine the kinetics of each of the mechanisms.

For the first time we have observed the quantised activation of percolation within a physical system of silver nanowires. This original phenomenon was observed when the electrical resistance of the nanowire networks was measured as a function of time on thermal plateaus and as a function of temperature during a thermal ramp. We were able to observe resistance plateaus and drops for which we propose a simple model based on the addition of efficient percolating pathways as resistors in parallel between the two system electrodes. This model provided excellent agreement with the experimental data. Further work related to this phenomenon is now focusing on the influence of nanowire morphology along with experimental trials to really "see" these efficient percolating pathways.

From the observation of different wire diameters under thermal annealing we demonstrated that the maximum thermal load a network can withstand is

diameter-dependent. This fact is related to the diffusion of the silver atoms: for smaller wires there is a much higher ratio of surface to volume and fewer atoms have to move before loss of conductivity occurs. We observed via *in-situ* AFM the process of thermal grooving occurring at a grain boundary in a single nanowire and the morphological evolution of a nanowire network.

Further work should focus on two aspects of the post-treatment of silver nanowire networks. The first one concerns the stabilisation of the nanowires at high temperatures. We have attempted several different methods for achieving this, all based around the encapsulation of the nanowires in a TCO. Unfortunately none of these methods produced reproducibly-stabilised nanowire networks in the case of silver nanowires coated with either ZnO, Al:ZnO or Nb:TiO_2 we found that the thermal stability of the networks was increased slightly but the networks still failed. In trying to match the requirements for the use of silver nanowires in TiO_2 dye sensitized solar cells we recognised the need for nanowire networks to with stand a temperature of 450°C for at least 1 hr. At this stage this is not achievable, however from the work that we have undertaken we believe that it will be possible to stabilise the nanowires if the PVP layer is completely removed first and the deposition of the oxide can be performed below 200°C. The second focus should be looking at non-thermal nanowire network treatments. Some of the devices for which transparent conductive materials are desired are very sensitive to thermal loads, such as organic solar cells, CIGS and CZTS solar cells. Therefore, improving non-thermal methods to optimise the electrical properties could open new applications to the use of silver nanowire networks.

In conclusion, we believe that silver nanowires represent a very promising emergent transparent conductive material which will continue to find growing applications over the next few years. While no one material will be able to satisfy all of the demands of applications requiring transparent electrodes, we suggest that silver nanowires will play a key role in the future of this field.